NASA Tech Briefs

National
Aeronautics and
Space
Administration

See Page A2
For Information About the
NASA Technology Utilization
Special Publications List.

A heat-reflecting film, originally developed to protect spacecraft from intense solar radiation, is now a commercially-available window coating that sharply reduces air conditioning costs. The thin metalized film blocks the Sun's rays, limits the escape of room heat, and protects draperies, carpets, and other furnishings from Sun fading. *[See page A1.]*

Vol. 4, No. 2

SUMMER 1979

About the NASA Technology Utilization Program

The National Aeronautics and Space Act of 1958, which established NASA and the United States civilian space program, requires that "The Administration shall provide for the widest practicable and appropriate dissemination of information concerning its activities and the results thereof."

To help carry out this objective, NASA's Technology Utilization (TU) Program was established in 1962. Now, as an element of NASA's Technology Transfer Division, this program offers a variety of valuable services to help transfer aerospace technology to nonaerospace applications, thus assuring American taxpayers maximum return on their investment in space research; thousands of spinoffs of NASA research have already occurred in virtually every area of our economy.

The TU program has worked for engineers, scientists, technicians, and businessmen; and it can work for you.

NASA Tech Briefs

Tech Briefs is published quarterly and is free to engineers in U.S. industry and to other domestic technology transfer agents. It is both a current-awareness medium and a problem-solving tool. Potential products . . . industrial processes . . . basic and applied research . . . shop and lab techniques . . . computer software . . . new sources of technical data . . . concepts . . . can be found here. The short section on New Product Ideas highlights a few of the potential new products contained in this issue. The remainder of the volume is organized by technical category to help you quickly review new developments in your areas of interest. Finally, a subject index makes each issue a convenient reference file.

Further Information on Innovations

Although some new technology announcements are complete in themselves, most are backed up by Technical Support Packages (TSP's). TSP's are available without charge and may be ordered by simply completing a TSP Request Card found at the back of this volume. Further information on some innovations is available for a nominal fee from other sources, as indicated. In addition, Technology Utilization Officers at NASA Field Centers will often be able to lend necessary guidance and assistance.

Patent Licenses

Patents have been issued to NASA on some of the inventions described, and patent applications have been submitted on others. Each announcement indicates patent status, if applicable.

Other Technology Utilization Services

To assist engineers, industrial researchers, business executives, city officials, and other potential users in applying space technology to their problems, NASA sponsors Industrial Applications Centers. Their services are described on page A6. In addition, an extensive library of computer programs is available through COSMIC, the Technology Utilization Program's outlet for NASA-developed software.

Applications Program

NASA conducts applications engineering projects to help solve public-sector problems in such areas as safety, health, transportation, and environmental protection. Applications teams, staffed by professionals from a variety of disciplines, assist in this effort by working with Federal agencies and health organizations to identify critical problems amenable to solution by the application of existing NASA technology.

Reader Feedback

We hope you find the information in *NASA Tech Briefs* useful. A reader-feedback card has been included because we want your comments and suggestions on how we can further help you apply NASA innovations and technology to your needs. Please use it; or if you need more space, write to the Director, Technology Transfer Division, P. O. Box 8757, Baltimore/Washington International Airport, Maryland 21240.

NASA Tech Briefs

National Aeronautics and Space Administration

SUMMER 1979
Volume 4, Number 2

COVERS: The photographs on the front and back covers illustrate developments by NASA and its contractors that resulted in commercial and nonaerospace spinoffs. You can use the TSP Request Card at the end of this issue to learn more about the Reflecting Film [Circle 81] and Collapsible Tower [Circle 82].

About This NASA Publication

NASA Tech Briefs, a quarterly publication, is distributed free to qualified U.S. citizens to encourage commercial application of U.S. space technology. For information on publications and services available through the NASA Technology Utilization Program, write to the Director, Technology Transfer Division, P. O. Box 8757, Baltimore/Washington International Airport, Maryland 21240.

"The Administrator of National Aeronautics and Space Administration has determined that the publication of this periodical is necessary in the transaction of the public business required by law of this Agency. Use of funds for printing this periodical has been approved by the Director of the Office of Management and Budget."

Change of Address

If you wish to have NASA Tech Briefs forwarded to your new address, use one of the Subscriptions cards enclosed in the back of this volume of NASA Tech Briefs. Be sure to check the appropriate box indicating change of address.

Communications Concerning Editorial Matter

For editorial comments or general communications about NASA Tech Briefs, you may use the Feedback card in the back of NASA Tech Briefs, or write to: The Publications Manager, Technology Transfer Division (ETD-6), NASA Headquarters, Washington, DC 20546. Technical questions concerning specific articles should be directed to the Technology Utilization Officer of the sponsoring NASA Center (addresses listed on page A4).

NASA Technology-Utilization Special-Publications List

A pricelist of NASA Technology Utilization Publications in the SP-5000 series may be obtained by circling 80 on the TSP Request Card at the back of this issue. The list covers over 250 reports, handbooks, surveys, compilations, and other special publications.

Acknowledgements

NASA Tech Briefs is published quarterly by the National Aeronautics and Space Administration, Technology Utilization Branch, Washington, DC: Administrator: **Robert A. Frosch;** Director, Technology Transfer Division: **Floyd I. Roberson;** Publications Manager: **D. W. Orrick.** Prepared for the National Aeronautics and Space Administration by **Logical Technical Services Corp.:** Editor-in-Chief: **Graham L. Gross;** Art Director: **Ernest Gillespie;** Managing Editor: **Jay Kirschenbaum;** Senior Editor: **Donald Blattner;** Chief Copy Editor: **Oden Browne;** Staff Editors: **Ted Selinsky, George Watson;** Graphics: **Bruce Appel, Concetto Auditore, Judy Tenenbaum;** Editorial & Production: **Richard Johnson, Rose Giglietti, Vincent Susinno, John Tucker, Madeline Tucker, Ernestine Walker.**

NASA TU SERVICES

THE NASA TECHNOLOGY UTILIZATION OFFICERS

They will help you apply the innovations described in Tech Briefs.

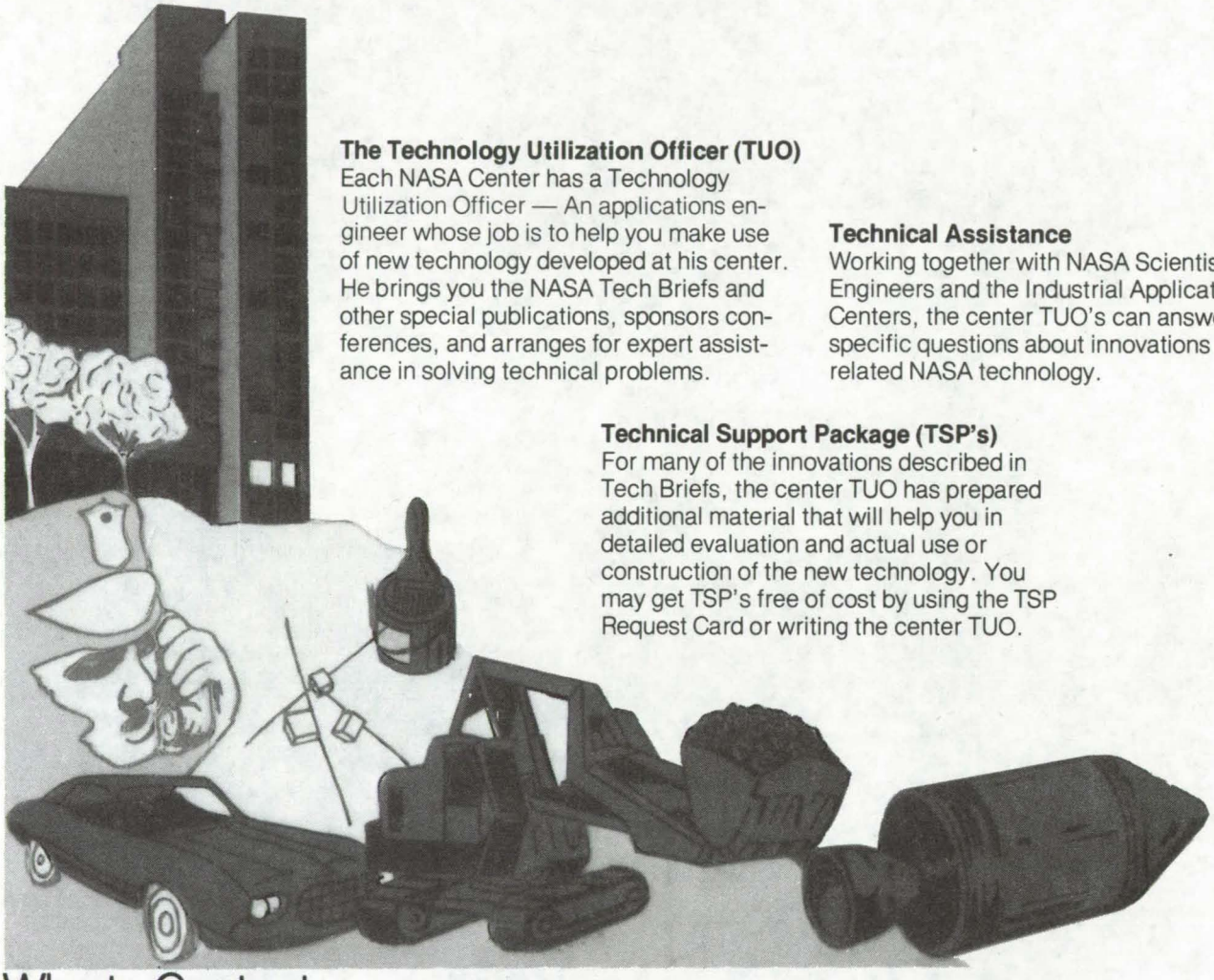

The Technology Utilization Officer (TUO)
Each NASA Center has a Technology Utilization Officer — An applications engineer whose job is to help you make use of new technology developed at his center. He brings you the NASA Tech Briefs and other special publications, sponsors conferences, and arranges for expert assistance in solving technical problems.

Technical Assistance
Working together with NASA Scientists and Engineers and the Industrial Applications Centers, the center TUO's can answer specific questions about innovations and related NASA technology.

Technical Support Package (TSP's)
For many of the innovations described in Tech Briefs, the center TUO has prepared additional material that will help you in detailed evaluation and actual use or construction of the new technology. You may get TSP's free of cost by using the TSP Request Card or writing the center TUO.

Who to Contact. Of course, many technical questions about Tech Briefs are answered in the TSP's, but when no TSP is available, or you have further questions, write the Technology Utilization Officer at the center that sponsored the research at the address listed below.

Charles K. Kubokawa
Ames Research Center
Code AU: 240-2
Moffett Field, CA 94035
(415) 965-5554

Gussie Anderson (TU Office)
Hugh L. Dryden Flight Research Center
Post Office Box 273
Edwards, CA 93523
(805) 258-3311, Ext. 787

Donald S. Friedman
Goddard Space Flight Center
Code 702.1
Greenbelt, MD 20771
(301) 344-6242

John T. Wheeler
Johnson Space Center
Code AT3
Houston, TX 77058
(713) 483-3809

Raymond J. Cerrato
John F. Kennedy Space Center
Code SA-RTP
Kennedy Space Center, FL 32899
(305) 867-2780

John Samos
Langley Research Center
Mail Stop 139A
Hampton, VA 23665
(804) 827-3281

Paul Foster
Lewis Research Center
21000 Brookpark Rd.
Cleveland, OH 44135
(216) 433-4000, Ext. 6832

Aubrey D. Smith
Marshall Space Flight Center
Code AT01
Marshall Space Flight Center, AL 35812
(205) 453-2224

Technology Utilization Officer
NASA Resident Legal Office-JPL
4800 Oak Grove Drive
Pasadena, CA 91103
(213) 354-6420

Gilmore H. Trafford
Wallops Flight Center
Wallops Island, VA 23337
(804) 824-3411, Ext 201

D. W. Orrick
NASA Headquarters
Code ETD-6
Washington, DC 20546
(202) 755-2244

COSMIC

(Computer Software Management & Information Center)

AN ECONOMICAL SOURCE OF COMPUTER PROGRAMS DEVELOPED BY THE GOVERNMENT.

COSMIC is sponsored by NASA to give you access to over 1400 computer programs developed by NASA and the Department of Defense, and selected programs from other government agencies. It is one of the Nation's largest software libraries.

COSMIC charges very reasonable fees for programs to help cover part of their expenses—and NASA pays for the remainder. Programs generally cost from $500 to $1000, but a few are more expensive and many are less. Documentation is available separately and very inexpensively.

COSMIC collects and stores software packages, insures that they are complete, prepares special announcements (such as Tech Briefs), publishes an indexed software catalog, and reproduces programs for distribution. COSMIC helps customers to identify their software needs, follows up to determine the successes and problems, and provides updates and error corrections. In some cases, NASA engineers can offer guidance to users in installing or running a program.

COSMIC programs range from management (pert scheduling) to information science (retrieval systems) and computer operations (hardware and software). Hundreds of engineering programs perform such tasks as structural analysis, electronic circuit design, chemical analysis, and design of fluid systems. Others determine building energy requirements, optimize mineral exploration, and draw maps of water-covered areas using NASA satellite data. In fact, the chances are, if you use a computer, you can use COSMIC.

COSMIC is eager to help you get the programs you need. For more information about services or software available from COSMIC, fill out and mail the COSMIC Request Card in this issue.

COSMIC: Computer Software Management and Information Center

Suite 112, Barrow Hall, University of Georgia, Athens, Georgia 30602 Phone: (404) 542-3265

WHERE IS THE WORLD'S LARGEST BANK OF TECHNICAL DATA ?

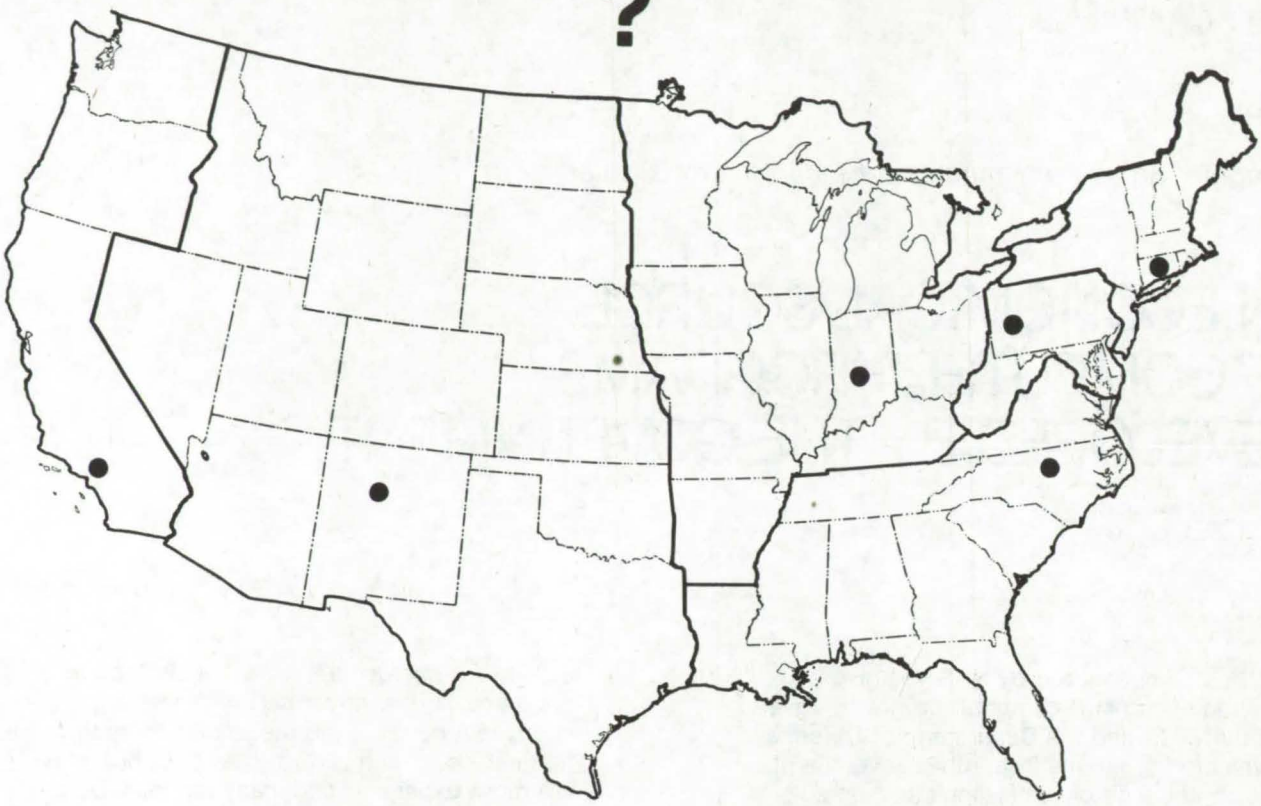

It's in Bloomington and Pittsburgh, it's in Storrs, Connecticut and Research Triangle Park, North Carolina; and it's in Albuquerque and Los Angeles.

NASA IAC's — INDUSTRIAL

You can get more information and more data on more technical subjects through NASA's network of IAC's than anywhere else in the world. About 8,000,000 documents and growing at the rate of 50,000 more each month!

Major sources include:

- 750,000 NASA Technical Reports
- Selected Water Resources Abstracts
- NASA Scientific and Technical Aerospace Reports
- Air Pollution Technical Information Center
- NASA International Aerospace Abstracts
- Chem Abstracts Condensates
- Engineering Index
- Nuclear Science Abstracts
- NASA Tech Briefs
- Government Reports Announcements

and many other specialized files on food technology, textile technology, metallurgy, medicine, business, economics, social sciences, and physical science.

The IAC's are one of the most economical ways of staying competitive in today's world of exploding technology. The help available from the network ranges from literature searches through expert technical assistance.

Literature Searches

Help in designing your search, typically from 30 to 300 abstracts in as narrow or broad an area as you need, and complete reports when you need them. The most complete "search before research" available!

Current Awareness

Consult with our applications engineers to design your personal program — selected monthly or quarterly abstracts on new developments in your speciality. It's like having your own journal!

Technical Assistance

Our applications engineers will help you evaluate and apply your literature-search results. They can help find answers to your technical problems and put you in touch with scientists and engineers at NASA Field Centers.

To obtain more information about how NASA's IAC's can help you —
Check the IAC box on the TSP Request Card in this issue,
Or write or call the IAC nearest you.

APPLICATIONS CENTERS

How to get reports and other documents discussed in this issue of Tech Briefs

Many of the innovations in Tech Briefs are described in detail in reports available at a reasonable cost through one or more of the IAC's. To order a report, call or write the IAC referenced at the end of the Tech Brief article at the address below. Be sure to list the titles and accession numbers (N76-..., N75-..., etc.) of those you wish to purchase.

Aerospace Research Application Center (ARAC)
Indiana University-Purdue University at Indianapolis
1201 E. 38th St.
Indianapolis, IN 46205
E. Guy Buck, Director
(317) 264-4644

Knowledge Availability Systems Center (KASC)
University of Pittsburgh
Pittsburgh, PA 15260
Dr. Edmond Howie, Director
(412) 624-5211

New England Research Application Center (NERAC)
Mansfield Professional Park
Storrs, CT 06268
Dr. Daniel U. Wilde, Director
(203) 486-4533

North Carolina Science & Technology
Research Center (NC/STRC)
P. O. Box 12235
Research Triangle Park, NC 27709
Peter J. Chenery, Director
(919) 549-0671

Technology Application Center (TAC)
University of New Mexico
Albuquerque, NM 87131
Stanley A. Morain, Director
(505) 277-4000

NASA Industrial Application Center
Denney Research Building - 3rd Fl.
University of Southern California
University Park
Los Angeles, CA 90007
Dr. Robert Y. Mixer, Director
(213) 741-6132

NASA INVENTIONS AVAILABLE FOR LICENSING

Over 3,500 NASA inventions are available for licensing in the United States - both exclusive and nonexclusive.

Nonexclusive Licenses

Nonexclusive licenses for commercial use are encouraged to promote competition and to achieve the widest use of inventions. They must be used by a negotiated target date but are usually royalty free.

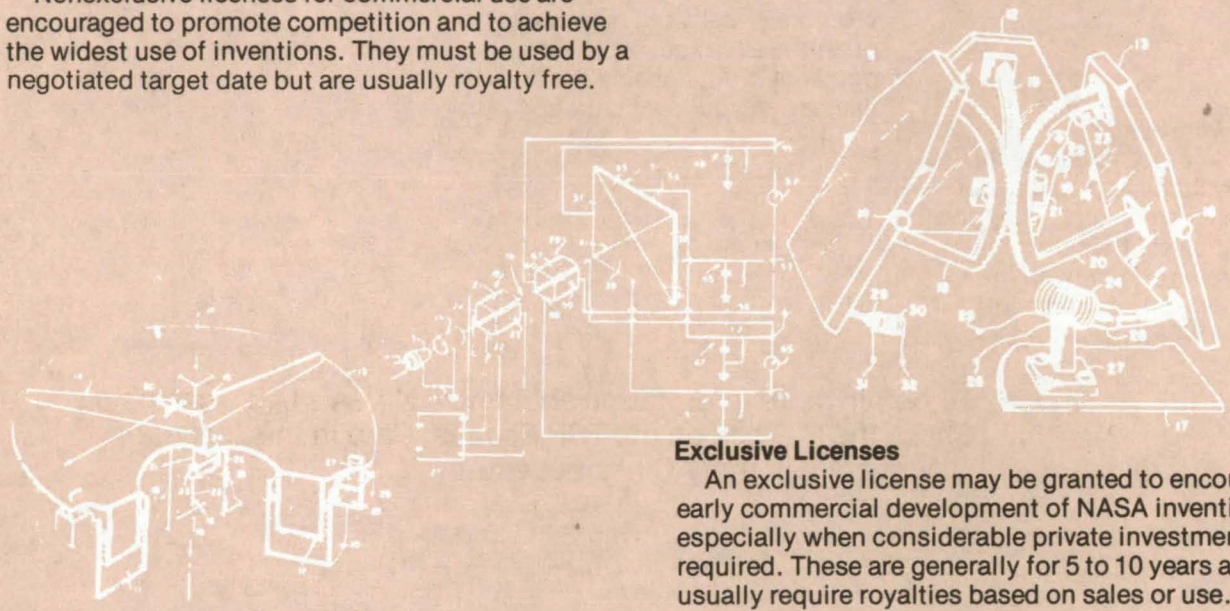

Exclusive Licenses

An exclusive license may be granted to encourage early commercial development of NASA inventions, especially when considerable private investment is required. These are generally for 5 to 10 years and usually require royalties based on sales or use.

The NASA patent licensing program also provides for licensing of NASA-owned foreign patents. In addition to inventions described in Tech Briefs, "NASA Patent Abstract Bibliography," containing abstracts of all NASA inventions, can be purchased from: National Technical Information Service, Springfield, Va., 22161. This document is updated semi-annually.

Patent Licenses and the NASA Tech Brief

Many of the inventions reported in Tech Briefs are patented or are under consideration for a patent at the time they are published. When this is the case, the current patent status is described at the end of the article; otherwise, there is no statement about patents. **If you want to know more about the patent program or are interested in license for a particular invention, write the Patent Counsel at the NASA Field Center** that sponsored the research. Be sure to refer to the NASA reference number in parenthesis at the end of the Tech Brief.

Gayle Parker
NASA Headquarters, Code GP-4
400 Maryland Ave., S.W.
Washington, DC 20546
(202) 755-3954

Darrell G. Brekke
Ames Research Center
Mail Code: 200-11A
Moffett Field, CA 94035
(415) 965-5104

John O. Tresansky
Goddard Space Flight Center
Mail Code: 204
Greenbelt, MD 20771
(301) 344-7351

Marvin F. Matthews
Lyndon B. Johnson Space Center
Mail Code: AM
Houston, TX 77058
(713) 483-4871

James O. Harrell
John F. Kennedy Space Center
Mail Code: SA-PAT
Kennedy Space Center, FL 32899
(305) 867-2544

Howard J. Osborn
Langley Research Center
Mail Code: 279
Hampton, VA 23665
(804) 827-3725

Norman T. Musial
Lewis Research Center
Mail Code: 500-311
21000 Brookpark Road
Cleveland, OH 44135
(216) 433-4000 ext. 346

Leon D. Wofford, Jr.
George C. Marshall Space Flight Center
Mail Code: CC01
Marshall Space Flight Center, AL 35812
(205) 453-0020

Monte F. Mott
NASA Resident Legal Office
Mail Code: 180-601
4800 Oak Grove Drive
Pasadena, CA 91103
(213) 354-2700

NEW PRODUCT IDEAS

NEW PRODUCT IDEAS are just a few of the many innovations described in this issue of NASA Tech Briefs and having promising commercial applications. Each is discussed further on the referenced page in the appropriate section in this issue. If you are interested in developing a product from these or other NASA innovations, you can receive further technical information by requesting the TSP referenced at the end of the full-length article or by writing the Technology Utilization Office of the sponsoring NASA center (see page A4). NASA's patent-licensing program to encourage commercial development is described on page A8.

Extra-Safe Tractor-Trailer Coupling

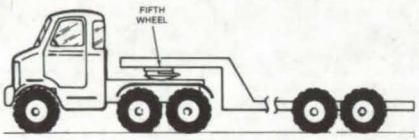

Improvements in the conventional "fifth-wheel" coupling found on tractor-trailers prevent the rig from separating in the event of kingpin failure. A curved lip and matching slot are added to the upper and lower wear plates along with two stop mechanisms that lock the lip and slot together. The stop mechanisms, which automatically latch when the fifth wheel is coupled, keep the wear plates together even if the kingpin should shear while in service. A lever on each stop mechanism is thrown horizontally to disconnect the coupling.
(See page 271.)

System Controls a Wide Range of Flow Rates

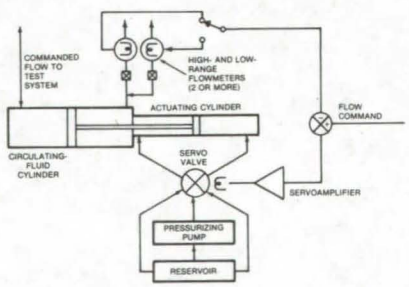

A new flow-control system regulates slow fluid flows from a high-pressure (20,000-psi) source. The rates are accurately metered from 2 ml/min to 3.785 l/min. As part of a laboratory instrument system to measure the properties of fluids analogous to those encountered in deep drilling operations, the system utilizes a servo-controlled valve to admit only enough fluid to an actuating cylinder to deliver the required flow in the instrument system. The servo valve effectively separates the flow-rate control from the pressurizing source, ensuring accuracy over a wide range of flow rates.
(See page 262.)

Monitoring Hydrazine and NO_2

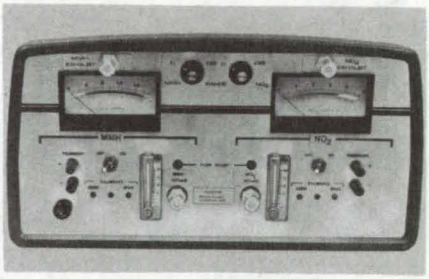

Two highly toxic gases — hydrazine and nitrogen dioxide — are detected in the air at concentrations as low as a few parts per million by a new family of inexpensive instruments. The instruments, two of which are portable and one of which mounts on a wall, use electrochemical cells as gas detectors. The sensing electrode (one of three in each detector) is porous and contains a catalyst specifically chosen for the gas to be sensed. Air diffuses through the electrode into the electrolyte where the electrochemical reaction generates a current proportional to the concentration of the gas. The portable versions of the detector weigh only 3.5 pounds, and they can be calibrated in the field. An alarm sounds if the concentration exceeds the maximum safe level.
(See page 222.)

Extra-Strong Floating Nut

A new "floating-nut" retainer can withstand up to 700 pound-inches of torque applied to a 3/8-in. bolt, nearly three times the maximum torque allowable with a previous design.

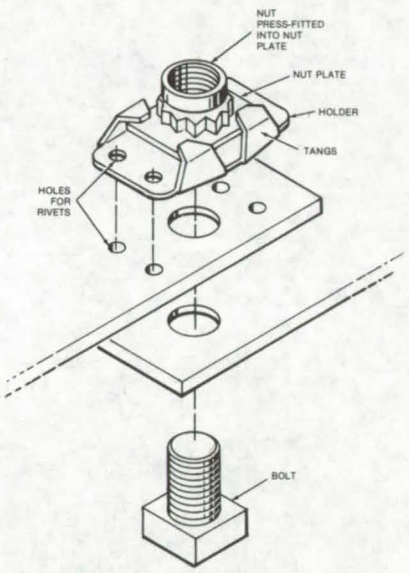

Potentially useful in any application demanding high torque for bolt tightening where the parts are accessible from one side only (such as on tractors, cranes, and other heavy-duty equipment), the retainer achieves higher load-bearing capability by using a nut plate and holder with ellipitically-contoured mating surfaces. Thus, without complicating the design, the effective bearing area is increased to support higher torques. As with conventional floating-nut retainers, parts can be joined even if the matching boltholes are not precisely alined.
(See page 283.)

High-Temperature Self-Lubricating Bearings

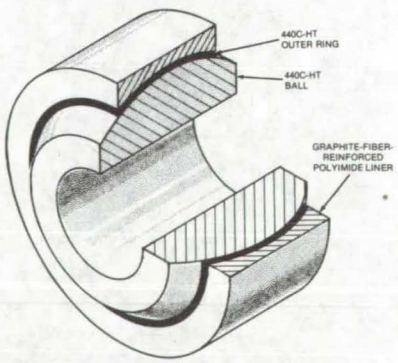

Self-lubricating spherical bearings with increased service temperatures are produced by molding graphite-fiber/polyimide composite into the space between the ball and race. A prepolymer-resin/fiber mix is transfer-molded into the space, and polymerization is completed under heat and pressure. As compared to previous self-lubricating bearing liners that are limited to low-temperature service (below 325° F), the new bearings are practical up to 608° F. Dynamic load capacities are adequate for many applications, and friction coefficients decrease with temperature from the range 0.15 to 0.20 at room temperature to 0.05 to 0.10 at 608° F.
(See page 274.)

Transducer Has a Sense of "Touch"

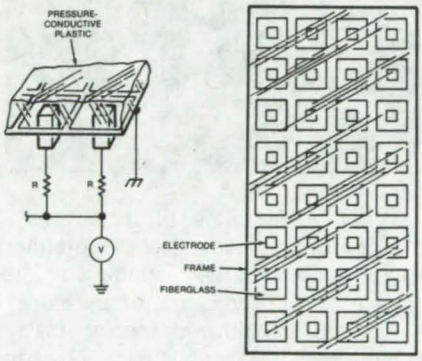

A matrix of pressure sensors determines the shape and pressure distribution of an object in contact with its surface. Originally developed for the "hand" of a robot, the sensor outputs can be displayed on a video monitor as alphanumeric symbols representing pressure, or they can be used to develop a color-coded map of the surface of the object. An array of electrodes in a metal frame overlaid with a sheet of pressure-conductive plastic forms the sensing surface. Pressure on the plastic varies the conductance of the path between each electrode and the frame. A 4-by-8 matrix has already been fabricated by using printed-circuit photoetching techniques, and arrays with more elements (for higher resolution) are possible.
(See page 173.)

Rotatable Fixture for Spray Coating

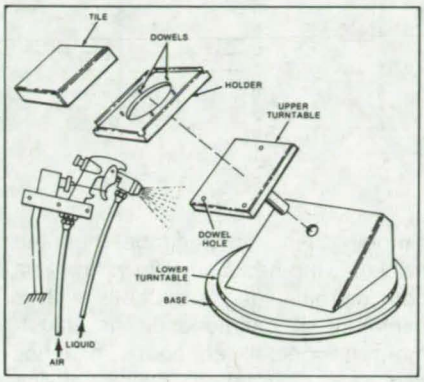

Paints, glazes, and other sprayed protective coatings are applied more quickly and more uniformly by mounting the parts to be coated on a special rotating fixture, originally used in production spraying of Space Shuttle insulation tiles. With two turntables, one in the horizontal plane and the other canted at 45°, the fixture rapidly orients all sides of the object to face the spray directly. Sections to be masked are covered by lips extending from the sides of a holder on the 45° turntable. Tiles and other parts are quickly installed on the fixture, sprayed, and then removed without requiring handling of the freshly coated surfaces.
(See page 289.)

Wide-Beam Flush-Mounted Antenna

A compact six-element phased-array antenna, containing a pair of dipoles and four monopoles, has an exceptionally-broad, circularly polarized beam and wide bandwidth.

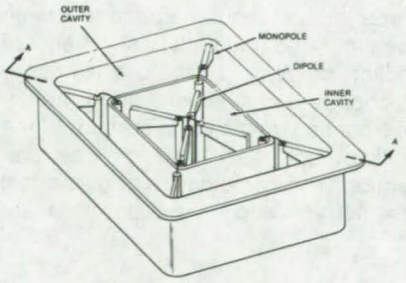

Suitable for flush mounting on a moving vehicle, the new antenna could find uses in high-altitude aircraft, communications satellites, and ground-based moving vehicles. For example, only four such antennas are needed aboard the Space Shuttle Orbiter for uniform communications coverage, instead of the many antennas normally required, saving weight, space, complexity, and cost.
(See page 184.)

Fibrous Refractory Composite Insulation

A new family of high-temperature, low-density refractory insulations is made by combining aluminoborosilicate and silica fibers according to a prescribed procedure. The properties of the insulation are controlled by varying the percentages of each component in the composition and by changing the proportions of the process chemicals. The addition of a percentage of boron oxide helps the silica to resist devitrification. After washing the fibers, they are combined as an aqueous slurry and poured into a mold. Once the liquid has been removed, the molded insulation is dried and fired in preparation for final machining.
(See page 235.)

Improved Metalized Polycarbonate Capacitor

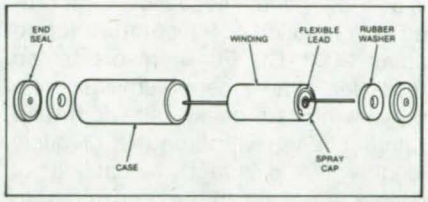

An improved metalized polycarbonate capacitor withstands 500 thermal cycles between -55° and +125° C, instead of 10 such cycles as is typical for this type of capacitor. The design modifications responsible for the improved durability are the installation of a rubber washer between the capacitor spray cap and end seal to absorb stress at high temperatures and the addition of a flexible lead to absorb contraction at low temperatures. Out of 150 modified capacitors tested for insulation and equivalent series resistance, drift, dissipation, and hermeticity, during 500 normal and accelerated thermal cycles, 149 survived without going out of specification.
(See page 168.)

Rapid Identification of Aerosol Pollutants

Aerosols are rapidly identified by a new thermoluminescence method that requires no bulkly or complex equipment. Besides being potentially useful in laboratory research on pollution, the technique could be used in the field (from vans or airplanes, for example) for monitoring industrial plants and other pollution sources. After collecting the aerosol on a sterile filter, the

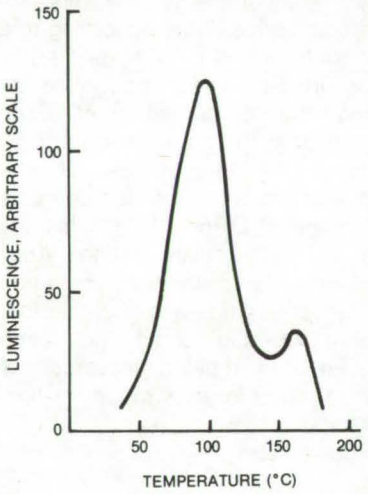

sample is exposed to a dilute mixture of ozone in oxygen. Then a fluorescer is added, and luminescence is recorded as a function of temperature (up to about 200° C). For aerosols tested thus far, the thermoluminescence curve exhibits a peak, half-width, and rate of change with time that uniquely identify the pollutant. A catalog of such curves could be consulted to analyze an unknown aerosol.
(See page 219).

Single-Axle, Double-Axis Solar Tracker

A solar concentrator is continuously pointed in the direction of incoming Sunlight by a tracking mechanism that has just a single axle and two synchronized drive motors. Considerably

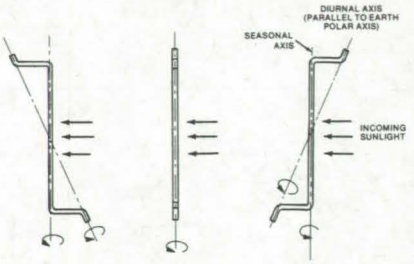

simpler than most gimbal-mounted trackers, the new unit follows the Sun both diurnally and seasonally with a minimum of maintenance or adjustment. Its specially configured axle has two axes of rotation: Daily tracking occurs as the collector housing is indexed at 15° per hour about one axis; for seasonal tracking, the housing is simultaneously rotated at a much slower rate about the other axis. The mechanism would be relatively easy to manufacture, and it could help to lower the costs of converting Sunlight to useful energy.
(See page 197.)

High-Performance Solar Collector

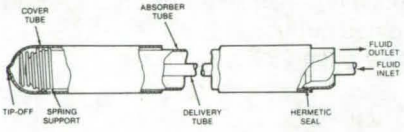

A highly-efficient solar collector is assembled from three concentric glass tubes. The transfer medium (either gas or liquid) enters through the innermost tube, travels the length of the collector, and then returns through the annular space between the inner and middle tubes. A vacuum jacket prevents heat loss by conduction and convection; and a selective coating on the outer surface of the middle tube assists in energy collection. The combination of cylindrical geometry and vacuum jacket substantially reduces the thermal-loss coefficient of this collector at high fluid temperatures, raising its efficiency above that of conventional flat-plate collectors. It may even be possible to heat the working fluid of a conventional heating system directly, without requiring expensive alterations or conversion of the existing equipment.
(See page 198.)

Analysis of Fatigue Damage In Composites

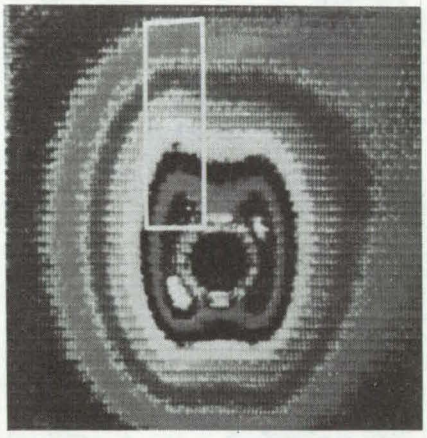

A finite-element heat-transfer analysis determines the sites of potential failure in composites. Boundary conditions for the analysis are temperatures measured by infrared thermography during cyclic fatigue tests. Already successfully tested on several boron/epoxy composites, the technique is sensitive to matrix damage and fiber disbonding that occur long before actual fiber breakage. It should therefore be useful in quality-assurance testing of these materials, which are becoming increasingly important as structural materials in vehicles, buildings, and other applications. In tests, the method has given results that compare favorably with those obtained by acoustic analysis and scanning-electron microscopy.
(See page 231.)

Electronic Components and Circuits

Hardware, Techniques, and Processes

Books and Reports

Computation-Saving Digital Filter

Less processor time is needed because low-pass filter circuit first averages its input.

Lyndon B. Johnson Space Center, Houston, Texas

A digital low-pass filter circuit extracts slowly-varying data signals from a high-speed data stream with a minimum of computation. The circuit first averages the high-speed signal, reducing its high-frequency content, and then filters out the signal components within the flow-frequency passband.

The new two-stage filter requires less computation from a central processor. Thus, more inputs can be fed to the processor, or a slower processor can be used. Moreover, the two-stage filter is not subject to the word-length truncation problem that afflicts conventional filters.

The usual digital filters, with sampling rates twice the highest frequency in the passband, demand considerable computation. However, if the input is averaged over a given period and the average is filtered at a comparatively slow rate, significantly less computation is required. The output is updated less frequently, but often enough to follow the slow output variations.

One application of the two-stage filter is preprocessing sensor data before they are sent to a central processor. For example, the effectiveness of the two-stage filter has been calculated for an instrument that measures the frequency difference between two similar rate gyros. The filter sends an updated output signal to a central processor every 960 ms. A conventional digital filter, in contrast, would present data more frequently — every 40 ms — but it would require many more central-processor computations to do the same job. In this example, the conventional filter requires 24 multiplies, 72 add/subtract operations, and 48 load/store operations over an approximately 1-s period, for a total processor time of 576 μs. Over the same period, the two-stage filter requires 2 multiplies, 50 add/subtracts, and 48 load/stores, for a total processor time of only 218 μs. Yet the gain characteristic of the two types is virtually identical (see figure).

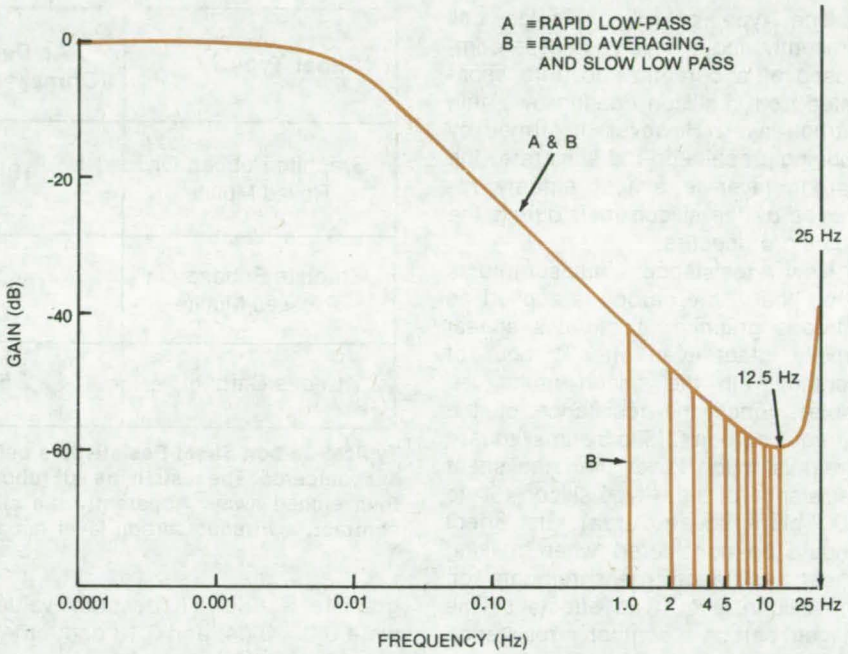

The **Gain Characteristic** for a two-stage (rapid-averaging followed by slow-low-pass) filter is virtually the same as for a conventional single-stage (rapid-low-pass) digital filter. The two-stage filter has a series of nodes near the top of its frequency range, but these have a negligible effect on its performance.

In general, the two-stage filter reduces speed and word-length requirements, and the reduction can be substantial when many filters are needed. In instrumentation for the Space Shuttle for correcting the biases of 12 gyros, the speed requirement was reduced by 90 percent.

This work was done by Delroy J. Sowada of Honeywell Inc. for **Johnson Space Center.** *For further information, Circle 1 on the TSP Request Card.*
MSC-18057

Improved Silicon/Carbon Interface for Solar Cells

Vitreous carbon may be superior to rubbed-on graphite.

NASA's Jet Propulsion Laboratory, Pasadena, California

One type of silicon solar cell presently under development is composed of a ceramic substrate separated from a silicon coating by a thin carbon layer. However, if formed by rubbing graphite on the substrate, the carbon layer is almost entirely removed by the silicon melt during the coating procedure.

New resistance measurements show that if the carbon is applied as vitreous graphite, it remains almost wholly intact even after 1 hour of contact with the silicon melt (see table). Since the resistance of the vitreous carbon (2.5 to 5 ohms/square area) is much lower than the sheet resistance of the p-type silicon (50 to 500 ohms/square area), its effect should be considered when making sheet resistance measurements on the silicon layer. The effects of the silicon/carbon contact resistance must also be ascertained.

Four-terminal resistance measurements between pads of silicon on vitreous graphite confirm two features of the silicon/graphite interface: (1) Typical zero-voltage contact resistances between silicon and vitreous graphite are low (measured values were 0.03, 0.04, and 0.13 ohm-cm^2); and (2) the contact resistance is not uniform over the silicon surface. The first result is encouraging because low contact resistances indicate that vitreous carbon could serve as an adequate base contact to the p-layer of the solar cell; however, the second result suggests that improvements in the processing cycle are needed to form a more uniform silicon/carbon contact.

Sheet Type	As Deposited (Ohms/square area)	After Etching To Remove Silicon Layer (Ohms/square area)
Graphite Rubbed On Rolled Mullite	10 to 25	250 to 600
Graphite Rubbed On Pressed Mullite	100 to 150	1K to 60K
Vitreous Carbon	2.5 to 5	2.5 to 5

Typical Carbon Sheet Resistivities before and after application of a silicon coating are compared. The resistivities of rubbed-on graphite rise after the silicon is applied, then etched away. Apparently the silicon melt removed much of the carbon. In contrast, a vitreous carbon layer remains stable.

This work was done by J. David Zook of Honeywell Inc. for **NASA's Jet Propulsion Laboratory.** *For further information, Circle 2 on the TSP Request Card.*
NPO-14421

Improved Metalized Polycarbonate Capacitor

Modified capacitor withstands severe thermal cycling.

Marshall Space Flight Center, Alabama

An improved metalized polycarbonate-film capacitor withstands 500 thermal cycles between -55° and +125° C. It replaces previous capacitors of this type, which typically withstand only 10 such cycles.

Two design changes (see figure) give the new capacitor its exceptional durability under thermal stress: (1) A rubber washer is installed between the capacitor spray cap and the end seal to absorb stress at high temperatures, and (2) a flexible lead is added to absorb contraction at low temperatures.

Capacitors were tested for insulation resistance, capacitance drift, dissipation, equivalent series resistance, and hermeticity, at intervals during 500 normal and accelerated thermal cycles. Out of 150 units tested, 149 survived the tests without going out of specification. It was also found that to screen defective units fully, the dissipation factor should be measured at 1 and 10 kHz. Measurement at only one frequency (e.g., 1 kHz) can allow a potentially defective capacitor to go unscreened (as did one unit during these tests).

A typical (unmodified) capacitor consists of a metalized polycarbonate film wound on a plastic core. Lead wires are attached to the film through spray caps at the ends of the winding. The metallic case (e.g., a copper/nickel alloy) is cylindrical, and the end seals are circular glass-to-metal compression seals.

In the unmodified capacitors, the winding expands against the end seal at high temperatures, causing the thin solder bead that attaches the lead wire to the spray cap to break after only a few cycles. Contraction of the winding

also can cause the solder bead to break; or it can cause the end seal to break, with a resulting loss of hermeticity.

As shown, the rubber washer between the spray cap and end seal absorbs the thermal stress that arises when the winding expands against the end cap at high temperatures. Also visible is a flexible wire that attaches the spray cap to the axial lead of the capacitor. This lead absorbs stress that arises when the winding contracts away from the end seal at low temperatures.

This work was done by Hillel J. Kellerman of Component Research Co. for **Marshall Space Flight Center.** *Further information [including extensive test data on the new capacitors] may be found in NASA CR-150460 [N77-85673], "Improvement of The Mechanical and Thermal Properties of The Metallized Polycarbonate Capacitor," a copy of which may be obtained at cost from the New England Research Application Center [see page A7].*
MFS-25142

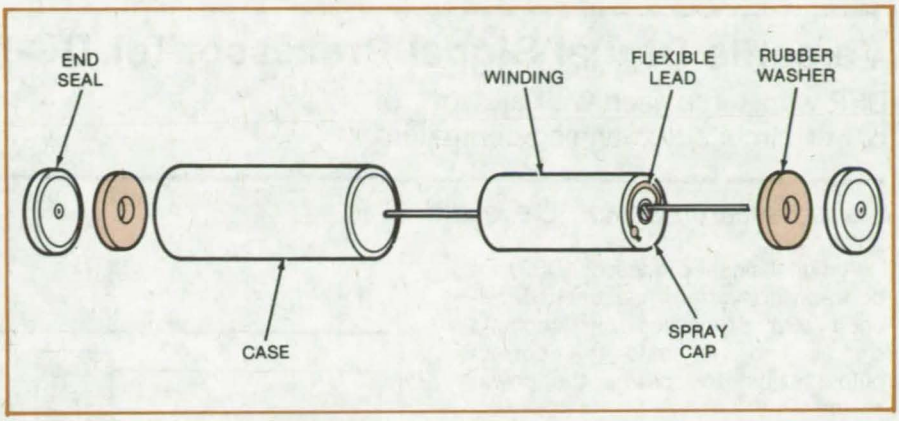

An **Improved Capacitor** withstands severe temperature cycling between -55° and 125° C. Three 30-V capacitors were tested: 0.01 μF, 0.1 μF, and 0.15 μF.

Binary-to-Manchester Encoders

Two circuits allow easy interface of flight simulators with aircraft communications equipment.

Lyndon B. Johnson Space Center, Houston, Texas

Two new circuits convert 16-bit-word binary encoded data to 24-bit Manchester II code. One circuit is an efficient TTL design that requires only 24 integrated circuits; the other circuit requires 35 IC's, but combines CMOS and TTL logic in low-power configuration that consumes only 2.6 watts.

The Manchester II format is a low-duty-cycle serial code used extensively in aircraft communications. When flight equipment is ground tested with simulation computers, the binary format of the ground-based hardware must be interfaced with the Manchester format: hence the need for the interface circuit.

The top part of the figure shows the biphase code that represents data bits in the Manchester format. In this scheme, a logic "1" is represented by a one-to-zero transition within a 1-μs bit period, and a logic "0" is represented as a zero-to-one transition. The 24-bit format used to transmit a data word is shown in the bottom part of the figure. The first 3 bits are either the message or word sync; bits 4 through 7 represent "0's"; the 16 data bits reside in bits 8 through 23; and the last bit is a parity bit. Four 16-bit words are stored in a register file, converted to the 24-bit Manchester format, and then transmitted serially along a 71-ohm twisted shielded pair. A 24-bit test word is sent after every four words.

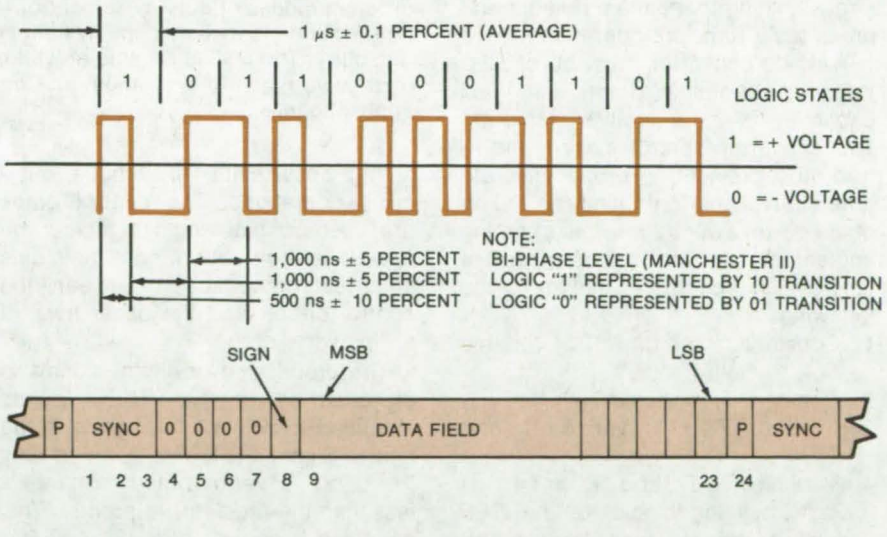

WORD FORMAT

In the **Manchester II Biphase Code** (top), a data "1" is encoded as a one-zero transition, and a data "0" is encoded as a zero-one transition. The 24-bit word format is shown in the bottom part of the figure.

This work was done by Richard H. St. Cyr III of Rockwell International Corp. and W. Hu and R. Latshaw of The Garrett Corp. for **Johnson Space Center.** *For further information, including detailed drawings of the two circuit configurations, Circle 3 on the TSP Request Card.*
MSC-16546

Versatile Digital Signal Processor for DC-to-DC Converters

DSP works in unison with all types of power circuits and analog controllers.

Lewis Research Center, Cleveland, Ohio

A digital signal processor (DSP) for dc-to-dc converters has been developed that processes all incoming signals and transmits the correct output signal to operate the power switch.

One of the main problems with existing switching-regulator technology is that of reliability. One means to increased reliability is to employ circuit techniques to limit, instantaneously, the electrical stresses in all power processor components. Existing regulators often omit this limiting function and, instead, rely on generous derating of all power components for achieving reliable operation. This practice places the regulator at the mercy of uncontrolled transient stresses, and becomes impractical in the prevailing trend to higher power. This newly developed DSP provides instantaneous power-component stress limiting to maintain reliable and predictable transient operations.

A dc-dc converter must be oscillatory in nature due to the finite flux capability of its inductive elements. The converter control system therefore must provide the proper discrete time intervals in controlling the on/off of the power switch. In terms of timing implementation, the various means of duty-cycle control include the following:

1. Constant "on" time T_n, variable "off" time T_f.
2. Constant T_f, variable T_n.
3. Constant $(T_n + T_f)$, variable T_n and T_f.
4. Variable T_n, T_f, and $(T_n + T_f)$.

Basic building blocks of the DSP consist of: isolator, time delay, memories, oscillator, control gates, and power/control interface.

The function of the isolator is to provide the control circuit input/output isolation. The time delay is used to effect the proper duty-cycle control during either steady-state or transient operations. The memories are used to effect logical state changes as a result of various input control signals. The oscillator produces signals to set timing constraints for various duty-cycle operations. The control gates are used to gate logic signals. The power/control interface maintains electrical compatibility between the control circuit and the base drive of the power switch.

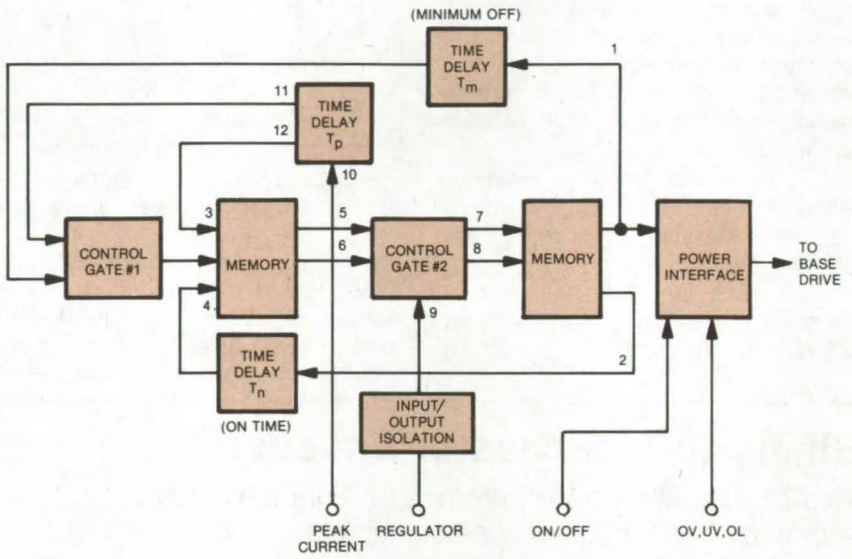

The Digital Signal Processor shown above utilizes a constant T_n (or E_iT_n). It improves switching-regulator control in two major ways: (1) the ability to perform different modes of duty-cycle control to achieve flexibility and standardization and (2) the ability to instantaneously limit power-component stress to enhance regulator reliability. The DSP is capable of working in unison with all types of power circuits and analog controllers, thus making it useful with many switching-regulator applications.

The processing of digital signals is explained by reference to key points identified as points 1 through 12 in the figure. Signal 9 is logical 1 if and only if the dc-converter output voltage is less than the regulator reference. This condition is equivalent to no regulator action. When signal 9 is logical 1, the blocks in the figure (except for the power-interface blocks) combine to form a free-running oscillator. The oscillating frequency depends upon whether signal 10 is logical 1 or logical 0. Signal 10 is defined to be the peak-current protection signal and is logical 1 when the inductor current is less than the predetermined peak protection current.

When the DSP receives the converter "on" command, a few cycles of current buildup must occur before the peak current in the energy-storage inductor reaches the predetermined protection level. During this time of buildup, signal 10 is logical 1, and the time delay T_p is not actuated by the peak-current sensor. The oscillating frequency of this DSP is $1/(T_n + T_m)$ where T_n is "on" time and T_m is minimum "off" time of the converter. These time intervals are coupled to the base drive circuit to control the power switch through the power-interface block. Also during this time of (peak current) buildup, the output voltage is less than the regulator reference so that signal 9 remains logical 1 throughout.

The time required for peak current buildup is less than the time required for output voltage buildup. Thus, when the time of peak current buildup has

come to an end, signal 10 becomes logical 0 in each cycle before T_n is timed out while signal 9 remains at logical 1. Time delay T_p is activated, T_n is shortened to T'_n, and T_m is replaced by $T_p \geq T_m$. The oscillating frequency during this interval of output voltage buildup is $1/(T'_n + T_p)$.

Eventually, the converter reaches its intended regulation level. Signal 9 becomes logical 0 in each cycle as the output voltage intersects the voltage reference. The circuit design insures that the inductor current remains below the peak-current protection level at all times, so that signal 10 is always logical 1. Minimum "off" time T_m is disabled, "on" time becomes T_n, while "off" time is increased to T_f. The oscillating frequency in steady state is thus $1/(T_n + T_f)$.

The converter on/off command signal and the converter shutoff signal are processed by the power-interface block. These signals respond to either external command or internal protection for the initiation or the termination of the converter operation. A logical 0 input always terminates the operation, and reset is required before restart.

Due to the latching function associated with the overvoltage (OV), undervoltage (UV), and overload (OL) shutoff, these signals are normally processed by another memory block before entering the power interface. This is different from the peak-current signal and the regulator signal, which are required to exhibit both logical 0 and logical 1 cyclically. Consequently, the regulator signal 9 and the peak-current signal 10 are generally obtained from a threshold detector.

A constant-frequency DSP can also be developed by using some of the basic building blocks of the constant-"on" DSP by processing the same signals. By utilizing an oscillator for defining a constant-"on" time plus "off" time, the regulator signal determines both T_n and T_f. The time-delay block T_n is thus eliminated. Furthermore, due to the availability of essentialy the entire period as the time delay following an excessive peak-current detection, time delay T_p can also be eliminated. Excluding these blocks along with their control gates results in a simple constant-frequency DSP.

This work was done by John L. Biess, Leonard Y. Inouye, and Yuan Yu of TRW, Inc., for **Lewis Research Center.** *Further information may be found in NASA CR-135072 [N77-32398], "Development of a Standardized Control Module for DC-to-DC Converters," a copy of which may be obtained at cost from the New England Research Application Center* *[see page A7]*.

LEW-13020

Digital Phase Shifter

Wide-range phase shifter employs simple circuitry.

Langley Research Center, Hampton, Virginia

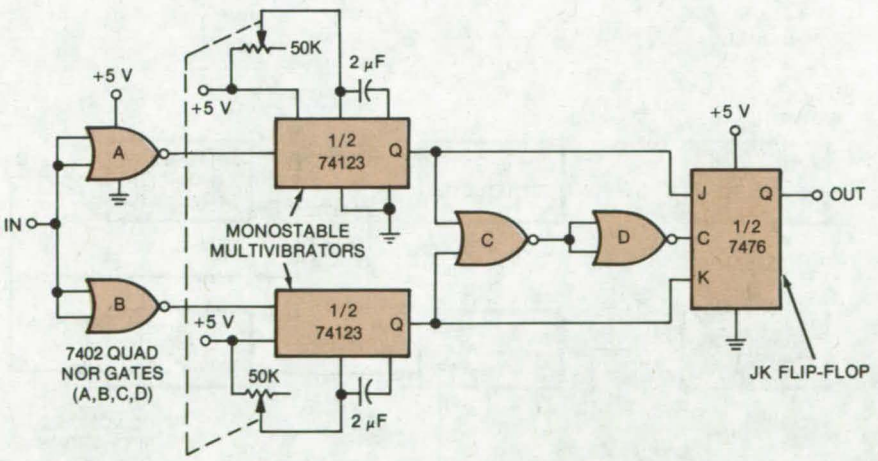

Digital Phase Shifter is shown configured for a 20-Hz input signal. Other values may be chosen to suit any input frequency within the operating range of the integrated circuits. Phase shifts closer to 0° may be obtained by using a smaller capacitor, and phase shifts closer to 180° may be obtained by using a larger capacitor. However, these shifts are accomplished at the sacrifice of range.

The phase shift of a digital input may be varied over the approximate range of 15° to 165° with the circuit shown in the figure. Only TTL integrated circuits and a single 5-volt power supply are required.

One monostable multivibrator is triggered on the leading edge of the input signal; the other is triggered on the trailing edge of the input signal. A flip-flop is toggled on the trailing edge of a clock pulse generated by "OR-ing" the two monostable outputs. Thus, the output of the flip-flop is a replica of the input signal delayed by the on time of the monostables. The on time may be varied by adjusting the two ganged potentiometers.

The advantages of this system are a wide range of control and good stability provided by relatively simple circuitry.

This work was done by Murray G. Perry of Vought Corp. for **Langley Research Center.** *No further documentation is available.*

LAR-12338

Improved Reader for Magnetically-Encoded ID Cards

Hybrid circuitry accommodates variations in insertion speed, yet is simpler than an all-digital version.

NASA's Jet Propulsion Laboratory, Pasadena, California

A hybrid demodulator in an electronic card reader for magnetically-encoded identification cards is simpler and less expensive than equivalent all-digital circuits. In the reader, used to control access to test facilities at the Jet Propulsion Laboratory, a pickup senses the magnetic variations on the card stripe and generates a phase-encoded digital signal. The card used at JPL is an ID card the size of a typical credit card.

The rate at which the user inserts the card defines the period of the "clock" that synchronizes the phase-encoded data. Although the insertion speed (by hand) can vary by a factor of 20, the demodulator is able to extract the data from the coded signal, allowing the reader to compare the pattern with a preset recognition code. If a match is found, the reader unlocks a door or performs some other positive action for the user.

The identification code is recorded on the card in binary "diphase" form (see Figure 1a). A data "0" is recorded as a signal-level transition at the midpoint of the clock period; and a data "1" is recorded as one transition at one-quarter of the clock period and another at one-half the clock period. The clock period is defined as twice the width of a "0" bit and depends on the speed at which the card stripe passes through the magnetic pickup. [Another way of looking at this code is that a string of "0's" is recorded at the clock frequency (f), and a string of "1's" is recorded at twice the clock frequency (2f).] This form of modulation is standard in the industry, and is of the same form as used by the credit card industry, digital recording for storage on disk or tape.

In the demodulator, shown in Figure 2, the diphase signal from the pickup is fed to a level converter, which changes the pickup pulses to levels compatible with transistor-transistor-logic (TTL) circuitry. A transition detector monitors these diphase signals and detects logic-level changes. Whenever a transition in either direction occurs, the transition detector produces a 6-microsecond pulse (Figure 1b).

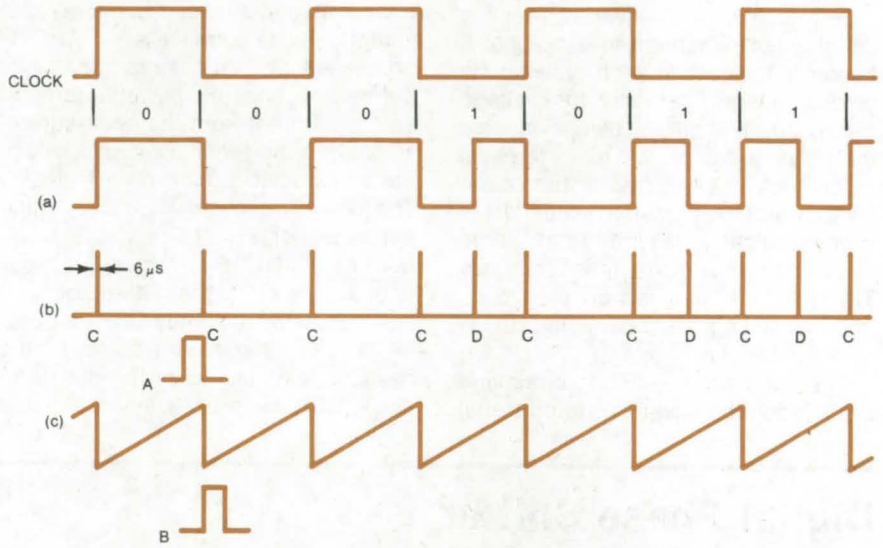

Figure 1. The **Diphase Code** [a] is used in a magnetic key-card reader. A transition detector in the reader produces a stream of clock and data pulses (b) from the coded information. The peak voltage of the ramp waveform (c) is proportional to the clock period and is used in demodulating the coded signal. At least 10 reference clock pulses are stored in front of the data on the card stripe.

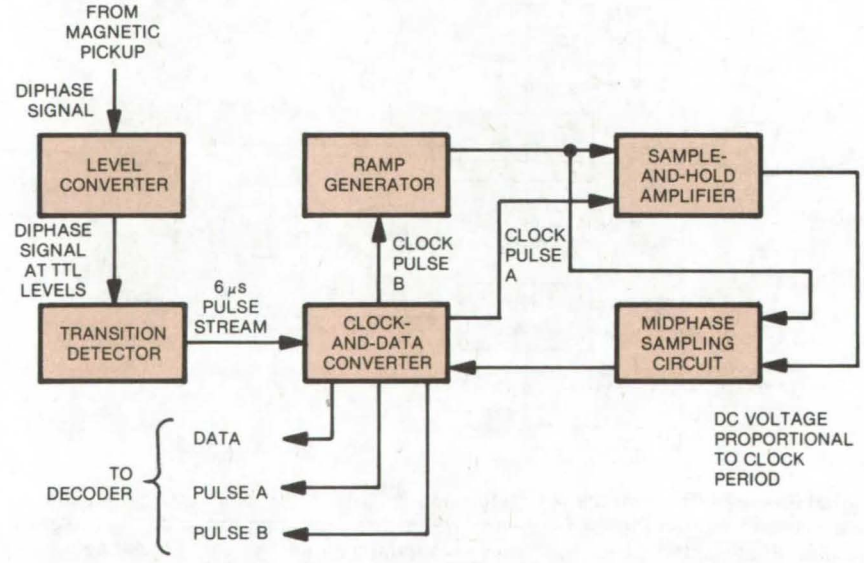

Figure 2. The **Demodulator Portion** of the card reader separates data signals from clock signals. The ramp generator, sample-and-hold amplifier, and midphase sampling circuit — all of which are analog circuits — identify the midpoints of the variable-length clock periods so that data can be extracted.

An autocorrelation method is now used, which stores the time period of the previous bit and uses it to compare

the time period of the following bit. It is implemented as follows: A clock-and-data converter separates the clock pulses from the data pulses. It includes a synchronous generator that produces a 6-microsecond pulse (A) immediately followed by another 6-microsecond pulse (B) that signals the start of a clock period.

Pulse B triggers a ramp generator (Figure 1c) that applies a linearly rising output to a sample-and-hold amplifier. When the next pulse A is applied to this amplifier, the amplifier stores the terminal value of the ramp voltage, which ranges from 0.5 to 10 volts, depending on the length of the clock period.

A midphase sampling circuit compares the stored voltage from the previous cycle and the voltage ramp of the present cycle to determine the midpoint of the current data period. The circuit then sends a sampling pulse to the clock-and-data converter so that it can check its input to determine whether a data pulse arrives within the ramp cycle. If such a pulse is received, it is recorded as a data "1"; if no pulse is received, a "0" is recorded.

Possible variations in the clock period from one ramp cycle to the next are accounted for by generating a midphase sampling pulse of longer than the 50 percent midpoint window. Up to 75 percent of the ramp cycle can be examined for the presence of a data pulse. This information is then transmitted to the pattern decoder. On separate lines, the clock-and-data converter also transmits pulse A and pulse B information to the decoder.

This work was done by Ta Tzu Wu of Caltech for **NASA's Jet Propulsion Laboratory.** *For further information, Circle 4 on the TSP Request Card.*

Title to this invention has been waived under the provisions of the National Aeronautics and Space Act [42 U.S.C. 2457(f)], to the California Institute of Technology, Pasadena, CA 91109.

NPO-13517

Transducer With a Sense of Touch

The area and shape of an object are recorded by a matrix of pressure sensors.

NASA's Jet Propulsion Laboratory, Pasadena, California

A matrix of pressure sensors determines the shape and pressure distribution of an object in contact with its surface. The sensor outputs can be displayed as an array of alphanumeric symbols on a video monitor, or they can be used to develop a pressure "map" of the surface of the object. The signals can also control mechanical or electrical equipment.

The sensor was developed as part of a mechanical hand for a remotely controlled robot. Sensors on the fingers of the mechanical hand give it a sense of touch so that it can examine and manipulate objects more effectively. Other potential applications include geological instruments and automatic parts-inspection and parts-handling equipment.

The touch sensor consists of a matrix of electrodes in a metal frame overlaid with a sheet of pressure-conductive plastic (see Figure 1). The frame is held at ground potential, and a common power source is applied to the electrodes of each cell. Pressure on the plastic sheet varies the conductance of the path between an

(continued on next page)

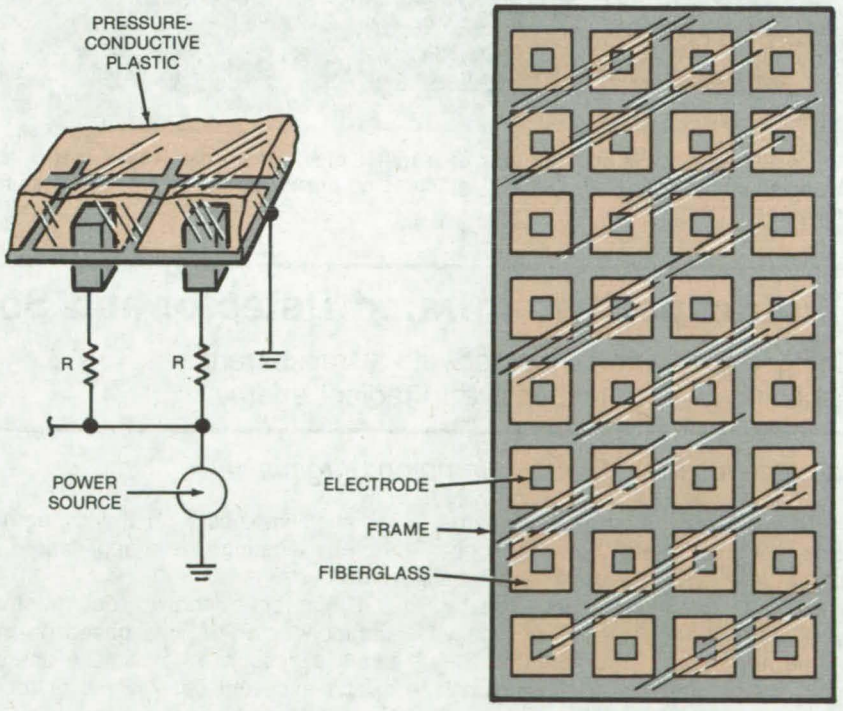

Figure 1. **Touch-Sensitive Electrodes** are embedded in fiberglass and surrounded by a metal frame. Pressure transmitted through a conductive plastic cover alters the resistance path between electrode and frame.

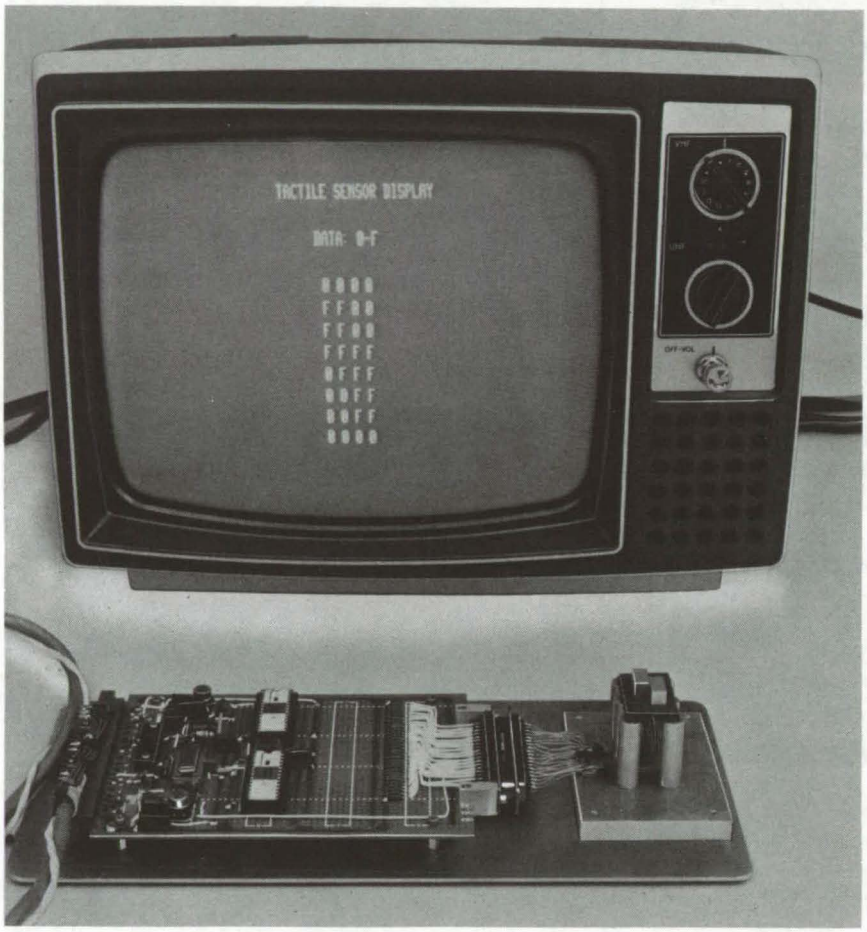

Figure 2. The **Outline and Contour** of a metal block are sensed by a matrix and displayed alphanumerically; an "O" indicates no pressure, and an "F" indicates full pressure.

electrode and the metal frame. Thus, the current flowing through the electrode generates a voltage measure of pressure across a resistor in series with the electrode. The voltages in the matrix convey information about the shape and surface contours of the object.

A touch sensor consisting of a 4-by-8 matrix has been fabricated by using printed-circuit photoetching techniques. A square shape was selected for the electrodes in this array, to give high resolution with the minimum number of cells. Larger arrays (with more elements) will give even higher resolution.

The pressure-induced voltages across the resistors are measured, converted to digital form, and processed by a microcomputer. The digital signals can be displayed as a matrix of hexidecimal integers or other symbols on a video monitor (see Figure 2); or, they can form a color image of the object on the monitor.

This work was done by Antal K. Bejczy and Garrett Paine of Caltech for **NASA's Jet Propulsion Laboratory.** *For further information, Circle 5 on the TSP Request Card.*
NPO-14656

Photocapacitive Infrared Detector and Solar Cell

Lightly doped semiconductor with a transparent insulating layer is responsive to radiant energy.

Langley Research Center, Hampton, Virginia

Radiant energy is normally converted to electrical energy by a semiconductor device relying upon a barrier layer or a resistance change, or by pyroelectric devices using cyclically heated and cooled ferroelectrics. The major disadvantage of such semiconductors as radiant-energy detectors is that they must usually be maintained at cryogenic temperatures to function most effectively. Furthermore, as solar-energy converters, they are generally not very efficient. Pyroelectric detectors tend to be noisy and often have sensitivities below the level of radiation impinging on the dielectric, thereby limiting their application in many systems.

It has been shown recently that semiconductor devices based on capacitive response to radiant energy exhibit excellent sensitivities at room temperatures. Such a photocapacitive optical-energy detector is illustrated in Figure 1.

The capacitor is a semiconductor substrate with an insulating layer facing the optical-energy source. The semiconductor is intrinsic or only lightly doped to increase the dynamic range of the capacitance variation in response to modulated light. The insulator should be as thin as it can be while still forming a blocking contact.

Metallic contacts are formed on the front over the insulating layer and on the back of the substrate. There are no junction barrier layers in the semiconductor substrate or between the insulating layer and the metal contacts; the only barrier layers are at the interface between the substrate and the insulating layer.

When the photocapacitor is used as a detector of infrared and relatively-

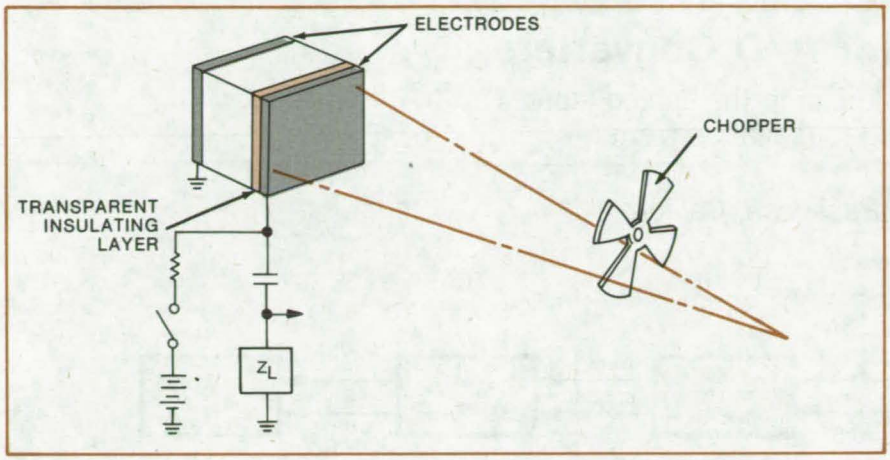

Figure 1. **Photocapacitive Radiant-Energy Detector** operates effectively at room temperatures. Radiation from the source illuminates the detector at a predetermined constant frequency. The semiconductor substrate is about 200 microns thick, and the relatively-thin electrically insulating layer is transparent to the radiant energy. Metallic contacts on the front and back of this variable capacitor form its electrodes. The front electrode is a film thin enough to be transparent to the radiant energy.

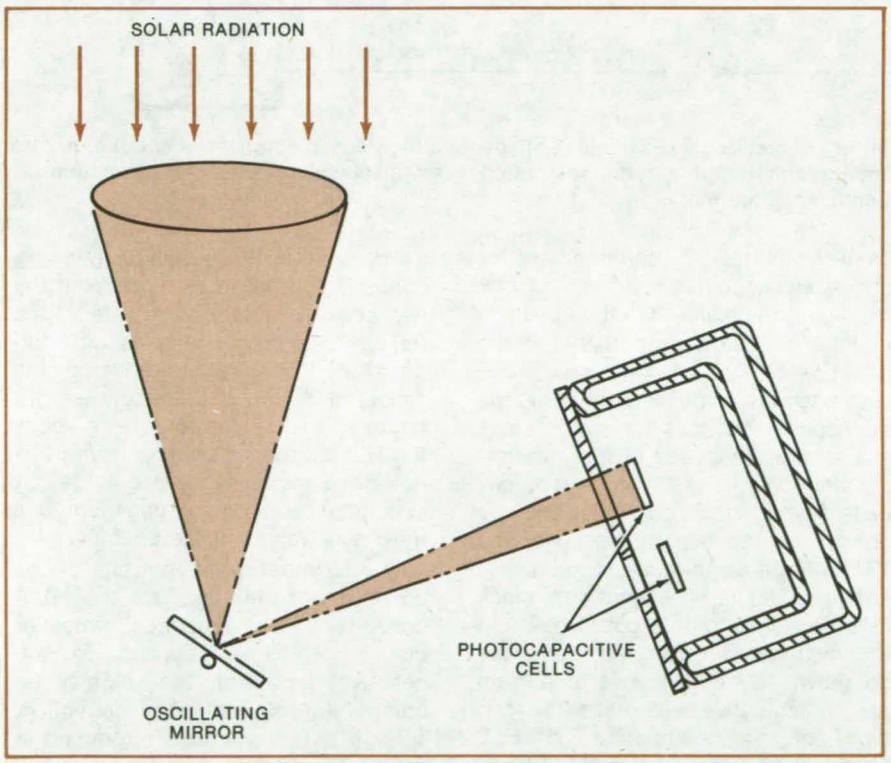

Figure 2. A **Proposed Photocapacitive Solar-Energy Converter** focuses incoming Sunlight on an oscillating mirror that is motor-driven to wobble at a selected frequency. The reflected light irradiates each of a pair of photocapacitive cells alternately, 180° out of phase. The resistance and capacitance of each cell are modulated to deliver power to its own load circuit.

long-wavelength radiant energy (Figure 1), the semiconductor substrate is formed of such narrow-band-gap materials as indium antimonide, indium arsenide, lead selenide, lead tin telluride, cadmium mercury telluride, or lead sulfide. Silicon and gallium arsenide detectors operating at room temperature in this mode have displayed normalized detectivities at 13 Hz in excess of 10^{13} $W^{-1}cm(Hz)^{1/2}$.

The theoretical optimum sensitivity of silicon is 10^{15} $W^{-1}cm(Hz)^{1/2}$ and of gallium arsenide is 10^{17} $W^{-1}cm(Hz)^{1/2}$. Silicon detectors have been operated at 20 MHz with an unoptimized sensitivity of 10^{11} $W^{-1}cm(Hz)^{1/2}$. An arrangement for using these cells as a solar-energy converter is shown in Figure 2.

This work was done by Roger K. Crouch and William E. Miller of **Langley Research Center** *and John A. Moriarty, Arden Sher, and Y.H. Tsuo of the College of William and Mary. For further information, Circle 6 on the TSP Request Card.*

Title to this invention has been waived under the provisions of the National Aeronautics and Space Act [42 U.S.C. 2457(f)], to Professor Arden Sher, College of William and Mary, Williamsburg, VA 23185.
LAR-12345

Offset Compensation for A/D Converters

Digital feedback circuit eliminates offset in the analog input and offset introduced by the analog-to-digital converter.

NASA's Jet Propulsion Laboratory, Pasadena, California

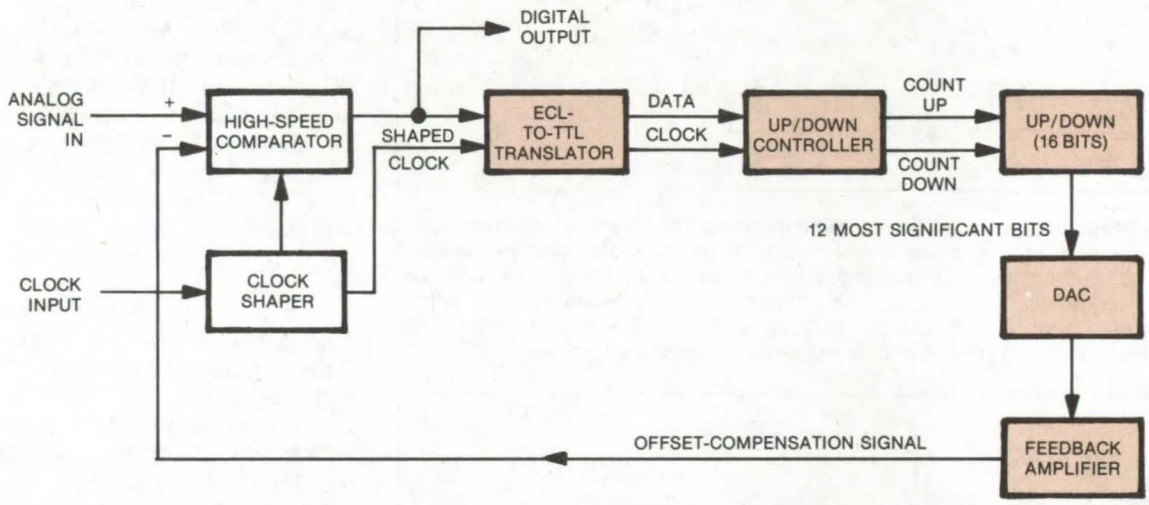

Analog-to-Digital Converter, consisting of emitter-coupled-logic (ECL) clock-shaper and high-speed comparator circuits, has dc restoration that is generated largely by TTL circuits. The digital output is integrated by an up/down counter, and the resultant is converted back to analog form as the offset compensation signal.

An analog-to-digital (A/D) converter eliminates dc offset in the final digitized signal as well as in the analog input, by using digital feedback for compensation. The circuit does not require capacitor or transformer coupling of the analog input, so its frequecy response is not limited by the frequency characteristics of such components. It is useful in data-processing applications in which analog-format data are entered at high rates — for example, supermarket and department-store point-of-sale data input systems.

In the digital feedback circuit, an up/down counter integrates the A/D converter output (see figure). The counter output is fed back to the A/D converter input through a digital-to-analog (D/A) converter and an amplifier. The feedback signal cancels the dc offset when, on the average, the A/D output has an equal number of plus ones and minus ones. The feedback circuit not only compensates for offset but measures it as well, since the digital value stored in the up/down counter is linearly proportional to the offset.

In one version of the converter, the high-speed comparator and clock shaper are composed of fast emitter-coupled-logic (ECL) integrated circuits. The up/down controller and up/down counter use moderate-speed TTL integrated circuits, which are adequate for a 40-megahertz clock rate. (A translator interposed between the high-speed comparator and the up/down controller converts current and voltage levels to make the two types of logic compatible.) If ECL circuits were used exclusively, a clock rate of 100 megahertz could be accommodated.

The high-speed up/down controller handles the serial input bits in pairs. It sends an up clock pulse to the up/down counter if both bits are plus one, a down clock pulse if both bits are minus one, and no clock pulse if the two bits are different. In effect, the up/down controller acts as an additional counter stage, reducing the clock rate to the up/down counter by a factor of 2. The controller also keeps the 16-bit up/down counter from overflowing if the offset is too large, by inhibiting counting for minimum and maximum values of the counter.

The 12 most significant bits of the up/down counter go to the D/A converter. The feedback amplifier output, which is applied to the negative input of the high-speed comparator, is equal to the input offset voltage plus any offset introduced in the A/D converter.

This work was done by Stanley S. Brokl and William J. Hurd of Caltech for **NASA's Jet Propulsion Laboratory.** *For further information, Circle 7 on the TSP Request Card.*
NPO-13438

Improved Ripple Rejection in a PWM

Line-ripple rejection improves better than 2 to 1 when an exponential pump ramp is used in a pulse-width modulator (PWM).

Lyndon B. Johnson Space Center, Houston, Texas

By substituting an exponentially-increasing ramp voltage for the conventional linear ramp, the line-ripple rejection of a pulse-width modulator is more than doubled, yet the circuit is simplified.

An exponentially-increasing ramp voltage R(t) controls the duration of pulses at the output of the pulse-width-modulated buck regulator shown in the figure. The start of a ramp (t = 0) begins an output pulse. When the ramp voltage equals the sum of two signals e_i and e_f (e_i is derived from the input line voltage, and e_f is an error signal derived from the output voltage), the output pulse is terminated.

The gain constants K_1 and K_2 are optimized to cancel ripple on the output voltage. If this is done assuming an exponential ramp (and using conventional circuit analysis), ripple rejection is substantially improved over circuits that use a linear ramp. Moreover, the exponential ramp can be implemented by a simple RC circuit, whereas a linear ramp requires a constant current source to charge a capacitor.

With the exponential ramp voltage in a nominally-28-volt-input, 21-volt-output, pulse-width modulator, ripple rejection is greater than 20 dB as the input is varied from 25 to 30 volts, and it is greater than 15 dB for input variations over a 23.5- to 32-volt range.

This large ripple rejection is particularly valuable when applying the modulator to power converters for which size and weight restrictions prevent the use of large capacitive filters. The high ripple rejection may also be helpful in computers, scientific and biomedical instruments, and other equipment demanding stable power sources.

In a PWM power supply built for the Space Shuttle communications and tracking equipment, an astable multivibrator generates the exponential ramp. The ramp frequency is 30 kilohertz, and the peak ramp voltage is 3.3 volts.

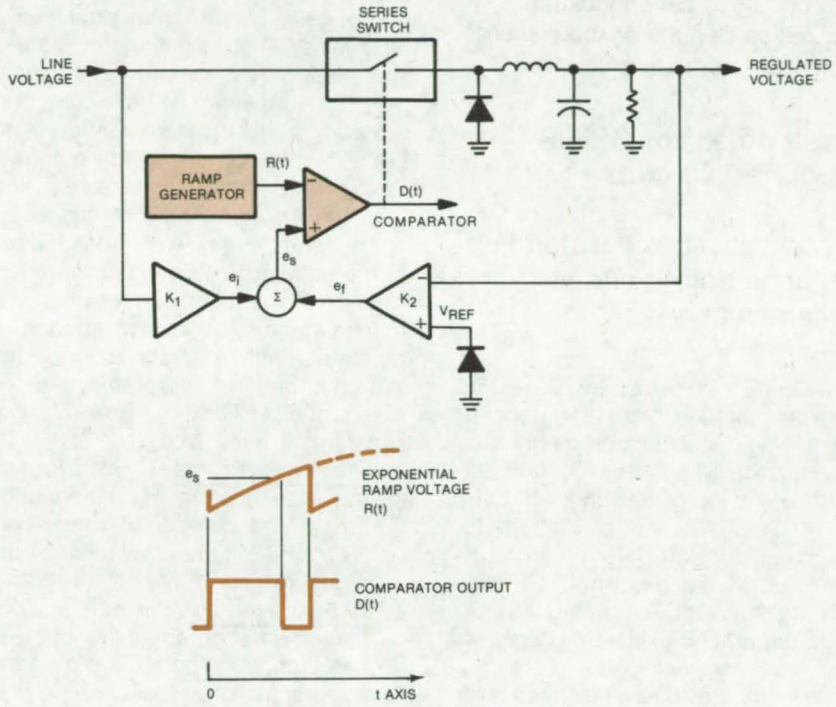

An **Exponentially Increasing Voltage** $R(t) = A_1(1 - e^{-t/\tau})$ from a ramp generator determines the pulse width in this PWM. When the amplifier gain constants are optimized for this ramp characteristic, line-ripple rejection is substantially improved.

This work was done by Charles B. Loftis, Jr., of Watkins-Johnson Co. for **Johnson Space Center.** *For further information, Circle 8 on the TSP Request Card.*
MSC-16923

Books and Reports

These reports, studies, and handbooks are available from NASA as Technical Support Packages (TSP's) when a Request Card number is cited; otherwise they are available from one of NASA's Industrial Application Centers or the National Technical Information Service.

Development of CMOS Integrated Circuits

Report describes the standard-cell approach to circuit implementation.

The life cycles of two custom integrated circuits, from their conception as logic diagrams through their design, fabrication, testing, and delivery, are documented in a 45-page report. One circuit is a 4-bit multiplexed register with shift-left and shift-right capabilities; the other is a dual 4-bit register. Both circuits use complementary-metal-oxide-semiconductor (CMOS) technology.

The computer-controlled standard-cell approach was used to design and fabricate these circuits. The logic diagram is partitioned into blocks of standard, predesigned "cells" for which mask patterns and artwork are known. The cells vary in complexity from simple 2-transistor inverters to complex 20-transistor networks. When the desired circuit function has been duplicated by the proper interconnection of cells, the program produces a tape for driving an automatic plotter. The plotter then generates the final precision artwork. Other computer programs verify the logic configuration in the original circuit, locate potential timing and "race" problems, and minimize the number of interconnects.

The report begins with a description of the standard-cell method, an overview of the computer programs, and logic diagrams for the two circuits. It continues with a description of the design-automation programs and the standard-cell library. Three major programs are involved:

1. Placement Program. This program minimizes the total interconnection length and number of crossovers by optimizing the placement of the standard cells.
2. Routing Program. The output of the placement program is the input for this program. The routing program interconnects the cells, giving preference to a metal interconnect over a p^+ tunnel or diffusion interconnection. If a p^+ diffused tunnel is used, the program takes steps to insure that parasitic devices are not formed with adjacent tunnels. Chip area is minimized at this stage.
3. Artwork Program. The artwork program takes the output of the routing program, combines it with stored data on the standard cells, and generates a tape for seven-level mask artwork to be drawn by the plotter.

A description of static and dynamic leakage tests and dynamic performance tests on the two circuits is included. Representative data are presented in tables and graphs.

This work was done by F. Bertino, A. Feller, J. Greenhouse, T.Lombardi, A. Merriam, R. Noto, S. Ozga, R. Pryor, P. Ramondetta, and A. Smith of RCA Corp. for **Marshall Space Flight Center.** *Further information may be found in NASA CR-150801 [N78-78414], "Design, Development, Fabrication and Delivery of Register and Multiplexer Units," a copy of which may be obtained at cost from the New England Research Application Center* [see page A7].

Inquiries concerning rights for the commercial use of this invention should be addressed to the Patent Counsel, Marshall Space Flight Center [see page A8]. *Refer to MFS-25121.*

Electronic Systems

Hardware, Techniques, and Processes

Books and Reports

Teletype Test Unit

Unit tests communications systems used by the deaf.

Langley Research Center, Hampton, Virginia

Many deaf people in the United States have begun to communicate with one another over telephone lines using teletype machines and acoustic couplers, or modems. The machines used by the deaf usually consist of surplus equipment that uses the five-level Baudot code. The acoustic couplers used are not the industry-standard modems but are much simpler inexpensive devices. Maintaining and troubleshooting this equipment can be very time consuming. One of the main problems is identifying the defective component: teletype or modem. A new Teletype Test Unit (TTU) can greatly facilitate field-testing these teletype and modem systems.

The primary function of the TTU is to generate repetitive lines of the test character pair RY. The TTU may be used to isolate faults in malfunctioning teletype and modem units and for adjustments during periodic preventive maintenance. As shown in the block diagram, the TTU is composed of two sections. One section, the teletype data generator, contains all the circuitry necessary to generate the switch closures that simulate a teletype signal. The second section, the FSK modulator, generates the simulated FSK signal that a modem "hears" coming from a telephone receiver.

All timing of signals in the TTU is derived from a 25.2-kHz master clock. The baud-rate generator is simply a binary counter with a feedback reset that divides the 25.2-kHz input by 555, yielding an output frequency of 45.4 Hz. This sets the baud rate for the character generator, which produces a sequence of 30 alternating RY character pairs followed by two carriage returns and two line feeds.

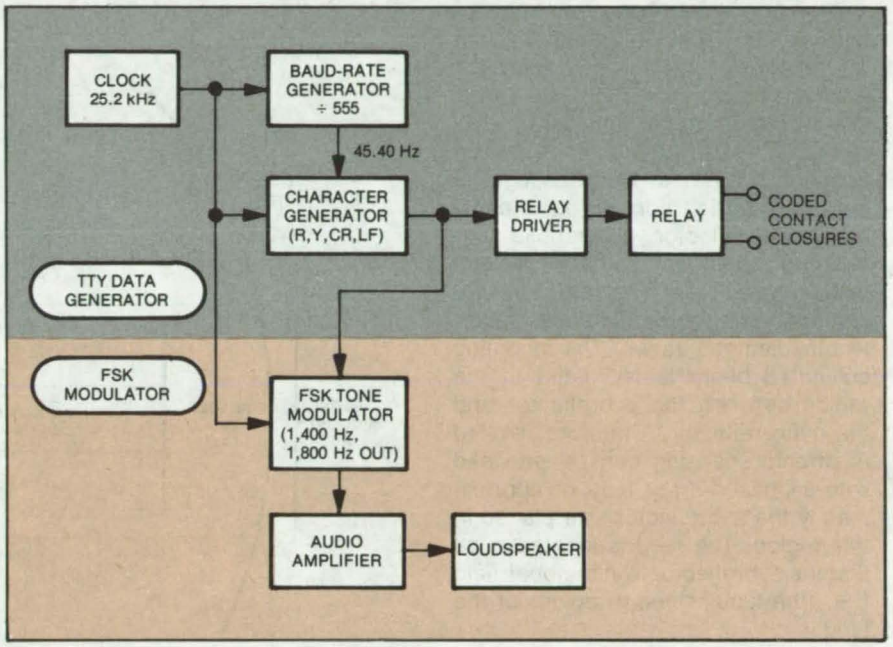

The **Teletype Test Unit** uses CMOS digital integrated circuitry, which may be operated from a relatively inexpensive battery of any voltage from 3 to 18 volts. CMOS logic is inherently low-power and yields excellent battery life. Since the circuit is relatively simple, it may be packaged in a small enclosure permitting easy handling and portability. The prototype was built using wire-wrap techniques on perforated board and was housed in a 4- by 5- by 6-in. (10- by 12.7- by 15.2-cm) aluminum minibox. Power was supplied from a 9-volt transistor-radio battery.

The result is a continuous printout of double-spaced lines of RY. The character pair RY is considered to be the most difficult alternating character for the Baudot teletype to print because the five information bits of the characters are interleaved and have alternating bit patterns: R = 01010 and Y = 10101.

The serial bit stream from the character generator is routed to both the relay driver and the FSK tone modulator. The relay driver operates a reed relay that is used to generate current pulses in the teletype selector magnets. The FSK tone modulator is a variable modulus counter controlled by the serial data from the character generator. The audio amplifier and loudspeaker are not critical items in this design, and several suitable choices are available commercially.

This work was done by Richard H. Couch of **Langley Research Center** *and H. Clark Beall of Research Triangle Institute. For further information, Circle 9 on the TSP Request Card.*

LAR-12527

Limited Scan Dual-Band High-Gain Antenna

Cassegrainian antenna operates on S- and X-band frequencies simultaneously.

NASA's Jet Propulsion Laboratory, Pasadena, California

A proposed dual-band communications and tracking antenna, with limited scan and large aperture, allows phased scanning of many beamwidths from the boresight.

Figure 1 shows the antenna design concept. It is a near field Cassegrainian configuration comprising a parabolic main reflector, a parabolic subreflector, and an S- and X-band phased-array feed. The reflectors are confocal and have the same focal-length/diameter ratios. The incoming colimated beam is recreated in the region between the subreflector and the main reflector. Therefore, limited electronic scanning can be provided with a phased-array feed of approximately the subreflector size placed in this region. The feed is located such that the subreflector is in the near field (i.e., the tubular beam region) of the feed.

The antenna feed is a combination of X-band square waveguides interlaced with S-band cross-slot waveguides (see Figure 2). These waveguides utilize TE_{10} modes. The S-band cross slots consist of two rectangular waveguides intersecting each other at their centers. The interleaving waveguide configuration gives the feed a uniform wavefront at both S- and X-band frequencies. A hybrid junction is used at each frequency band to produce circular polarization.

The phasing circuitry incorporated in this design is a conventional configuration using mechanical phase shifters. However, other conventional phasing circuts are also suitable. To restrict the number of elements, the beam for each element can be narrowed by using waveguide (circular or square) to launch the microwave energy into a cigar antenna. The elements can then be spaced further apart. An important design consideration is to use a minimum number of radiating elements, because each element requires phase-shifting that adds to the cost of the scanning antenna.

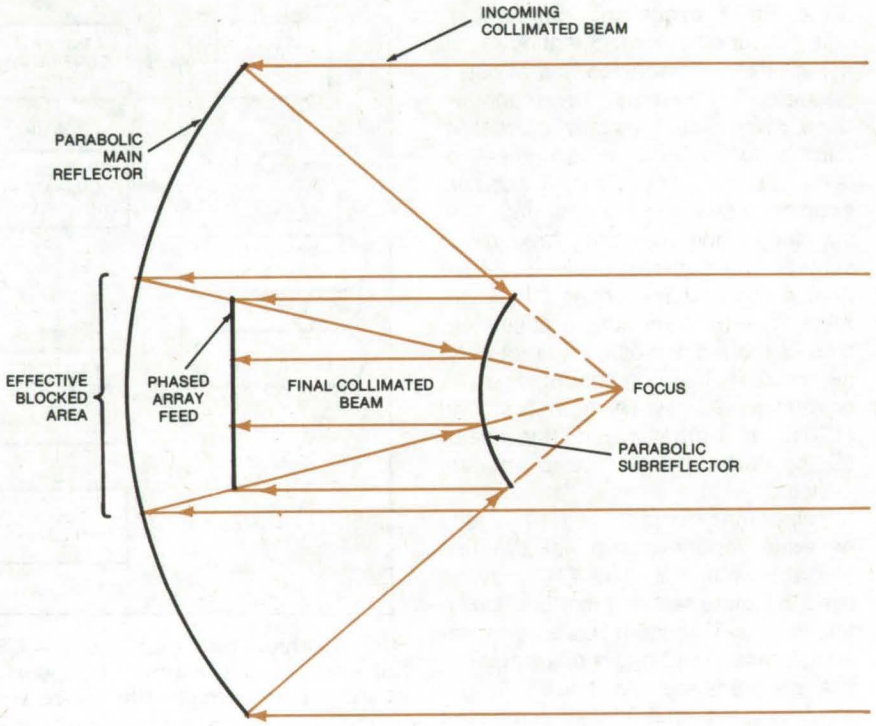

Figure 1. This **Antenna Concept** combines S- and X-band high-gain performance in a near field cassagrainian configuration. The design incorporates a subreflector in the near field of the feed. This arrangement permits limited electronic scanning with a phased-array feed of approximately the subreflector size placed in the region between the subreflector and the main reflector.

Although the near-field Cassegrainian design operates most efficiently for large antennas, a small test antenna (1.22-m diameter) has been built, using a 0.28-m-diameter phased-array feed. The feed is composed of 52 X-band square-waveguide radiators interlaced with nine S-band cross-slot waveguide radiators. The S-band radiators present a quasi-short for X-band signals to minimize coupling. The experimental feed is scanned in only one plane and is linearly polarized, to simplify hardware. A conventional power-dividing and phasing network produces a uniform amplitude distribution and adjustable linear phase.

Test results from the experimental antenna indicate that the on-axis efficiencies and scan characteristics are as predicted by spherical-wave scattering calculations. Coupling between the S- and X-band radiators is negligible. Calculations for a similarly designed 15-m-diameter antenna predict an on-axis efficiency of over 70 percent and a scan capability over many beam widths at both S- and X-bands without excessive scan loss.

This work was done by Paul W. Cramer, Jr., and Kenneth E. Woo of Caltech for **NASA's Jet Propulsion Laboratory.** *For further information, Circle 10 on the TSP Request Card.*

This invention is owned by NASA, and a patent application has been filed. Inquiries concerning nonexclusive or exclusive license for its commercial development should be addressed to the Patent Counsel, NASA Resident Legal Office-JPL [see page A8]. Refer to NPO-14038.

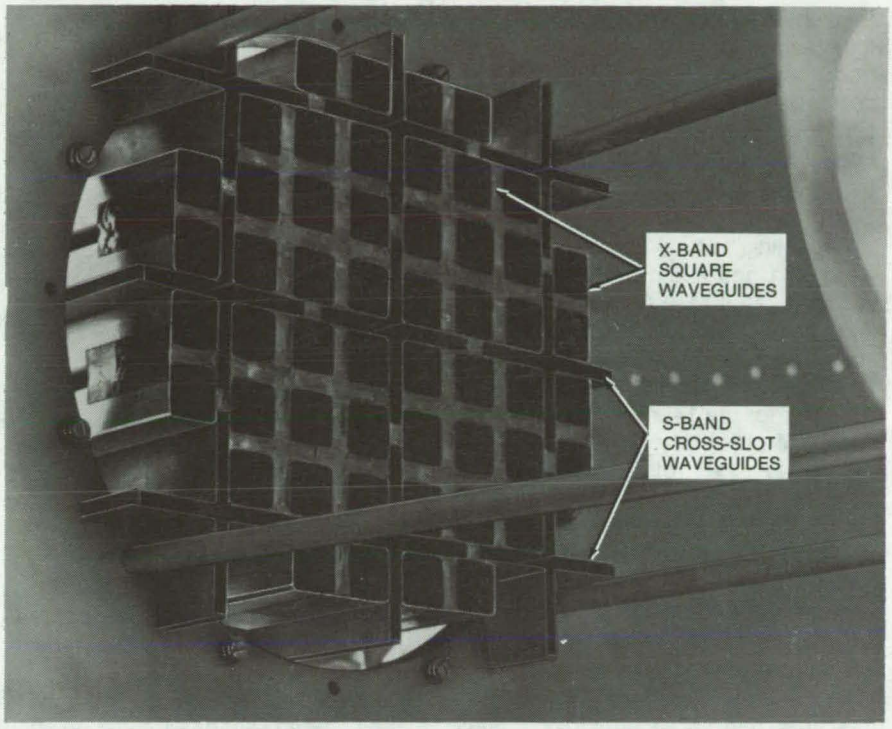

Figure 2. The **Dual-Band Feed** incorporates X-band square waveguides interlaced with S-band cross-slot waveguides.

Dual Hybrid Mode Feed Horn

An improved feed horn increases the efficiency of microwave antennas.

NASA's Jet Propulsion Laboratory, Pasadena, California

A new antenna feed horn is a combination of corrugated, round, and tapered waveguide configurations that are dimensioned to excite the HE_{11} and HE_{12} modes to illuminate a reflector antenna more uniformly than antenna horns excited only in the HE_{11} mode. The horn is adaptable to both symmetrical and asymmetrical Cassegrainian antennas. It provides a 0.36-dB gain improvement feeding a symmetrical antenna and a 0.29-dB gain improvement feeding an asymmetrical system.

The throat region of the new dual hybrid-mode horn is shown in the illustration. The design is based on the center frequency of 8.45 GHz. Although most of the elements of the dual hybrid-mode horn influence the impedance bandwidth to a minor degree, the horn is very well matched near the design center frequency without the use of additional elements. By experiment, the phase center of the new horn is determined to be 7.88 in. (20.02 cm) inside the aperture.

Efficiencies at $\Theta = 14.784°$		Single Hybrid-Mode Horn	Dual Hybrid-Mode Horn
Spillover	η_S	0.9483	0.9554
Illumination	η_I	0.8443	0.8989
Cross-Polarization	η_X	0.9999	0.9999
Phase	η_P	0.9983	0.9926
TOTAL	η_T	0.7993	0.8523
Maximum Efficiency	η_{MAX} at Θ =	0.8153 at 13.293°	0.8646 at 13.784°

Single Hybrid-Mode and Dual Hybrid-Mode Horn Efficiencies at 8,450 MHz

In this design, the TE_{11} input waveguide was constrained to remain the same as previously-developed X-band horns. The abrupt step (3.477 to 7.938 cm), in addition to exciting the HE_{12} mode, also plays a major role in controlling the amplitude ratio between the two hybrid modes. The step ratio is finally sized to cut off higher order modes at the upper end of the

(continued on next page)

frequency range. The 6°15′15″ half-flare angle has remained unchanged from the previous single-hybrid-mode designs. While somewhat conservative, this moderate flare angle is slow enough to prevent field distortion at the aperture for horns with less than 30 dB gain.

Beginning at the interface of sections 1 and 2 shown in the figure, the corrugated flare section continues for 43.050 in. (109.347 cm) to an aperture of 12.563 in. (31.910 cm). This aperture size is approximately optimum for the 14.784° half-aperture angle of the 64-m antenna with tricone-feed subreflector. Corrugations are selected to be $\lambda_0/4$ deep at the center frequency with 5 cycles per free-space wavelength.

The efficiency of the new horn is compared with a single hybrid-mode horn in the table. The data shown for the single hybrid-mode horn are computed rather than using the noisier measured data, while data for the dual hybrid-mode horn are measured. This results in a slightly conservative estimate of the improvement in the new design. It is seen that the new horn pattern exhibits a slightly-improved (<1-percent) spillover efficiency and a substantial (5-percent) improvement in illumination efficiency.

This work was done by Dan A. Bathker and Robert F. Thomas of Caltech for **NASA's Jet Propulsion Laboratory.** *For further information, Circle 11 on the TSP Request Card.*
NPO-13594

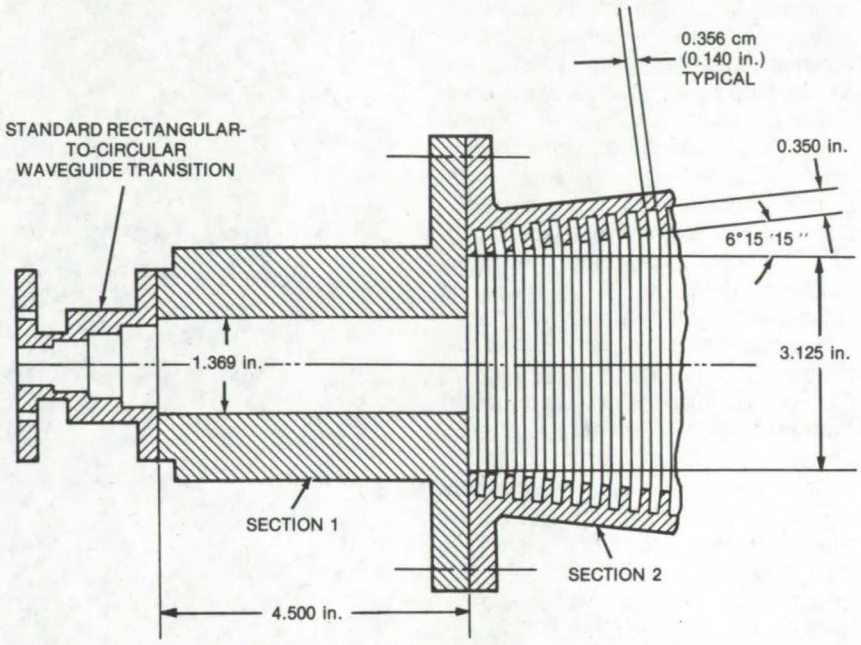

The **New Dual Hybrid-Mode Antenna Feed Horn** comprises two sections. The abrupt step between sections 1 and 2, in addition to exciting the HE_{12} mode, also plays a major role in controlling the amplitude ratio between the two hybrid modes. The corrugations are selected to be $\lambda_0/4$ deep at the center frequency (8.45 GHz) with 5 cycles per free-space wavelength. The new horn improves gain by 0.36 dB when feeding a symmetrical Cassegrainian antenna and by 0.29 dB feeding an asymmetrical system.

Wide-Beam Flush-Mounted Antenna

A six-element phased array produces a broad-bandwidth, wide-angle, circularly polarized beam.

Lyndon B. Johnson Space Center, Houston, Texas

The compact, phased-array antenna shown in the figure has an exceptionally broad, circularly polarized beam and wide bandwidth. Suitable for flush mounting on the surface of a moving vehicle, the six-element S-band antenna operates with a nearly π-steradian field-of-view, 3 decibels of circularly polarized gain, and a bandwidth that extends ±30 percent around the center frequency. Although it was originally intended for use on the Space Shuttle Orbiter, the antenna may also be useful in high-altitude aircraft, communications satellites, and ground-based moving vehicles.

Flush-mounted antennas are normally limited to narrow-bandwidth transmission within a limited field-of-view. Thus, when it is necessary to communicate in all directions, many such antennas must be installed around the transmitting or receiving structure. In contrast, only four of the new antennas are needed for uniform coverage aboard the Orbiter, saving weight, space, complexity, and cost.

The antenna has two coaxial cavities (see figure). The inner cavity contains a pair of dipole radiators arranged with their elements along the orthogonal diagonals of the cavity. The outer cavity contains four monopoles, each alined with one of the radiator elements in the inner cavity.

To transmit a signal, the six antenna elements are energized by a feed network that creates a 90° phase difference between the two dipoles in the inner cavity and a 180° phase difference between these dipoles and the monopoles in the outer cavity. The radiation fields of the elements combine to form a single, circularly polarized beam.

To receive a signal, the six antenna elements absorb circularly polarized energy transmitted from a remote

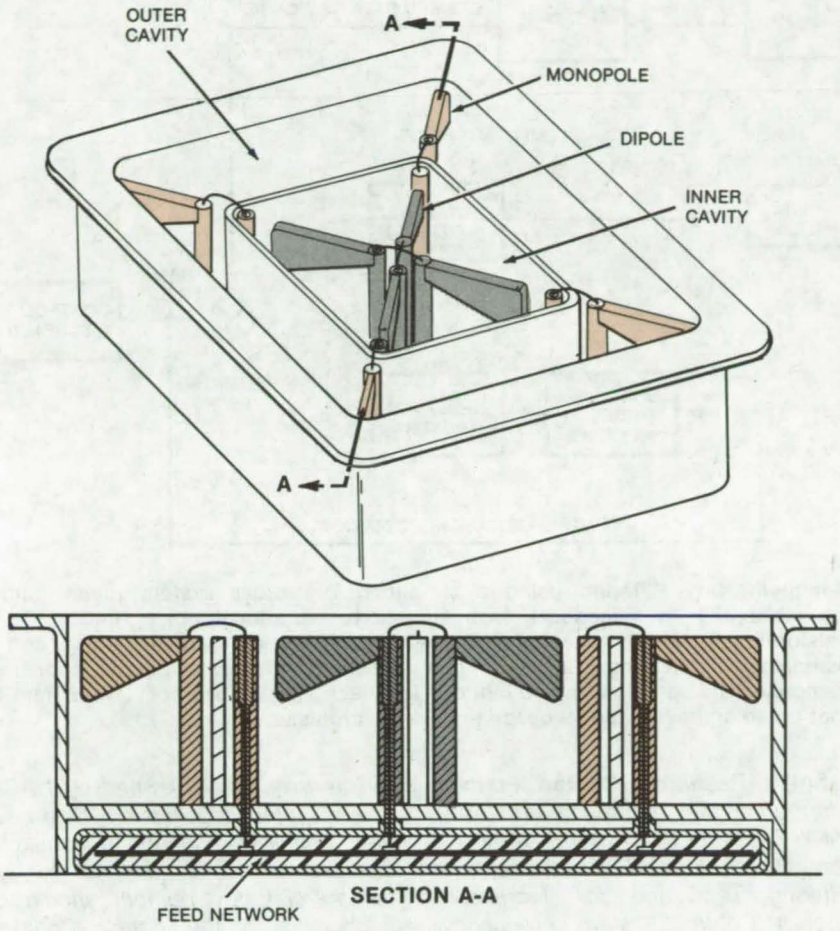

The inner cavity of this **Wide-Beam Antenna** contains a pair of dipoles; the outer cavity contains four monopoles. The feed network is shown in the section drawing at the bottom of the figure. Note that the balun feed for each radiator includes one coaxial post (through which the transmission line passes) and one solid post.

station. The six signals are fed to a network that shifts their phase and combines them into a single signal containing the transmitted information.

Within the wall separating the two cavities are baluns (balance/unbalance impedance transformers) that match the impedances of the antenna elements. Slots can be machined in the corners of the wall to fine-adjust the impedance match; and, loading structures in the outer cavity can be added to modify the shape of the radiation pattern.

This work was done by Haynes Ellis, Jr., of Rockwell International Corp. for **Johnson Space Center.** *For further information, Circle 12 on the TSP Request Card.*

This invention is owned by NASA, and a patent application has been filed. Inquiries concerning nonexclusive or exclusive license for its commercial development should be addressed to the Patent Counsel, Johnson Space Center [see page A8]. *Refer to MSC-16800.*

Higher Gain for Feedback Control Subject to Vibrations

Complementary filtering and a simple system model combine to increase gain and bandwidth.

Langley Research Center, Hampton, Virginia

Complementary filtering and a simple electronic model greatly increase the amount of useful gain achievable in a feedback control system subject to environmental vibration. This technique, devised for a sensor-actuator control loop on a CH-47 helicopter, has increased useful gain from 2 to 4 and increased system bandwidth from less than 0.5 Hz to over 1 Hz.

Useful gain between sensor signal and actuator in a vibrating system is limited by the vibrational noise, which is amplified along with the sensor signal. Some improvement is possible by putting the sensor signal through a low-pass filter to remove the relatively-high-frequency components (sharp vibrational accelerations). However, the time lag introduced by the filter limits the achievable gain through its effect on the control-system limit cycle.

In a feedback control loop, there is a certain amount of hysteresis (or "slop") between system response and actuator signal. This hysteresis lag leads to oscillations, called the limit-cycle effect, if the gain is increased beyond a certain point. The additional time lag produced by simple filtering further lowers the tolerable gain.

The effect of this hysteresis can be compensated for by attempting to predict the response of the controlled portion of the feedback loop and incorporating this prediction into the actuator signal. An implementation of this approach is shown in the block diagram. The sensor (rate gyro) is fed

(continued on next page)

through a conventional low-pass filter to remove vibrational noise. At the same time, a simplified model predicts the controlled-surface response to an infinitesimal actuator signal. This prediction signal is put through a high-pass filter that removes the long-term errors in the calculated response and leaves a good estimate of the high-frequency components of the system motion.

The time constants (0.2 in the illustrated application) of the two filters are matched so that the sum of their outputs is a complete angular-rate feedback signal, with noise and lag removed.

The effect of filter time constant on noise boundary for the complementary filter is the same as for a conventional filter, but the effect on the limit-cycle boundary is changed profoundly because no lag is added. Therefore by increasing the filter time constant, gains can be made much higher than with a low-pass filter alone.

In tests with the CH-47 helicopter, results were impressive. Gain and bandwidth improvements were found to be relatively insensitive to the accuracy of the system model. Even a zero-order model showed measurable improvement, and all first-order models tried resulted in reduced system noise with significant increases in gain and bandwidth without encountering a limit-cycle problem.

This work was done by John F. Garren, Jr., and Frank R. Niessen of **Langley Research Center.** *Further information may be found in NASA TM-X-74004 [N77-17103], "Application of a Modified Complimentary Filtering Technique for Increased Aircraft Control System Frequency Bandwidth in High Vibration Environment," a copy of which may be obtained at cost from the North Carolina Science & Technology Research Center [see page A7].*

This invention is owned by NASA, and a patent application has been filed. Inquiries concerning nonexclusive or exclusive license for its commercial development should be addressed to the Patent Counsel, Langley Research Center [see page A8]. Refer to LAR-12215.

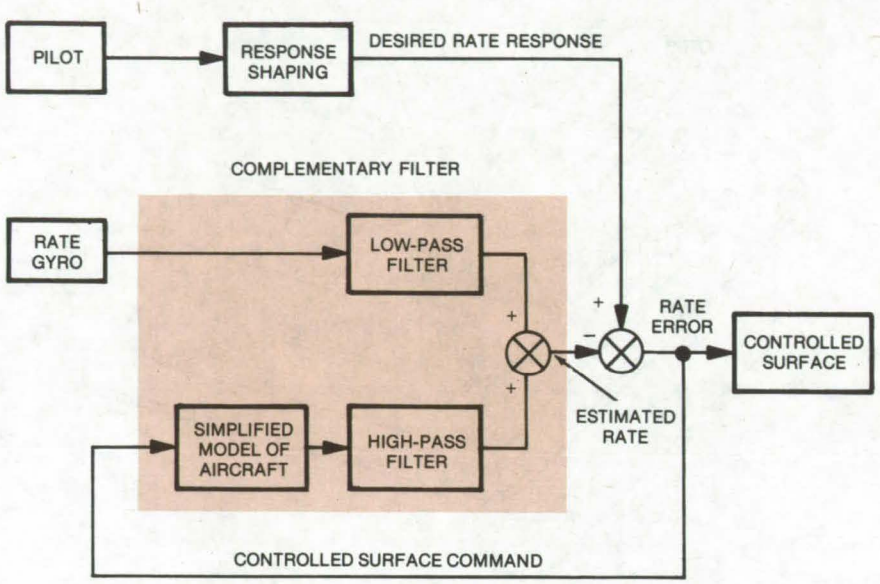

Complementary Filtering using a simplified first-order system model allows increased gain in a feedback loop subject to vibrational noise. In the CH-47 helicopter, the rate-gyro sensor is filtered to remove high-frequency noise, and an estimated vehicle-model signal is complementary-filtered to predict short-term response. The combined noise-reduced feedback signal does not have a time lag that could aggravate the feedback limit-cycle problem.

Fault-Tolerant Computer System

Self-checking "building blocks" would increase reliability.

NASA's Jet Propulsion Laboratory, Pasadena, California

More reliable computers could be assembled by using proposed VLSI "building-block" circuits with built-in error detection. Four such circuits would be connected with standard microprocessors and memory devices to form a self-checking computer module. Each building block detects its own malfunctions, and the complete module also corrects single-bit errors found in memory (usually the most fault-susceptible part of a computer). Noncorrectable faults are handled by switching in replacement computer modules, shutting down operation, or by taking other corrective steps.

The four fault-tolerant building blocks, designated memory interface, programable bus interface, input/output interface, and core, are interconnected as shown in the figure. A three-state internal bus is shared by the building blocks. Each block signals faults in its circuitry to the core. The core also checks the bus signals for proper coding.

Upon detecting a fault, the core disables the bus-control and I/O functions, isolating the computer from its environment. The core can then either halt further processing, initiate rollback and restart, or initiate a memory reload and restart. If the fault repeats, an external module could take over processing.

The fault-detecting and correcting memory-interface building block interfaces the computer memory to the internal bus. The block feeds Hamming corrections to damaged memory

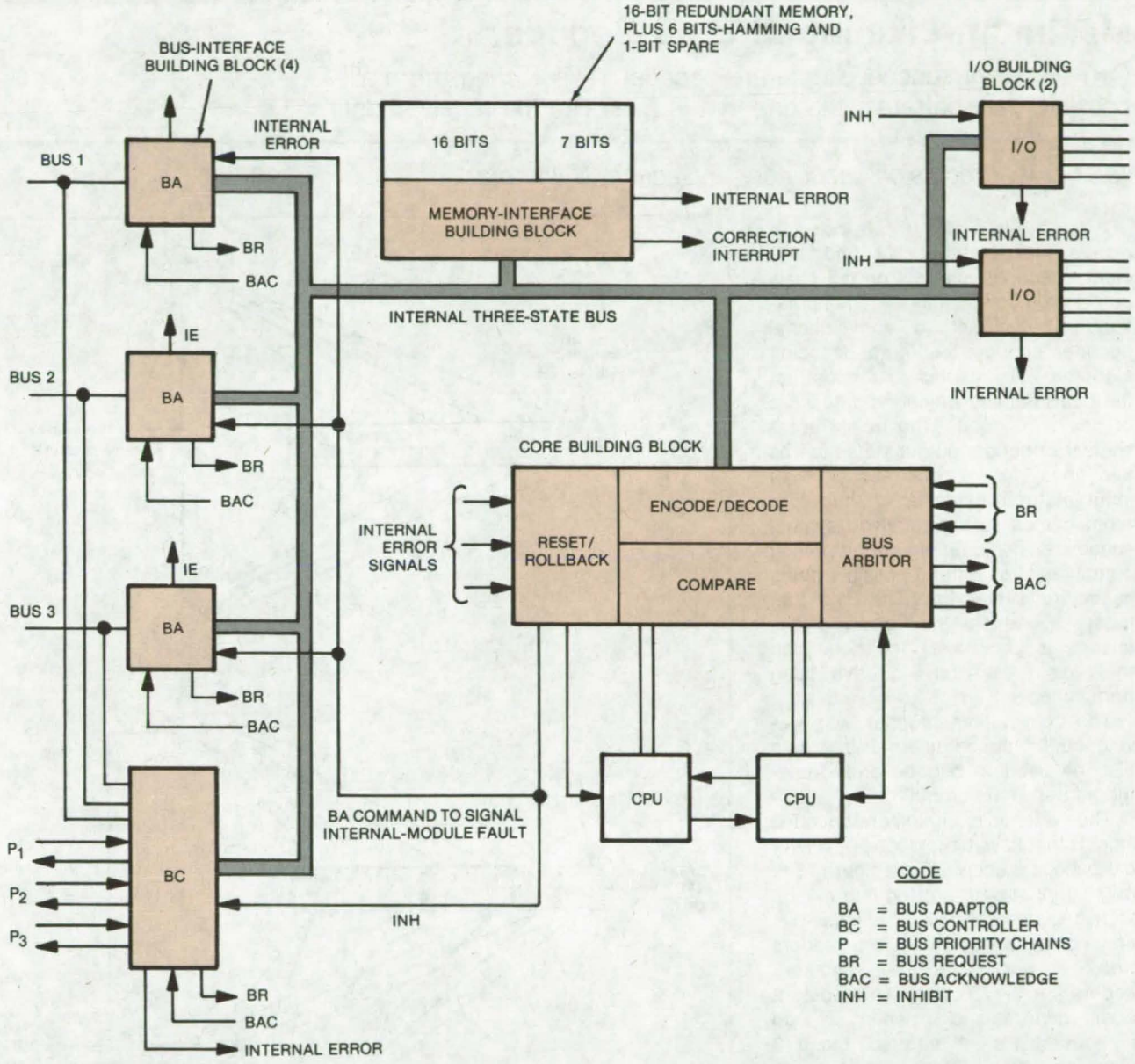

Proposed **Self-Checking Computer Module** has a core building block, a memory-interface building block, four bus-interface building blocks (three programed as bus adapters and one programed as a bus controller), and two I/O building blocks. The core receives error signals from the other blocks and also checks itself for faults. Malfunctions are responded to by shutting down, restarting, or transferring control to replacement computer modules.

data, automatically replaces a faulty bit with a spare, generates parity coding and decoding, and detects its own internal faults.

The bus-interface building block transfers information between computer modules or between a computer module and I/O devices over an external bus. This block can be microprogramed as a bus adapter or bus controller. Faults are detected through parity coding and through internal duplication, with morphic comparison for most of the logic circuitry.

Since I/O hardware has different voltage ranges, currents, timing parameters, and word formats, the I/O building block would offer a standard set of functions for interfacing the most common configurations. The user could supply additional functions for special or nonstandard applications.

The core building block detects central-processing unit (CPU) faults, collects fault indications from itself and other building blocks, and disables its host computer module upon detection of a permanent fault.

Preliminary cost studies indicate that as the level of large-scale integration is increased in the building-block circuits, memory becomes the dominant cost in the network. However, as the level of integration is increased, the cost of producing the self-checking computer approaches that of conventional computers.

This work was done by Algirdas A. Avizienis, David A. Rennels, and Milos Ercegovac of Caltech and UCLA for **NASA's Jet Propulsion Laboratory.** *For further information, Circle 13 on the TSP Request Card.*
NPO-14562

Maximum-Likelihood Data Decoder

Convolutionally encoded data are decoded by selecting, from all possible data patterns, the one that is most like the received data.

NASA's Jet Propulsion Laboratory, Pasadena, California

A digital circuit for a data-communication receiver quickly and efficiently decodes the data on the basis of "maximum-likelihood" computations. The circuit, a convolutional decoder, employs the Viterbi decoding algorithm, which tries to reconstruct the trellis path by which the data were originally encoded. [The trellis represents the encoder output states (zeros and ones) for a given sequence of input states.] Essentially, the algorithm compares the received symbol sequence (which, of course, may contain errors) with all possible paths in the trellis diagram. The path that most resembles the received sequence is chosen as the sequence that was most likely to have been transmitted.

The convolution decoder was developed for space telemetry. It can also be used to decode data transmitted between computers.

The system described here decodes signals that have been coded by one of the encoders shown in the figure. The original input data are fed into a 7-bit shift register that has various bits connected to two modulo-2 adders (for 7-1/2 code) or to three modulo-2 adders (for 7-1/3 code). (A modulo-2 adder generates a 1 when an odd number of 1's are entered and a 0 when an even number of 1's are entered.) The outputs from the adders are sequentially sampled and together form a symbol word; i.e., each data bit entered at the input to the encoder produces a 2-bit data word (C_1C_2) or a 3-bit word ($C_1C_2C_3$) as an output.

The Viterbi algorithm is a decoding technique for reconstructing the most probable sequence of data bits originally fed into the encoder and then generating an output data bit, after 20 to 40 symbol words have have

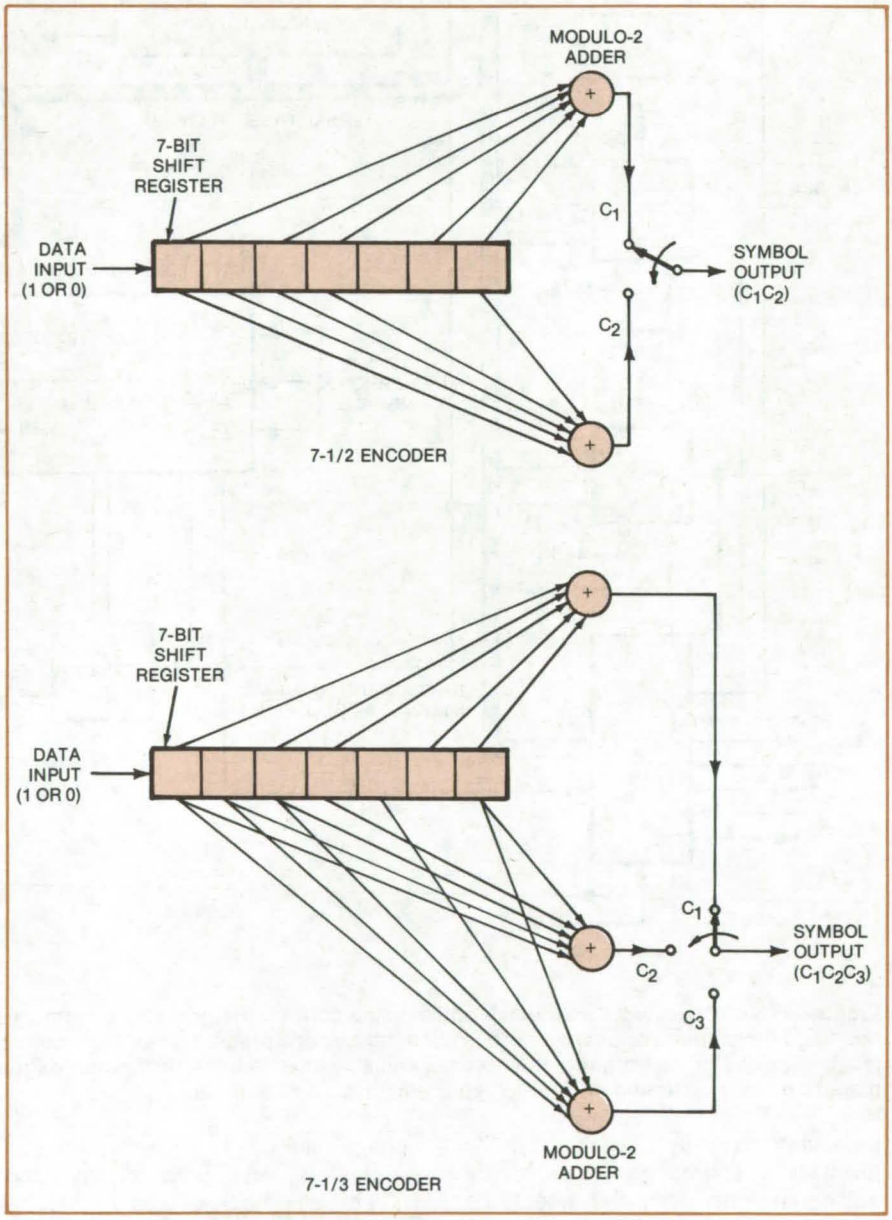

Data Are Encoded in 7-1/2 or 7-1/3 code by a 7-bit shift register and two or three modulo-2 adders. The data can be decoded by circuitry for efficient implementation of the Viterbi algorithm, as explained in the text.

received (N = about 30). The two or three input bits to the decoder produce a single output bit, depending on whether the decoder is operating at the 1/2 or 1/3 rate. Each symbol bit is input as a 3-bit binary valve ("soft" quantized). (The 1/3 code offers an improvement of about 0.3 decibel in signal-to-noise ratio over the 1/2 code, at the same bit-error rate.)

The decoder output bit is determined by constructing many possible data sequences, or paths, within the decoder. These paths are constructed on the basis of accumulated probability values, or "metrics". The decoder has $2^6 = 64$ different states, and a metric is assigned to each state. Each state metric is an accumulation of the selected branch metric values (which correspond to the more likely of the two possible branches traversed in entering a state), summed over the N symbol words received.

For each symbol word received, all state metrics are updated once, according to the appropriate branch metrics, and each update corresponds to a transition from one state to another. Each time a state metric is updated, a new path-history bit is generated and inserted in a path record. In this way, all possible paths (one path per state) are constructed for each received symbol word. The older parts of each path converge and eventually become the same bit as N increases — in other words, a majority vote among the oldest bits in each path determines the decoder output bit.

The convolutional-decoder code rate is selected by an external control command. The decoder uses a random-access memory (RAM) for state metrics and path records. Separate read-only memories (ROM's) are used for the code-rate 1/3 and 1/2 branch metrics. The decoder tests itself with a unique test sequence from a bit generator that feeds a combination rate-1/2 or rate-1/3 encoder. For greater processing speed, the decoder operates on two pairs of state metrics simultaneously.

This work was done by Marvin E. Alberda of Caltech for **NASA's Jet Propulsion Laboratory.** *For further information, Circle 14 on the TSP Request Card.*
NPO-13574

Microprocessor-Based Interface for Oceanography

Standard interface units simplify an ocean-floor imaging system.

NASA's Jet Propulsion Laboratory, Pasadena, California

A data-collection system developed for spacecraft has been adapted to surveying and mapping the ocean floor. The system consists of control modules and five identical microprocessor-based interface units, each of which is assigned to a sonar instrument. The command and control idiosyncrasies of each sonar are handled by the control and interface software. This approach eliminates the need for "custom tailoring" of hardware interfaces. Also, it eliminates separate data links and redundant displays by time sharing of a single bus. The same approach can be used for data collection in other applications.

In the oceanographic system, the vessel-towed FISH (fully-instrumented submersible housing) is analogous to a spacecraft. The towline is the single data and command channel, which corresponds to the radio link for a spacecraft; and the shipboard computer and control for the FISH are very much the same as the spacecraft ground control.

As shown in Figure 1, FISH incorporates five sonars. Three are position indicators giving depth, height

(continued on next page)

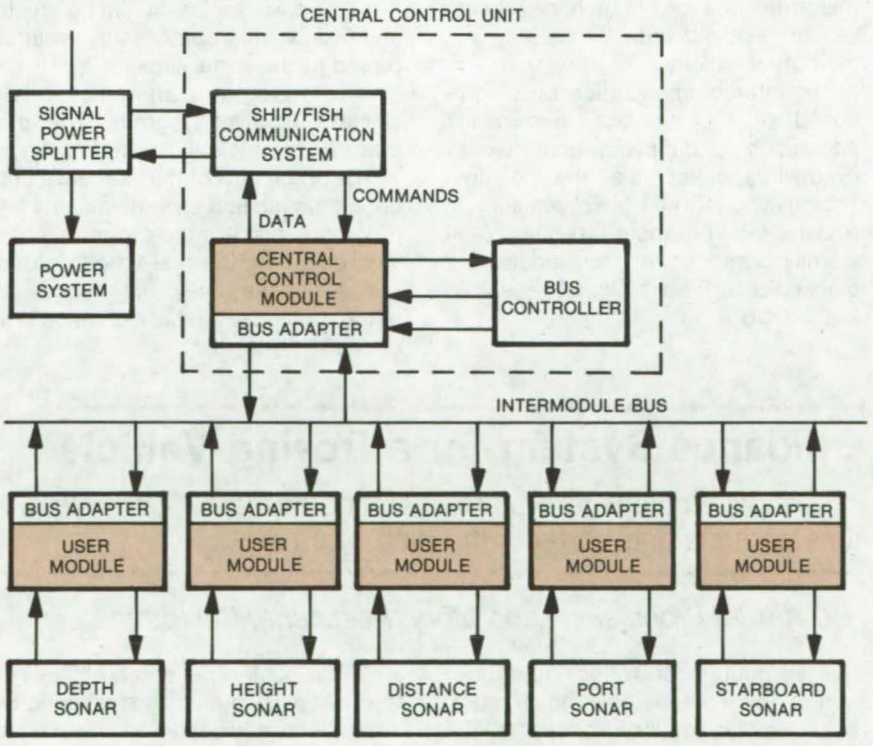

Figure 1. The **FISH Data System** incorporates microprocessor-based standardized user modules. These simplify interfacing between the sonars and the data-collection equipment. System operation is controlled by a central control module that is also based on the same microprocessor. This approach eliminates "custom tailoring" a hardware interface for each measuring instrument.

above bottom, and distance to bottom-anchored transponder beacons. The port and the starboard side-scan sonars gather the acoustic imagery of the ocean floor. All five operate in a pulsed CW (continuous-wave) mode. The side scanners generate fan-shaped, vertical beams covering the ocean floor from straight down to the horizontal. The continuous echoes build up a line-by-line image of the ocean bottom on each side of the towpath.

Each sonar is connected to a user module (UM). A UM contains a microprocessor, 2K of random-access memory, an input/output (I/O) addressing module, and a bus adapter to the data and address buses.

A central control unit (CCU) coordinates processing in the UM's. The CCU contains, in addition to the components found in the UM, a bus controller, an analog input system, and an interface with the ship. The CCU collects and distributes commands and data received and transmitted over the communication link.

The bus controller moves data between the memories of all modules connected to the bus. It allows the CCU to place commands into the memories and also to monitor processes or received data by reading out memory locations.

The intercommunication bus, composed of a data bus, command/address bus, bit sync, and "word" sync wires, connects all the modules. The bit sync rate is 1 MHz, resulting in a data rate of about 40,000 16-bit words per second. All the modules are clocked by a 5-MHz signal generated in the CCU.

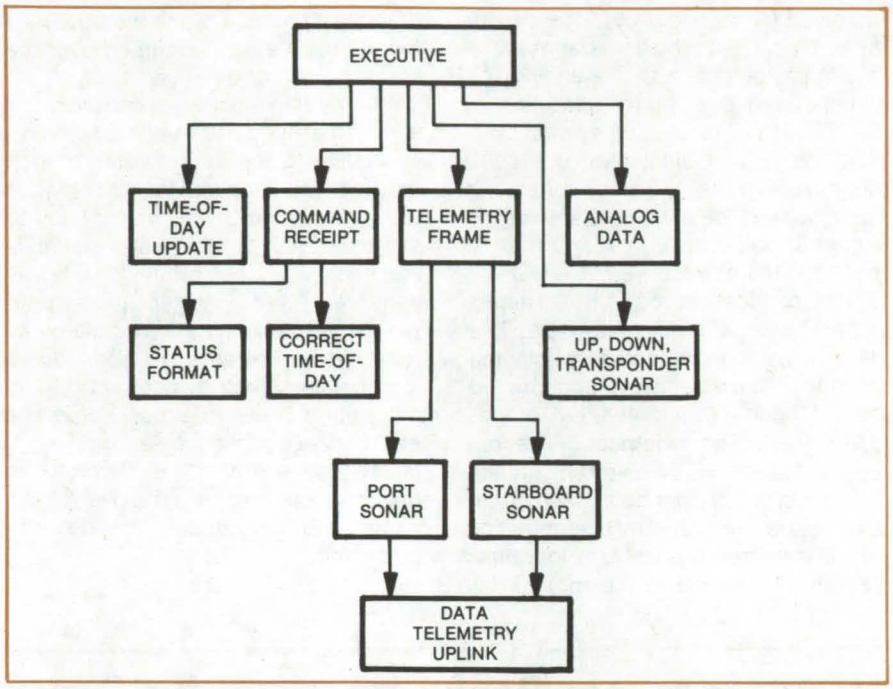

Figure 2. The **System Software** is initiated by an executive program. The executive updates all software counters, invokes appropriate user programs, executes user programs as dictated by the software counter contents, and controls the number of user programs executed during an interrupt period.

Each UM is synchronized with the rest of the system by a real-time interrupt occurring every 5 ms. The 5-ms unit is the basic timing cycle, and every microprocessor is interrupted at the same time.

All UM programs are initiated by a single executive program. The program hierarchy is illustrated in Figure 2. The prime task of the executive is to control timing and execution of the UM programs, and it is the program that is invoked during the real-time interrupt. The executive uses only about 15 percent of the available execution time during the interrupt.

The new system may be expanded. Instruments under consideration include a television camera and a "forward-looking" sonar for obstacle avoidance. Still cameras, pressure gages, thermometers, and conductivity and speed-of-sound devices are also being considered.

This work was done under the direction of George R. Hansen of Caltech for **NASA's Jet Propulsion Laboratory.** *For further information, Circle 15 on the TSP Request Card.*
NPO-14566

Guidance System for a Roving Vehicle

An adaptive guidance system operating in real time controls and corrects the path of a robot.

NASA's Jet Propulsion Laboratory, Pasadena, California

A computer-controlled guidance system for a semiautonomous robot [see "Self-Navigating Robot" (NPO-14190) on page 31 of *NASA Tech Briefs*, Vol. 3, No. 1] guides the robot in an incompletely defined environment. The system operates in real time, avoiding obstacles detected by its stereo-television and laser-rangefinder "eyes." Its navigation hardware is a gyrocompass and optical-encoder odometers.

The robot (called "Rover") is controlled by a local minicomputer in communication with a large remote time-shared computer. The system software (see Figure 1) is an integrated set of subsystems, which include the Prototype Ground System, the Rover Executive, the Vision and Manipulation subsystems, and the Locomotion subsystem.

A trajectory plan (based upon available environmental information) is generated in the Locomotion subsystem by a path-planning module, which feeds the planned path to the guidance system for execution. Ideally, the planned trajectory would be presented in segments called links (see Figure 2), where each link is a constant minimum-radius turn in forward or reverse to a desired heading, followed by a straight path link (also either forward or reverse). In actuality, since the robot moves as its wheels are being steered, the true path deviates from the ideal. This error is computed and accounted for by the guidance system software. Each path link has a width associated with it, which defines the maximum deviation from the ideal path within which the vehicle may operate. The guidance software minimizes errors between planned and actual trajectories by determining the optimum point to change direction at a given speed to reach a specified point.

Real-time maneuver planning is invoked in response to changes in goal definition, environmental and vehicle performance models, hazard detection, or significant execution errors. When in the planning mode, the guidance system assesses the maneuver required, establishes accuracy requirements for the maneuver, and determines speeds and steering points. The guidance system then returns to the execution/monitoring mode until an event occurs that again invokes the planning process.

There are two aspects of path correction: heading correction (a change in direction) and "crosspath" correction (a transverse displacement to a parallel path). The former is executed by steering the wheels in the appropriate direction until half the error is corrected and then resteering to straight while maintaining the vehicle speed to complete the correction. The crosspath deviation is corrected by selecting the fastest steering speeds capable of executing a maneuver within a given distance.

Hazards or obstacles are avoided by using the same approach as in crosspath correction. The vehicle is placed on a parallel path displaced by the proper distance to avoid the obstacle. A similar process returns the vehicle to its original path.

Experiments show longitudinal errors of less than 1 percent and transverse errors of less than 5 percent of the net-turn arc length. The orientation errors are about 1° in a relatively-simple uncluttered environment. All of these are mainly due to the detection apparatus and its associated hardware.

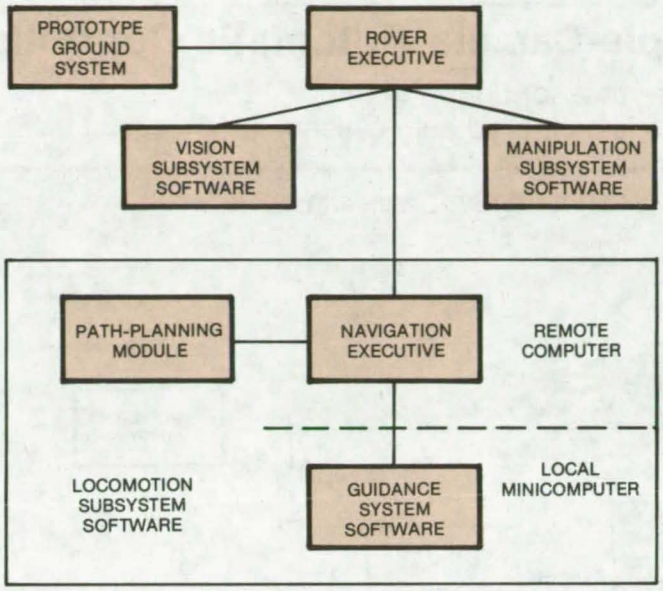

Figure 1. The **Robot Guidance-System Software** controls a semiautonomous robot over an incompletely defined environment, avoiding hazards encountered en route.

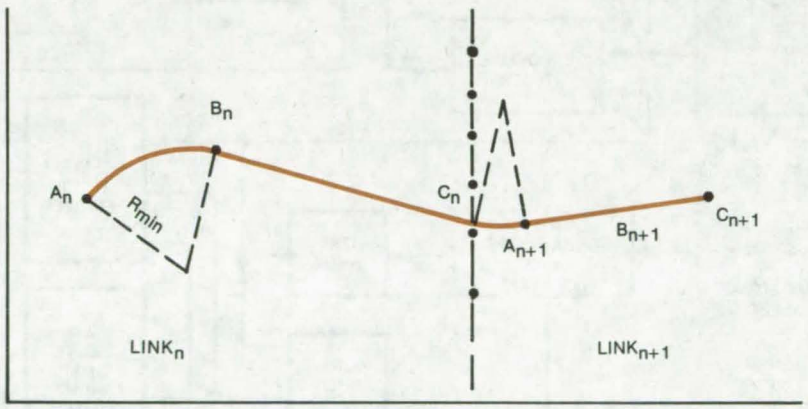

Figure 2. Each **Path Link** is planned as a minimum-turn radius followed by a straight segment. The actual path differs from the planned path because steering maneuvers are not executed instantaneously. Nonetheless, the deviations are accounted for, and minimized, by the path-planning software.

This work was done by James A. Miller of Caltech for **NASA's Jet Propulsion Laboratory.** *For further information, Circle 16 on the TSP Request Card.*
NPO-14376

Multiple-Camera Automatic Controller

Exposure time for up to three cameras is controlled automatically.

Lewis Research Center, Cleveland, Ohio

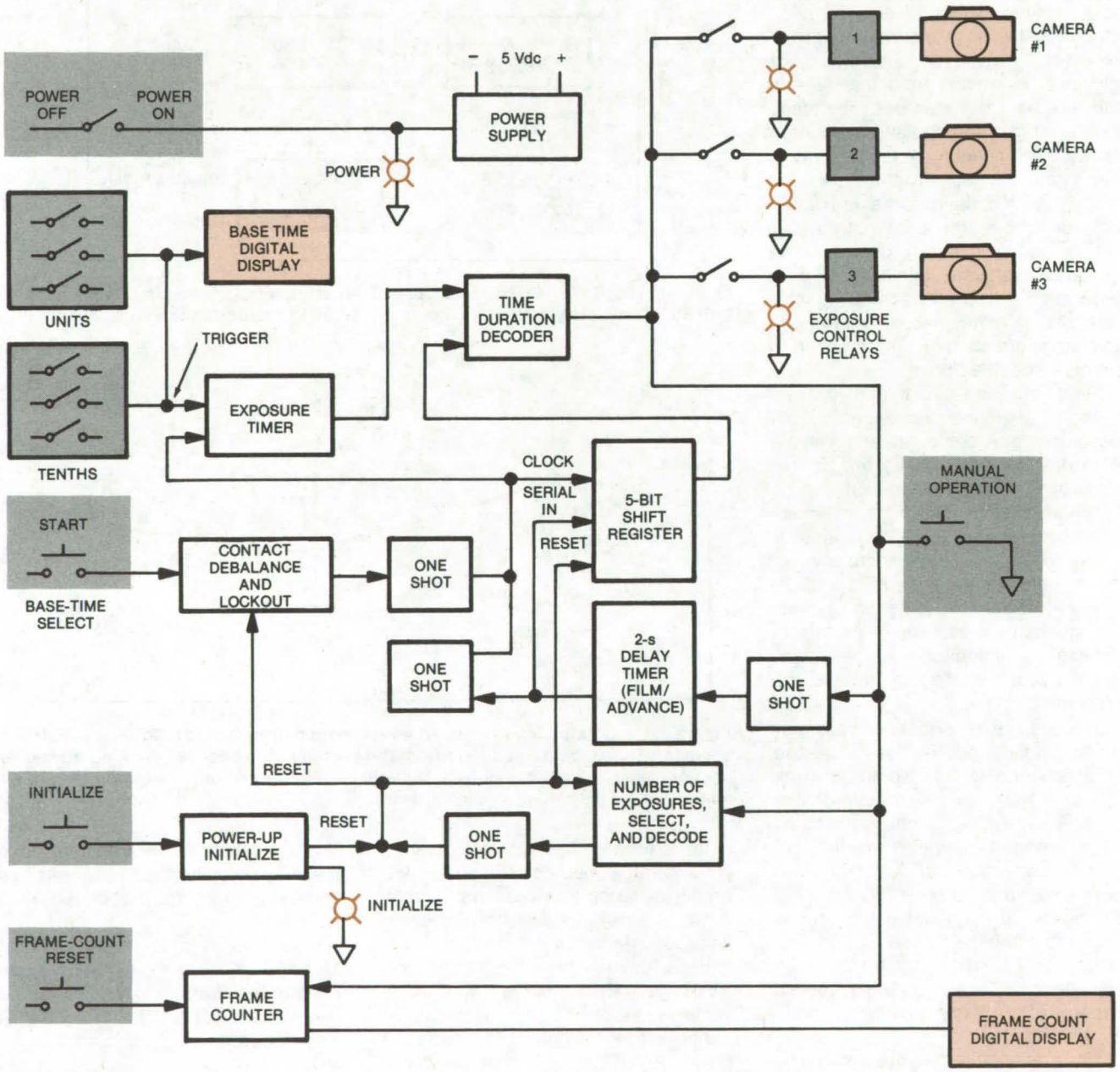

Automatic Controller is shown for three cameras. Digital readout on the controller panel displays the base time selected. The second digital readout, the exposure counter, indicates the total number of pictures taken through the automatic sequencing.

An automatic-camera controller has been developed to vary the exposure time of remotely located cameras with motorized film advance. The cameras are used for photographing the internal-combustion chamber of a jet engine through special viewing ports. Since photographs are taken over a range of exposures and since the camera operator cannot approach the cameras during engine test operations, it is necessary to remotely vary the camera "f" stop exposures.

The controller can simultaneously control the exposure time of one to three remotely located cameras. The cameras are operated electronically through the "bulb" shutter control, which disengages the shutter control from the camera and allows the shutter to remain open as long as the shutter release is activated. The controller allows the sequencing of one to five exposures (at the choice of the operator) for which each succeeding exposure time is twice the previous exposure time. This is equal to opening the shutter by one "f" stop following each exposure. Thus photographs can be taken over a predetermined exposure range in order to obtain the best pictures.

The operator can select the base time; i.e., the first exposure time within a range of 0.1 second to 99 seconds in 0.1-second increments. For any base time selected for a series of five exposures, the camera will take five pictures with the succeeding exposure times in multiples of 1, 2, 4, 8, and 16 times the base time. The controller then automatically stops, resets, and waits for the next manually-initiated start signal.

When the unit is turned on, the circuit automatically resets itself, causing the shift register, counters, and indicators to reset to zero. This is indicated by an "Initialize" light on the panel. The operator can also manually initialize the circuit at any time by use of a pushbutton. The operator then selects, by panel switches, any combination of the three cameras to be controlled, and indicating lights show which cameras have been selected. The operator also selects the base time by panel switches, and selection is indicated by the digital indicator. Switches are also used to select the number of exposures (1 to 5) per sequence.

When the start button on the controller is manualy activated, the circuitry will step through the selected number of exposures. When the selected number of exposures per sequence is completed, the sequence stops, the circuit resets, the "Initialize" light comes back on, and the circuit is ready for the next start signal.

As an option, the manual operation button can also be used to operate the camera manually; however, manual operation does not register on the exposure counter.

This work was done by E. T. Bloam of **Lewis Research Center.** *For further information, Circle 17 on the TSP Request Card.*
LEW-12711

Computer Programs

These programs may be obtained at very reasonable cost from COSMIC, a facility sponsored by NASA to make new programs available to the public. For information on program price, size, and availability, circle the reference letter on the COSMIC Request Card in this issue.

Navigation-Aid Power Systems

Design synthesis and performance analysis of solar-cell-power system

The Design Synthesis and Performance Analysis (DSPA) program package is a collection of subroutines for computing the design and performance characteristics of a navigation-aid power system. DSPA programs are used to obtain ambient temperature and solar radiation data from weather tapes and to develop specifications for viable, solar-array-charged, battery-power systems for the flashing-lamp buoys employed as maritime aids to navigation.

The program can also simulate the operation of these power systems under specified conditions. In the past, circuits and modules were evaluated by nodal analysis. In a system with more than a few modules, that approach is costly because of the multiplicity of nodes needed in the solution. DSPA uses a graphical analysis method that decreases the complexity of solving the problem and lends itself to a more accurate modeling of battery-current and voltage characteristics. This program should be of interest to anyone designing solar-array-charged, battery-power systems for maritime or shore-based applications.

The DSPA computer program combines design synthesis and performance analysis. A flexible modular program, it accepts data on solar insolation, wind, or wave motion as primary power sources. Wind and wave motion can be included in the analysis by adding subprograms that describe the characteristics of these generators.

Options include design synthesis, design synthesis followed by a performance analysis, or performance analysis only.

For design synthesis, load and environmental profiles and a profile energy balance are calculated based on the data input. Using the profile energy balance, an estimate of the electrical size of the equipment is calculated. From this the physical size of the equipment is determined.

For performance analysis, the parameters necessary to determine the various profiles are input, and values for the load and environment are calculated at the beginning of the mission period. These values are used to calculate the operational characteristics of the equipment at the beginning of the mission. This process is repeated for the selected time intervals until the operational characteristics of the power system have been determined for the entire mission period.

(continued on next page)

DSPA requires three forms of input: (1) control cards to direct execution of the program, (2) namelist data, and (3) time-variant-force data such as weather data. The solar insolation and temperature data can be obtained from NOAA data tapes for a period of up to 12 years by using subprogram MERGE. Alternately these data can be entered on cards for up to 52 weeks. If performance analysis follows design synthesis in the same run, then the values input for design synthesis become the default values for the performance analysis.

DSPA outputs tabular printouts and graphics. Graphical output is produced only for performance analysis runs and consists of current-versus-voltage plots or summary-performance plots. Output from the design synthesis routines is in the form of four tables. The first table is an overview of the solar-array-charged, battery-power system, including load and system requirements and subsystem procurement quantities, costs, and weights. The second table gives more detailed engineering information for the power source and energy storage groups. The third table lists additional battery-performance data. The fourth table is powerload profile-analysis information. Each table is labeled, and each printed-data item is accompanied by a descriptive label that includes the units associated with the variable.

There are three types of output associated with the performance analysis portion of the DSPA program: optional "instantaneous" current-voltage plots, summary plots, and a summary printout. These plots show the current-versus-voltage curves of the several power-system elements (solar array, shunt limiter, and batteries) at a particular "instant" in time. The performance-analysis summary output consists of three print tables and their corresponding plots. The first table (there is no plot associated with this table) presents summary data for the unregulated bus system. The second table and its corresponding plot show power-source group-summary data. The third table and its associated plot give summary data for the batteries and the energy storage unit.

The program has been written in FORTRAN V for execution on a UNIVAC 1100-series computer. The program is designed to be segmented and requires 30K of 36-bit words of main memory when loaded as a segmented program. It requires CALCOMP plotting routines for the production of plotted output.

This program was written by Gene L. Goltz, Leo M. Kaiser, and Howard Weiner of Caltech for **NASA's Jet Propulsion Laboratory.** *For further information, Circle A on the COSMIC Request Card.*
NPO-14466

Physical Sciences

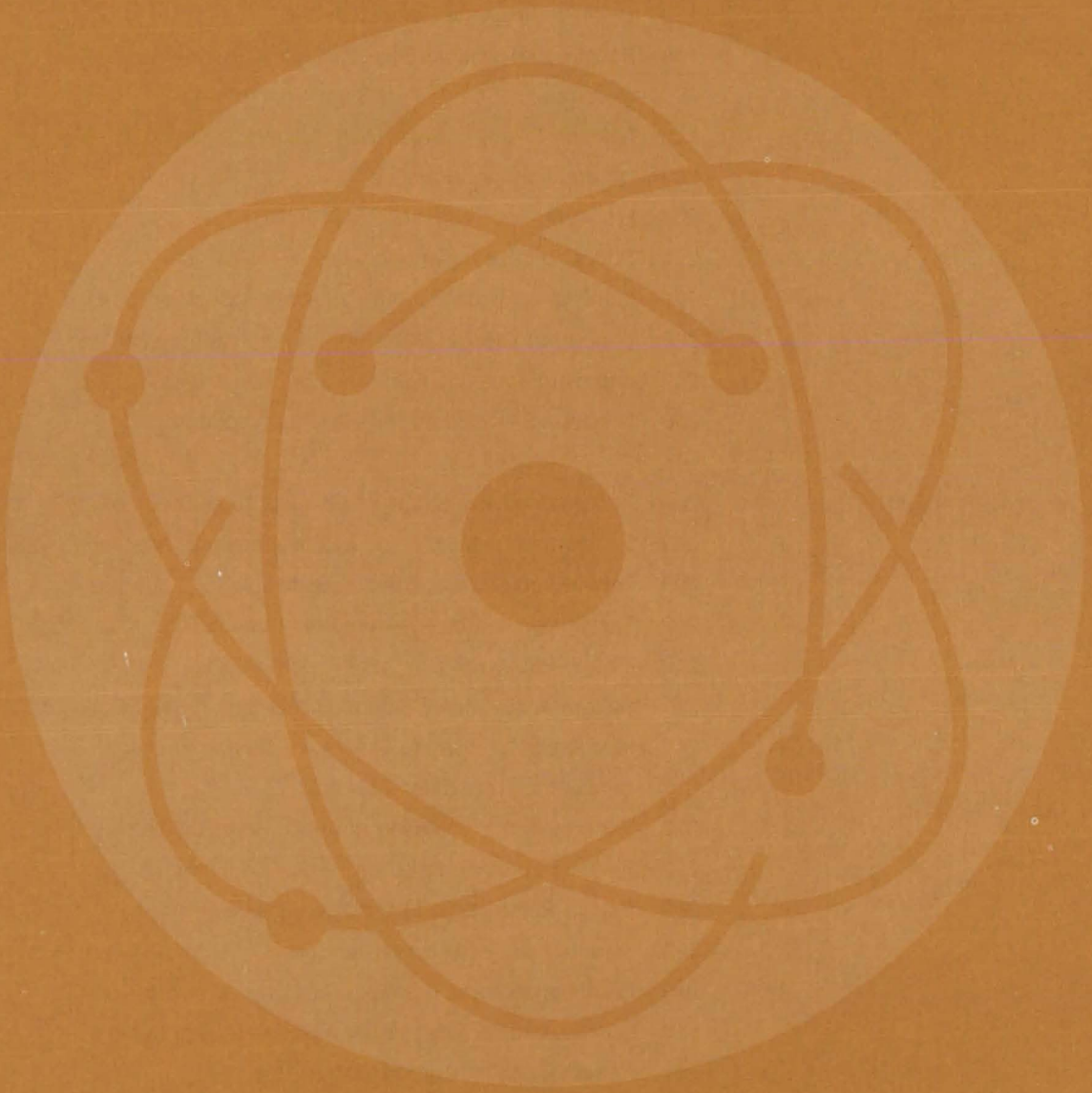

Hardware, Techniques, and Processes

Books and Reports

Computer Programs

Single-Axle, Double-Axis Solar Tracker

Tracking mechanism for a solar concentrator follows seasonal changes in Earth's orientation with respect to incoming Sunlight.

Marshall Space Flight Center, Alabama

A new tracking device for a solar concentrator follows the Sun both diurnally and seasonally. Considerably simpler than conventional gimbal-mounted mechanisms, the new tracker consists of an angular axle, two drive motors, and a circular housing on which the collector dish is supported. Continuous tracking throughout the year is possible by synchronizing the rotations of the two motors.

As shown in Figure 1, the long center segment of the axle passes diametrically through the housing. Shorter end segments at right angles to the center segment are terminated by wristpins that rotate in journal bearings.

The tracker has two axes of rotation: a diurnal axis that passes through the wristpins and a seasonal axis that passes through the center segment of the axle. The diurnal axis is alined parallel to Earth's polar axis, and the seasonal axis is alined perpendicular to the direction of incoming Sunlight.

A drive motor outside the housing rotates the entire assembly about the diurnal axis at a constant rate of 15° per hour, to follow the daily motion of the Sun across the sky. The other drive motor, inside the housing, rotates the reflector housing and dish about the center axle segment. By indexing this motor at about 1° per day (360° per year), the dish is rotated about the seasonal axis, and the perpendicular relationship between the reflector and the incoming Sunlight is maintained throughout the year (see Figure 2).

The simpler design of this tracker, as compared to many conventional gimbal-mounted mechanisms, could help lower the costs of converting Sunlight to useful energy. Other features, such as a Sun sensor for developing the reference signal for a feedback-controlled motor drive and an automatic reset function after Sunset, are easily added.

This work was done by Lott W. Brantley and Billy D. Lawson of

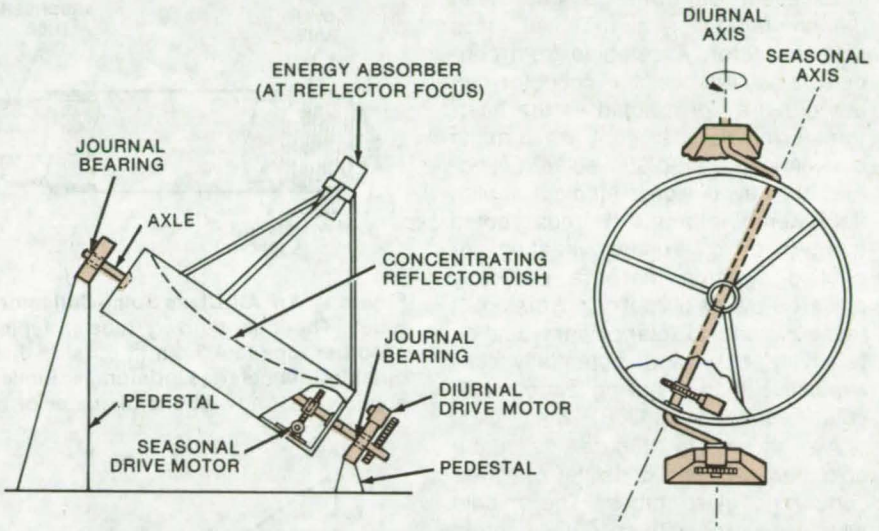

Figure 1. This **Tracking Solar Concentrator** continuously orients the reflector dish perpendicularly to incoming Sunlight. The two drive motors are synchronized for seasonal tracking.

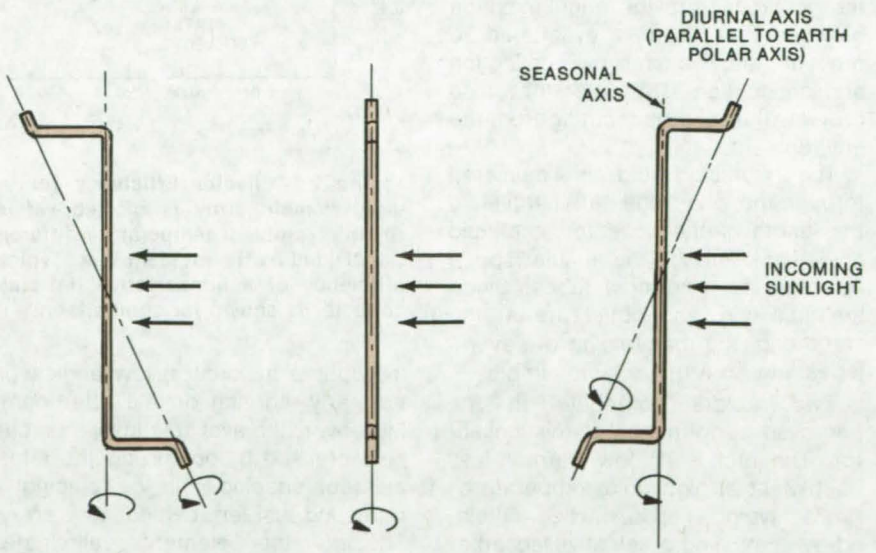

Figure 2. The **Two Rotational Axes** (diurnal and seasonal) change their relative orientation to compensate for the changing direction of incoming Sunlight as Earth orbits about the Sun. The orientation at the left corresponds to the December solstice, the center orientation is at the equinox, and the orientation at the right is for the June solstice.

Marshall Space Flight Center. *For further information, Circle 18 on the TSP Request Card.*

This invention has been patented by NASA [U.S. Patent No. 4,011,854].

Inquiries concerning nonexclusive or exclusive license for its commercial development should be addressed to the Patent Counsel, Marshall Space Flight Center [see page A8]. Refer to MFS-23267.

High-Performance Solar Collector

An evacuated, concentric-tube collector performs better than many conventional flat-plate collectors.

Marshall Space Flight Center, Alabama

Excellent performance has been demonstrated for a new, all-glass solar collector. Assembled from concentric glass tubes, the collector can use either air or a liquid as the heat-transfer medium. In contrast to many conventional flat-plate solar collectors, the new design is efficient at high fluid temperatures. It thus could directly drive existing heating or cooling systems that are presently powered by fossil fuel. Conversion of these systems to solar power would be relatively easy and potentially less expensive than installing a complete solar-heating system.

As shown in Figure 1, each collector element consists of three concentric glass tubes. The middle tube is covered with an outer coating that has high absorptance in the solar spectrum and low emittance in the infrared. A transparent tube surrounds the absorber, and the annular space between the tubes is evacuated to prevent heat transfer by convection and conduction. The outer tube also protects the absorber coating from the environment.

The working fluid is delivered through the inner tube. After traveling the length of the collector, the fluid flows back through the annular space between the innermost tubes. Since the fluid inlet and outlet are at the same end, the manifolding of several tubes into an array is quite simple.

Two factors contribute to the improved performance of this collector: The first is its low thermal-loss coefficient at high fluid temperatures (tests have gone up to 130° C), obtained by combining a selective absorber coating with a vacuum jacket. The second is the advantages gained by the cylindrical geometry. The elements have an effective aperture of 360° for light collection, and they are more effective than a flat plate when the light is incident at low angles (in the early morning or late afternoon). Moreover, the available insolation can be increased by optimizing the interelement spacing and by placing a reflecting screen behind the array. Spacing the elements eliminates shadowing at low angles of incidence, and it allows more light to reach the reflecting screen. Roughly 50 percent of the light that reaches the reflector is eventually collected. The net effect is that the collector efficiency is relatively insensitive to operating temperature, ambient temperature, and windspeed.

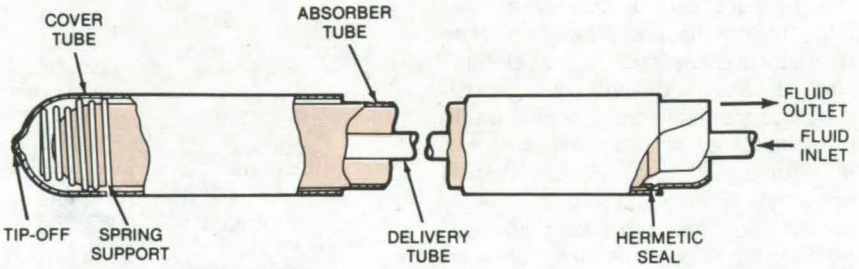

Figure 1. An **All-Glass Solar-Collector Element** is assembled from three concentric tubes. The inner delivery tube is typically 1.2 cm in outside diameter; the middle absorber tube is 4.3 cm in outside diameter; and the outer cover tube is 5.3 cm in outside diameter. Optimum interelement spacing (center-to-center) for most applications is twice the diameter of the cover tube.

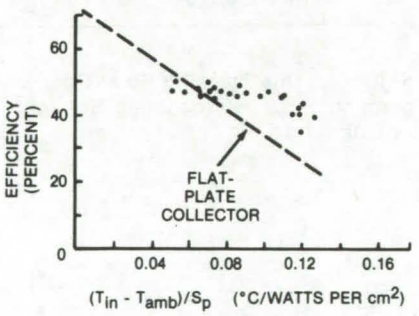

Figure 2. **Collector Efficiency** for an eight-element array is plotted versus the inlet/ambient temperature differential divided by the incident flux. Typical efficiency of a nonselective flat-plate collector is shown for comparison.

The insensitivity to temperature means that the collector will operate with air as the transfer fluid with roughly the same efficiency as when a liquid is used. Air imposes a severe penalty on flat-plate collectors by causing the absorber surface to run hotter than with a liquid, lowering the overall efficiency. Although the absorber will run hotter even for this collector, the loss coefficient is low enough so that there is no significant decrease in efficiency.

An eight-element array with ethylene glycol as the working fluid was recently tested at a site in Toledo, Ohio. The measured efficiencies are shown in Figure 2. The efficiency of a typical two-cover, nonselective flat plate is shown for comparison. Fluid temperatures during the tests reached 130° C.

This work was done by D. C. Beekley and G. R. Mather, Jr. of Owens-Illinois, Inc., for **Marshall Space Flight Center.** *For further information, Circle 19 on the TSP Request Card.*
MFS-25135

Simple, Economical Solar Collector

An inexpensive hot-air solar collector is assembled from only three parts.

Marshall Space Flight Center, Alabama

A hot-air solar collector that is assembled from only three parts is in the final stages of development at Marshall Space Flight Center. Designed for economy and simplicity, the collector consists of only a molded urethane-foam body, a flat sheet-metal collector panel, and a transparent cover. Male and female duct fittings are molded into the collector body. Thus, large arrays are assembled by simply inserting the male fitting of each collector panel into the female fitting of the adjacent panel. No additional ducting is required to make the attachments. Cost estimates using materials tested thus far are less than 80 cents per square foot ($8.61/m^2$) of collector area. Work is continuing to optimize the choice of materials.

As shown in Figure 1, the sheet-metal absorber plate rests on a ledge in the molded urethane-foam body, and the transparent cover is mounted above the absorber on another ledge. A double thickness of glass covers the panel in several prototype collectors; however, a single or double layer of transparent plastic could also be utilized.

Air is forced into the inlet duct fitting and under the absorber plate. The air travels the length of the panel, around a separating rib (molded into the collector body), back down the length of the panel, and out the exit duct fitting to the adjacent collector.

Most of the development work has been directed at optimizing the molding process and the choice of foam. Thirty-two prototypes are presently undergoing 1½-year stagnation tests to check for cracking and warpage.

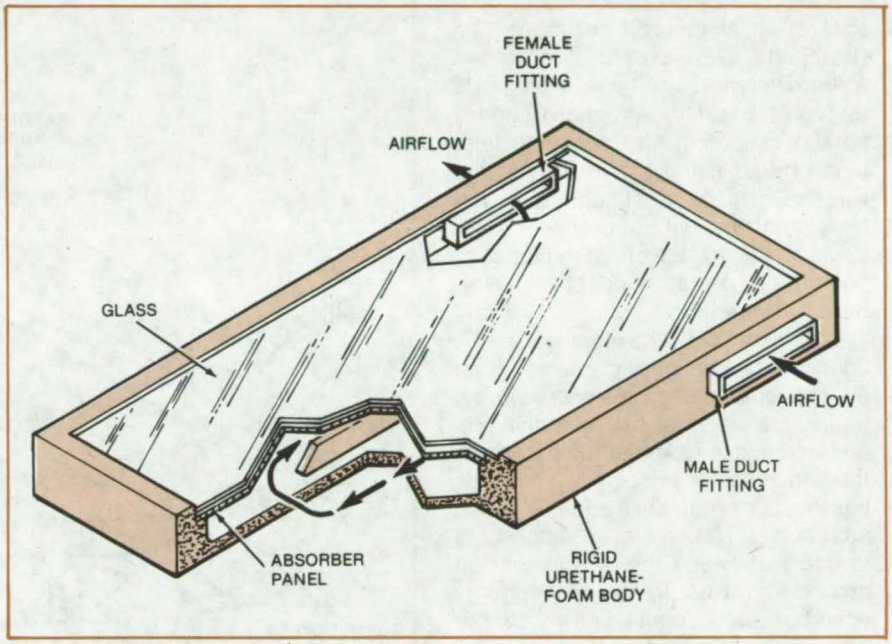

Figure 1. This **Simple Hot-Air Solar Collector** is assembled from a foam body, a flat-plate absorber, and a transparent cover. Duct fittings are molded into the cover. The collector weighs only 21 lb (9.5 kg) and measures 3 by 6 ft (0.9 by 1.8 m).

Various gel coatings for the foam body are also being studied, as are candidate absorber-panel coatings. In preliminary efficiency tests (see Figure 2), the collector performed well, particularly at the lower operating temperatures. [Related information may be found in "Performance and Structural Tests of Hot-Air Solar Collectors" (MFS-23911), on page 215 of *NASA Tech Briefs*, Vol. 3, No. 2.]

This work was done by Kenneth Anthony of **Marshall Space Flight Center.** *For further information, Circle 20 on the TSP Request Card.*
MFS-25109

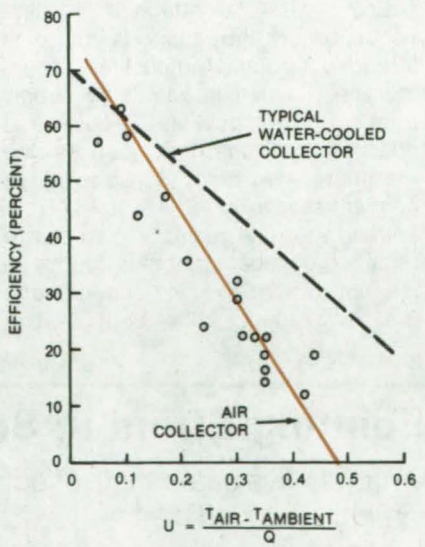

Figure 2. The **Collector Efficiency** (data points) is plotted against a parameter U: the average air temperature in the collector minus the ambient temperature divided by the solar flux.

Lightweight, Economical Solar Concentrator

A reflecting film stretched over a wire frame would make a simple, low-cost solar concentrator.

Marshall Space Flight Center, Alabama

A proposed solar concentrator consists of an aluminized polymeric film stretched over parallel tensioned wires. The wires are held by supports that give the film an approximately parabolic contour. Its shape is fine-tuned by adjusting the tension in the wires. Designed for economy, lightness, and simplicity, the concentrator could help to lower the costs of commercial and residential solar-heating systems.

The new concentrator would be housed in a transparent enclosure on the roof of a building. As shown in the figure, the edges of the reflective film are fastened to rods that run parallel to the concentrator axis. One of the rods has levers at each of its ends. A spring attached to each lever applies a torque that keeps the film in tension around the wire frame. The energy absorber tube, containing water or other heat-transfer medium, is supported along the concentrator axis. Its position is adjustable for maximum absorption of the focused Sunlight.

Each wire is attached to the concentrator end supports by pins threaded through turnbuckles. Thus, the wire tension is varied by simply rotating the turnbuckles. Each wire is adjusted until the film focuses the maximum amount of Sunlight at the concentrator axis.

In an alternate design, the wires are replaced by tubes attached directly to the film by adhesive. No end supports are required for this configuration since the tubes are not held in tension. Instead, a solid rod of selected mass is placed in each tube. The weight of the rods loads the film to create the desired shape. This concentrator is fine-tuned by adjusting the mass of the rods and positioning the absorber tube precisely along the concentrator axis.

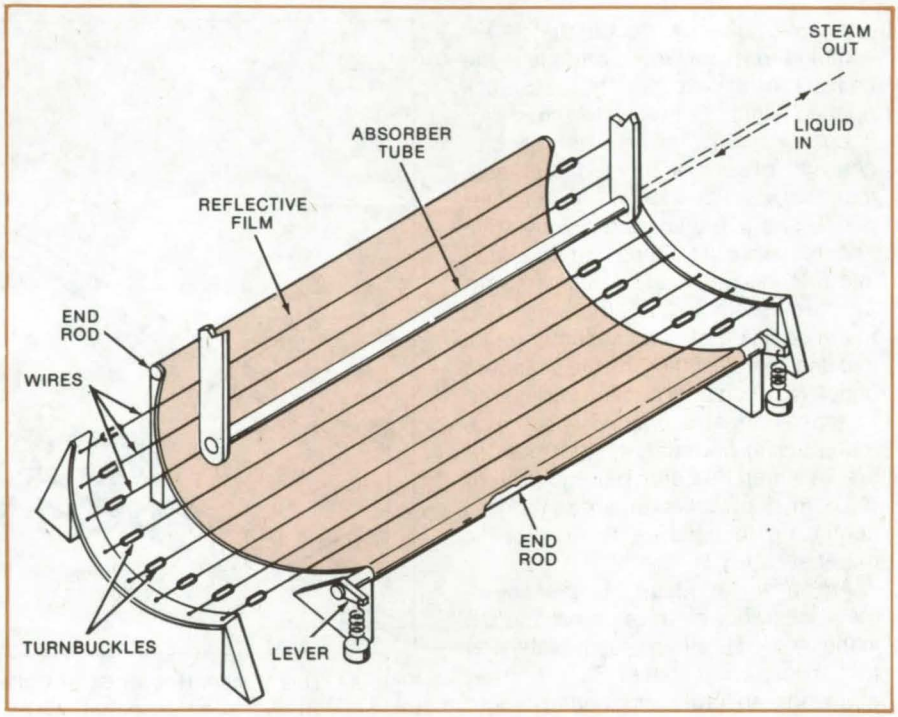

A proposed **Economical, Lightweight, Solar Concentrator** consists of a reflective film stretched over parallel tensioned wires. It can be used with or without a tracking drive.

This work was done by John G. Simpson of **Marshall Space Flight Center.** *For further information, Circle 21 on the TSP Request Card.*

This invention is owned by NASA, and a patent application has been filed. Inquiries concerning nonexclusive or exclusive license for its commercial development should be addressed to the Patent Counsel, Marshall Space Flight Center [see page A8]. *Refer to MFS-23727.*

Pointing Errors in Solar Dish Collectors

Analysis evaluates their effects on collection efficiency.

NASA's Jet Propulsion Laboratory, Pasadena, California

Transient pointing errors degrade the efficiency of solar collectors. Caused by wind and inaccuracies in the tracking drive, they displace the focused Sunlight from the center of the receiver aperture. As a result, not all the concentrated flux is collected, and the receiver output drops.

The effects of transient pointing errors are calculated by a new mathematical analysis. Whereas previous models lumped errors due to imperfect optics and poor structural support with pointing errors, the new analysis treats pointing errors separately. This

approach considerably simplifies programing of simulation models for the tracking drive, wind effects, and other design parameters.

The analysis assumes that the flux distribution at the focal plane is known (from an analysis of the optics) and that it is radially symmetric about its center. Pointing errors displace the center of the distribution from the center of the circular receiver aperture by a distance δ (see Figure 1). The fraction of the total flux that is actually collected, shown as the overlap region, is calculated for an arbitrary flux distribution f(z), aperture radius R, and displacement δ. This function, known as the intercept factor Φ, is also given.

The model has been solved for a Gaussian flux distribution (often a good approximation to the true distribution in a real system). The results are shown in Figure 2. If the concentrator has complex optics, the distribution cannot be written in closed form and is expressed as a "lookup table." For these cases, the equation for the intercept factor is solved numerically.

The model was applied in a computer simulation of a 10-meter parabolic-dish concentrator for which the receiver aperture radius is 11 cm. A control drive was modeled that applies a tracking correction when the pointing error reaches a specified "deadband" limit. The percent of energy lost for different deadband limits and an assumed pointing error distribution were determined by the model. In a real system, each deadband option would have its own cost, maintenance, and power consumption. Thus the model can be applied in a tradeoff analysis between these factors and system performance.

This work was done by Robert O. Hughes of Caltech for **NASA's Jet Propulsion Laboratory.** *For further information, Circle 22 on the TSP Request Card.*

Inquiries concerning rights for the commercial use of this invention should be addressed to the Patent Counsel, NASA Resident Legal Office-JPL [see page A8]. Refer to NPO-14630.

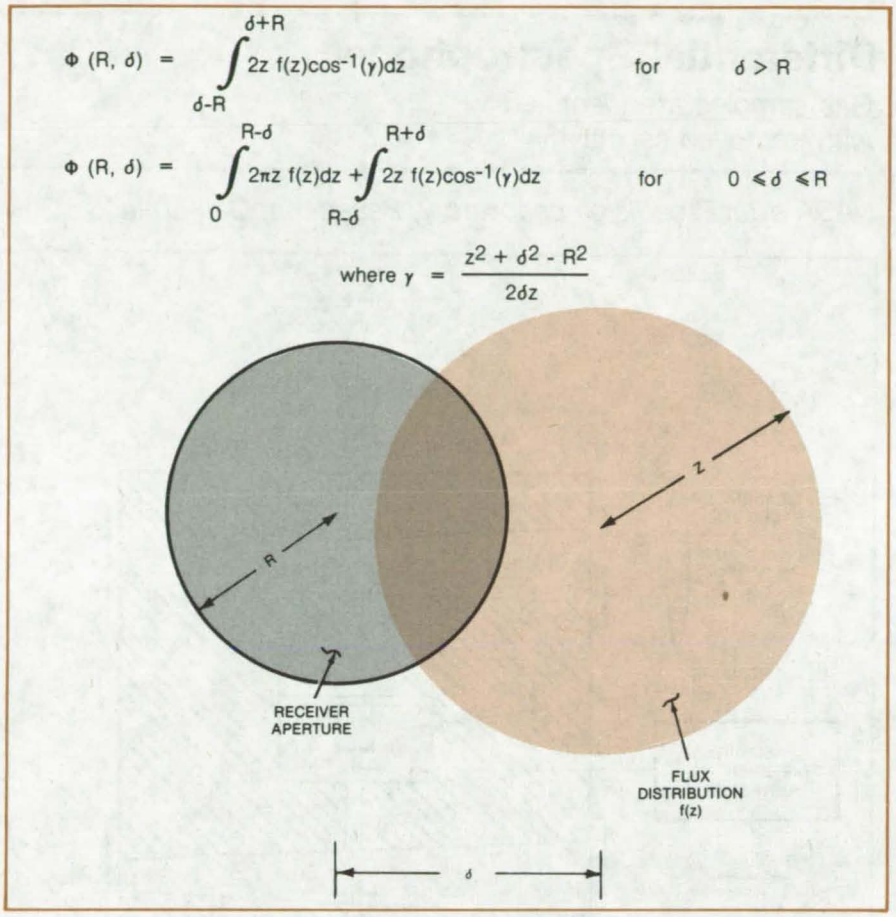

Figure 1. A **Pointing Error** in a point-focusing solar collector displaces the distribution of concentrated Sunlight by a distance δ from the center of the receiver aperture. The aperture radius is R. Only the flux within the depicted overlap region reaches the receiver. This fraction of the total flux is called the intercept factor Φ; it is given for an arbitrary radially-symmetric flux distribution by the expression at the top of the figure.

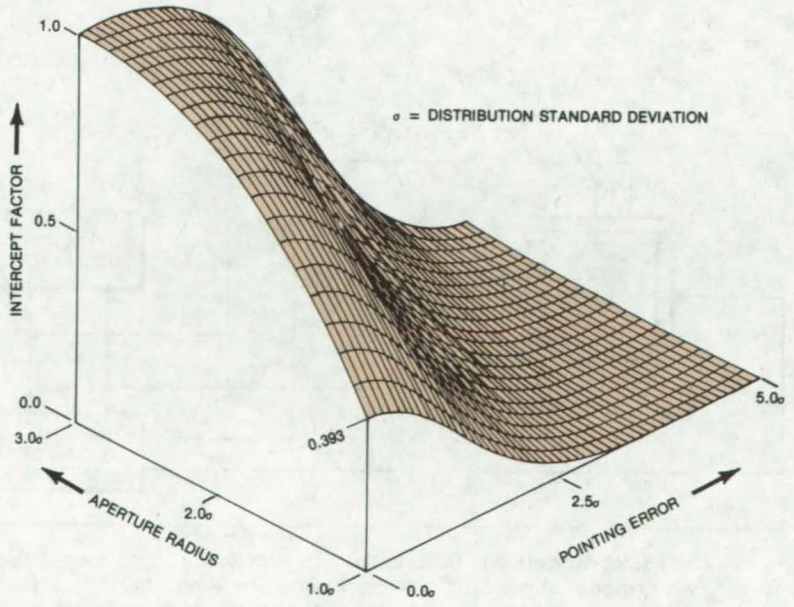

Figure 2. The **Intercept Factor** is shown for a normalized Gaussian flux distribution. $f(z) = (1/2\pi\sigma^2)e^{-z^2/2\sigma^2}$

Differential Spectrophone

Gas samples are identified with improved sensitivity.

NASA's Jet Propulsion Laboratory, Pasadena, California

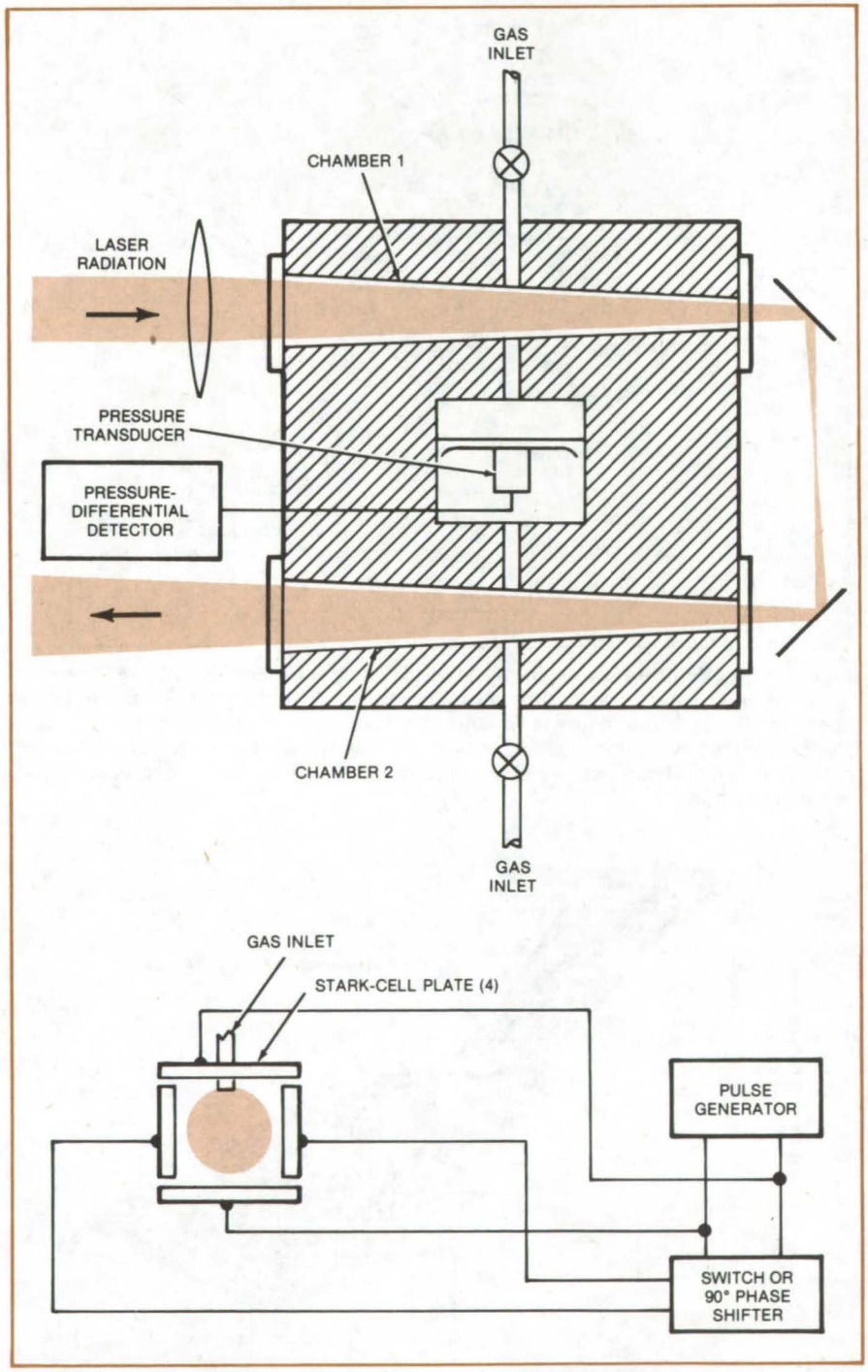

Figure 1. This **Stark-Modulated Differential Spectrophone** has two gas-filled chambers. Two orthogonal pairs of plate electrodes in each chamber set up the modulating electric fields. A pressure transducer between the chambers monitors the differential pressure and converts it to a voltage.

The sensitivity and measuring capability of an optoacoustic gas analyzer (spectrophone) are enhanced by combining differential monitoring with Stark modulation. [See related articles: "Improved Spectrophone" on page 187 of *NASA Tech Briefs*, Vol. 3, No. 2, and "Low-Noise Spectrophone" on page 46, Vol. 4, No. 1.)

The proposed spectrophone (see Figure 1) tests unknown gas samples in two chambers, each of which is equipped with orthogonal pairs of Stark cell plates. A single laser beam (as shown), or two beams, simultaneously excites the samples, and a microphone connected to a transducer between the chambers monitors the differential pressure. The pressures fluctuate in response to heating

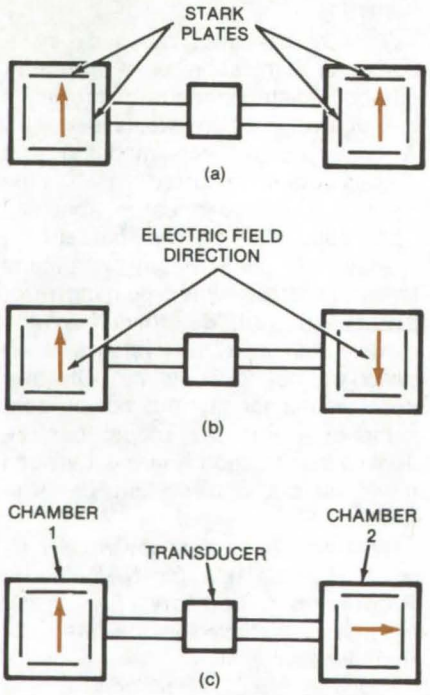

Figure 2. **Three Operating Modes** are possible with the differential spectrophone shown in Figure 1: (top) the electric field lines are in phase, and the chamber pressures cancel; (middle) the field lines are 180° out of phase, and the pressure changes due to absorption in the chambers augment each other; and (bottom) the field lines are orthogonal, allowing the polarization state (if any) of the absorption to be measured.

when the laser radiation is absorbed by the gases.

Three modes of operation are possible (see Figure 2):

1. The electric field in one chamber is in phase with the field of the other in which case the Stark-induced absorptions cancel.
2. The electric fields are 180° out of phase, in which case the Stark-induced absorptions add, and the microphone signal is enhanced.
3. The electric fields are orthogonal. In this case, if the absorption is independent of polarization, the differential spectrophone produces no signal; however, there will be a signal if the absorption is polarization dependent. The polarization state of the absorption is determined by comparing the phase of the signal with the polarization of the electric field.

Besides giving better sensitivity than previous spectrophones, the new design (in mode 3) allows modulation and measurement of the polarization state of the absorption without using rotating polarizers or rotating electric fields.

This work was done by Jack S. Margolis of Caltech for **NASA's Jet Propulsion Laboratory.** *No further documentation is available.*
NPO-14599

Lens Window Simplifies TDL Housing

Replacing the plane window in the cooler head of a tunable-diode-laser (TDL) housing simplifies optics requirements.

Langley Research Center, Hampton, Virginia

A modification of the housing used to control the temperature and pressure environment of a tunable diode laser (TDL) operating in the far infrared spectral range significantly improves and simplifies the output optics of the TDL head assembly.

The quality of radiation from TDL's used in optical systems for spectroscopic or heterodyne applications should be as close to diffraction limited as possible. Current TDL cooler heads use a plane parallel window to seal the evacuated housing and to couple the output radiation from the TDL to the optical system. Such an arrangment causes aberration and interference effects in the output laser beam due to the highly-diverging radiation pattern from the TDL. Additional optics, either reimaging or collimating, must then be incorporated to collect and transmit the laser radiation through the optical system.

A relatively simple modification to the current cooler head that eliminates this problem is shown in the illustration. The plane parallel window is replaced by a lens that serves both as an optical-output coupler and as a sealer window for the evacuated cooler housing. Any type of lens can be used, the particular choice depending upon its intended application. The system shown requires a collimated output beam and uses a simple germanium meniscus lens. The laser-lens separation is adjusted by a bellows and jackscrew. This adjustment allows the laser to be positioned in the focal plane of the lens. A reasonably well collimated beam having relatively-little energy loss can thus be obtained. This modification both eliminates an optical component from the system and improves the output beam quality.

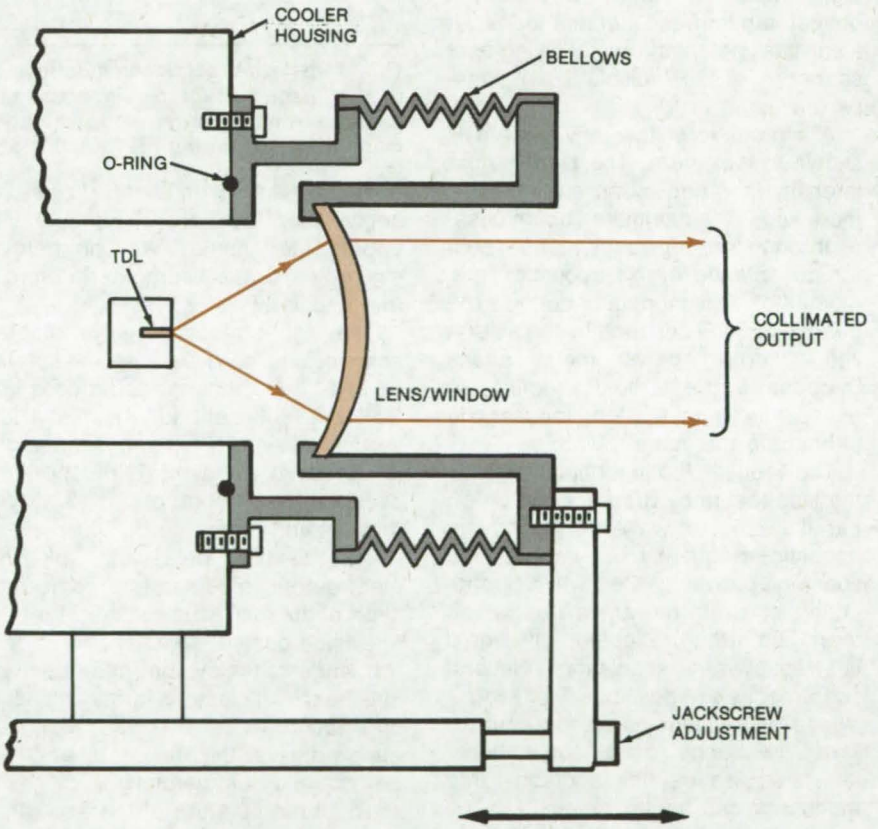

Lens Window Seal in a tunable-diode-laser housing replaces a plane parallel window. The lens seals the housing and acts as an optical-output coupler, thus doing away with additional reimaging or collimating optics.

This work was done by D. M. Robinson and C. W. Rowland of **Langley Research Center.** *No further documentation is available.*
LAR-12437

Focusing Laser Scanner

A laser is scanned and modulated to give television-quality images.

Marshall Space Flight Center, Alabama

A new laser scanner modulates and scans a focused laser beam over an area up to 2 by 2 in. (5.1 by 5.1 cm). Assembled from commercially available components that were carefully selected for compatibility, cost, and performance, the scanner gives image resolution comparable to that of conventional television. In addition to its original use in processing data stored on transparent film, the scanner has possible applications in the storage and retrieval of analog and digital data on video disks and in optical random-access memories. It also has potential as a flying-spot scanner for the display of transparencies.

A schematic of the new system is shown in the figure. The laser output intensity is varied by an electro-optic modulator. The modulated beam passes through forming optics that shape it for acceptance by an acoustic/optic modulator. This modulator deflects the beam along the horizontal scan axis. A light-deflecting galvanometer scans the beam in the vertical direction. At the scanner output, a lens focuses the beam onto the image plane.

The acoustic/optic modulator scans the laser beam by Bragg reflection off parallel acoustic wave fronts. As the acoustic frequency is varied, the spacing between the wave fronts changes; and the angle for which there is a strong reflected light signal is swept over the scan range. Several scan modes are possible, including a sweep at frequencies up to about 16 kHz, the range of a conventional television scan. In addition, the modulator can be set manually or by an externally applied voltage to a fixed deflection angle; or it can be set by applying a 12-bit digital word at the appropriate inputs. A commercial single-board microcomputer controls the modulator.

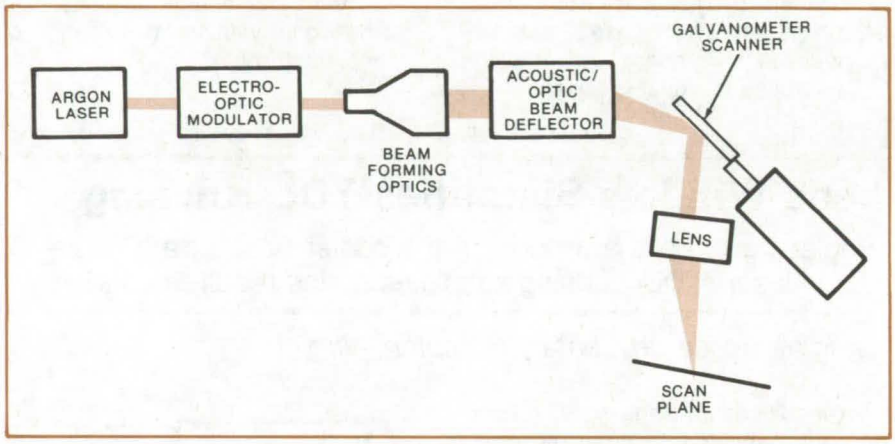

This **Two-Axis Laser Scanner** deflects and intensity-modulates an argon laser beam to give image resolution comparable to standard television. The system is optimized for the strong 514.5-nm line, which is within the range of highest sensitivity for many image-recording media, such as nonlinear crystals.

The light-deflecting galvanometer scanner can be driven sinusoidally at up to 140 Hz, although a frequency of 30 Hz is sufficient for the television vertical sweep. Its full deflection angle is 20° peak-to-peak. (It is operated over a full deflection of only 3.43° in this system.)

The 3-MHz bandwidth of the electro-optic modulator is somewhat short of the 4.46 MHz required for true television-quality signals. The performance of the system has nonetheless been satisfactory for its intended application. The 3-MHz modulator bandwidth was the broadest that could be obtained commercially.

To fill the aperture of the acoustic/optic deflector, the laser beam is expanded and collimated by lenses with focal lengths of 200 mm and 3 mm, respectively. The galvanometer scanner is placed as close as possible to the output aperture of the acoustic/optic scanner, eliminating the need for relaying optics. A focused spot is formed by a 500-mm-focal-length lens at the output of the deflector pair.

This work was done by W. R. Callen and J. E. Weaver of the Georgia Institute of Technology for **Marshall Space Flight Center.** *Further information may be found in NASA CR-150810 [N78-31412], "A Laser Scanner for 35mm Film," a copy of which may be obtained at cost from the New England Research Application Center* *[see page A7]*.

Inquiries concerning rights for the commercial use of this invention should be addressed to the Patent Counsel, Marshall Space Flight Center *[see page A8]*. *Refer to MFS-25102.*

Multiplexed Mass Spectrometer for Desorption Studies

A microprocessor-controlled gas analyzer simultaneously monitors up to nine species.

Ames Research Center, Moffett Field, California

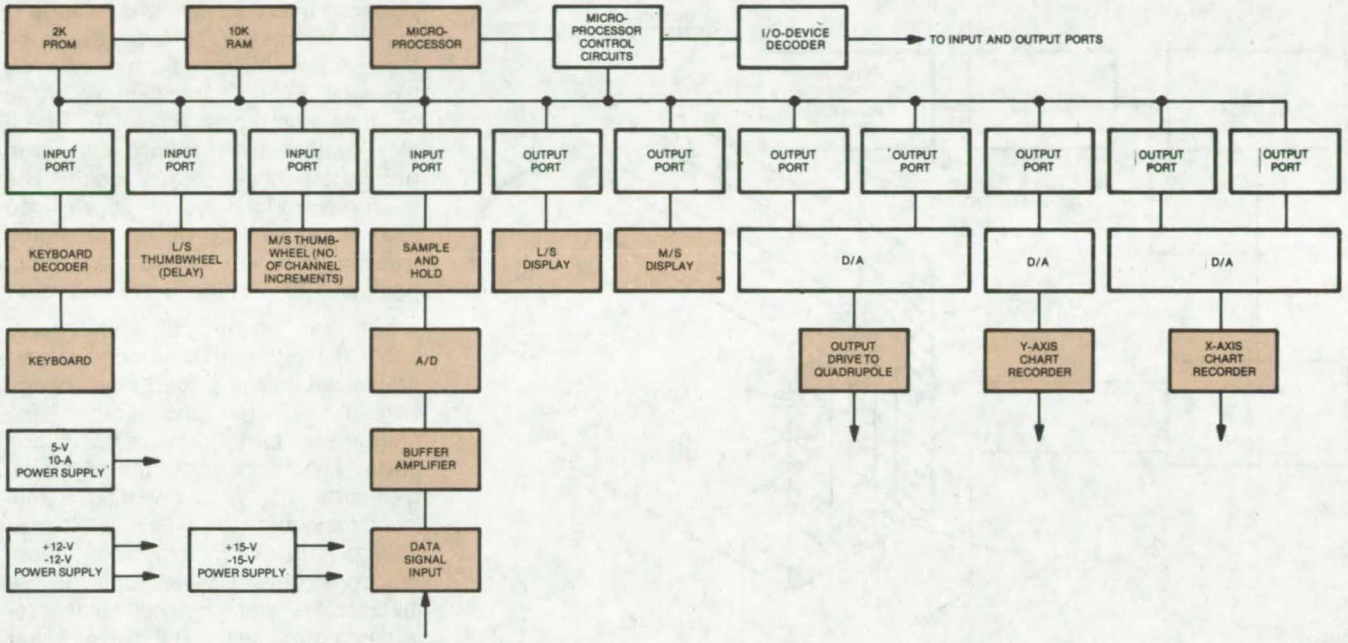

This **Mass-Spectrometer Data-Acquisition System** interfaces with a precision mass analyzer. The system can monitor up to nine gaseous products emitted from a heated substrate during thermal desorption experiments.

Thermal desorption spectroscopy measures the energy that binds atoms or molecules to the surface of a substrate. As the substrate is heated, a precision mass analyzer detects the gaseous desorption products and generates a graph showing the temperatures at which desorption maximums occur. However, with most mass analyzers, only a single gas species can be recorded on each thermograph. Thus, energy interchanges between the species are not apparent during the run.

A new microprocessor-controlled system simultaneously monitors up to nine gases undergoing thermal desorption. An operator selects the gases by keying in the appropriate mass numbers before the start of a run. The system, as shown in the block diagram, includes the microprocessor, a random-access memory (RAM) for data storage, and a programable read-only memory (PROM) for software storage. There are additional digital and analog circuits for signal acquisition and processing.

In operation, the acquisition system sets the mass analyzer to one of the preselected mass numbers. The desorption signal is measured, converted to digital form, and then stored in memory. The system repeats the same cycle at each selected mass number until all the mass numbers are processed and the RAM is full (about 9,000 data points). The time between the acquisition of successive data points can be adjusted from 1 to 100 ms in increments of 1 ms. The data are retrieved from the memory in analog form and are plotted on an X-Y recorder that shows the time variation of each mass number. The time axis can then be related to the temperature variation.

The system automatically accommodates for spectrometer drift and instability. It scans a zone that is adjustable in width around the expected location of the selected mass, and the maximum measured signal amplitude is the value stored in memory. Thus, even if the apparent position of the mass peak changes, the maximum reading is still stored in memory (as long as the peak value remains within the scan zone).

This work was done by Maurice Bales of the University of California, Berkeley, for **Ames Research Center.** *For further information, Circle 23 on the TSP Request Card.*

Inquiries concerning rights for the commercial use of this invention should be addressed to the Patent Counsel, Ames Research Center [see page A8]. Refer to ARC-11134.

Preionized Discharge for Short-Wavelength Laser

Preionization of high-pressure gas is key to chemical excitation transfer reaction.

NASA's Jet Propulsion Laboratory, Pasadena, California

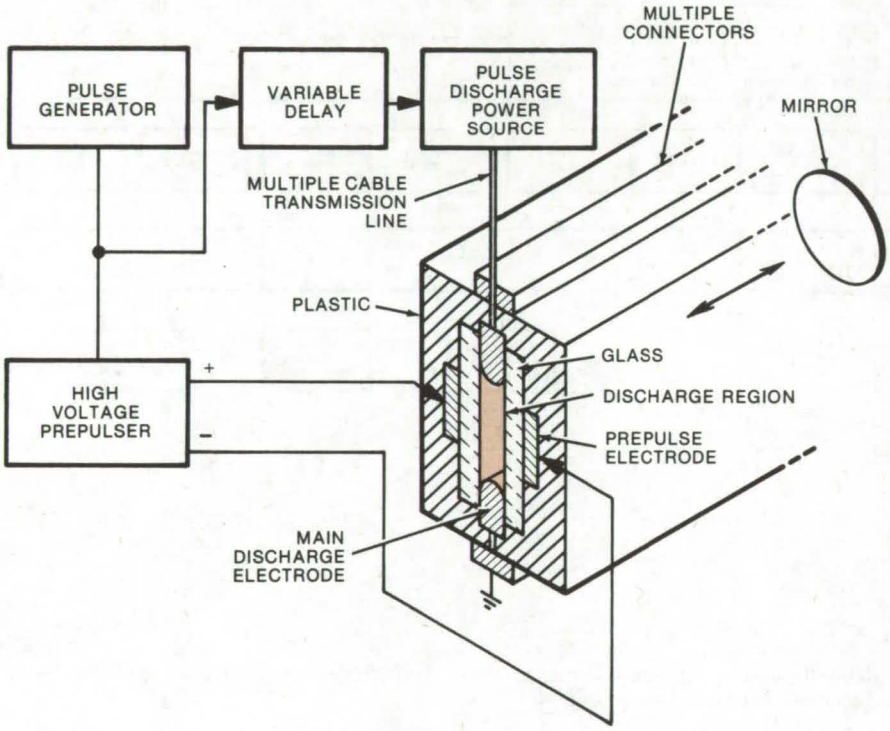

Violet Laser uses helium and nitrogen gases at a pressure of several atmospheres. Preionization by a transverse discharge insures that the main discharge is a glow (not an arc) for the proper charge-transfer reaction mechanism.

A high-pressure double-discharge laser cell can produce laser emissions in the visible and ultraviolet regions. The helium/nitrogen charge-transfer reaction that is the chemical laser pumping mechanism requires a gas pressure of several atmospheres; and because it is extremely difficult to effect a discharge in high-pressure gases, the gas is preionized prior to the main discharge.

The figure shows the laser system. The discharge cell is an elongated rectangular hollow chamber made of a plastic such as Plexiglas or equivalent. The main discharge electrodes are elongated stainless-steel bars configured to minimize arcing. Together with the insulating glass plates, they enclose the discharge region filled with pressurized gases in which the lasing discharge takes place. The prepulse electrodes are disposed behind the glass plates as shown to introduce the preionization discharge into the reactant gases.

A pulse generator drives the high-voltage prepulser to produce the preionization, and a delayed pulse generator drives the pulsed-discharge power source. The pulsed discharge is fed to the main discharge electrode through a multiple-cable transmission line and multiple connectors. It is essential that the main discharge be a glow, rather than an arc discharge from some high-potential point. The main electrode is fed by 25 shielded coaxial cables (making up the transmission line) to produce an equipotential gradient along the electrode.

The gas mixture of helium plus about 0.1 percent of nitrogen is first preionized by the pulsed high-voltage corona discharge and is then discharged by the delayed high-voltage pulse. The He absorbs the electrical discharge energy, converting it into ionization and excitation. Selective charge-transfer or metastable-neutral reactions between He ions or He metastables and N_2 molecules produce electronically excited N_2^+. Laser emissions originating from these electronically-excited molecular ions are obtained in the visible or ultraviolet region. [See NASA Tech Brief B75-10115 (NPO-13289).]

The discharge cell is closed off at its ends by windows (not shown in the figure). It is positioned between mirrors for effecting amplification, as in conventional laser operations.

This work was done by James B. Laudenslager and Thomas J. Pacala of Caltech for **NASA's Jet Propulsion Laboratory.** *For further information, Circle 24 on the TSP Request Card.*

This invention has been patented by NASA [U.S. Patent No. 4,088,965]. Inquiries concerning nonexclusive or exclusive license for its commercial development should be addressed to the Patent Counsel, [see page A8]. Refer to NPO-13945.

Improved Time-of-Flight Mass Spectrometer

External signal-conditioning electronics improve spectrometer data acquisition.

Ames Research Center, Moffett Field, California

The dynamic capability of a time-of-flight mass spectrometer is improved by external signal-conditioning electronics assembled from commercially available components (see Figure 1). By operating only on the signal at the final, or "scope," anode following the electron multiplier within a conventional spectrometer, the processing circuitry avoids interfering with multiplier operation. Inferences in the display of the total spectrum caused by internal gating are removed, and by using external components the number of mass peaks is not limited by the number of internal channels in the multiplier.

Developed for time-resolution analysis of vapor plumes from materials heated by pulsed lasers, the new system has other advantages: The external electronics simplify remote data collection; and the output signal consists of clean square-wave pulses (Figure 2) with heights directly proportional to the areas of preselected mass peaks. The pulses are easily digitized, averaged, stored, or otherwise processed.

As shown in Figure 1, a fanout dc amplifier following the electron multiplier of a conventional spectrometer expands the signal into 16 isolated, identical channels (only 5 are shown). One signal is applied to a dc meter that measures the total mass current, and two others are applied to a scope to display the mass spectrum in the conventional way. (A delayed signal is applied to the scope z-axis input for brightening all mass peaks.)

In the new system, gated integrators sort out preselected mass values from the spectrum. The integrators accept signals only for the duration of a delayed gating pulse. The gate delay coincides with a selected mass peak, and the gate width is set at about 50 nanoseconds to bracket the mass peak. The gated integrator then produces a 3-microsecond output pulse with an amplitude directly proportional to the area of the preselected peak.

The electronics in Figure 1 are easily assembled from nuclear-instrument plug-in modules available commercially. Thus, no custom-designed circuits need to be built. As an option the analog scanners found in a conventional mass spectrometer can be used to provide the external delay-and-gate pulses required by the gated amplifiers.

This work was done by Kenneth A. Lincoln of **Ames Research Center.** *For further information, Circle 25 on the TSP Request Card.*
ARC-11090

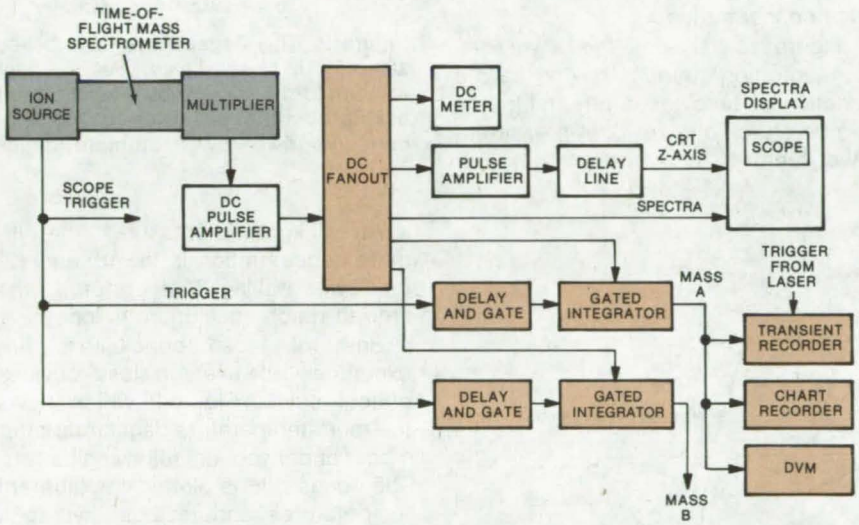

Figure 1. **Signal-Conditioning Electronics** consist of a fanout dc amplifier, delay-and-gate generators, and gated integrators. The amplifier output applies the total mass spectrum to the integrators, which only respond during the delayed-gate interval. The delays are set so each integrator samples a particular mass peak.

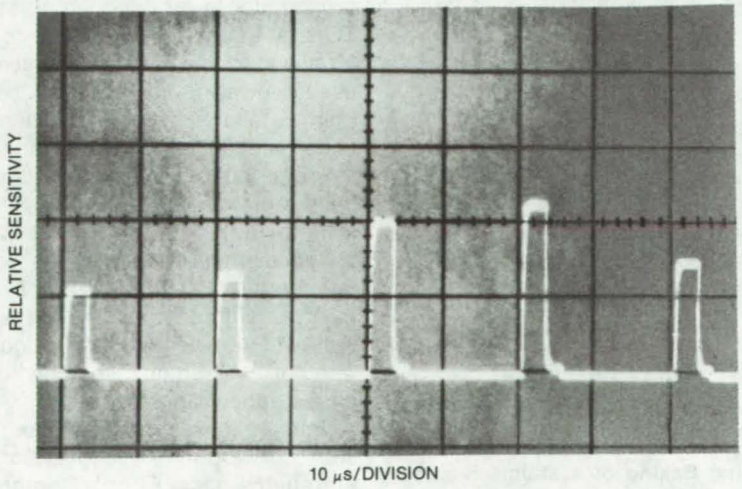

Figure 2. Typical **Clean-Topped Peaks** of a spectrum output after conditioning at a repetition rate of 50 kHz are seen in this photograph. These 3-microsecond peaks correspond to mass-number 28.

Degassing Procedure for Ultrahigh Vacuum

Baking at reduced temperatures
can give lower ultimate pressures.

Marshall Space Flight Center, Alabama

Recent calculations based on diffusion coefficients and degassing rates for stainless-steel vacuum chambers indicate that baking at lower temperatures for longer periods gives lower ultimate pressures than rapid baking at high temperatures. If so, low-temperature baking could reduce pressures in chambers for particle accelerators, fusion reactors, materials research, and other applications.

After an initial rapid high-temperature outgassing to drive off water vapor, carbon dioxide, nitrogen, oxygen, and hydrocarbons, the residual gas in stainless-steel chambers is predominantly hydrogen, since hydrogen diffuses relatively slowly from within the metal walls. The hydrogen concentration can be reduced by continued long-term baking; however, the final concentration is ultimately limited by the amount of hydrogen that was present in the chamber during the bakeout. (A steady-state situation is set up, with hydrogen molecules both entering and leaving the metal surface.) It is therefore advantageous to degas at as low a residual hydrogen pressure as possible to reduce the final concentration.

Figure 1 shows the hydrogen concentration during baking as a function of time for different furnace temperatures and residual pressures. Two features are evident: (1) For lower background pressures, the ultimate concentration is lower; and (2) for lower baking temperatures, the time to reach equilibrium is longer.

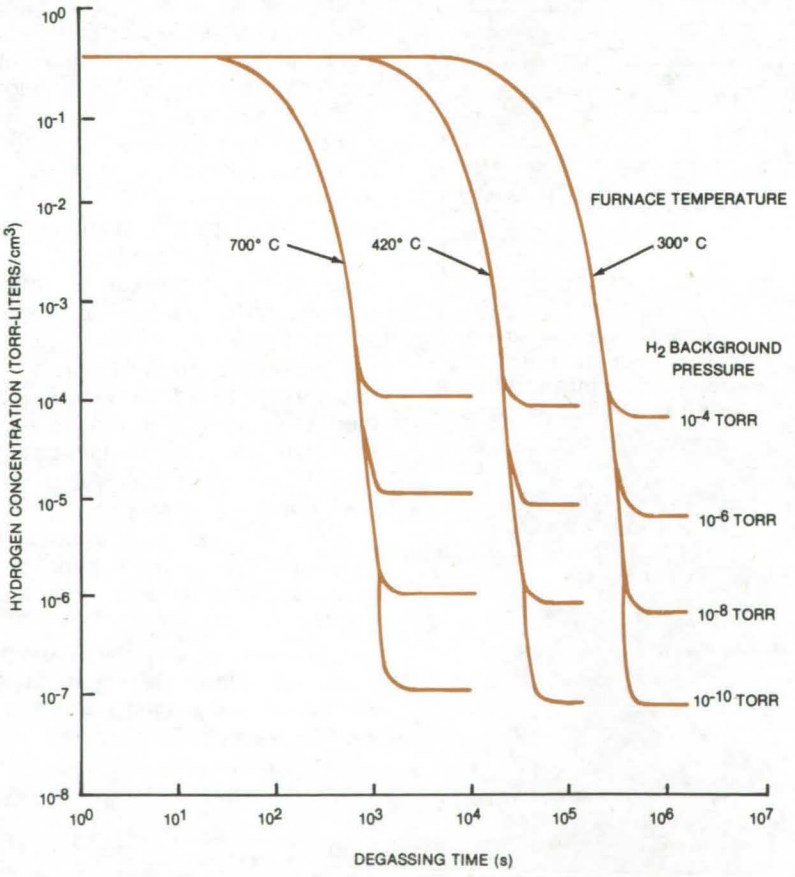

Figure 1. The calculated **Degassing Transient During Baking** of a stainless-steel sheet 1 mm in thickness is shown. The sheet is assumed to be exposed to vacuum on both sides. Plotted is the concentration of hydrogen at the center of the sheet as a function of time, for different baking conditions.

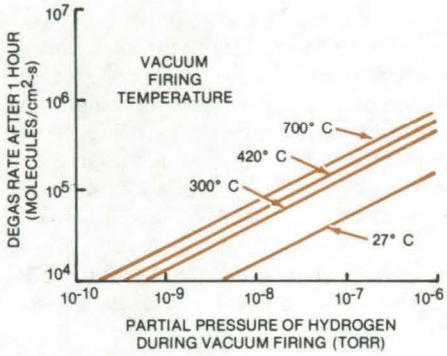

Figure 2. The **Degas Rate** of a baked sample that has also been under vacuum for 1 hour is shown for different baking conditions. Lower baking temperatures give lower ultimate degas rates.

Both of these conclusions are expected. However, a less obvious effect is seen in Figure 2, which shows the room-temperature degas rate after 1 hour under vacuum following baking. The degas rate is plotted for different temperatures and residual hydrogen pressures during baking. Here it is seen that the ultimate degas rate at room temperature is high if the original firing temperature was high. It is reduced for lower firing temperatures. Thus, at the penalty of having to bake for a longer time, it is advantageous to use a lower firing temperature and then to follow baking with outgassing under vacuum at room temperature.

From these calculations it is expected that a stainless-steel sheet up to 1 mm in thickness can be degassed to equilibrium within 24 hours at temperatures of 400° to 500° C If the residual hydrogen background is 10^{-8} torr, a room-temperature outgassing rate of 10^5 molecules hydrogen/cm^2-s appears possible.

This work was done by Boude C. Moore of McDonnell Douglas Corp. for **Marshall Space Flight Center.** *For further information, Circle 26 on the TSP Request Card.*
MFS-25103

Books and Reports

These reports, studies, and handbooks are available from NASA as Technical Support Packages (TSP's) when a Request Card number is cited; otherwise they are available from one of NASA's Industrial Application Centers or the National Technical Information Service.

Performance Evaluation of a Liquid Solar Collector

Program includes thermal-performance and structural-load tests.

A 28-page report describes thermal-performance and structural-load tests on a commercial flat-plate solar collector. Test instrumentation and procedures are documented, data are presented as tables and graphs, and the results are analyzed by standard data-reduction methods. The tested collector is single glazed, with a gross area of 63.5 ft^2 (5.9 m^2). Water is the heat-transfer medium.

Preconditioning prior to the main test program involved exposure for at least 3 days to an average insolation of 1,500 Btu/ft^2-day (35.1×10^3 cal/m^2-day) while the collector was stagnant (no coolant flow). The absorber surface temperature was measured at either four or five locations.

The main performance evaluation measured the collector time constant (the time for the differential temperature across the collector to fall to 0.368 of its initial value after the solar flux is reduced to zero), thermal efficiency (the rate of useful energy extraction for a given insolation), and incident-angle modifier (a measure of the efficiency drop for nonnormal incidence). All testing was done outdoors.

Uniform loads were applied to the collector glazing to test its structural stability. A transparent flexible diaphragm was placed over the glazing and covered to various depths with a liquid. The collector was then inspected for leakage or breakage. No problems were found at loads up to 120 lb/ft^2 (49.5 N/m^2).

This work was done by the Solar Energy Systems Division of Wyle Laboratories for **Marshall Space Flight Center.** *To obtain a copy of the report, "Thermal Performance Evaluation of The Solargenics Solar Collector at Outdoor Conditions," Circle 27 on the TSP Request Card.*
MFS-25026

Design and Installation of a Solar-Powered Hot-Water System

Package includes performance specifications, hazards analysis, and installation information.

Design and installation information for a complete solar-powered hot-water system may be obtained by requesting the Technical Support Package referenced at the end of this article. The package includes performance specifications, design drawings, a brief hazards analysis, and an installation manual.

The main elements of the system are two flat-plate solar collectors, a 120-gallon (454-l) storage tank, an auxiliary electric heater, circulating pumps, and a differential controller with temperature sensors to govern pump operation. Gross collector area is 80 ft^2 (7.36 m^2). In one variation of the design, a silicone fluid flows through the collectors, and a liquid/liquid heat exchanger transfers heat to the domestic water supply. Another design has water as the heat-transfer fluid in a direct-feed system.

Performance criteria for one operational test site specify 75 gal (284 l) of hot water delivered at 3 gal/min (11.3 l/min) at temperatures of at least 140° F (60° C). Recovery time is less than 8 hours. The system will supply an average hot-water load of 1.125×10^6 Btu/month (1.186×10^9 J/month), of which 10 percent is supplied by auxiliary heating. The maximum electrical power to drive the solar portion of the system is less than 0.1 kW.

Installation information is supplied for each subcomponent of the system, and diagrams illustrate the text discussion. Information on system startup and maintenance is also included.

This work was done by Solar Engineering & Manufacturing Co. for **Marshall Space Flight Center.** *To obtain a copy of the design package, "Design and Installation Package for Solar Hot Water System," Circle 28 on the TSP Request Card.*
MFS-25080

The Design of Solar-Heating Systems

An organized approach to selecting the optimum system for a specific site

An organized approach to the design of solar-heating systems is described in a new report. Starting from a consideration of available hardware and constraints and ending with a computer simulation of candidate systems, an "optimum" design is developed for a proposed site. Such parameters as collector area, storage capacity, and pump sizes are determined, and a complete cost-and-performance analysis is made. The report traces the development of several systems sized for single-family, multifamily, and commercial buildings in the Minneapolis area.

The solar-heating system is assumed to be composed of five subsystems:

- collectors,
- thermal-storage medium,
- auxiliary-energy subsystem,
- working fluid, and
- supplementary elements (e.g., pumps, controls, and piping).

At the outset, several candidates are considered for each subsystem. Possible collectors are liquid flat-plate, concentrating, and air flat-plate; water and rock-bed are among possible storage media.

The system constraints narrow the possibilities: Thus, air collectors are not well matched with liquid storage; and concentrating collectors, while offering the possibility of better performance, are more complex and more subject to development risk than air or liquid flat-plate collectors. These considerations and such factors as the importance (or unimportance) of modularity, architectural constraints, and auxiliary-energy availability define a

(continued on next page)

"baseline" system for which the components are specified; however, such details as collector area, pump size, and storage capacity are not yet determined.

The next phase of the analysis is a quantitative assessment of performance and economic factors to arrive at a final design. The system is simulated on a computer. Available weather data, estimated energy and maintenance costs, data on building heat load and insulation, and other relevant data are used as input. The program models a multi-loop solar system as a set of nonlinear differential equations. Tradeoff studies are made by varying the design parameters and calculating their effects on performance. Both performance and economy are analyzed.

This work was done by the Energy Resources Center of Honeywell, Inc., for **Marshall Space Flight Center.** *To obtain a copy of the report, "Preliminary Design Package for Prototype Solar Heating System," Circle 29 on the TSP Request Card. MFS-25108*

The Design of Solar-Heating and Cooling Systems

Designs for single-family, multifamily, and commercial buildings are specified.

The methods described in the report referenced in the preceding article were also used to develop specifications for Rankine-cycle solar-heating and cooling systems. Preliminary designs for single-family, multifamily, and commercial buildings have been developed and are documented in a 284-page report, referenced at the end of this article.

The subsystems considered during the initial selection of hardware are:

- collector,
- thermal storage medium,
- working fluid,
- Rankine power loop,
- air-conditioning subsystem,
- electric-motor auxiliary cooling, and
- supplementary elements (e.g., controls, pumps, and piping).

Except for the Rankine loop and electric-motor auxiliary cooling, several candidates are listed for each subsystem. By considering development risks, architectural aspects, fuel availability, and other constraints, the relative strengths and weaknesses of the candidates are compared, and the possible choices are ranked.

After accounting for the overall system objectives, the levels of control and reliability required, and other factors, a "baseline" design is specified. At this stage, the subcomponents that will go into the final design are chosen, but their sizes and capacities are not yet known.

Baselines are given for single-family, multiple-family, and commercial buildings. Some of the major components selected for the baseline single-family system are:

- liquid flat-plate collector,
- water storage,
- gas-fired auxiliary hot-water heater,
- Rankine direct-expansion air-conditioner, and
- water pump and cooling tower.

Ten modes of operation are possible, including direct solar heating, heating from storage, Rankine cooling from collectors or storage, electric-motor auxiliary cooling, and auxiliary heating.

Sizing and cost specifications are generated during computer simulations that evaluate the baseline performance under specific weather, energy load, and building specifications. Weather data for Atlanta, Georgia, are used in the reported simulations. Such economic factors as energy costs, maintenance costs, and interest rates are part of the input. The computer output is a quantitative specification of subsystem sizes, costs, and performance.

The report also contains a brief discussion of a market analysis for systems of the type under consideration. Some of the conclusions establish additional criteria for the baseline.

This work was done by the Energy Resources Center of Honeywell, Inc., for **Marshall Space Flight Center.** *To obtain a copy of the report, "Preliminary Design Package for Prototype Solar Heating and Cooling Systems," Circle 30 on the TSP Request Card. MFS-25106*

Design Package for a Solar-Heating System

Report contains sufficient information to assemble a residential solar-heating system.

Engineers, contractors, and others who design or install residential solar-heating systems will be interested in a new report on a complete, tested system assembled from commercially available components. Described in detail in two previous articles in *NASA Tech Briefs* [see "Solar-Heating System — Design Data Brochure" (MFS-23977) on page 521 of Vol. 3, No. 4, and "Solar-Heating System — Performance Tests" (MFS-25021) on page 522 of that issue], the modular system has liquid flat-plate collectors, hot-water energy storage, pumps, heat exchangers, a controller, and other hardware. It can be sized to meet the needs of each installation.

The 77-page report, which contains drawings, tables of data, and descriptive material, is intended to "provide design, performance, and hardware specifications sufficient for architectural engineers and contractors to procure, install, operate, and maintain a similar solar application." The first two chapters are descriptions of the complete system and of each of the subsystems. Manufacturers' literature is included.

Performance specifications are given in the second chapter. These include general criteria and specific criteria for two operational sites: one in Huntsville, Alabama, and the other in Glendo, Wyoming. The Wyoming site has an annual heating load of 94×10^6 Btu (99×10^9 joules) of which 46 percent of the space-heating portion will be supplied by solar energy. Seventy-five gallons per day of hot water will be delivered, for which 80 percent of the energy load will be supplied by solar heating.

The remaining chapters are devoted to a certification procedure for verifying that the system is performing according to specifications and a "hazards analysis." The hazards analysis lists safety problems that are avoided by proper controls and design.

This work was done by the Federal Systems Division of IBM Corp. for **Marshall Space Flight Center.** *To obtain a copy of the report, "System Design Package for SIMS Prototype System 3, Solar Heating and Domestic Hot Water," Circle 31 on the TSP Request Card.*
MFS-25136

Performance After Weathering of a Liquid Solar Collector

No changes were measured after 11-1/2 months of weathering.

The liquid solar collector described in "Performance Evaluation of a Liquid Solar Collector" (MFS-23931) on page 216 of *NASA Tech Briefs,* Vol. 3, No. 2, has been retested after long-term exposure to natural weathering. As summarized in a report that has been made available, weathering caused no detectable degradation in collector performance and no visible deterioration in its appearance. Supporting data and a comparison of pretest and posttest efficiencies are included.

The single-glazed flat-plate collector was held stagnant (no flow) for approximately 4 months on the weathering test stand at Marshall Space Flight Center. It was then held intermittently stagnant and active over a 5-month period. The final weathering was for 2-1/2 months.

Collector efficiency was measured (on a solar simulator) at a flow rate of 0.57 gal/min (2.19 l/min) for inlet temperatures of 0°, 25°, 50°, and 100° F (0°, 14°, 28°, and 56° C) above ambient. The solar flux was 300 Btu/h-ft^2 (3.4×10^6 J/h-m^2), and windspeed was 7.5 mi/h (12 km/h). Within experimental error, the posttest collector-efficiency curve was unchanged from the pretest curve.

This work was done by the Solar Energy Systems Division of Wyle Laboratories for **Marshall Space Flight Center.** *To obtain a copy of the report, "Long Term Weathering Effects on The Thermal Performance of The Sunworks [Liquid] Solar Collector," Circle 32 on the TSP Request Card.*
MFS-25137

Modular Solar-Heating System — Design Package

Includes drawings, performance specifications, and other data

A 140-page compilation report of design data, drawings, and other information on a complete solar-heating and hot-water system is available on request. The compilation describes design, performance, and hardware specifications in sufficient detail to fabricate or procure the hardware and to install, operate, and maintain the system. A design data brochure for this system is described in "Solar-Heating System" (MFS-25022) on page 522 of *NASA Tech Briefs,* Vol. 3, No. 4.

Intended for installation in a small single-family dwelling, with the collectors adjacent to the building, the modular prepackaged system consists of solar collectors that use air as the heat-transfer medium, a rock-storage container, blowers, dampers, ducting, and air-to-water heat exchanger, a domestic-hot-water preheat tank, piping, and system controls. Solar collector arrays with areas of 135, 203, and 271 square feet (12.5, 18.8, and 25.1 square meters) are available; larger sizes are possible.

The report gives a system overview in the first two chapters, and then it devotes a chapter to each of the subsystems (collectors, storage, transport, domestic hot water, auxiliary energy, and control). These descriptions are followed by a performance specification for a system that can be installed anywhere in the continental United States except the extreme North, southern California, and Florida. Specific parameters for a Clinton, Mississippi, site are given. Also contained in the report are chapters on performance verification procedures and a hazards analysis. Thirty detailed design and assembly drawings are included.

This work was done by Dwaine S. Sinton of IBM Corp. for **Marshall Space Flight Center.** *To obtain a copy of the report, "System Design Package for SIMS Prototype System 4, Solar Heating and Domestic Hot Water," Circle 33 on the TSP Request Card.*
MFS-25130

Concentric-Tube Solar Collector

Brochure contains design, performance, and installation information.

Design, performance, and installation information on a commercial solar collector is presented in a new brochure. The 147- by 103-in. (3.73- by 2.62-m) collector consists of 72 cylindrical airflow tubes, each of which surrounds and is concentric with 1 of 72 return tubes. The tubes are manifolded together at one end. Air is forced through the annular space between the tubes and back through the return tubes.

The five-part brochure includes a summary of the essential features of the collector, thermal performance specifications, fluid flow data, installation information, and operating tips. An installation package for this collector was described in "Air Solar Collector — Installation Package" (MFS-25031) on page 59 of *NASA Tech Briefs,* Vol. 4, No. 1.

This work was done by Owens-Illinois for **Marshall Space Flight Center.** *To obtain a copy of the brochure, "Design Data Brochure for the Owens-Illinois Sunpak™ Air Solar Collector," Circle 34 on the TSP Request Card.*
MFS-25133

Performance Verification of an Air Solar Collector

A battery of performance, environmental, and structural tests finds a solar collector suitable for field installation.

The procedures and results of qualification tests on a commercial air solar collector are presented in a new report. In judging the collector suitable for use in residential and commercial solar-heating systems, an independent certification agency performed a battery of performance and environmental tests. All procedures and results are thoroughly documented, making the 144-page report useful to those who might want to use this collector and to those interested in setting up a certification test program of their own.

Design details of a similar collector are given in "Air Solar Collector — Installation Package" (MFS-25031) on page 59 of *NASA Tech Briefs*, Vol. 4, No. 1 (also see the preceding article). Solar energy is transferred to air flowing down the annular space between concentric tubes (a typical array has 72 pairs of tubes) and back through the inner tube. The outer tube is glass, and the outer surface of the inner tube has a heat-absorbing coating.

Thermal performance of the collector was evaluated in a carefully-calibrated outdoor test setup. Collector efficiency was measured for varying insolation, inlet temperatures, and flow rates. The results are plotted as efficiency versus the ratio of inlet/ambient temperature differential to incident flux. Plots of the collector pressure drop versus airflow rate are also given; and the results of stagnation (no-flow) tests are presented.

Among other tests reported are those for vibrational stress (on a shake table) and thermal stress from ambient temperatures to 325° F (163° C). No problems were found. A series of load tests was carried out by inflating an airbag between the collector and a fixed reference plane. Pressures were carefully monitored and controlled to apply the required loads.

Other conditions tested directly or indirectly are the effects of wind, snow, Earthquakes, and particle impact. A very thorough discussion of simulated hail-impact tests is presented.

This work was done by David C. Miller and Robert F. Romaker of Owens-Illinois, Inc., for **Marshall Space Flight Center.** *To obtain a copy of the report, "Qualification Test and Analysis Report — Solar Collectors," Circle 35 on the TSP Request Card.*
MFS-25131

Preliminary Design of an Air Solar Collector

Report contains performance specifications and engineering drawings.

A new report contains design information on the concentric-tube air solar collector referenced in the preceding articles. The 56-page report includes 22 pages of engineering drawings showing details of the collector and its subcomponents. The drawings and other data were submitted as part of a preliminary review of progress by the contractor. Data submitted for review show the collector efficiency to surpass the predetermined performance "baseline" for an air collector.

The collector is designed to absorb a minimum of 800 Btu/ft^2-d (9.1x10^6 J/m^2-d) at an inlet fluid temperature equal to or less than 220° F (104° C) and an airflow rate above 2 stdft^3/min per square foot (0.6 stdm^3/min per square meter) of collector area. This specification is for any latitude, at an ambient temperature of 50° F (10° C).

The report contains a summary of the development of the collector. The measured thermal performance is presented as a graph of efficiency versus inlet/ambient temperature difference divided by the incident flux. A "hazards analysis" discusses a study of possible failure modes, such as overpressurization and tube breakage. No serious dangers were uncovered.

This work was done by Owens-Illinois, Inc., for **Marshall Space Flight Center.** *To obtain a copy of the report 'Preliminary Design Package for "Sunair" SEC-601 Solar Collector,' Circle 36 on the TSP Request Card.*
MFS-25138

Design Review of a Liquid Solar Collector

Problems encountered in operational systems are analyzed.

The procedures, results, and recommendations of an in-depth analysis of problems with the liquid-filled version of the concentric-tube solar collector (see preceding articles) are documented in a new report. The problems related to the loss of vacuum and/or violent fracture of the collector elements, fluid leakage, freezing, flow anomalies, manifold damage, and other component failures.

The analysis showed that the basic collector design is sound; most problems could be traced to defective equipment or improper operating procedures. It is recommended that care be taken to avoid these problems in present and near-term applications. A long-term performance evaluation and improved materials in critical components would reduce problems in future installations.

In a review of operating procedures and materials at nine existing sites, it was discovered that system failures were preceded or accompanied by boilout, freezeup, or hot fill (filling of an already-heated collector). It is recommended that users prevent these occurences by using correct operating procedures.

Tests on a solar simulator showed that an unscratched stagnant collector tube does not fail in a 2-day boilout during which it reaches temperatures above 600° F (315° C). A "good" tube will fail, however, if hot-filled; and violent fractures were observed in previously scratched tubes. Thus, tubes should be proof-tested before installation; and careful operating procedures should be used to prevent accidental boilout, hot fills, stagnation, and freezeup. Assembled arrays should be leak-tested before use.

Two aspects of collector design were reviewed: (1) the tube alinement tolerances in the manifold and (2) the tube structural strength. Alinement tolerances in the manifold were considered adequate to prevent binding and breakage. A simplified finite-element strength analysis indicates that the tube strength is adequate;

however, a more refined analysis that would account for temperature effects and residual stresses and defects is recommended.

This work was done by Bernhard L. Wiesenmaier of **Marshall Space Flight Center.** *To obtain a copy of the report, "Final Report on MSFC Assessment of Owens-Illinois Sunpack™ Collector Problems," Circle 37 on the TSP Request Card.*
MFS-25140

Development of Nonmetallic Solar Collector and Solar-Powered Pump

A report traces the progress of an 18-month program.

The results of an 18-month contract to design and build two unique components for solar heating are summarized in a 26-page report. Delivered to Marshall Space Flight Center at the end of the contract period were (1) a flat-plate solar collector using no metal components and (2) a solar-powered pump for heating and cooling systems. The report describes the hardware, lists deliverable end items, discusses problems encountered during fabrication and testing, and includes performance-certification statements.

The nonmetallic solar collector consists of a flexible grid of 30 pairs of elastomeric tubes cemented to an insulation-board base. A black, high-temperature urethane layer covers the grid and base. The tube grid is a substitute for the absorber plate of conventional metal solar collectors. A removable fiberglass panel covers the collector in the factory-assembled model. The field-assembled version has a cement-sealed reinforced plastic cover. [See related articles: "Design and Installation of a Flat-Plate Solar Collector" (MFS-25010) on page 523 of *NASA Tech Briefs,* Vol. 3, No. 4, and "Liquid Solar Collector — Performance Tests" (MFS-25082) on page 524 of that issue.]

The solar-powered pump is described in "Solar-Powered Pump (MFS-23996) on page 39 of *NASA Tech Briefs,* Vol. 4, No. 1. It is driven by steam from a concentrating solar collector. Its efficiency (18 percent) is relatively low compared to conventional mechanical pumps. However, with some improvement in efficiency it could be used in a solar collector loop, since some of the heat that is not converted to mechanical energy could be used for home heating. The pump can develop a pressure head of 50 feet (15.2 meters) of water at a flow rate of 10 gal/min (38 l/min).

This work was done by John C. Parker of **Marshall Space Flight Center.** *To obtain a copy of the report, "Development, Testing, and Certification of Calmac Manufacturing Corporation Solar Collector and Solar Operated Pump — Final Report," Circle 38 on the TSP Request Card.*
MFS-25143

Certification Tests on the Solar-Powered Pump

Over 50 criteria were applied by judging the pump suitable for use by the public.

The solar-powered pump (see preceding article) was evaluated for compliance with national standards and codes. It is judged suitable for public use. Procedures and results of the evaluation are presented in a report that is now available.

Over 50 performance criteria were applied. For each, the pump was evaluated either by direct tests or by a review of documentation and drawings. Pump efficiency was measured and plotted, load tests were carried out, and such factors as noisiness, freeze and hail resistance, and leakage were checked.

For each test criterion, the method of evaluation is given along with a summary of the findings. Data on pump pressure and efficiency are presented in a table and graphically.

Typical of a test evaluation is the one for excessive vibration. The criterion is that vibration should be below the level that could cause damage or excessive noise. Engineering drawings and specifications were reviewed to look for components that have natural resonances within ±20 percent of the operating frequency. Measurements were carried out to determine if the pump reached vibration velocities above 0.10 in./s (0.25 cm/s) for different orientations. No problems were found, and the pump passed this evaluation.

This work was done by Calmac Manufacturing Co. for **Marshall Space Flight Center.** *To obtain a copy of the report, "Certification Report for the Calmac Solar Powered Pump," Circle 39 on the TSP Request Card.*
MFS-25144

Cost-Reduction Analysis for a Solar-Heating System

Cost-saving steps are proposed in all areas of system design and installation.

More details on the economic study referenced in "Cost Analysis of Hot-Air Solar-Heating Systems" (MFS-25092) on page 61 of *NASA Tech Briefs,* Vol. 4, No. 1, are contained in the report referenced at the end of this article. Much of this report is devoted to a cost-reduction analysis of the solar-heating system installed at Huntsville, Alabama.

Initial findings for this system were that it is considerably more expensive to install than other available systems. Some of the extra costs are incurred because, for the purposes of testing and performance evaluation, the system is more elaborate than the version that would be sold to private customers.

Other costs could be reduced by implementing changes in the performance specifications, in the design of components, and in the installation procedures. These possibilities were reviewed by a team of consultants which made specific cost-saving recommendations. The suggestions range from redesign of the solar collector panels to more efficient washing and handling procedures for the rock-storage bed and to better coordination between the architectural plans and the solar design. Estimated cost savings are given for each of the recommendations, along with the original cost estimates for the installed system. The report also includes a listing of the performance specifications on which the original cost estimate is based, copies of the documentation exchanged between consultants, and the final report and recommendations.

This work was done by William L. Reid and Robert E. Shannon of The University of Alabama in Huntsville for **Marshall Space Flight Center.** *To obtain a copy of the report, "Cost Analysis and Optimization Study for Solar Heating and Cooling Systems," Circle 40 on the TSP Request Card.*
MFS-25152

Remote-Sensing Applications to Geology

The results of a 2-day workshop are summarized in a 69-page report.

The results of a 2-day workshop on the applications of remote sensing to geology are summarized in a new report. The consensus of those attending the workshop is that remote-sensing technology has progressed beyond the experimental stage to become a unique and useful tool for solving geologically related problems.

Simply put, remote sensing is "obtaining information about . . . surfaces and objects from a distance." This is done with cameras, infrared scanning radiometers, radar, and related equipment. When the objects of interest are terrestrial resources, environmental features, and geological structures, the equipment is carried by aircraft and spacecraft; and the relevant distances are measured in miles or kilometers. Solid-state electronics play an important role in modern remote sensing.

The first section of the report gives short summaries of several applications of remote sensing, including:

- environmental analysis,
- crop classification,
- plant epidemics and diseases,
- irrigation reform,
- soil surveys,
- hydrology,
- snow cover,
- flooding,
- meteorology, and
- engineering sites.

Two specific applications, a study of the Mississippi alluvial plain and monitoring of strip mining, are described in some detail.

The report next discusses remote-sensing surveying of lineaments, which are linear surface features that are often miles in length. The causes and means of detection of lineaments are described, as are possible applications of lineament surveys.

Other topics covered are remote-sensing analysis of ground stability near mining operations, Earthquake hazards, water resource studies, and water-pollution monitoring. A summary of 12 remote-sensing projects in Tennessee is given. The last section of the report describes applications of remote sensing to geological basic research.

This work was done by the Remote Sensing Division of The University of Tennessee Space Institute for **Marshall Space Flight Center.** *To obtain a copy of the report, "Applying NASA Remote Sensing Data to Geologically Related Regional Planning Problems in Tennessee," Circle 41 on the TSP Request Card.*
MFS-25151

Computer Analysis of Landsat Data

Possible ways of improving accuracy are suggested.

Analyzing Landsat data by computer has not been particularly successful; human observers, it seems, can interpret Landsat images of the Earth more accurately than can computers. A report, "Some Observations About Landsat Digital Analysis," advances several ideas as to why this situation prevails and how computer analysis might be improved.

The report considers Landsat data gathered from two sites: a region of southwest Alabama west of Mobile Bay and the Large Area Crop Inventory Experiment (LACIE) site in Finney County, Kansas. The latter site was expressly developed as controlled cropland for checking Landsat interpretations. LACIE contains vegetation almost exclusively, whereas the Alabama site contains a variety of ground features. The sites are examined as composite color images, as scatter diagrams for the Landsat spectral bands, and as "enhanced" images in which certain spectral bands are emphasized to reveal, for example, vegetation.

Among the suggestions offered in the report:

- Landsat does not discriminate among the types of vegetation; instead, it "sees" largely chlorophyll.
- Except for vegetation, most features in the ground scene have about the same amount of color in each of the Landsat spectral bands. Thus, a black-and-white image, with shades of gray, would furnish as much information as the color images.
- There are relatively few features present in the spectral data.

It is possible then that computers are being asked to examine Landsat data for the wrong things. Perhaps they should analyze brightness instead of spectral data to distinguish features in land cover; and, perhaps broad new definitions of features should be developed.

This work was done by Robert R. Jayroe, Jr., of **Marshall Space Flight Center.** *Further information may be found in NASA TM-78184 [N78-30634], "Some Observations About Landsat Digital Analysis," a copy of which may be obtained at cost from the New England Research Application Center [see page A7].*
MFS-25105

Computer Programs

These programs may be obtained at very reasonable cost from COSMIC, a facility sponsored by NASA to make new programs available to the public. For information on program price, size, and availability, circle the reference letter on the COSMIC Request Card in this issue.

SKYMAP Star Catalog

Data and data-handling programs for 255,000 stars

The SKYMAP programs include an accurate and complete catalog of all stars with blue or visual magnitudes brighter than 9.0. Developed for use with spacecraft star cameras for attitude determination programs, SKYMAP contains data on approximately 255,000 stars. The principal data sources were the Henry Draper and Smithsonian Astrophysical Observatory catalogs. SKYMAP should prove useful to astronomers, spacecraft designers, and others who have a need for a comprehensive star catalog.

Because of the massive amount of data in the SKYMAP programs, there are smaller catalogs containing only the data of interest for a specific application. The Master Catalog contains all the star data, the Mission Catalog contains the subset of data needed for a particular spacecraft mission, and the Run Catalog contains a minimum subset of the Mission Catalog data that is sufficient for attitude determination.

The SKYMAP programs can be used to create and to update catalogs and to transfer all or part of the Run Catalog to disk storage from magnetic tape. These functions are provided by the four programs within the SKYMAP system (UPDATE, CAT, SWITCH, LOOKAT). UPDATE creates Mission Catalogs, makes corrections, additions, or deletions to the Master and Mission Catalogs, and prints data from the Master Catalog. SWITCH conveniently transfers all or selected parts of the Run Catalog from magnetic tape to disk storage. It may be executed interactivity under TSO.

CAT is used to create the collection of subcatalogs covering overlapping zones in the sky that make up the Run Catalog. The last component, LOOKAT, reads the disk storage version of the Run Catalog as input. It can either store star data for a given part of the sky in main memory for use by attitude-determination programs or provide statistical information on star density and produce plots of stars in selected portions of the sky.

The program package consists of one program tape and four data tapes containing the Master Catalog. It is written in FORTRAN IV for the H-level compiler and has been implemented in batch mode on an IBM 360/95 with a maximum central memory requirement of 390K (decimal) bytes.

This program was written by Dave Gotlieb of Computer Science Corp. for **Goddard Space Flight Center.** *For further information, Circle B on the COSMIC Request Card.*
GSC-12445

Meteorological Data-Processing Package

Satellite data are used to develop cloud-tracking maps.

METPAK, a meteorological data-processing package, is part of the Atmospheric and Oceanographic Information Processing System, AOIPS, developed by the NASA Goddard Space Flight Center. METPAK is used by NASA scientists who work with data from satellites and other sources to investigate the dynamics of severe storms. This research aims to develop and enhance numerical prediction models for mesoscale phenomena and to improve the ability to detect and predict storms.

Meteorological investigations with METPAK have concentrated on deriving information from geostationary satellite data, particularly the visible and infrared image data from the Synchronous Meteorological Satellites. Aircraft, radiosonde, and other satellite data bases may also be used by METPAK. The package provides image navigation, registration, and related functions required to support cloud-motion and wind-vector-field analyses.

The software includes five meteorological and supporting functions: (1) landmark extraction, (2) navigation, (3) cloud tracking and height determination, (4) wind-vector overlay, and (5) objective analysis. In addition, a save/restart function and a collection of image-processing functions are included to help manipulate image data.

The landmark extraction and navigation functions accurately transform satellite-image coordinates to Earth coordinates. The landmark extraction function generates basic Earth location data required by the navigation function to establish an accurate coordinate transformation. Landmark data consist of the image line and pixel number and the associated latitude and longitude corresponding to a recognizable Earth location. Both single-point and image-registration methods are provided for defining the landmark points.

The navigation function accurately computes the latitude and longitude of any point on an image and similarly computes the image coordinates of a given latitude and longitude. The parameters required to transform coordinates are called the "navigation solution." The METPAK navigation function generates, stores, edits, and tests the navigation solution of an image sequence. This solution is essential for automatic image alinement, windspeed computation from raw tracking data, and finding Earth locations for cloud-height and wind-flow-field calculations.

The METPAK cloud-tracking function extracts wind-velocity information from digital images of the Earth taken by a geosynchronous satellite. The change in position of a selected cloud tracer is determined for images recorded at different times. Wind motion is assumed to be equal to cloud motion at the base of a cloud, provided that the tracer selected for cloud tracking has a small vertical dimension. Clouds can be tracked by an image correlation method or by single-point tracking. With a good cloud tracer, the image correlation method can accurately track the tracer using an efficient Euclidean norm correlation algorithm. When a good cloud tracer cannot be found,

(continued on next page)

the single-point tracking method employs the user's skill and judgment in the selection and tracking of cloud movements.

Since clouds at different altitudes may have totally different types of motion, a cloud-height determination program is provided. It employs a lookup-table approach. The wind-arrow-overlay function produces a picture of the wind vectors that result from the cloud-tracking function. This function allows one to edit the wind vectors and superimpose the final wind-arrow overlay on the cloud images.

The objective analysis function enables the meteorologist to perform detailed interactive analysis of the wind fields generated by the cloud-tracking function. The wind vectors generated by the cloud-tracking function are randomly distributed. These vectors are interpolated to a uniformly spaced grid in the latitude and longitude coordinate system. Once the uniform wind field is generated, a variety of derived field parameters can be computed. In addition, contour plots of divergence, vorticity, stream function, and other meteorological quantities can be produced and superimposed on the cloud images for further evaluation.

The METPAK system is written in FORTRAN and Assembler for interactive execution on the PDP 11/70 using the RSX-11D operating system and has a central memory requirement of approximately 32K of 16-bit words not including system facilities. The system consists of 44 tasks, which are functionally modularized to increase program efficiency. Images are manipulated with METPAK on a Hazeltine Interactive Terminal or on a specially-modified GE Image 100 image-processing system. The installation of METPAK on a system other than the configuration used at NASA Goddard may require significant modification to the program.

This program was written by James B. Billingsly and Peter A. Braken of **Goddard Space Flight Center.** *For further information, Circle C on the COSMIC Request Card.*
GSC-12372

AOIPS Classification Package

Interactive program for classifying multispectral data

A multispectral classification package, CLASSPAK, is part of the Atmospheric and Oceanographic Information Processing System, AOIPS, developed by the NASA Goddard Space Flight Center. CLASSPAK is an interactive, user-oriented software package that performs a supervised maximum-likelihood classification of multispectral image data. CLASSPAK allows one to input up to 24 bands of image data from tape. Selected bands can be displayed on a screen. Training and testing areas can be defined from the image, and a selected area may be classified using up to eight bands. CLASSPAK has been used in connection with land-cover studies, urban-boundary delineation, geological studies, forestry and agriculture investigations, and the development of hydrological models for watershed studies.

Data are classified based on a maximum-likelihood decision rule that assumes (1) all a priori probabilities are equal and (2) each class has a Gaussian probability distribution. The mean and covariance matrix for each class may be input directly or may be computed from a predefined training sample.

Menu-formatted prompts are displayed whenever one must interact with the program. The CLASSPAK main menu offers 11 options, including current image definition and display; the definition, modification, and deletion of training and testing data; the classification of a master image using previously-accumulated class training statistics; the display and printing of classification results; and the production of gray-level dump of selected image areas.

When an option is selected from the main menu, the associated system functions are initiated, and the user is prompted through the use of the selected option by further menus. As a selected-option function is completed, control returns to the main menu, which prompts the user for further instructions. Classification results may be displayed on the terminal video screen or output to a tape in Dicomed format for hard-copy generation.

CLASSPAK is written in FORTRAN and Assembler for interactive execution on a PDP 11/45 using the RSX-11D operating system and supporting a modified GE Image 100 system. The central memory requirement is approximately 128K of 16-bit words. The installation of CLASSPAK on systems other than the configuration used at NASA Goddard may require some modification on the program.

This program was written by James B. Billingsly and Peter A. Braken of **Goddard Space Flight Center.** *For further information, Circle D on the COSMIC Request Card.*
GSC-12374

Materials

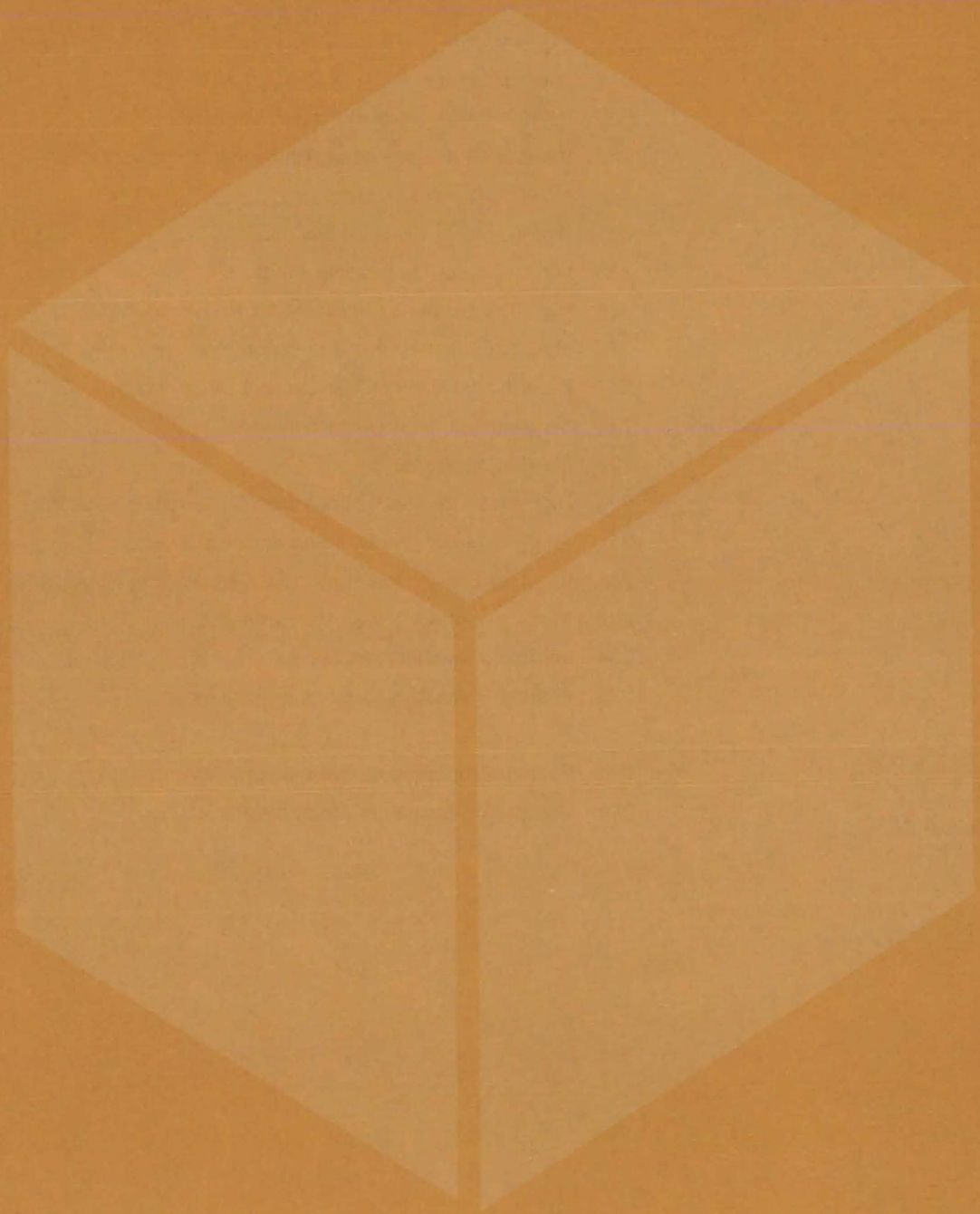

Hardware, Techniques, and Processes

Books and Reports

Thermoluminescence Analysis of Aerosols

A simple method for identifying air pollutants in the field or laboratory

Langley Research Center, Hampton, Virginia

Trace amounts of solid or liquid pollutants suspended in the air can be detected and identified by a simple technique that is based on thermoluminescence. Unlike gas and liquid chromatography, mass spectroscopy, or X-ray fluorescence, the new technique does not require expensive or cumbersome equipment. It is therefore suited for measurements in the field (from vans and airplanes, for example).

A measured sample of an aerosol is exposed to ozone gas; then, a material that fluoresces is added, and the mixture is heated. The characteristics of the graph of luminescence versus temperatures identify the pollutant (Figure 1).

Suitable fluorescers are organics such as rubrene, naphthacene, and certain anthracenes. These materials are excited to luminescence by energy transfer from the heated ozonide, which is formed by the reaction of ozone with the particles in the aerosol.

To make an analysis, an aerosol sample is collected as a solid deposited on a sterile filter. The sample (about 2 milligrams are sufficient) is placed in a reaction chamber (Figure 2). A mixture of 1 percent ozone in oxygen is introduced, allowed to react with the sample for 5 minutes, and is removed and replaced with ambient air. A drop of rubrene dissolved in benzene is then placed on the specimen. After a few minutes, the benzene evaporates, leaving the rubrene dispersed throughout the sample.

Next, the sample is heated to 200° C at a programed rate of 30° C per minute. The ozonide in the sample decomposes, causing the rubrene to emit light (in the yellow portion of the visible spectrum). The light is detected by a photomultiplier and is plotted as a function of temperature.

For the aerosols and aerosol components analyzed thus far (see table), the light output rises to a maximum and then drops off as the temperature approaches 200° C. The temperature at which the light output peaks and the half width of the peak are unique to each material.

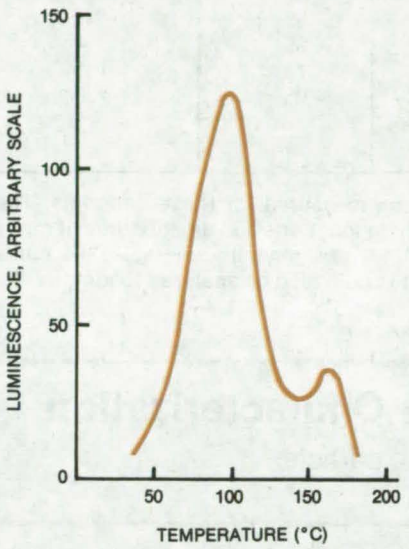

Figure 1. This **Graph of Luminescence Versus Temperature** is obtained from a mixture of a fluorescer with an ozonide of a pollutant. The peak position and half width identify this material as 1,2-benzanthracene.

For rapid analysis of aerosol samples collected in the field, luminescence curves measured onsite could be compared with a "catalog" of curves for known aerosol constituents and mixtures. This approach could help to track down pollution sources in and around steel mills, factories, and chemical plants. It could also trace the dispersion of pollutants over a geographical region.

The thermoluminescent technique should prove useful in basic research into aerosol chemistry; and it could be used in studies of the production of mutation- and cancer-causing agents by ozone in the upper atmosphere.

This work was done by Edward R. Long, Jr., and Robert S. Rogowski of

(continued on next page)

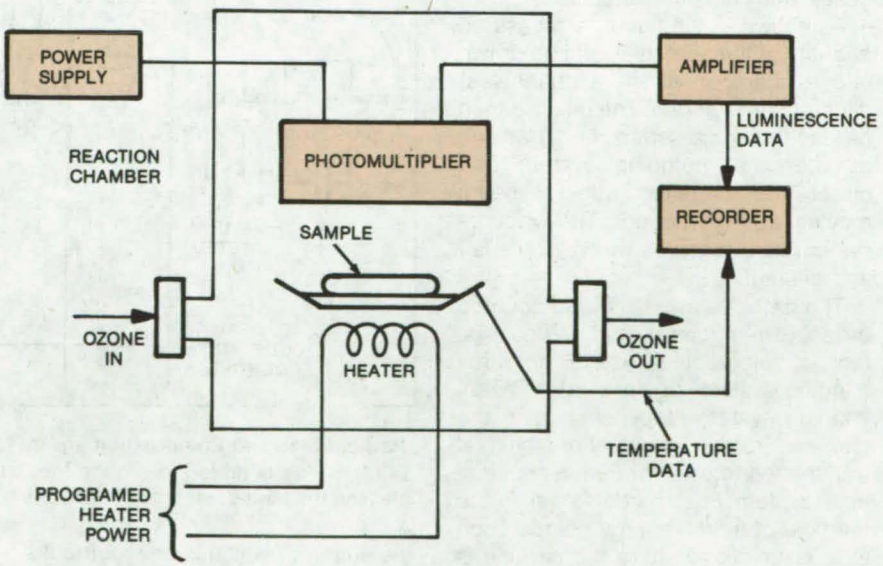

Figure 2. The **Apparatus for Measuring Thermoluminescence** consists of a chamber for reacting ozone with the pollutant sample, a heater for raising the temperature of the sample at a controlled rate, a photomultiplier for measuring the light output of the sample, and a recorder for plotting the light output as a function of temperature.

Substance	Initial Maximum (°C)	Initial Half Width (°C)	Maximum 4 Hours After Ozonation (°C)
1293 Aerosol	97	81	100,122,151
Rogo Aerosol	83	64	102
Ammonium Sulfate	110	44	---
Sodium Chloride	152	52	---
3,4-Benzopyrene	103	69	---
1,2-Benzanthracene	99	35	---
Coronene	85	72	101
N-Octacosane	122	96	130
Al_2O_3	No reaction		

Ozone/Aerosol Thermoluminescence has been measured for these materials. The first two aerosols were collected at different field locations and are mixtures of many compounds. Since the ozonides formed initially are generally unstable, the curve characteristics change with time. The rate data could also be analyzed to identify the aerosol.

Langley Research Center. *Further information may be found in NASA TM-X-72795 [N76-21743], "A Thermoluminescent Method for Aerosol Characterization," a copy of which may be obtained at cost from the North Carolina Science & Technology Research Center [see page A7].*

This invention has been patented by NASA [U.S. Patent No. 4,062,650]. Inquiries concerning nonexclusive or exclusive license for its commercial development should be addressed to the Patent Counsel, Langley Research Center [see page A8]. Refer to LAR-12046.

Instrument for Aerosol Characterization

Proposed instrument would measure particle size and chemical composition.

NASA's Jet Propulsion Laboratory, Pasadena, California

A proposed instrument would measure both the size distribution and chemical composition of aerosols. It could find uses in the study of atmospheric contamination, smog, stack gases, and chemical aerosols.

As shown in the figure, a measured quantity of the aerosol would be drawn into a chamber where a quantity of dilutant gas is added. The mixture then passes through a series of nozzles and a differential pumping system that direct the particles into a beam moving at high speed. The vacuum system also removes much of the air and dilutant.

The particles are sized and counted by a laser-imaging or scattering system, a holographic system, an X-ray imaging system, or an electron-beam imaging system (depending upon the particle sizes). The image signal is transmitted to an information-management system. Each particle then enters the field of a high-energy source such as a laser beam where the particle is vaporized and ionized. The ions are extracted and focused by an electromagnetic lens into the entrance slit of a mass spectrometer. The ions then impinge on an electro-optical detector, the output of which is an electrical signal from which the chemical composition of the vaporized particulate can be determined. The size-distribution and chemical-composition signals are fed into the information-management system for processing.

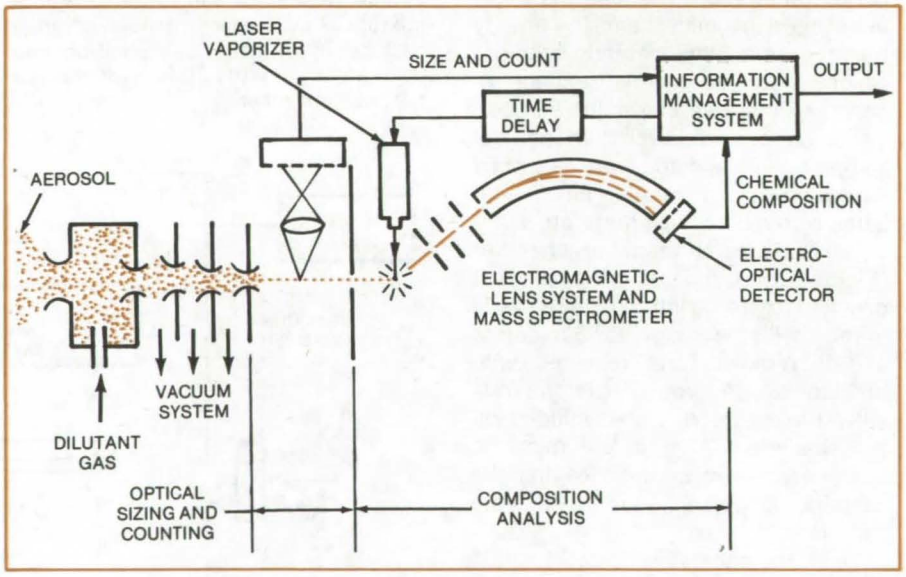

Particle Size and Composition are measured by this proposed two-stage instrument. Dilutant gas is added to reduce the sample density sufficiently so that only one particle is in the field-of-view of the counter at any time.

This work was done by Giulio Varsi of Caltech for **NASA's Jet Propulsion Laboratory.** *For further information, Circle 42 on the TSP Request Card.*
NPO-14320

Remote Measurement of Atmospheric Pollutants

Infrared heterodyne spectrometer (IHS) is used for both ground-based and airborne measurements.

Langley Research Center, Hampton, Virginia

Both ammonia and ozone are important in studies of atmospheric processes and pollution; tropospheric measurement data, particularly in the case of ammonia, are limited. Atmospheric ammonia is involved in aerosol production and may constitute a significant source or sink in NO_x chemistry. Ammonia is produced by natural organic breakdown and is a byproduct in the chemical industry, domestic incinerators, and automobile exhausts. As a result, ammonia is frequently found in urban atmospheres. Atmospheric ozone accounts for much of the pollution injury to vegetation; excessive ozone levels are considered evidence of photochemical smog formation.

The concentration and vertical distribution of atmospheric ammonia and ozone have been remotely sensed, using a dual-CO_2-laser multichannel IHS. Recent wideband infrared-heterodyne-receiver developments make atmospheric pollutant measurements possible with nearly-quantum-noise-limited sensitivity and ultrafine spectral resolution. These features are of particular significance in remote gas-sensing applications, where low-level signals often exist in a background of interfering gases. The IHS is suitable for both ground-based and airborne atmospheric measurements. It is nearly independent of source temperature and ground albedo variations as a result of a dual infrared channel design.

A simplified block diagram is shown in Figure 1. The IHS has been applied to ground-based solar-radiance measurements to infer the concentration and vertical profiles of tropospheric ammonia and ozone. Airborne ozone measurements have also been carried out. The high specificity and nearly-quantum-noise-limited sensitivity of the IHS provide the capability of scanning individual signature lines of selected gases in the 9- to 11-μm region.

Some sample results of IHS measurements of tropospheric ammonia and atmospheric ozone concentrations are shown in Figure 2. These results were obtained from ground-based remotely sensed data.

(continued on next page)

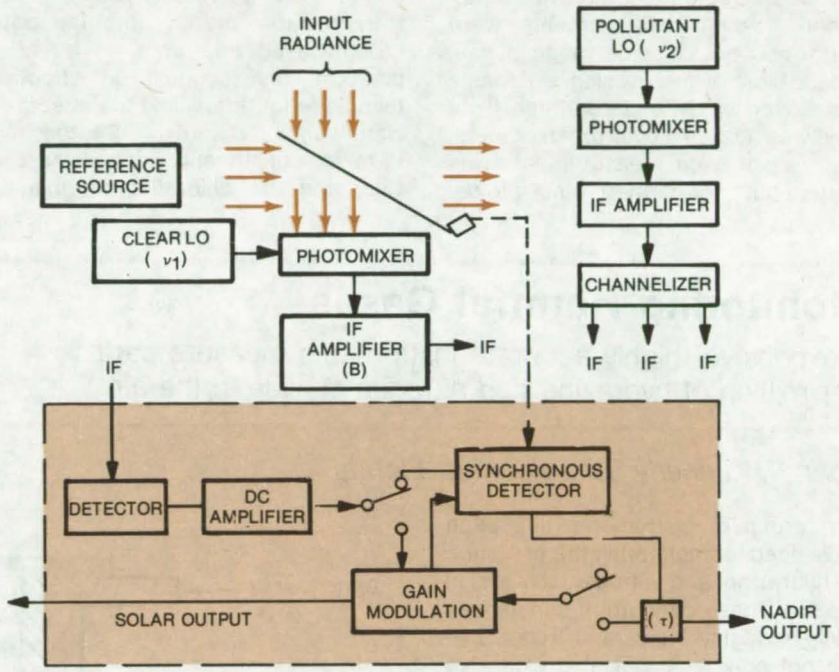

Figure 1. The **Infrared Heterodyne Spectrometer** is made up of two Dicke-switched infrared heterodyne radiometer channels, which share a solar tracker, a common field-of-view (FOV), an infrared Dicke switch, and a calibration channel. The IHS employs two wideband PV:HgCdTe photomixers; two sealed-off, grating, tunable CO_2 lasers; three pollutant IF processors and one reference IF processor; two blackbody sources for measurement reference and calibration; and data recorders. The infrared Dicke switch alternately switches the two receiver FOV's between the collecting aperture and a reference blackbody and supplies a synchronizing signal to the processing channels. The common reference blackbody and Dicke switch are used for the matched photomixers to provide a common receiver FOV for each radiometer receiver and to minimize the effects of laser LO instabilities. A blackbody source is inserted between the collecting aperture and the optical Dicke switch for IHS calibration.

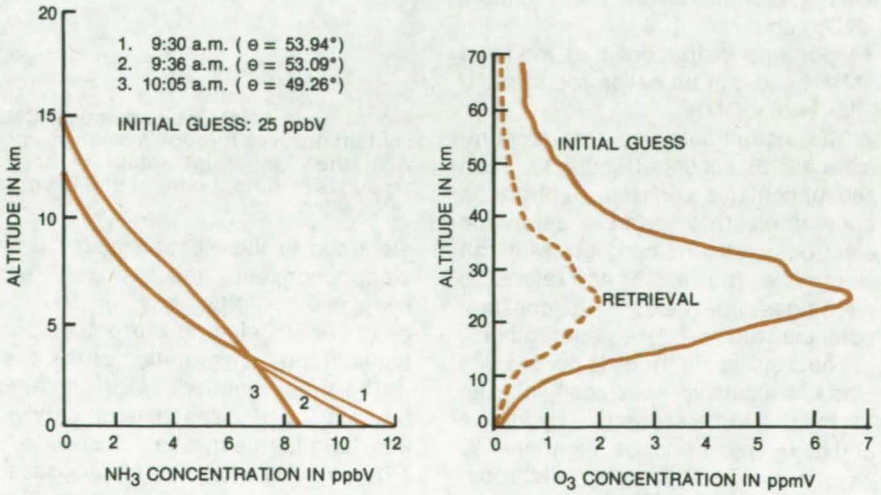

Figure 2. **IHS Measurements** are shown for tropospheric ammonia (NH_3) on the left and atmospheric ozone (O_3) on the right.

Ozone was the selected atmospheric species for the airborne flight measurements. The IHS was operated in the solar viewing mode to determine ozone distributions in the stratosphere and in the nadir viewing mode to determine the ozone distribution in the troposhere. The IHS was mounted in the NASA CV 990 test aircraft. Stratospheric ozone measurements were performed over a wide range of latitudes. Most of the mission flightpaths were over water, and very little flight time was available over urban centers. A series of nadir measurements was carried out over northern Alaska to determine whether the IHS reference-channel output tracks the actual ground temperature. Results indicate that the reference channel is effective in minimizing the effects of changes in the ground brightness temperature.

The atmospheric propagation data demonstrate the capability of the dual-channel IHS for remote atmospheric-transmission measurements, both ground-based and from an airborne platform, and suggest an effective technique for unraveling the effects of water vapor and aerosols. Stratospheric minor constituents such as NHO_3, ClO, and the chlorofluoromethanes, which have signature lines in the 9- to 11-μm region, appear to be particularly attractive for future IHS measurements. The use of tunable diode lasers as LO's in the IHS may extend solar viewing measurements to additional atmospheric gases as well as to other portions of the infrared spectrum.

This work was done by F. Allario, J. Hoell, and R.K. Seals of **Langley Research Center** *and R.A. Lange, B.J. Peyton, and M.G. Savage of Cutler-Hammer, Inc. For further information, Circle 43 on the TSP Request Card.*
LAR-12277

Monitoring Harmful Gases

Inexpensive, highly accurate instruments measure parts per million of hydrazine and nitrogen dioxide in the air.

John F. Kennedy Space Center, Florida

A group of instruments has been developed for monitoring the presence of hydrazine and nitrogen dioxide in the air. These dangerous substances (NO_2 is highly toxic, and hydrazines are not only toxic but also explosive and corrosive) are widely used as propellants in rocket engines. The new relatively-inexpensive instruments detect these substances in concentrations as low as a few parts per million.

The developments include:

- A wall-mounted instrument that monitors both NO_2 and hydrazine vapors [hydrazine (H), monomethylhydrazine (MMH, and unsymmetrical dimethylhydrazine (UDMH)];
- A portable instrument that monitors NO_2; and
- A portable instrument that monitors MMH and can be calibrated to monitor H or UDMH.

The instruments use electrochemical cells as sensors (Figure 1). Each sensor contains a sensing electrode, a counter electrode, and a reference electrode. all in contact with an electrolyte. The sensing and reference electrodes are held at a constant potential with respect to each other.

The sensing electrode is porous and contains a catalyst specifically chosen for the gas to be sensed — hydrazine or NO_2. The air to be monitored is passed over the sensing electrode, and a portion diffuses into the electrode to the electrolyte where an electrochemical reaction of any hydrazine or NO_2 gas in the air produces an electric current proportional to the concentration of the gas.

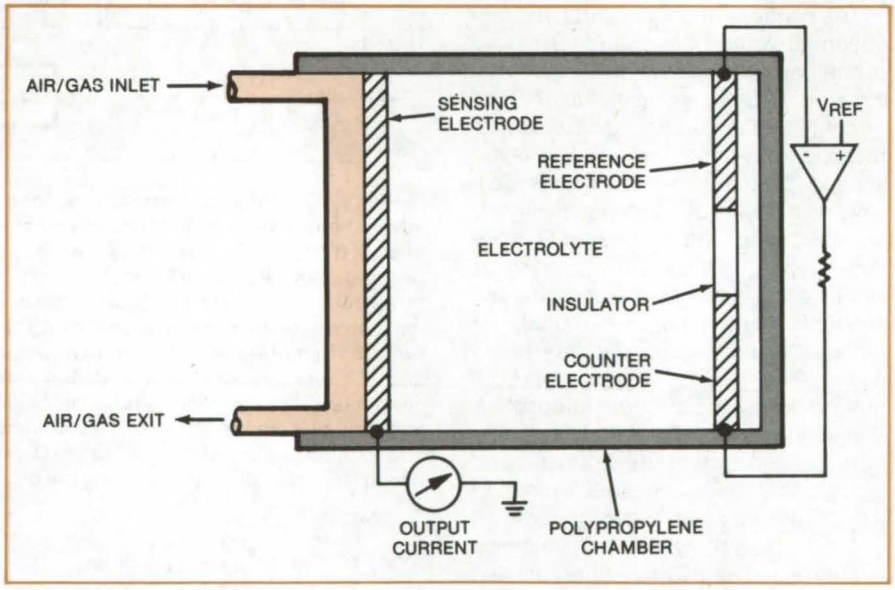

Figure 1. In this **Electrochemical-Cell Sensor,** the air to be monitored for gas content diffuses through a catalyst-impregnated sensing electrode to an electrolyte. With the right combination of catalyst and gas, an electrochemical reaction produces an output current that is proportional to the concentration of gas in the air.

The three electrodes are prepared by spraying a dispersion of catalyst and tetrafluoroethylene (TFE) onto a TFE film. The catalysts, all purchased as high-surface-area powders, include platinum, gold, palladium, iridium, ruthenium, rhodium, and carbon. These electrodes are sealed to a polypropylene chamber that is then filled with an electrolyte consisting of either 28 percent H_2SO_4 or 23 percent KOH.

The electrochemical-cell sensor is remarkably selective. A hydrazine-sensor cell, for example, does not respond to NO_2, and vice versa. Also,

neither a hydrazine- nor an NO_2-sensitive cell responds to such gases as helium, argon, oxygen, nitrogen, methane, hydrogen, carbon dioxide, and carbon monoxide.

The wall-mounted instrument (Figure 2) contains two gas pumps, two electrochemical sensors, two meters, and potential-control and amplification circuits. One pump supplies a constant flow of gas to the hydrazine sensor, and the other supplies constant flow to the NO_2 sensor. The output current of each cell is indicated by its own meter, which is calibrated in parts per million. The portable instruments, which weigh only 3.5 pounds (1.6 kg) each, have a single pump, sensor, and meter, since they monitor only one gas.

So that the instruments can be calibrated in the field, sample bags of known concentrations of hydrazine-type vapors in nitrogen have been specially prepared. The nitrogen and the bag material (TFE) ensure maximum stability of the vapor. Calibration samples of NO_2 are commercially available.

This work was done by William R. Helms of **Kennedy Space Center** *and Joseph R. Stetter of Energetics Science, Inc. Further information may be found in:*

NASA CR-153048 [N77-23439], "A Study for Hypergolic Vapor Sensor Development — Final Report April 8, 1977," and

NASA CR-155770 [N78-18224], "A Study for Hypergolic Vapor Sensor Development Final Report — November 1977."

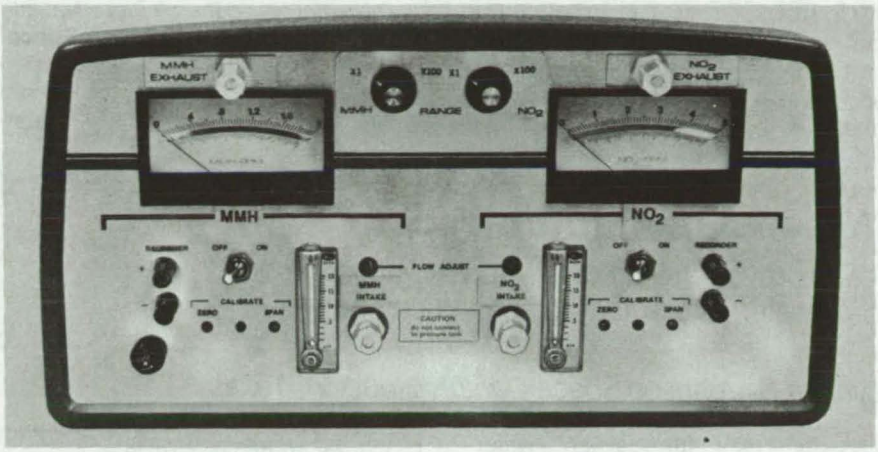

Figure 2. This **Wall-Mounted Monitor** indicates separately the concentrations of monomethylhydrazine (MMH) vapors and nitrogen dioxide (NO_2) in the air. Portable monitors, which can be worn by a worker, have also been developed; they indicate the concentration of either hydrazine-type vapors or NO_2 (but not both) and include an alarm feature.

Copies of these reports are available for **$6** *each [prepayment required] from the National Technical Information Service, Springfield, Virginia 22151.*

Inquiries concerning rights for the commercial use of this invention should be addressed to the Patent Counsel, NASA Resident Legal Office-JPL [see page A8]. Refer to KSC-11086.

Water-Soluble Fluorocarbon Coating

A durable nonpolluting coating for a variety of substrates

Lyndon B. Johnson Space Center, Houston, Texas

Various systems have been devised for depositing thin films and protective coatings of fluorocarbon polymers. However, the organic liquids that are usually used as solvents for these coatings require high cure temperatures (exceeding 175° C) and release quantities of volatile and toxic organic chemicals.

A new water-soluble fluorocarbon coating is nonpolluting, yields durable and tough coatings, and air-dries at ambient temperatures (15° to 50° C). The coatings may be applied to a wide variety of substrates, including wood, metal, masonry, textiles, paper, and glass by conventional coating methods, such as spraying or brushing. The dried and cured coatings have superior hardness and flexibility; strong resistance to chemicals, fire, and weather; and possess good thermal stability. Their finish is smooth, glossy, and uniform.

The system consists of an aqueous coating composition containing dispersed vinylidene fluoride particles, a liquid epoxy resin, and an emulsifying agent. About 30 to 70 parts of dispersed vinylidene fluoride polymer particles are used for each 100 parts by weight of aqueous medium. Instead of the vinylidene fluoride, up to 50 percent tetrafluorotheylene, trifluoroethylene, chlorotrifluoroethylene, hexafluoropropene, or any mixture of these may be substituted.

About 8 to 20 parts of liquid epoxy resin is added to the polymer particles. A typical epoxy resin is a blend of from about 10 to 12 parts by weight of a glycidyl ether of a polyhedric compound such as bisphenol A, and from about 1 to 3 parts of diglycidyl ether of propylene glycol. About 1 part of an emulsifying agent that is capable of rapidly curing the epoxy resin upon the removal of water is also added. The emulsifying agent may be one of a group of compounds having attached amino-alkylated groups with the formula.

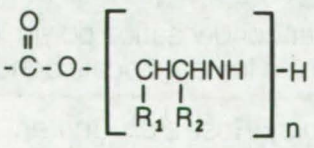

where the R_1 and R_2 denote either hydrogen or lower alkyl radical groups having 1 to 4 carbon atoms. The value

(continued on next page)

of n ranges from 1.0 to 2.5. The composition may also include various surfactants, pigments, antifoams, preservatives, thickening agents, or other additives.

This work was done by Piero Nanelli of Pennwalt Corp. for **Johnson Space Center.** *No further documentation is available.*

Title to this invention has been waived under the provisions of the National Aeronautics and Space Act [42 U.S.C. 2457(f)], to the Pennwalt Corp. King of Prussia, PA 19406. MSC-16562

Water-Based Intumescent Paint

An improved fire-protective coating is safer and easier to use than oil-based paints.

Lyndon B. Johnson Space Center, Houston, Texas

A family of fire-resistant water-based paints is made by adding intumescing agents to the fluorocarbon coatings described in the previous article, "Water-Soluble Fluorocarbon Coating" (MSC-16562). In a fire, the intumescing paint protects a flammable substrate by swelling and forming a dense char that cuts off the oxygen supply.

Because the paints are water based, they do not pollute the atmosphere as they dry, unlike previous oil-based intumescent paints, which give off volatile hydrocarbons. In fact, they could be used in closed-loop air-recirculation systems (in spacecraft and submarines, for example) without high-temperature curing. Other potential applications are in residences, factories, hospitals, and vehicles for mass transit. The water-based paints are not degraded by humidity, are more resistant to ultraviolet radiation, and are more durable than oil-based paints.

A typical paint composition (see table) consists of a fluorocarbon latex resin (a terpolymer of tetrafluoroethylene, hexafluoropropene, and vinylidene fluoride), intumescing agents, and epoxy or acrylic resins.

Intumescing agents may be chosen from sulfanilamide, melamine pyrophosphate, polysulfonamide derivatives of polycyclic aromatic compounds, and other materials. Other possible additives include chlorinated paraffin to stabilize the char, starches or polyhydric alcohols to increase char yield, and inorganic fibers to increase the strength of the char.

Fluorocarbon latex resin (62% vinylidene fluoride, 24% tetrafluoroethylene, 14% hexafluoropropene)	40%
Intumescing agent	40%
Pigment	5% to 10%
Chlorinated paraffin	5%
Miscellaneous (defoamers, char builders, stabilizers, thickeners, fibrous materials)	5% to 10%
Volatile components	Water is added for the desired consistency.

One possible **Intumescing Paint Formulation:** Percentages are by weight.

The new paints can be applied by brush or by commercially-available spray equipment. In most applications, facemasks or blowers for ventilation are not required.

This work was done by Dale G. Sauers of **Johnson Space Center** *and Piero Nannelli of Pennwalt Corp. No further documentation is available.*

Title to this invention has been waived under the provisions of the National Aeronautics and Space Act [42 U.S.C. 2457(f)] to the Pennwalt Corp., King of Prussia, PA 19406. MSC-16609

High-Temperature Adhesives for Polyimide Films

Linear condensation polyimides show promise for large-scale bonding.

Langley Research Center, Hampton, Virginia

Polyimides are rapidly becoming a preferred material in the packaging and other industries because of their strength and usefulness at high temperatures. However, very few adhesives are suitable for long-term high-temperature use with polyimides. Those adhesives that can withstand heat generally contain additives that make the resins too brittle for bonding film.

This problem was faced in the design of the proposed NASA Solar Sail, which would be made from a polyimide film. Thus, a number of potentially suitable adhesives were investigated. One group of high-temperature polymers that showed promise as adhesives can form flexible film coatings that are compatible with the polyimide films. They were linear condensation polyimides.

Three promising polyimide adhesives were prepared in the amic acid form in the aliphatic ether solvent, diglyme, and were studied along with a new experimental precursor adhesive (NR-150-B2X) prepared in an amide solvent as a monomeric mixture. The monomers used in the preparation of the adhesives were 3,3′,4,4′-benzophenone tetracarboxylic dianhydride (BTDA), pyromellitic dianhydride (PMDA), and 3,3′- or 4,4′-diaminobenzophenone (DABP). The experimental precursor-adhesive solution, NR-150-B2X, was obtained as a mixture of monomers in N-methylpyrrolidone (NMP). The polyimide resins used and some of their properties are listed in the table.

Polyimide film panels were brush-coated about 0.6 cm from the edge with either the polyamic acid solutions in diglyme or the NR-150-B2X in NMP/ethanol. The coated adherends were B-staged 1 hour at 373 K and ½ hour at 448 K in a forced-air oven. Each primed panel was then overlapped 0.6 cm with an unprimed panel and bonded at 616 K with a hot iron for 20 seconds. Only contact pressure of the iron on the bond line was necessary for bonding. Final bond-line thicknesses ranged from 0.3 to 0.5 mil (0.008 to 0.013 mm).

Results from room-temperature and elevated-temperature lap shear tests are shown in the graph. The four experimental polyimide compounds all show promise as high-temperature adhesives for polyimide film. The fast, low-pressure bonding should work especially well for joining large polyimide sheets as required in the Solar Sail program.

Resin	Formulation	Amic Acid ηinh	T_g K (°F)
LARC-2	BTDA 3,3′-DABP	0.70	520 (477)
LARC-3	2 BTDA/1 PMDA 3,3′-DABP	0.63	542 (516)
LARC-4	3 BTDA/1 PMDA 4,4′-DABP	0.50	570 (567)
NR-150-B2X	6F (1.5% excess) 3 PPD/2 ODA	—	595 (612)

Polyimide Adhesives, developed at NASA's Langley Research Center, are especially suitable for bonding large sheets of polyimide film.

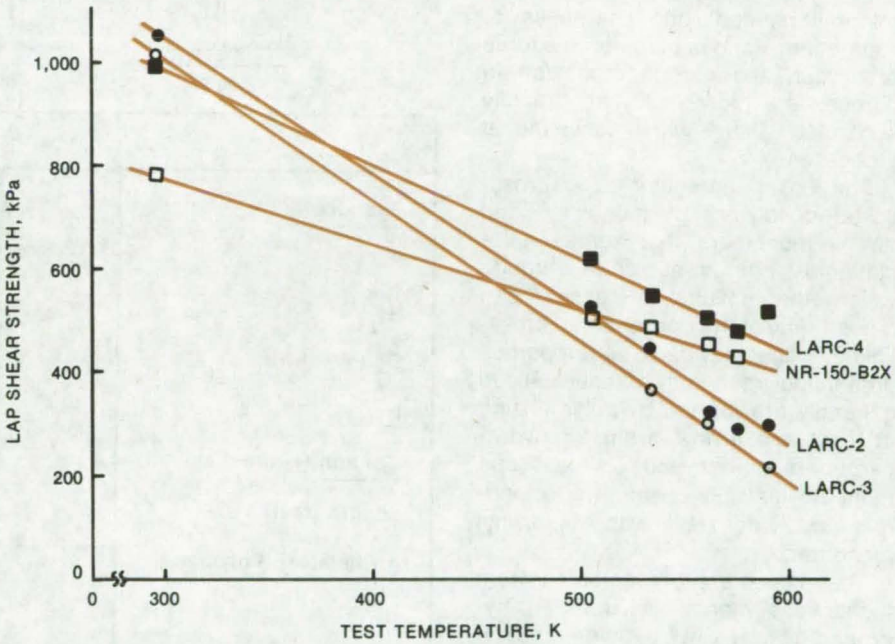

Lap Shear Strengths of the adhesives listed in the table were determined when bonded to 2-mil polyimide film. Note that at 575 K materials with the higher T_g values tend to retain their properties better than those with lower values.

NR-150-B2X and LARC-4, the materials, characterized by higher T_g values, also best retained their properties upon long-term aging at elevated temperature in vacuum. An important advantage of these materials is that they can be supplied as flexible tape, already B-staged and ready for instant bonding. In addition, the nontoxic ether solvent, diglyme, from which the LARC resins were prepared, is easily removed on bonding, disallowing any plasticization of the polymers by solvent (as compared with the NMP problem with NR-150-B2X).

This work was done by Anne K. St. Clair, Terry L. St. Clair, and Wayne S. Slemp of **Langley Research Center.** *For further information, Circle 44 on the TSP Request Card.*
LAR-12348

Modified Polymers for Gas Chromatography

Chelate-modified polymers simplify separation of atmospheric gases.

Ames Research Center, Moffett Field, California

Polymeric materials have been modified to serve as a stationary phase in chromatographic columns used for the separation of atmospheric gases. The new materials simplify and improve the separation of atmospheric gases in the terms of time, quantity of material needed, and sharpness of separation. Various common mixtures of oxygen and carbon monoxide in nitrogen are more easily and rapidly separated than with conventional processes.

The basic ingredient is a cross-linked copolymer of monovinyl and divinyl monomers that serves as a stationary porous substrate through which the mixture of gases can diffuse. Any of the conventional cross-linked, finely-divided, microporous organic polymers can be used. These generally are formed by polymerizing at least one divinyl aromatic hydrocarbon monomer and at least one monoethylenically unsaturated monomer copolymerizable with the divinyl monomer.

The monomers are selected from monocyclic monovinyl aromatic hydrocarbons, N-vinyl pyridine and N-vinyl pyrrolidone. The usable polymers are prepared by bulk or suspension polymerization processes in the presence of a suitable quantity of a nonpolar organic liquid to produce the required porosity in the final polymer (divinyl benzene). Diethylbenzene and n-heptane-toluene mixtures are preferred for the divinyl benzene copolymers.

Inorganic complexed-ion compounds, or chelates, are embedded into the polymer matrix. These can include such compounds as cobalt salicylaldehyde ethylenediamine (salconime) and other cobalt complexes made with the derivatives of salicylaldehyde, such as 3-fluorosalicylaldehyde, cobalt acetylacetone-ethylenediamine [Co (acacen)], iron imidazole salts, and iron tetraphenylporphyrin. The proportion of the chelate to polymer matrix varies, depending on the chelate and on the gas components to be separated. For example, Co (acacen) combined with cross-linked polydivinyl benzene is used in quantities of from 0.025 g to more than 0.2 g per gram of polymer, depending on mixture, of gas to be separated.

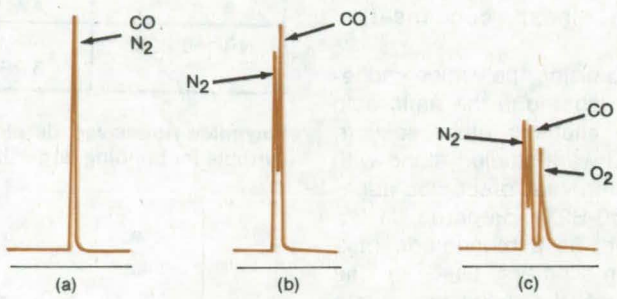

	RUN				
Gas Mix	(a)	(b)	(c)		
CO (%)	0.2	0.2	0.1		
N_2 (%)	0.2	0.2	0.1		
O_2 (%)	-	-	0.2		
He (%)	99.6	99.6	99.6		
Column (1-mm-diameter)					
Length (feet)	4	4	4*	+	4*
g Chelate/g Polymer	-	0.05**	0.20		0.05**
Base	-	amino pyridine	amino pyridine		

*Columns in tandem, operated at gas flow of 20 to 24 cm^3/min
**Treated at 200° C for 24 hours with an He flow of 20 to 24 cm^3/min before chromatography

Figure 1. The **Utility of Chelate-Polymer Complexes** is shown for various chelate levels in separating carbon monoxide from nitrogen and from mixtures of oxygen and nitrogen. Without the chelate (a), there is no separation.

The effect of chelate is demonstrated in Figure 1, which shows the results of experiments with mixtures of carbon monoxide, oxygen, and nitrogen chromatographed in 1-mm-diameter columns at room temperature with a helium carrier-gas flow rate of 20 to 24 cm^3/min. The polymer-chelate complex quickly resolves mixtures containing nitrogen, carbon monoxide, and oxygen [shown on (b) and (c)] whereas the polymer matrix alone cannot (a).

In some cases as in the chromatography of undiluted air, an organic nitrogen base is incorporated into the polymer-chelate complex. The base is used in concentrations of two to four times greater than the chelate. Usable bases include pyridine and its various substituted derivatives, such as aminopyridine, cyanopyridine, and

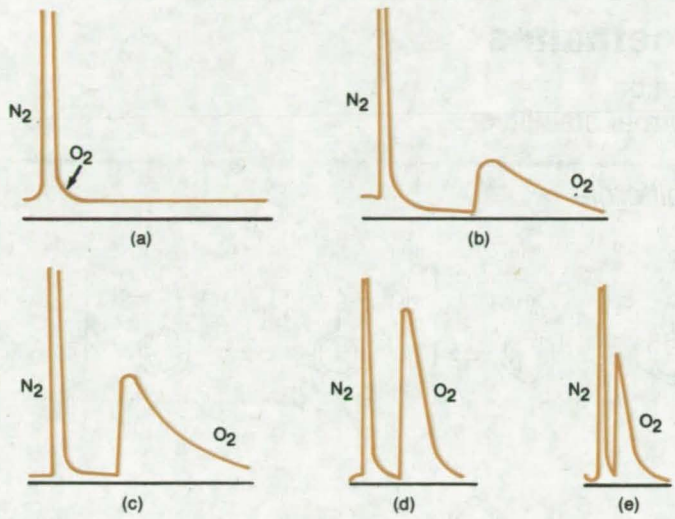

	STATIONARY PHASE				
	(a)	(b)	(c)	(d)	(e)
Heptane: Toluene ratio	3:3	3:3	2:4	3:3	3:3
g Co(acacen)/g Polymer	0.1	0.1	0.1	0.1	0.025
Coordinated base	-	pyr*	pyr	cyano-pyr	pyr

*pyr = pyridine

Figure 2. The **Chromatograms Using Modified Chelate-Polymer Complexes** indicate how various factors influence the oxygen retention.

vinyl pyridine, as well as imidazoles, and pyrazoles.

Figure 2 shows the effect of the nitrogenous organic base on the separation of oxygen from 100 percent air. As demonstrated in part (a), the separation does not occur without the base. Also the nature of the coordinating base (b) and (d) affects the retention time of oxygen. A similar effect is produced by charging the chelate content [e.g., (b) and (e)] and the ratio of components in the inert diluent used in the first-stage polymerization of the packing matrix [e.g., (b) and (c)].

This work was done by Fritz H. Woeller of **Ames Research Center** *and Warren Christensen and Ludwig Mayer of San Jose State University. For further information, Circle 45 on the TSP Request Card.*

This invention is owned by NASA, and a patent application has been filed. Inquiries concerning nonexclusive or exclusive license for its commercial development should be addressed to the Patent Counsel, Ames Research Center [see page A8]. Refer to ARC-11154.

Determining Resin/Fiber Content of Laminates

Hydrazine is used to extract graphite fibers from cured polyimide resin.

Langley Research Center, Hampton, Virginia

While developing graphite/polyimide laminates, a new method of digesting the cured resin was employed to free the fibers for weighing. This method does not attack the graphite fibers and is faster than the common hot-concentrated-acid digestion process.

A 0.3- to 0.4-g sample of the cured laminate is placed on a tall-form coarse-glass filter of known weight. The sample and filter are weighed together and placed in an electrolytic beaker taller than the filter. Extraction and filtration are carried out under a fume hood as follows: Hydrazine (absolute grade) is added to the beaker until the sample is covered by a 1- to 2-cm layer. A watchglass cover is put on the beaker to prevent excessive evaporation of hydrazine. The sample is left standing until the hydrazine penetrates the laminate, about 4 hours for an 8-ply laminate. After soaking, the hydrazine is heated to a very light boil for 5 to 10 minutes to separate the graphite fibers. The mixture is cooled to room temperature, and the filter holding the graphite fibers is removed, allowing the hydrazine and digested polyimide to drip into the beaker. The fibers on the filter are washed over a suction flask with absolute ethanol and rinsed with distilled water.

After drying in an oven, the filter with fibers is weighed and the fiber content determined. A batch of five samples can be processed using about an hour's labor.

This work was done by George G. Garrard and Donald W. Houston of Rockwell International Corp. for **Langley Research Center.** *No further documentation is available.*

Inquiries concerning rights for the commercial use of this invention should be addressed to the Patent Counsel, Langley Research Center [see page A8]. Refer to LAR-12442.

Synthesis of Triaryltrifluoroethanes

Synthesis via hydroxyalkylation condensation reaction yields compounds with high thermal stability.

Ames Research Center, Moffett Field, California

New triaryl-2,2,2-trifluoroethanes are prepared from α,α,α-trifluoroacetophenones by condensation with various substituted aromatic compounds. Some of these compounds can be prepared directly from the acetophenone by the condensation reaction, while others such as the tris-(acetamidophenyl)-trifluoroethane are derived from a condensation product [e.g., the tris-(aminophenyl) species] by conventional synthetic methods.

The aromatic rings within the new structures (see figure) promote a high degree of thermal stability suitable for the formulation of heat-resistant plastics and flame-resistant materials. The new compounds are obtained from a reaction that was either stopped at the carbinol stage or proceeded without control to the formation of polymers.

The new products are all crystals with relatively high-melting points. Examples include:

a. 1,1-Bis-(4-aminophenyl)-1-phenyl-2,2,2-trifluoroethane produced from a mixture of trifluoroacetophenone and aniline hydrochloride refluxed for 24 hours; the melting-point temperatures of the product crystals are 201° to 204° C.

b. 1,1-Bis-(4-acetamidophenyl)-1-phenyl-2,2,2-trifluoroethane using diamine stirred into hot acetic anhydride; white crystals of the substance have melting-point temperatures of 255° to 256° C.

c. 1,1,1-Tris-(4-acetamidophenyl)-2,2,2-trifluoroethane made using acetylated triamine to produce white crystals with melting-point temperatures of 343° to 345° C; and

d. 1,1,1-Tris-(4-cyanophenyl)-2,2,2-trifluoroethane prepared from 1,1,1-tris-(4-aminophenyl)-2,2,2-trifluoroethane diazotized and treated with cuprous cyanide at pH 7; the pale yellow crystal product has a melting-point temperature of 233° to 235° C.

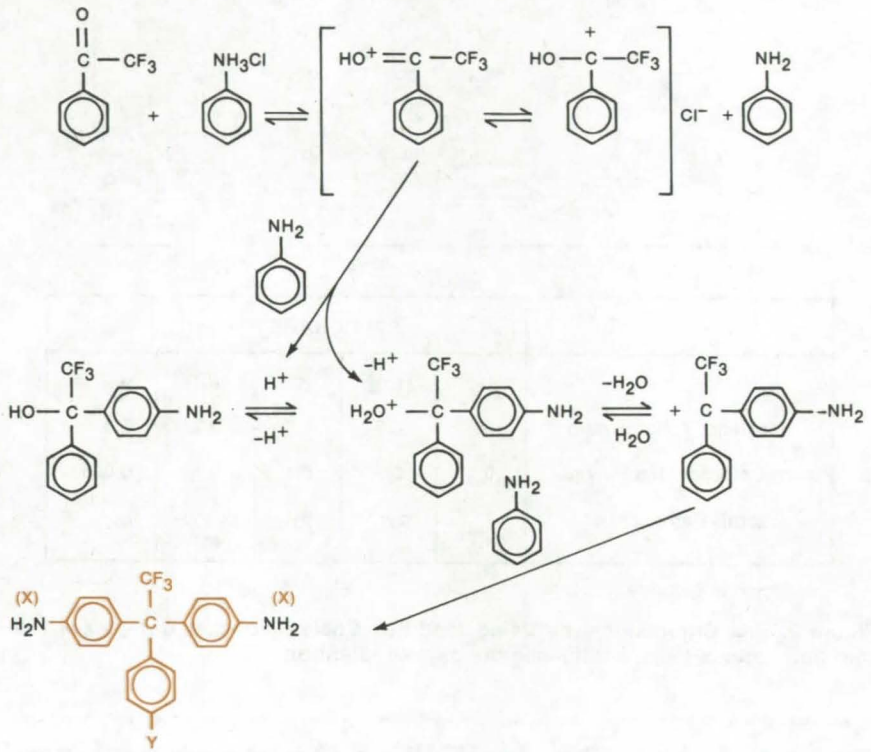

The structure of the **New Multifunctional 1,1,1-Triaryl-2,2,2-Trifluoroethanes** is shown in color. X is an amino, nitrile, or acetamino group and Y is a hydrogen or halogen atom, or a group selected from the class consisting of the amino, nitrile, acetamido, methyl, trifluoromethyl, and nitro groups. Triarylethanes are synthesized by a hydroxyalkylation condensation reaction in which a trifluoroacetophenone is refluxed with aniline and at least a catalytic quantity of aniline hydrochloride. Salts and other inorganic acid with aniline may also be used instead of the hydrochloride. The process reaction is believed to follow the mechanism involving the formation of strongly-electrophilic carbonium ions.

This work was done by Robert W. Rosser of **Ames Research Center** *and William D. Kray of Talladega College. For further information Circle 46 on the TSP Request Card.*

This invention is owned by NASA, and a patent application has been filed. Inquiries concerning nonexclusive or exclusive license for its commercial development should be addressed to the Patent Counsel, Ames Research Center [see page A8]. *Refer to ARC-11097.*

Flat-Flame Burner

Inorganic salt for study in gas flame is introduced into fuel-mixing chamber.

Lewis Research Center, Cleveland, Ohio

Laminar, one-dimensional, flames can be "doped" with salts for study by nebulizing salt solutions into the mixing chamber of a flat-flame burner.

In order to study the chemistry of additives to combustion environments, a means of introducing the additives into a suitable flame system is required. Flame structure studies very often employ a flame holder or burner that has the ability to support a positionally stable, one-dimensional flame. Such a flat-flame burner provides a premixed, laminar flame that can be studied or probed by various analytical techniques.

If the problem at hand is to study the behavior of inorganic salts in flames, the salts must be added to the premixed reactant gases used to produce the flat flame. In the device described herein, aqueous solutions of inorganic salts are first aspirated and then nebulized into the mixing chamber of a flat-flame burner.

The fuel and oxidant are introduced into the mixing chamber through the gas inlets of a commercially available nebulizer (see figure). The aqueous salt solutions are aspirated by the flow of these gases and then atomized into a fine mist that sprays into the chamber. Additional fuel, oxidant, or any other gas of interest can be introduced directly into the mixing chamber through tubes inserted in the chamber wall. The premixed combustible mixture flows through a pipe in which two flow straighteners are situated. These flow straighteners are honeycomb grids fabricated from Hastelloy-X with openings 0.08 cm on a side, which results in 135 openings per square centimeter. Upon ignition, the combustible mixture burns in a plane slightly above the top flow straightener. The flame is screened from the atmosphere by a circumferential laminar flow of nitrogen that passes through a flow straightener positioned around the water-cooled flow pipe.

[A mass-spectrometric sampling system that is used in conjunction with this burner is described in "High-Pressure Mass-Spectrometric Sampling System" (LEW-12913) on page 230 of this issue.]

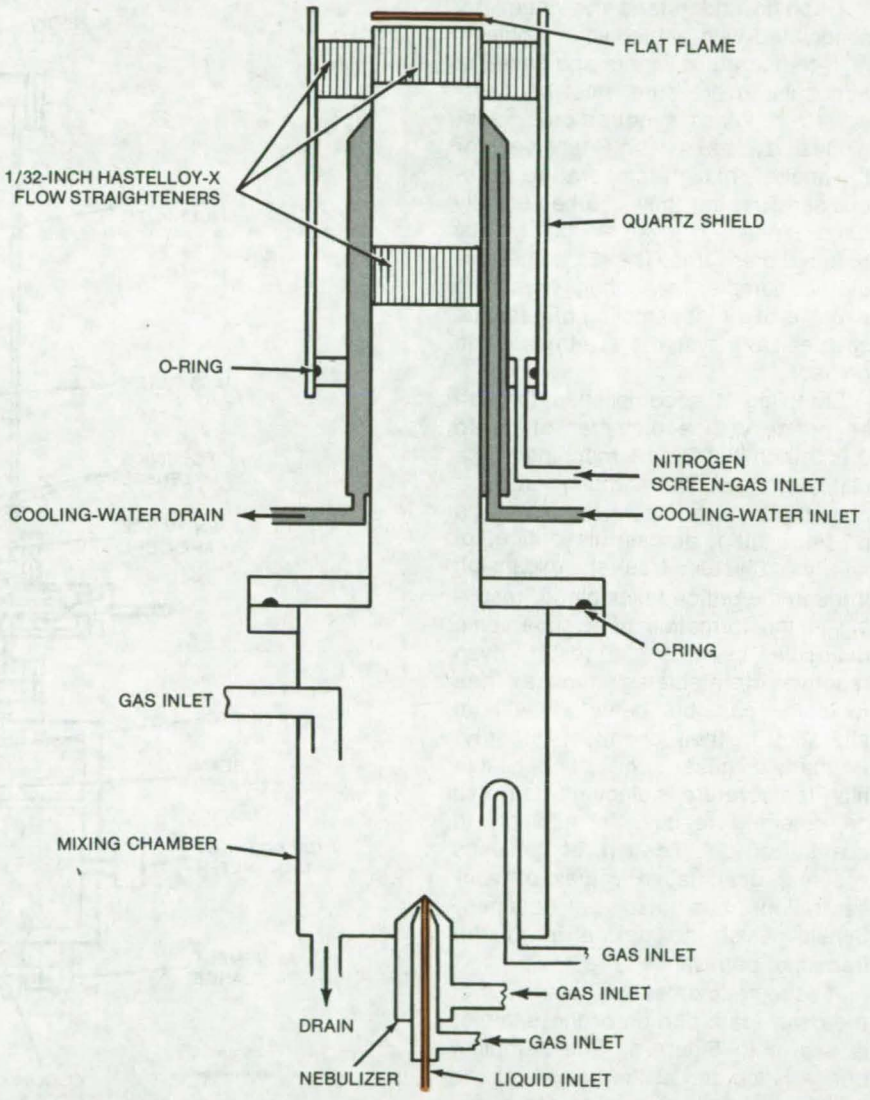

A **Flat Flame Is Doped** with an inorganic salt by allowing an aqueous solution of the salt to be aspirated through the liquid inlet into the fuel-mixing chamber of the burner assembly.

This work was done by George C. Fryburg, Fred J. Kohl, Robert A. Miller, and Carl A. Sterns of **Lewis Research Center.** *Further information may be found in:*

NASA TM-X-73600 [N77-19209], "Gaseous Sodium Sulfate Formation in Flames and Flowing Gas Environments," and

NASA TM-73794 [N78-13157], "Formation of Sodium Sulfate and Potassium Sulfate in Flames Doped with Sulfur and Alkali Chlorides and Carbonates."

Copies of these reports may be obtained at cost from the New England Research Application Center [see page A7].

LEW-13161

High-Pressure Mass-Spectrometric Sampling System

Reactive intermediates and condensable high-tempeature molecules are directly sampled from systems at atmospheric pressure and analyzed mass spectrometrically.

Lewis Research Center, Cleveland, Ohio

Often to understand the chemistry associated with a technical problem, high-temperature vapors and gases at atmospheric pressure must be characterized. Mass spectrometric techniques have been used extensively for the analysis of high-temperature gaseous species, but their use has usually been limited to systems at greatly reduced pressures. The mass spectrometric sampler described herein is capable of direct sampling of gaseous species from systems at atmospheric pressure.

Sampling is accomplished through an orifice with a diameter of up to 0.008 inch (0.02 cm) machined in a platinum cone. The sampler vacuum-pumping system is able to maintain a pressure ratio, across this orifice, of nearly 10^6. A free-jet expansion through the orifice takes place, resulting in the formation of a supersonic molecular beam. As a result, even reactive intermediates, such as free radicals, can be detected without alteration in their chemical integrity. Permanent gases and condensable high-temperature molecules can also be detected readily. In addition to qualitative identification of gaseous species, quantitative values of concentrations can also be obtained. Sensitivity of the device is in the fractional ppm range.

A schematic cross-sectional view of the beam-path portion of the sampler is shown in Figure 1. The sampling orifice is located at the bottom of the vertical configuration. For sampling-orifice Knudsen numbers less than 10^{-2}, the gas expands into Stage I as free jet. Stage I vacuum pumping maintains pressure ratios of nearly 10^6 across the sampling orifice. The conical skimmer intercepts the gas flow and passes the central portion or core of the flow into Stage II where it is periodically interrupted by a rotating toothed disk or "beam chopper." Pressure in Stage II is less than 10^{-5} torr. The chopped gas beam enters the Stage III differential-pumping vacuum chamber through a collimating aperture. Pressure in Stage III is less than 10^{-6} torr. The beam exits from Stage III through another aperture and passes into Stage IV and the ionizer of the quadrupole mass spectrometer. Pressure in Stage IV is less than 10^{-7} torr. Ions formed in the electron-bombardment ionizer are electrically focused and transmitted to the quadrupole mass filter. Selected ions transmitted by the filter are electrically deflected into the off-axis electron multiplier, which has an output that is electronically monitored. Thus a gas sample at high pressure is continuously transferred to the low-pressure mass spectrometer where the gas is analyzed on the basis of the mass-to-charge ratio of its constituents.

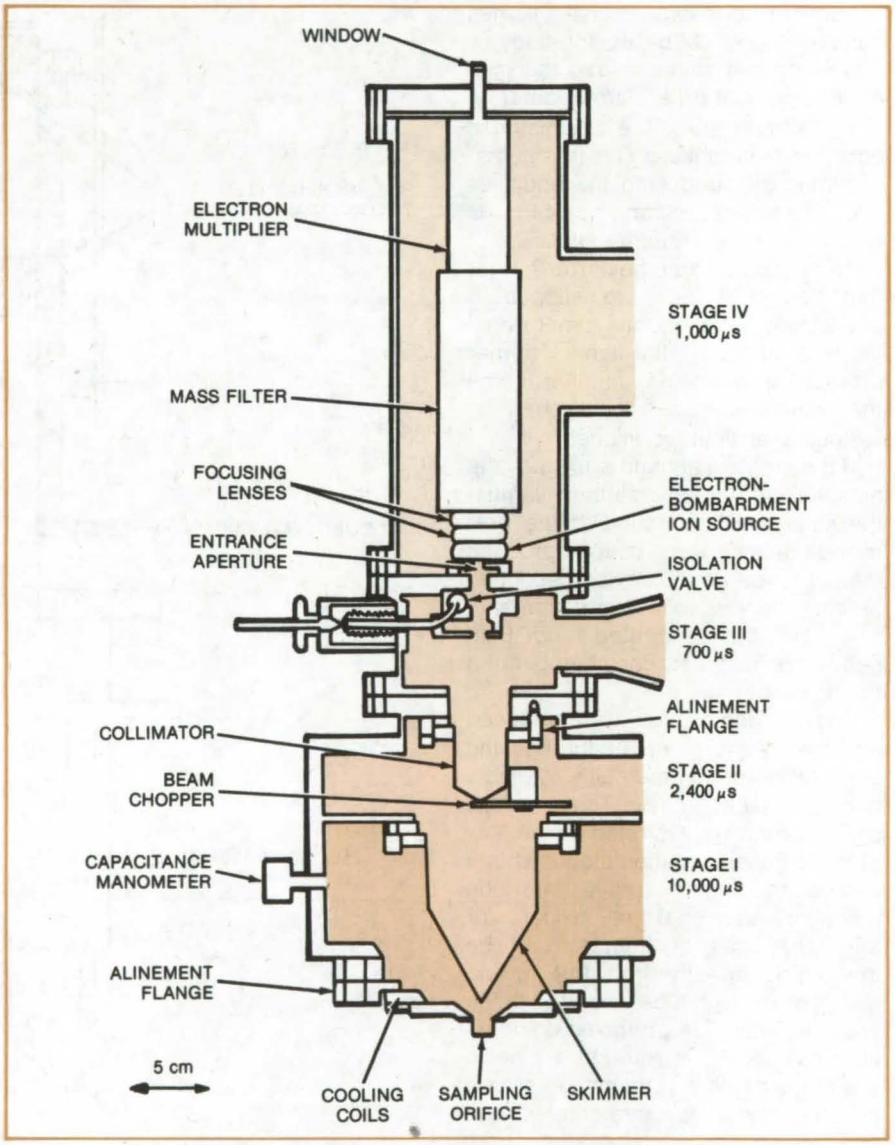

Figure 1. **High-Pressure Sampler** for a mass spectrometer accepts input gas samples at atmospheric pressure and reduces the mass and pressure of the sample so that a processed sample at 10^{-7} torr is fed to the mass spectrometer.

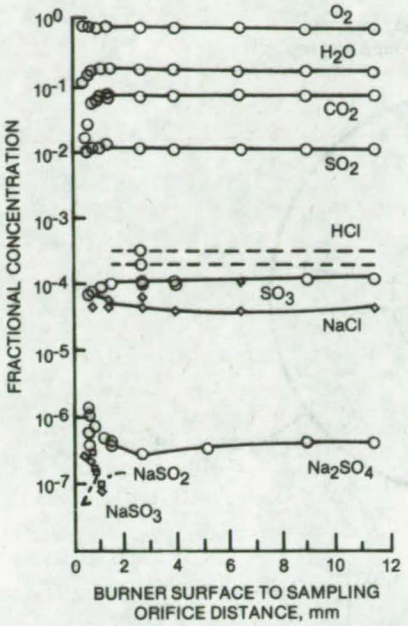

Figure 2. The **Composition Profile** shown above was taken by using the high-pressure gas sampler for a methane oxygen flame doped with NaCl and SO_2.

Maintaining the fidelity of the sample is a function of specific design parameters of the apparatus.

The system described herein has the ability to sample any gaseous system at atmospheric or lower pressure. This device is especially powerful for sampling high-temperature gaseous systems containing reactive, short-lived intermediates or condensable high-temperature molecules, neither of which can be detected by ordinary mass-spectrometric methods. It has been used to obtain concentration profiles of gaseous species occurring in combustion systems and to identify high-temperature molecules in flowing-gas systems. One example of species identification and concentration determination is given in Figure 2. Representative areas where this technique might be used include the characterization of combustion systems, MHD systems, corrosive gas systems, glass industry processes, metallurgical processing, and vapor transport systems.

[A flat-flame burner that is used in conjunction with this System is described in "Flat-Flame Burner" (LEW-13161) on page 229 of this issue.]

This work was done by George C. Fryburg, Fred J. Kohl, Robert A. Miller, and Carl A. Stearns of **Lewis Research Center.** *Further information may be found in NASA TM-73720 [N77-32242], "A High Pressure Modulated Molecular Beam Mass Spectrometric Sampling System," a copy of which may be obtained at cost from the New England Research Application Center [see page A7].*
LEW-12913

Analysis of Fatigue Damage in Composites

Sites of potential failure are located by a finite-element analysis of temperatures obtained from an infrared thermogram.

Langley Research Center, Hampton, Virginia

A finite-element heat-transfer analysis determines the sites of potential failure in composite materials. Boundary conditions for the analysis are temperatures measured with an infrared camera during cyclic fatigue tests. The method, which has been tested with success on several boron/epoxy composites, is sensitive to matrix damage and fiber disbonding that occur long before actual fiber breakage.

A correlation between the zones of maximum temperature rise during cyclic fatigue tests and sites that will eventually fail has been found by several researchers. The new analysis obtains the geometry of these heat-generating zones from an infrared thermogram (see Figure 1).

In the finite-element analysis, the sample area is divided into subregions, or elements. The elements are four-node isoparametric quadrilaterals, for which the inside tempera-

(continued on next page)

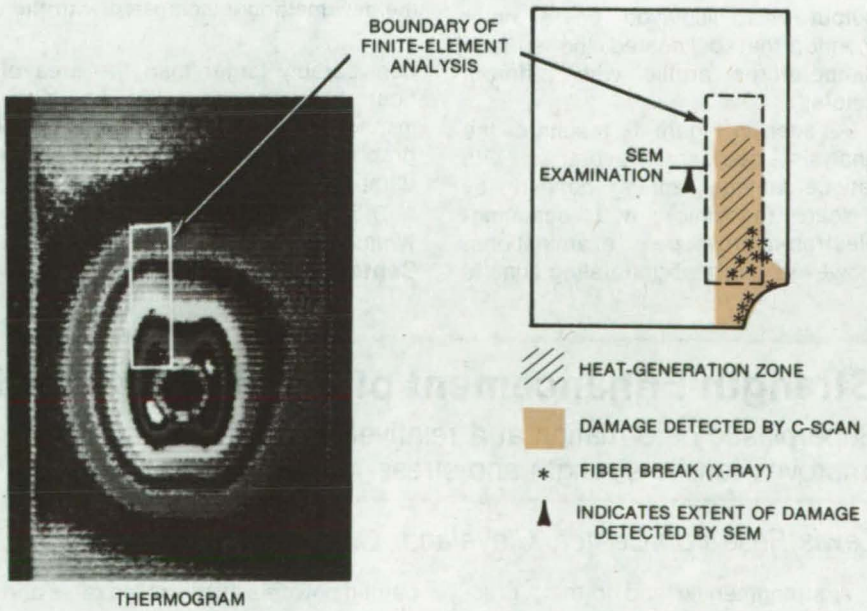

Figure 1. **Areas of Fatigue Damage Are Located** by thermographic analysis and are compared with damaged zones revealed by acoustic C-scan, scanning-electron microscopy, and X-ray inspection. The boundary of the finite-element analysis is shown as a dotted outline. Specimen is a $(45/0/-45/0)_S$ boron/epoxy composite.

ture map is approximated by a linear function of the nodal temperatures. Using temperatures from the thermogram as boundary conditions, a computer program solves a set of linear simultaneous equations for the geometry of the heat sources.

Results obtained by using the finite-element approach compare favorably with a direct analytical solution of the heat-transfer problem. The two methods are compared by solving the problem of a 1-mm-thick circular plate with a hole in the center (Figure 2). The plate is assumed to be heated internally with an intensity that varies inversely as the square of the radius in an annulus around the hole. The intensity is zero elsewhere. Heat transfers by convection and radiation are assumed to be zero.

Figure 2 (left) shows the temperature distribution (obtained from an analytic solution). Figure 2 (right) shows the heat-generation profiles obtained from the exact and the finite-element methods. The approximate solution agrees very well with the $1/r^2$ exact solution.

Three types of boron/epoxy composites were tested: the (0_8), $(45/0/-45/0)_S$, and $(45/90/-45/0)_S$ specimens. These were tension-tension fatigue-tested, with loading in the 0° direction. The specimens, which exhibited different modes of fatigue damage, were monitored with an infrared camera, and the camera output was displayed on a color monitor that delineated the surface temperatures profile with different colors.

As seen in Figure 1, results of the analysis compare favorably with fatigue-damage zones defined by C-scan (acoustic) and scanning-electron-microscope examinations. However, the heat-generating zone is considerably larger than the area of fiber breakage revealed by X-ray inspection, indicating that the thermographic analysis is sensitive to fatigue damage that precedes fiber breakage.

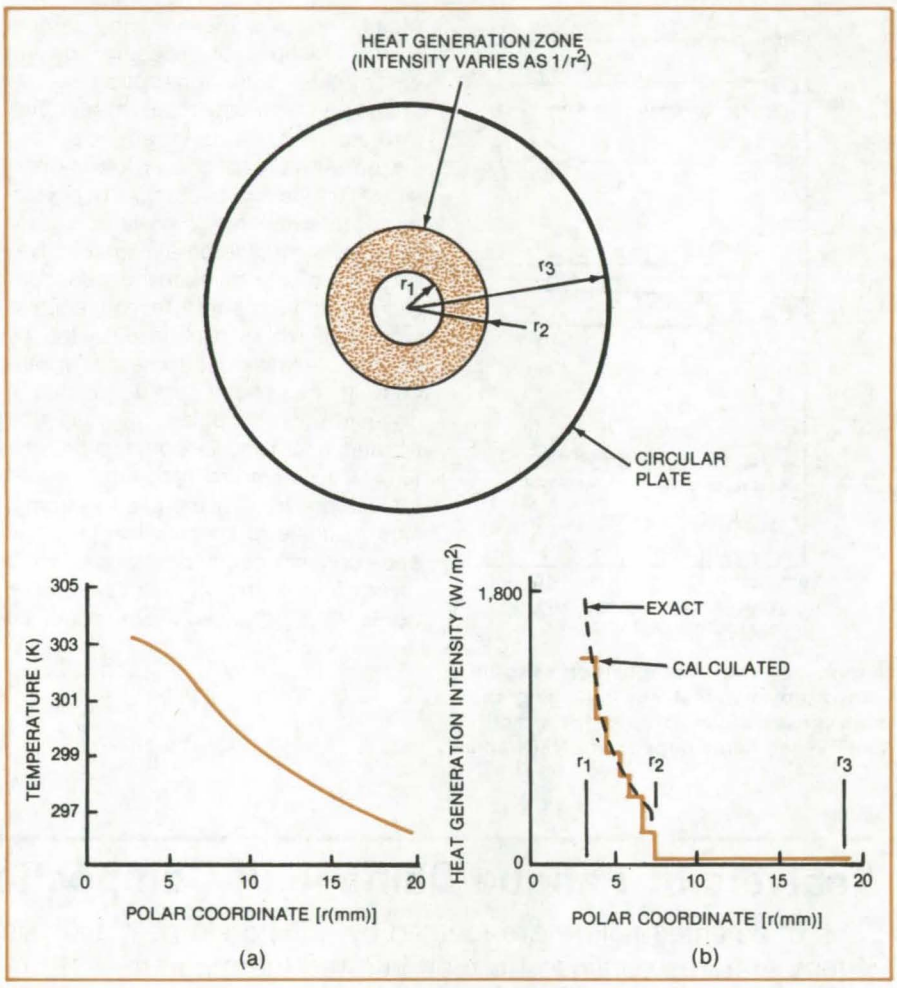

Figure 2. **Finite-Element and Analytic Solutions Are Compared** for a circular plate with a hole in the center. The temperature profile (left) is for a heat source that varies as $1/r^2$ in the shaded region around the hole. The heat-source profile calculated by the new method is compared with the exact solution, in the graph at the right.

This work was done by John D. Whitcomb of **Langley Research Center.** *Further information may be found in NASA TM-78693 [N78-23457], "Thermographic Measurement of Fatigue Damage," a copy of which may be obtained at cost from the North Carolina Science & Technology Research Center [see page A7].*

LAR-12431

Strength Enhancement of Prealloyed Powder Superalloys

Superplastic deformation at a relatively-low unit loading improves tensile strength and stress-rupture life.

Lewis Research Center, Cleveland, Ohio

A strengthening and forming process for prealloyed powder superalloys can greatly increase material strength in the 900°-to-1,200° F (480° to 650° C) temperature range. This process involves superplastically deforming compacted powders at controlled rates and temperatures. It has been demonstrated with a typical high-temperature nickel-base alloy that is otherwise usually cast.

There is an increasing demand for materials with high strength and good ductility in the 900°-to-1,200° F temperature range. A large number of products used in the industrial commu-

nity employ highly stressed components that operate in this temperature range. Typical applications include rotating machinery requiring a combination of high strength and high ductility.

Materials currently being used for highly stressed rotors are either conventionally-forged wrought superalloys isostatically-pressed and forged prealloyed powder alloys. Tensile strength levels of these products now are limited to less than 250,000 psi (1725×10^6 N/m^2) in the 900°-to-1,200° F range. Their stress rupture lives at 1,200° F and 150,000 psi (1035×10^6 N/m^2) stress are limited to approximately 100 hours. Since these materials require the use of massive forging equipment to achieve near-final product shape, their processing and fabricating costs are high.

A significant advance has been made in enhancing material strength and in simplifying the forming procedures for prealloyed powder alloy parts. The procedure can utilize prealloyed powders of strong, normally cast, nickel-base alloys, such as the NASA-TRW VI-A alloy. In this new process, these powders are extruded and then superplastically deformed at a controll rate at 2,000° F (1095° C). This deformation rate is much less than usual forging rates. An ultimate tensile strength of 415,000 psi (2865×10^6 N/m^2) and an elongation greater than 7 percent were obtained at 900° F. Stress-rupture life at 1,200° F and 150,000 psi exceeded 3,000 hours, more than an order of magnitude greater than that of the most advanced disk alloys. Deformation of this strong, normally cast, nickel-base alloy was achieved with a low unit loading of less than 10,000 psi (69×10^6 N/m^2). This suggests that reduced fabrication costs could be expected, sine the massive forging facilities required for present-day manufacture of components such as turbine disks would not be needed with this approach.

This work was done by J. C. Freche and W. J. Waters of **Lewis Research Center.** *Further information may be found in NASA TM-78834 (N78-21266), "Strength Enhancement Process for Prealloyed Powder Superalloys," a copy of which may be obtained at cost from the New England Research Application Center (see page A7).*

Inquiries concerning rights for the commercial use of this invention should be addressed to the Patent Counsel, Lewis Research Center (see page A8). Refer to LEW-13173.

Improved Ion-Selective Membranes

Membranes for electrochemical systems improve selectivity by three orders of magnitude.

Lewis Research Center, Cleveland, Ohio

Significantly-improved ion-selective membranes have been developed in the evolution of the REDOX (reduction-oxidation) electrochemical bulk energy storage concept (see "REDOX - Electrochemical Energy Storage," *NASA Tech Briefs*, Vol. 1, No. 1, page 78, LEW-12220). These new membranes have exceptional selectivity, giving three orders of magnitude improvement over commercially available membranes in this application; they may also be applicable in other separation processes where highly-selective anion membranes are needed.

Development of improved, ion-selective membranes for use as separators is a major prerequisite to establishing practicality of the REDOX system. Extended useful life for the REDOX system depends on the ability of the membrane to limit cross-diffusion of the reactant species without seriously limiting the reactant capabilities of the system.

Significant improvements in membrane performance in the REDOX environment have been achieved by developing membranes with very high ion-exchange capacity and a high degree of the cross-linking necessary to stabilize the membrane in aqueous acidic solutions.

Conventional ion-exchange membranes normally are chemically prepared by the copolymerization of a bifunctional cross-linking monomer, a unifunctional monomer, and a diluent. After this composite polymer is prepared, it is further reacted with other chemical reagents to effect the introduction of ionic sites into the molecule.

A much easier method of fabrication is used with the improved ion-selective membranes. Preparation involves simultaneous polymerization of unifunctional monomers containing reactable groups that form ionic cross-linking sites during polymerization. This one-step synthesis of ion-exchange membranes yields materials with high ion-exchange capacities and low ionic resistivities.

Experimental membranes with selective permeability for anions were tested in the REDOX environment. The most selective membranes were shown to have good chemical stability. Cycle lives for REDOX cells incorporating these membranes have been extrapolated to several thousand hours based on results of short-term, cell cycling tests.

Membrane conductivity has also shown some improvement but not to the dramatic extent that selectivity has improved. Techniques are being investigated for increasing membrane conductivity while still maintaining the exceptional selectivity achieved with these new membranes.

This work was done by Samuel S. Alexander of Ionics, Inc., for **Lewis Research Center.** *Further information may be found in: NASA CR-134931 (N76-18670), "Anion Selective Membrane"; NASA CR-135316 (N78-18515), "Anion Permaselective Membrane"; NASA TM-73751 (N78-14631), "Anion Exchange Membranes for Electrochemical Oxidation-Reduction Energy Storage System," August 1977; and NASA TM-73873 (N78-19656), "REDOX Flow Cell Development and Demonstration Project - Calendar Year 1976," December 1977. Copies of these reports may be obtained at cost from the New England Research Application Center (see page A7).*

LEW-12678

Improved Inverted Stepanov Apparatus

Modifications improve heat transfer and energy efficiency in growing silicon ribbon crystals.

NASA's Jet Propulsion Laboratory, Pasadena, California

Recently tested improvements in the inverted Stepanov process could make it more attractive for growing inexpensive silicon ribbon crystals, suitable for solar cells and other semiconductor devices.

In one form of the Stepanov process (see figure), silicon is melted and pulled through a narrow slot at the bottom of a V-shaped die. Heat is supplied by an induction heater. To minimize contaminating interactions, the die is preferably a material (such as quartz) that is not "wetted" by the silicon; however, since quartz tends to soften at the temperatures of molten silicon (near 1,400° C) the die is supported by an outer jacket of tungsten or molybdenum. Called a "susceptor," the outer jacket gives the needed extra strength at high temperatures.

Experiments show that most of the energy from the induction heater is transferred to the walls of the susceptor. Thus, rather than being heated directly, the silicon is melted indirectly by heat that conducts from the susceptor walls through the die. Besides wasting energy, this arrangement sets up thermal gradients and high temperatures that make it difficult to inhibit contaminating reactions. The gradients also make it hard to monitor and control the process.

An improved system uses a split susceptor made of two symmetric parts that are joined by an electrical insulator. The susceptor wall thickness is less than 2 radio-frequency skin depths. In this design, the silicon is directly heated by induction, minimizing many of the heat-transfer and contamination problems. Tests show that, rather than being at a higher temperature, the susceptor is actually 50° to 200° C cooler than the silicon melt. This not only improves the process and makes it easier to control contamination but it also saves energy. Moreover, the modifications are made without major redesign of the basic system.

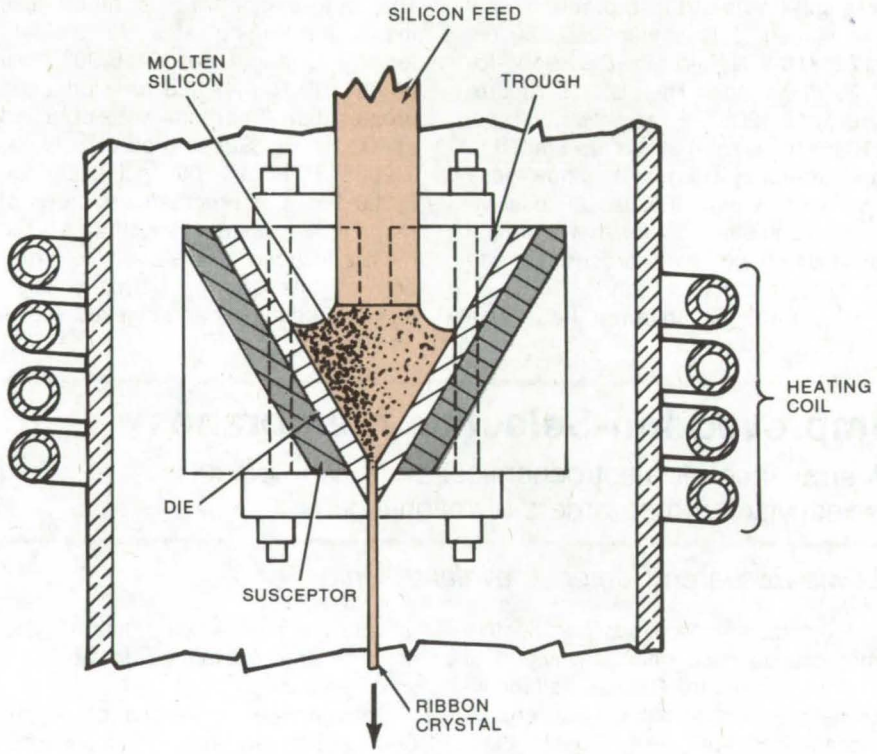

An **Inverted Stepanov Apparatus** for drawing silicon ribbon crystal is improved by using a split susceptor with wall thickness less than 2 radio-frequency skin depths. Heat transfer is by induction heating in the silicon, rather than by conduction from the susceptor walls.

This work was done by Samuel Berkman and Harold E. Temple of RCA Corp. for **NASA's Jet Propulsion Laboratory.** *For further information, Circle 47 on the TSP Request Card.*

This invention is owned by NASA, and a patent application has been filed. Inquiries concerning nonexclusive or exclusive license for its commercial development should be addressed to the Patent Counsel, NASA Resident Legal Office-JPL [see page A8]. Refer to NPO-14297.

Fibrous Refractory Composite Insulation

An insulating material with improved mechanical and thermal properties

Ames Research Center, Moffett Field, California

A new family of high-temperature, low-density refractory composite insulations is made from aluminoborosilicate and silica fibers in a weight ratio ranging between 1:19 to 19:1. This ratio determines the properties of the resultant composite insulation. For example, the temperature capability of the insulation can be increased by increasing the ratio of aluminoborosilicate fiber to silica fiber, but at the expense of a higher thermal conductivity and thermal expansion coefficient. The reverse is also true. Improved resistance to silica fiber devitrification if required can be obtained by adding 0.5 to 30 percent of the total fiber weight boron oxide. Fibrous refractory composite insulation has a strain to failure that is greater than 0.5 percent because it does not contain any nonfibrous binder, which would inherently limit its strain to failure. Other properties include a modulus of rupture of above 6.4×10^6 N/m^2 at 0.32 g/cm^3 density and a temperature capability of 1,540° C or higher in transient applications.

The insulation is prepared using high-purity silica fibers that are first washed and dispersed in a hydrochloric acid solution and/or deionized water. About 30 to 150 parts liquid (pH 3 if acid is used) are used for 1 part fiber. The fibers are washed for 2 to 4 hours to remove the surface chemical contamination and nonfibrous material. After washing, the fibers are rinsed three times for 10 to 15 minutes with deionized water using the same liquid-to-fiber ratio. Excess water is drained off, leaving a ratio of 5 to 10 parts of water to 1 part fiber.

The aluminoborosilicate fibers are prepared by dispersing them in deionized water. About 10 to 40 parts of water are mixed with 1 part fiber in a V-blender for 2-1/2 to 5 minutes. In general, as the diameter and length of aluminoborosilicate fibers are increased, sufficient dispersion is obtained with more mixing time.

The dispersed silica and aluminoborosilicate fibers are then combined, and the pH is adjusted to basic with ammonium hydroxide. The slurry, containing 12 to 25 parts water to 1 part fiber, is mixed to a uniform consistency in a V-blender for 5 to 20 minutes.

The mixed slurry is poured into a mold for pressing into the desired shape (tiles in this case). The water is withdrawn rapidly, and the resulting felt is compressed at 10 to 20 psi (6.9×10^4 to 13.8×10^4 N/m^2). Rapid removal of the water prevents the two fibers from separating. The final density of the finished tile is determined in part by the amount of compression placed on the felt, varying the wet molded dimension in relation to the fiber content. Typical densities used have ranged from about 0.08 to 0.48 g/cm^3; however, higher densities can be prepared.

Following molding, the insulation tile is oven-dried for 18 hours and fired. The initial drying temperature of 38° C is raised at 11° C per hour to 104° C and is held there for 4 hours. From that level, the temperature is raised again at 11° C per hour to 150° C and is held there for 4 hours.

The dried tile is taken directly from the oven and placed into the firing furnace. There it is fired at a temperature rise rate of 220° C per hour (or less) to prevent warping or cracking the tile. The maximum firing temperature may vary from 1,260° to 1,360° C, depending on the fiber ratio used and the final density of the insualtion tile desired. After the firing, the tiles are machined to final dimensions.

The process has been studied using various proportions of the described constituents and process chemicals and temperatures. A very-thermally-shock-resistant, low-density insulation has been obtained with a ratio of about 4:1 silica fibers to aluminoborosilicate fibers, the latter containing about 14 percent of boron oxide. This composition has been found appropriate for use as a reusable heat-shield material.

This work was done by Howard E. Goldstein and Marnell Smith of **Ames Research Center** *and Daniel B. Leiser of Stanford University. For further information, Circle 48 on the TSP Request Card.*

This invention is owned by NASA, and a patent application has been filed. Inquiries concerning nonexclusive or exclusive license for its commercial development should be addressed to the Patent Counsel, Ames Research Center [see page A8]. *Refer to ARC-11169.*

Books and Reports

These reports, studies, and handbooks are available from NASA as Technical Support Packages (TSP's) when a Request Card number is cited; otherwise they are available from one of NASA's Industrial Application Centers or the National Technical Information Service.

Fatigue Properties of Columbium Alloy

Room-temperature fatigue data from axial fatigue and rotating-beam fatigue tests

A report presents data from a series of tests undertaken to determine the room-temperature fatigue properties of C-103 columbium alloy and its combination with Ti-6Al-4V weldments. The following material combinations are covered:

a. uncoated C-103 alloy,
b. electron-beam-welded C-103 alloy,

(continued on next page)

c. fused-silica-coated C-103 alloy, and
d. C-103 alloy electron-beam welded to Ti-6Al-4V.

The test results are tabulated and in some cases plotted, using S-N (maximum stress/fatigue life) diagrams.

Samples for the study were made from blanks 1/2 in. (1.3 cm) wide by 2-5/8 in. (6.7 cm) long cut from 1/2-in. (1.3-cm) by 12-in. (30.1-cm) unwelded and electron-beam-welded plates, the plate-rolling direction being parallel to the specimen axis. Other samples were made from bar blanks 3/8 in. (0.38 cm) square by 3 in. (8 cm) long, the axis of these specimens being normal to the rolling direction of the raw bar stock. All of the specimens were single-point turned on a lathe for a final configuration having a reduced diameter of 0.2 in. (0.5 cm) at midlength.

The electron-beam-welded specimens were C-103 alloy plates joined through square-butt joints rough-machined to 0.3 in. (0.8 cm) thickness. Both the C-103 to C-103 and C-103 to Ti-6Al-4V plates were welded on a single pass.

The axial fatigue data were obtained from tension-tension tests carried out at stress ratios of $R = +0.1$ and $R = +0.5$ and at a frequency of 141 Hz, using both fused-silicide-coated and uncoated samples. The endurance limit was arbitarily defined as 1×10^7 cycles, and an individual test was terminated when it reached this number. The rotating-beam fatigue tests were conducted at a frequency of 83 Hz.

Results from axial tension-tension tests indicated uncoated endurance limits at both R ratios of +0.1 and +0.5 were above the static tensile yield strength of the material at approximately 5/6 [50 ksi (345×10^6 N/m^2)] ultimate tensile strength. The fused-silicide coating reduced the material endurance limit to about 1/3 [18 ksi (124.2×10^6 N/m^2)] of the ultimate test strength at $R = +0.1$ and to about 1/2 [34 ksi (234.6×10^6 N/m^2)] of the ultimate test strength at $R = +0.5$.

Further results show that axial tension-tension S-N fatigue diagrams for uncoated C-103 + C-103 electron-beam-welded alloy have similarly high endurance limits as the unwelded samples. The uncoated C-103 + Ti-6Al-4V weldment has an endurance limit of about 2/3 [43 ksi (296.7×10^6 N/m^2)] ultimate tensile strength at $R = +0.1$.

The rotating-beam fatigue tests generated tension-compression ($R = -1$) data. Analysis of these bending fatigue data reveals an endurance limit of uncoated C-103 greater than 34 ksi (234.6×10^6 N/m^2) and greater than 24 ksi (165.6×10^6 N/m^2) for the coated samples.

This work was done by R. A. Crosby and F. K. Lampson of The Marquardt Co. for **Johnson Space Center.** *To obtain a copy of the report, Circle 49 on the TSP Request Card.*
MSC-18256

Use of Composites in Electric Vehicles

Materials are evaluated for weight reduction, performance, and costs.

A new report presents a study of possible weight savings in electric vehicles by using alternative structural materials, particularly composites. Component and total weights were established for a "baseline" vehicle, and weight savings were calculated for new lightweight materials in place of existing materials in the baseline. The selection process takes safety, aerodynamics, esthetics, and cost into account.

Following introductory chapter 1, a comparison of candidate materials is presented in chapter 2, including a table of 18 materials tested for density, strength, flammability, repairability, durability, and cost. The effectiveness of graphite/epoxy composites is explored in chapters 3 and 4, with a list of weight savings in every major vehicle part. Manufacturing cost impact (chapter 5) and the effect of weight reductions on performance (chapter 6) are also assessed.

The impact of weight reductions on national energy and cost savings is considered in chapter 7. Finally, a concept car was designed, accompanied by recommendations for improvements. A detailed bibliography is also included. The appendixes list the calculations of physical parameters evaluated in the investigation along with drawings of the "concept car."

This work was done by Russell H. Dawe, Dean B. Edwards, and Harvey A. Frank of Caltech for **NASA's Jet Propulsion Laboratory.** *To obtain a copy of the report, Circle 50 on the TSP Request Card.*
NPO-14615

Life Sciences

Hardware, Techniques, and Processes

Books and Reports

Improved Temperature-Control Garment

Silver mesh around polyurethane tubing transfers heat effectively between the thermal fluid and the skin.

Ames Research Center, Moffett Field, California

A new multilayer "fabric" is used in the fabrication of improved liquid-cooled garments. The garment material contains polyurethane tubing (which carries the cooling fluid) sandwiched between layers of silver mesh and polyurethane film (Figure 1). Prototype cooling helmets have been assembled from the material, and other garments (including those for heating) are being developed.

The silver mesh improves heat transfer between the body and the thermal fluid in the tubing, and it increases the effective cooling area; yet it keeps the fabric flexible enough to conform to body surfaces. In contrast, other fabrics for temperature control are made from low-conductivity materials, and most heat is transferred through a small heat-transfer area. Since it is necessary to use a very cold fluid to compensate for the small transfer surface, these fabrics must contend with vascular constriction (the physiological response to low temperatures), which inhibits effective cooling. Since the mesh in the new fabric allows a more moderate coolant temperature, vascular constriction is substantially reduced.

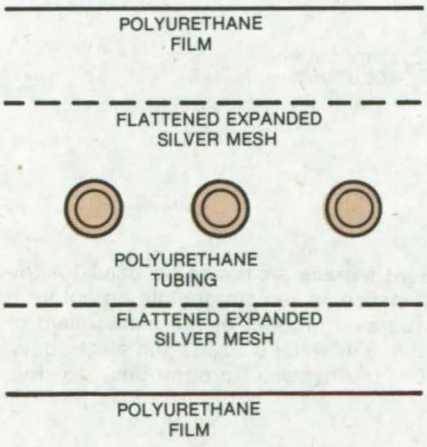

Figure 1. **Fabric for Body Cooling or Heating** consists of polyurethane tubing surrounded by silver mesh and polyurethane film. The inside diameter of the tubing is 0.062 inch (0.16 cm), and the polyurethane film thickness is 1.5 mils (0.038 mm).

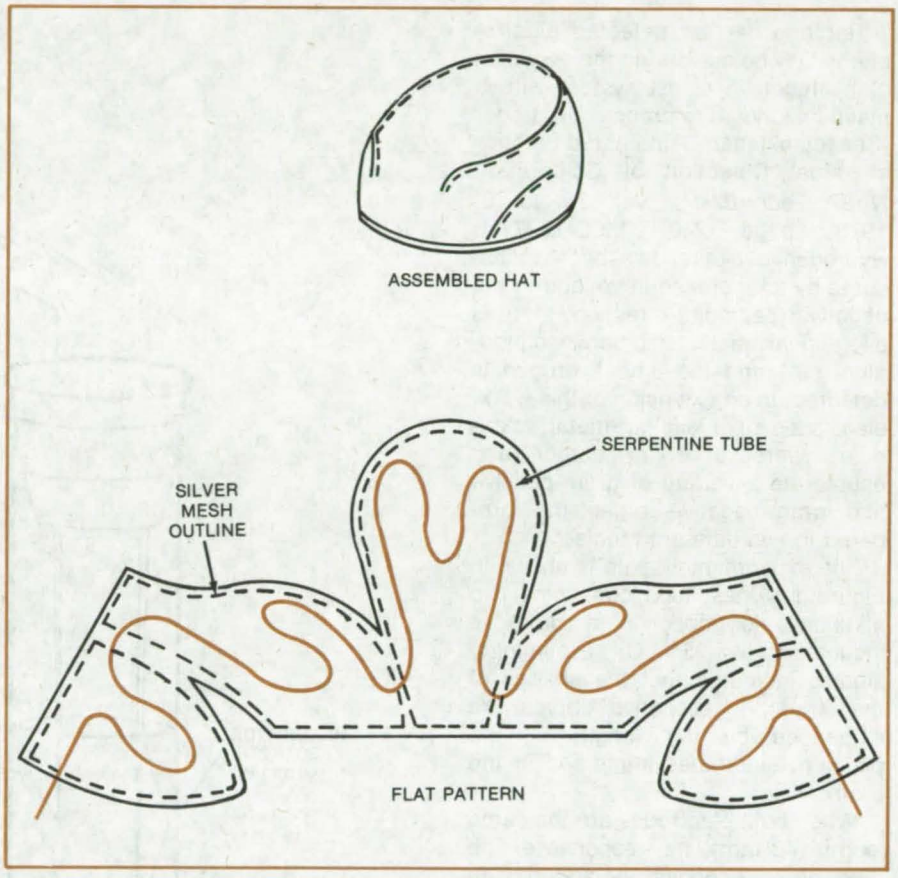

Figure 2. A **Cooling Hat** is first cut out as a flat pattern; then it is stitched together.

Garments can be cut from a flat pattern and stitched together, as shown in Figure 2. Since the fabric is flexible and elastic, it stretches to accommodate body movements and maintain contact with the skin (which also improves the heat-transfer efficiency).

The effectiveness of the fabric depends on the spacing between tubes, since the fluid is brought into contact with a larger skin area when more tubing is included. Also, as the inlet temperature of the fluid is increased, the temperature difference between the fluid and the skin decreases, and the transfer efficiency is reduced. Increasing the fluid flow rate keeps it from heating up as much; this increases the fluid-to-skin temperature difference and improves heat transfer.

This work was done by R. L. Cox and C. W. Hixon of Vought Corp. for **Ames Research Center.** *For further information, Circle 51 on the TSP Request Card.*

Inquiries concerning rights for the commercial use of this invention should be addressed to the Patent Counsel, Ames Research Center [see page A8]. Refer to ARC-11239.

Platinum Electrodes for Electrochemical Detection of Bacteria

Similar-metal electrodes prove better than platinum and reference electrode combination.

Langley Research Center, Hampton, Virginia

Bacteria can be detected electrochemically be measuring the evolution of hydrogen in a test system with a platinum and a reference electrode. [See for instance "Automated Electrochemical Detection of Coliforms," *NASA Tech Briefs*, Vol. 3, No. 2, 1978, page 243 (MSC-16777)]. Hydrogen evolution has been measured by an increase in voltage in the negative (cathodic) direction; there is a log-linear relationship between inoculum size and the time hydrogen is detected. In an extension of this work, electrodes of a similar metal, platinum, were used to detect and enumerate a variety of gram-positive and gram-negative organisms prepared in two different media.

The experimental setup is shown in Figure 1. A test tube containing two platinum electrodes in a broth is incubated at 35° C. Preliminary studies indicated that the shapes of the strip-chart response curves are influenced by the length of the platinum electrodes immersed in the broth.

When both electrodes are the same length (40 mm), the response at the time of an endpoint is jagged with oscillations in both the positive and negative directions. By decreasing the length of one electrode to 10 mm, more consistent response curves were obtained. The fact that the surface area ratios of the two electrodes must be different to obtain consistent responses suggests that a differential in potential was being established between the electrodes. Therefore, the 10-mm electrode could be considered the measuring electrode and the 40-mm electrode the reference electrode.

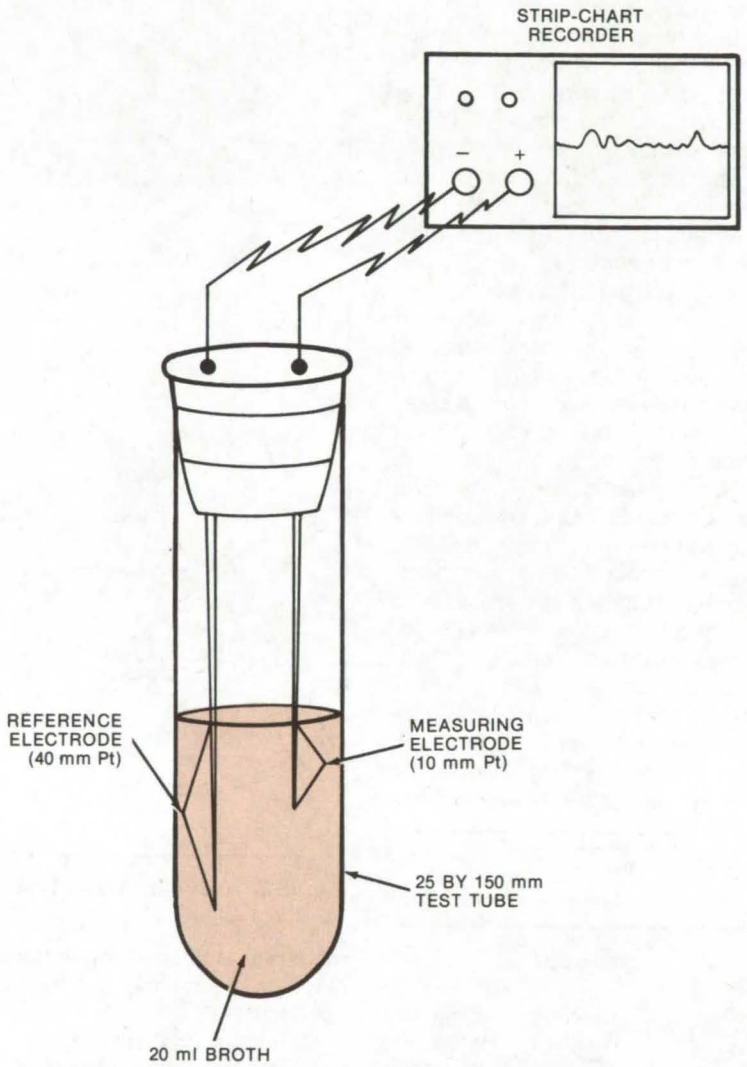

Figure 1. **Similar-Metal Electrodes** of different surface areas can be used for the electrochemical detection of bacteria. For instance, a sample containing coliform bacteria is incubated until hydrogen is evolved as a product of the metabolism of lactose. The evolved hydrogen causes a rapid rise in voltage across the electrodes. The time required for hydrogen evolution is inversely proportional to the concentration of coliforms.

When inoculum size was plotted against detection time, the relationships were linear for the organisms tested. Generally, the gram-negative species had similar dose-response curves with detection times ranging from 2 hours for 10^6 cells/ml to 9 hours for 10° cell/ml (see Figure 2). Detection time endpoints for the gram-positive organisms were considerably longer, ranging generally from 14 to 24 hours for 10° cell/ml. No differences were noted between the two media used with regard to endpoints, shape of the responsive curve, slopes, correlation coefficients, and standard error of the estimate.

A comparison of platinum electrodes with the platinum and reference electrode combination reveals that, for both test systems, the hydrogen-

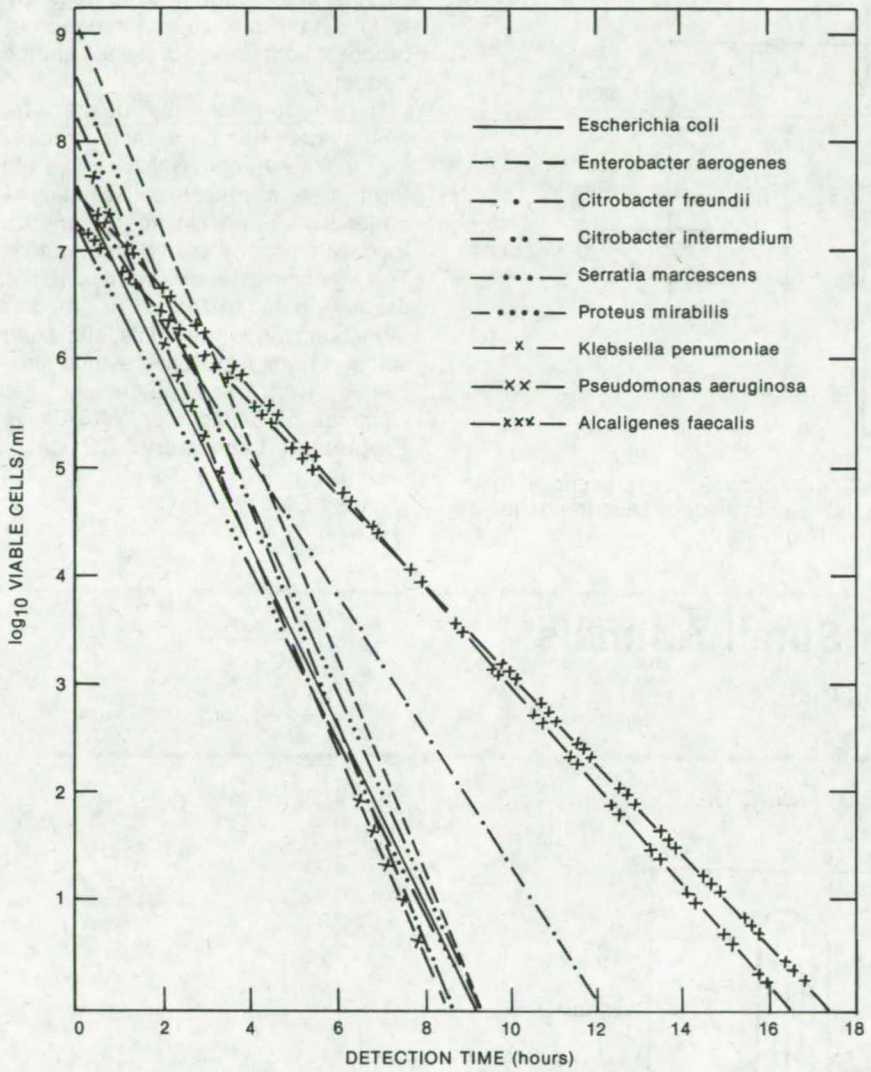

Figure 2. **Dose-Response Curves** for gram-negative organisms

producing bacteria have similar response patterns — a lag period followed by a sharp increase in voltage and then a decline period. The magnitudes of the responses are greater with the combination electrodes: 0.4 to 0.5 volt versus 0.1 to 0.2 volt for the platinum electrodes. Detection time endpoints with platinum electrodes are 2 hours longer than with the combination electrodes.

Limited studies indicate that palladium could also be used to detect bacteria and that noble metals in general are suitable electrode material. On a comparative basis, platinum electrodes cost considerably less than combination or redox electrodes, and they are easier to handle, maintain, and sterilize. Detection time endpoints with platinum electrodes are easier to read than the gradual responses observed with the combination electrodes.

This work was done by Judd R. Wilkins of **Langley Research Center.** *For further information, Circle 52 on the TSP Request Card.*

This invention has been patented jointly by NASA and the University of Virginia [U.S. Patent No. 4,009,078]. Inquiries concerning nonexclusive or exclusive license for its commercial development [NASA's share] should be addressed to the Patent Counsel, Langley Research Center [see page A8]. Refer to LAR-12462.

Wideband Electronics for Ultrasonic Tissue Characterization

A rapid and inexpensive technique could characterize tissue in vivo.

NASA's Jet Propulsion Laboratory, Pasadena, California

Research on the frequency dependence of ultrasonic properties of tissue and of materials is often done by using sweep generators or spectrum analyzers. Much of the expense and complications of these instruments is eliminated by a system that utilizes the natural ringing frequency of an electronic circuit coupled to a wideband transducer.

Operation of a typical system is shown in the figure. A pulser generates a short burst of energy that induces damped oscillations in a tank circuit. The computer selects the ringing frequency, typically 1 to 10 MHz, by switching the appropriate component values into the circuit. The electrical oscillations are applied to a wideband ultrasonic transducer coupled to part of the body or to a material sample through a water bath or other coupling medium.

A portion of the ultrasonic energy is received by an ultrasonic transducer. (Typically, another transducer would be used for transmission measurements, whereas the same transducer is used for reflection mode measurements.) The received signal is processed; and a representative value, such as the peak reading or the mean squared value, is sampled by the computer system. The computer then

(continued on next page)

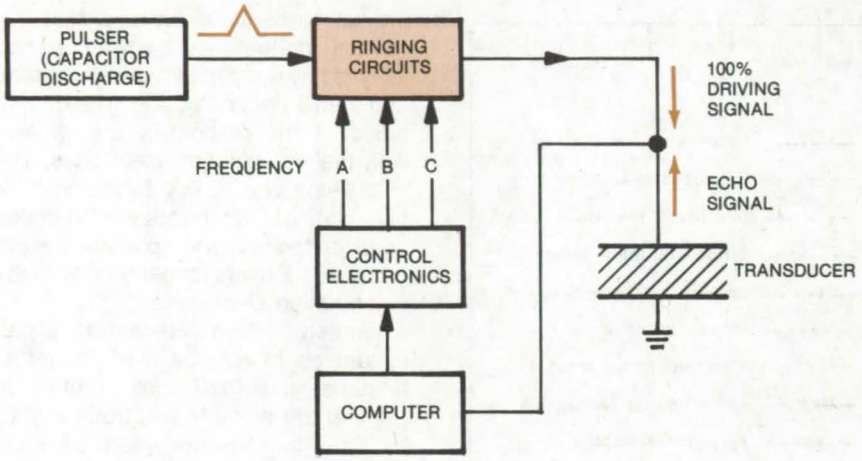

An **Automated Tissue Characterization** system includes a variable-frequency ringing circuit to send ultrasonic frequencies into the tissue to be tested. The attenuation of the echo signal is recorded and plotted against frequency.

selects a different ringing frequency for the tank circuit and repeats the process, obtaining data at another frequency.

In this manner, the desired frequency data can be obtained rapidly, inexpensively, and with a more uniform system response (resulting in better signal-to-noise characteristics) than with most other implementations. This technique may be applied to tissue characterization in medical ultrasound or to materials characterization in nondestructive evaluation.

This work was done by Paul Gammell of Caltech for **NASA's Jet Propulsion Laboratory.** *For further information, Circle 53 on the TSP Request Card.*
NPO-14461

Coupler for Surgery on Small Animals

Instrument transfers fluids with minimal obstruction of the work area.

Ames Research Center, Moffett Field, California

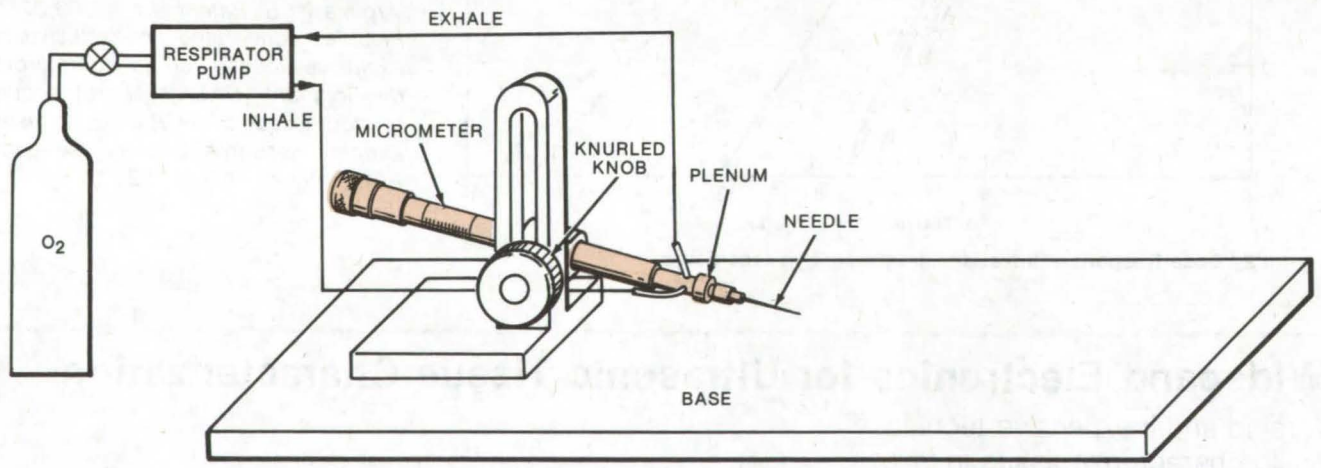

A **Microcoupler With a Respirator** would be used to regulate the breathing of an anesthetized rat or mouse. The coupler can also be used to inject liquids.

A new microcoupler simplifies the exchange of fluids with the organs of laboratory animals. The microcoupler makes it possible for one person to perform surgery on experimental animals such as rats and mice and it eliminates obstructing hands and instruments from the area of surgery.

The coupler is used with a microrespirator or microperfusion apparatus for regulating the flow of fluids to and from the animal. With a microrespirator, for example, the coupler holds a syringe-needle tip in the trachea while surgery is performed on the thorax.

The microcoupler consists of a syringe needle connected to a plenum having inlet and outlet ports (see figure). The plenum is held by a micrometer head, which allows longitudinal movement of the needle into a vessel or an organ of the small animal. The micrometer head is pivoted about

a horizontal axis so that the angle of insertion of the needle can be adjusted. When an oxygen respirator pump is connected to the microcoupler, the inhalation and exhalation of the small animal can be controlled during surgery.

After the angle and height of the needle are adjusted by a knurled nut, the micrometer head is then turned to advance the needle into the trachea (typically a distance of 2 to 4 millimeters for a mouse).

The microcoupler plenum has a quick-disconnect fitting that accepts different syringe-needle sizes. In addition to its use with a microrespirator, the coupling is also suited for injecting animals with a fixative in preparation for electron microscopy or other diagnostics.

This work was done by John E. Johnson, Jr. and Paul F. Swartz of **Ames Research Center.** *For further information, Circle 54 on the TSP Request Card.*

This invention is owned by NASA, and a patent application has been filed. Inquiries concerning nonexclusive or exclusive license for its commercial development should be addressed to the Patent Counsel, Ames Research Center [see page A8]. *Refer to ARC-11114.*

Cinemicrographic Specimen Housing

Microbial specimens can be studied "standing up" in the vertical plane.

Langley Research Center, Hampton, Virginia

A new housing supports microbial specimens vertically for time-lapsed cinemicrographic studies. It is used to observe how gravity affects specimens embedded in a support media, such as agar. This cannot be done with conventional microscopes, which "see" specimens in the horizontal plane.

As shown in the figure, the housing encloses a specimen container in a vertical sample holder. The holder is positioned horizontally and vertically by screws located outside an air-curtain incubator. The incubator generates the heat necessary for microbial growth. A thermistor temperature sensor is installed adjacent to the glass specimen container.

Outside the housing and directly behind the specimen is a 60-W lamp. A vertically-mounted binocular microscope (6X to 50X magnification) is aimed at the sample holder, and the time evolution of the sample is recorded by a movie camera. The camera and its drive motor are inverted to compensate for the inverted image formed by the microscope. A slotted baseplate allows alinement of the camera, microscope, and specimen housing.

The apparatus includes a photocell and exposure meter (part of a commercially-available cinemicroscopic apparatus) and a viewing telescope. Exposures are made through a ground-glass green filter, using sensitive black-and-white reversal film.

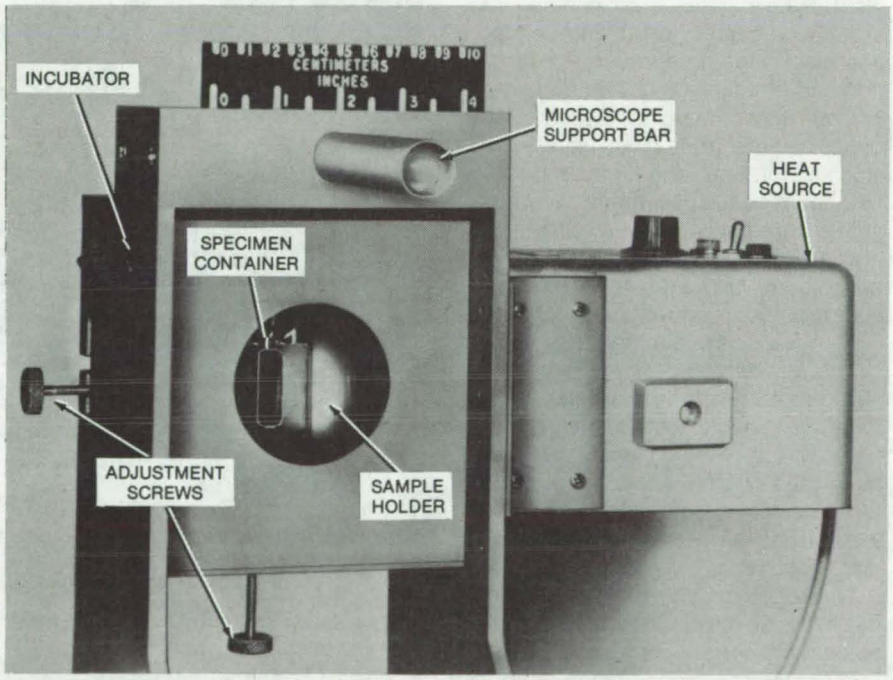

The **Incubated Housing** supports a specimen container vertically. The sample is illuminated from behind and viewed from the front by a movie camera through a low-power binocular microscope.

The equipment has successfully recorded the subsurface growth of bacteria in various media and agar concentrations. It has also been used in studies of gas-bubble formation and movement as well as motility patterns of micro-organisms.

This work was done by Judd R. Wilkins of **Langley Research Center.** *For further information, Circle 55 on the TSP Request Card.*
LAR-12047

Improved Capacitive EKG Electrode

Lighter, more compact electrode monitors heart signals through burn ointment and requires no electrolyte paste for coupling to the skin.

Lyndon B. Johnson Space Center, Houston, Texas

Hybrid integrated-circuit technology has improved the design and performance of a capacitively coupled electrode for electrocardiographs (EKG's). The new electrode, an improved version of an earlier device fabricated from discrete components, is lighter and more compact than the previous design.

Capacitive EKG electrodes are often superior to conducting electrodes for long-term monitoring of patients since they do not require electrolytic paste for coupling to the skin. Such pastes, used with conducting electrodes, can cause skin irritation and infections in some patients.

Even more importantly, the new capacitive electrode gives usable EKG signals through the nonconductive petroleum-based ointment normally applied to badly burned skin, thus making it possible to monitor the heart condition of burn victims. Conducting electrodes, in contrast, are rendered ineffective by the ointment.

The new electrode (see figure) is a disk about 1.5 cm in diameter with a thin-film capacitor on the side adjacent to the skin and a hybrid integrated-circuit impedance-matching network on the other side. Wire leads from the network connect to a display or recording instrument.

Unlike conducting EKG electrodes, the new electrode operates by displacement current through an insulator (instead of conduction current through a metal). The capacitor half is a circular silicon substrate on which a thin film of tantalum pentoxide has been deposited by radio-frequency sputtering. The skin and the silicon substrate are the electrodes of the capacitor, and the tantalum pentoxide (and any adjacent burn ointment) is the dielectric. The capacitor and the impedance-matching network are joined by a nonconducting epoxy, leads are attached by a conducting epoxy, and the network is encapsulated in a silicone resin.

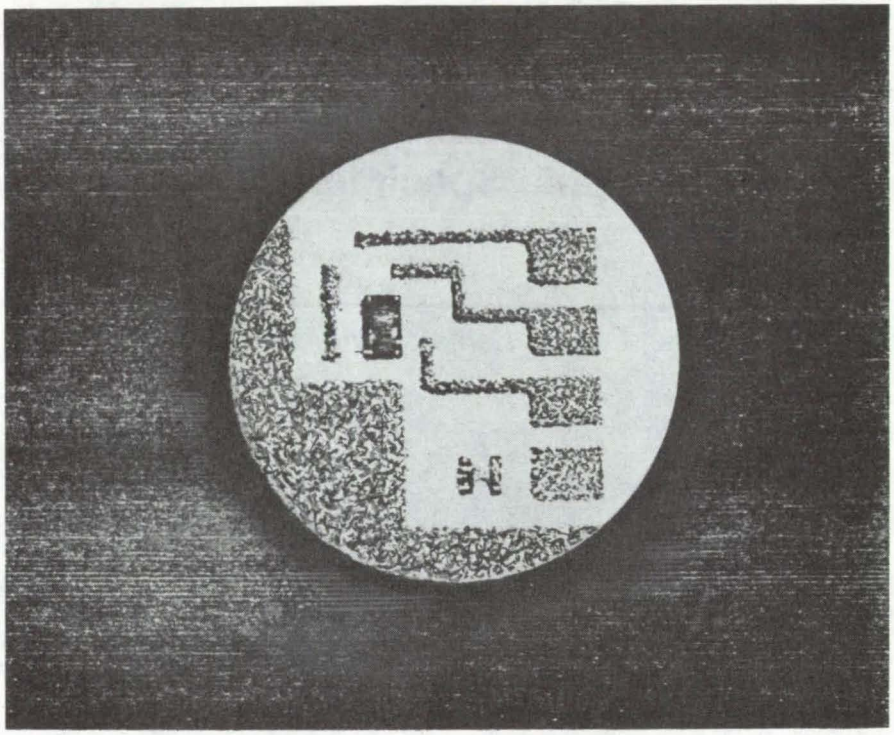

The **Capacitive Electrode for an Electrocardiograph** is mounted on a disk 1.5 cm in diameter. Here, the hybrid impedence-matching circuit is shown; the film capacitor is deposited on the reverse side. After leads are attached, the circuit is encapsulated and installed in a plastic housing.

The impedance-matching network consists of a ceramic substrate, a 100-megohm input resistor, an operational amplifier chip, and screen-printed thick-film conductors. Microwelded gold wires join the circuit elements.

The capacitive electrode was compared with a conventional electrode in tests on a healthy human subject. In both cases, the skin under the electrode was coated with a burn ointment. Although the capacitive-electrode measurements were noisy, they were usable, whereas the measurements from the conducting electrodes were lost in noise.

This work was done by Joe L. Day of **Johnson Space Center** *and Michael E. Griffith, William M. Portnoy, and Lawrence J. Stotts of Texas Tech University. For further information, Circle 56 on the TSP Request Card.*
MSC-18321

Books and Reports

These reports, studies, and handbooks are available from NASA as Technical Support Packages (TSP's) when a Request Card number is cited; otherwise they are available from one of NASA's Industrial Application Centers or the National Technical Information Service.

Low-Dose Total-Body-Calcium Analysis

Calcium analysis by neutron activation of ^{40}Ca requires only 10 mrd.

A new report contains details of a technique for measuring total body calcium by collecting exhaled ^{37}Ar gas after exposure of the patient to 14-MeV neutrons. Requiring a radiation dose of only 10 mrd, as compared to 100 to 200 mrd for methods involving slow neutron capture by ^{48}Ca, the ^{37}Ar technique is considerably safer for both the patient and the administering technician.

The report contains a summary of the theoretical basis for the technique, a description of a developmental facility for measuring body calcium changes of astronauts after exposure to zero gravity, a thorough analysis of the accuracy and precision of the method, and recommendations for system improvements. A listing of references on in vivo measurement of body calcium is included, along with a summary of published and presented papers.

The developmental irradiation facility consists of a neutron generator and a water-filled tank in which the patient is immersed to shoulder level during the exposure. The tank is mounted on a turntable. A calibrated dosimeter measures the neutron dose, while dose uniformity is monitored by 45 vials of calcium nitrate within the tank. Exposure time is 3 hours.

The breath sample is collected by a closed-circuit recirculating breathing system that maintains the patient on a 25-percent-O_2/75-percent-He atmosphere to minimize processing and purification time. Argon is extracted from the breath sample in a molecular sieve that traps the ^{37}Ar, which is subsequently detected by a low-background proportional detector.

This work was done by Thomas K. Lewellen and Wil B. Nelp of the University of Washington for **Johnson Space Center.** *This report is identified as NASA CR-151675 [N78-22696], "Total Body Calcium Analysis Using the $^{40}Ca[n,\alpha]^{37}$ Ar Reaction" [$4.50]. A copy may be purchased [prepayment required] from the National Technical Information Service, Springfield, Virginia 22151. MSC-18282*

Anthropometric Sourcebook

A three-volume compilation of anthropometric data, design information, and references

A three-volume "Anthropometric Source Book" contains a large body of anthropometric data, design information, and references. Originally compiled to assist engineers in the design of equipment, workspaces, and astronaut's clothing for the Space Shuttle, the book will also be useful to workers in many other fields. It is not only a comprehensive source of data but is also a thorough guide to the applications of anthropometric information.

Subjects covered in volume I include variability in body size, mass distribution properties of the human body, arm and leg reach, joint motion, strength, the design of clothing and workspaces, physical changes to the human body in a zero-g environment, and guidelines for the statistical analysis of anthropometric data. Many of the data are previously unpublished. Also included are body-size projections for the year 1985 and the cutouts of quarter-scale, two-dimensional manikins for use by designers.

Volume II contains tabulated dimensional anthropometric data from the surveys of 61 military and civilian populations (of both sexes) in the United States, Europe, and Asia. Roughly 295 measured variables are defined, illustrated, and tabulated in one of the most comprehensive compilations of summarized body-size data currently in existence.

Volume III is an annotated bibliography covering topics on applied physical anthropology with emphasis on anthropometry and its applications to sizing and design. Listed are 236 references including every anthropometric survey outlined in volume II. Also listed are references to other works on static and working anthropometry of U.S. and foreign populations, anthropometry related to the design of specific items (such as gloves or helmets), and other topics.

This sourcebook was prepared under the direction of Robert L. Bond, John T. Jackson, Allen J. Louviere, and William E. Thornton of **Johnson Space Center** *and Stanley Deutsch of* **NASA Headquarters.** *Copies may be purchased [prepayment required] from the National Technical Information Service, Springfield, Virginia 22151. The individual volumes are identified as:*

NASA RP-1024 [N79-11734], "Anthropometric Source Book Volume I: Anthropometry for Designers" [document $19, microfiche $3];

NASA RP-1024 [N79-13711], "Anthropometric Source Book Volume II: A Handbook of Anthropometric Data" [document $14, microfiche $3]; and

NASA RP-1024 [N79-13712], "Anthropometric Source Book Volume III: Annotated Bibliography of Anthropometry" [document $7.25, microfiche $3].

MSC-18500

Analyzing Water Resources

An overview of current and future water utilization

A new report on water resources discusses problems in water measurement, demand, use, and availability. It also considers sensing accuracies, parameter monitoring, the status of forecasting, modeling, and future measurement techniques. A number of maps, plots, and tables illustrate many points in the discussion.

(continued on next page)

Water is becoming scarce. Current estimates for the year 1990 indicate that natural precipitation, the major source, will be about one-third of the per capita daily requirement. This situation calls for significantly more efficient utilization of the natural water supply and increased Government and public awareness of the problem.

Principal concerns of water users are the effects of water and the demands for water. The effects include flood, wetlands toxicants, disease vectors, landslides, and saltwater intrusion; the demands come from domestic, agricultural, industrial, and recreational sectors.

The report defines key terms in water-resource studies. Maps of the United States show critical, near-critical, and noncritical water regions. Currently, management of water resources is fragmented among thousands of Federal, State, and local agencies; interstate commissions; user cooperatives; and private concerns. A centralized effort is proposed to resolve shortages predicted for the early eighties.

Certain areas of water-resources management can be studied with remote-sensing imagery. For example, maps of remote-sensing data obtained from aircraft or satellites can be analyzed to locate sites for projected reservoirs. Such factors as geography, climate, topography, and soil characteristics may be obtained to determine an optimum reservoir site for maximum cost effectiveness in delivering water for irrigation and industrial and urban projects.

Remote sensing can also help in hydrologic modeling. The purposes of such modeling are:

a. To predict the water outflow in real time corresponding to precipitation events,
b. To compute the outflow corresponding to unusually intense rainfalls so that the waterworks are not so small that they would be damaged by excess water nor too large to be prohibitively costly, and
c. To simulate the changes to the hydrologic regime of a watershed consequent to modification of its land use.

A third important area adaptable to remote-sensing imagery is the cooling of industrial sites. A number of industrial plants, particularly powerplants, use large quantities of water for cooling. In certain cases, these are thermal pollution sources affecting local aquatic life. Remote-sensing can help select the plantsite by generating the statistics of circulation and diffusion of the water in nearby estuaries or bays.

Remote sensing can also help study the pollution of water around large metropolises. The knowledge of circulation and diffusion of water masses will determine the amount of treatment and/or dilution necessary to produce sewage water with acceptable oxygen levels.

This work was done by ECOsystems International, Inc., for **Marshall Space Flight Center.** *Further information may be found in NASA CR-150467 [N78-13509], "Applications of Remote Sensing to Water Resources," a copy of which may be obtained at cost from the New England Research Application Center [see page A7].*
MFS-25104

Mechanics

Accurate Determination of Work in Three-Point Bend Tests

Correction curve accounts for coincidental displacement and simplifies data analysis

Lewis Research Center, Cleveland, Ohio

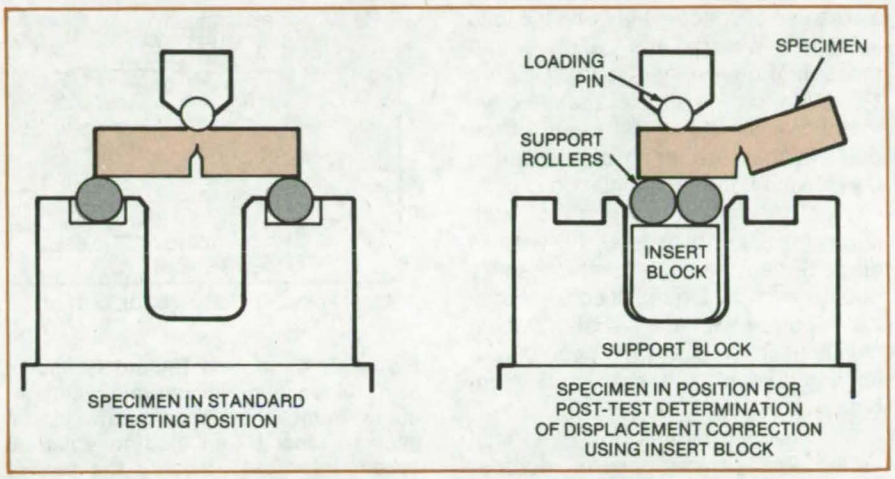

Figure 1. **Bend Test Apparatus** with specimen in position for testing and for posttest correction determination (displacement gages not shown)

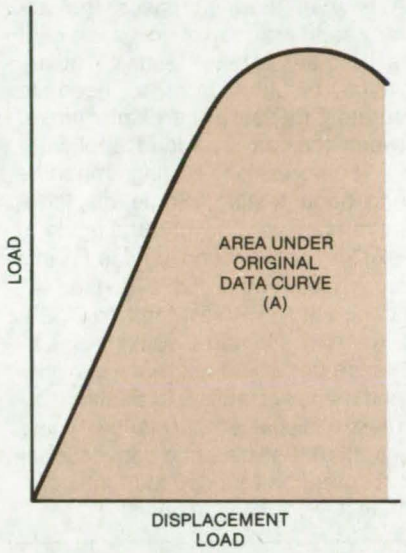

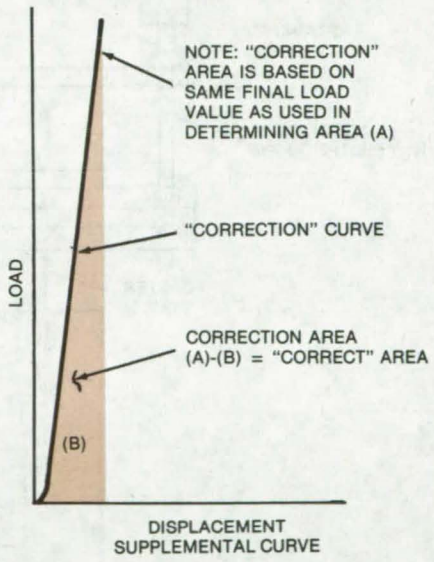

Figure 2. **Examples of Methods** of applying correction for coincidental displacement to load-displacement record

The notched or precracked three-point bend test is important in the field of materials testing. It is often necessary to determine the work associated with the testing of such a specimen to a specific load displacement. This is accomplished by measuring the area under the load-vs.-load-displacement curve. However, the area under this curve may contain a substantial error due to coincidental displacement from extraneous deformation in load and support points and in the test apparatus. For exact work values it is necessary to eliminate this coincidental displacement.

A simple means for eliminating the work contributed by the coincidental displacement is illustrated in Figure 1. First, the standard test is performed, and a test curve (see Figure 2) is obtained. The area under this curve includes the work obtained from coincidental displacement. Then, a second test is run to obtain a correction curve. Maximum load on this second test is equal to or slightly higher than that of the standard test. The area under this correction curve closely approximates the coincidental work at any load level. The work determined in the standard test can be corrected for the contribution of the coincidental displacement by subtracting the area under the correction curve taken to the final load value attained in the standard test.

This procedure is applicable to any test regardless of load displacement. In the cases of tests continued past the displacement of maximum load, an error in the correction curve results from that portion of the coincidental displacement due to unrecoverable plastic deformation. However, this error is negligible.

This work was done by Robert J. Buzzard and Douglas M. Fisher of **Lewis Research Center.** *Further information may be found in NASA TM-X-73596 (N77-19486), "Load-Displacement Measurement and Work Determination in Three-Point Bend Tests of Notched or Precracked Specimens," a copy of which may be obtained at cost from the New England Research Application Center (see page A7).*

LEW-13034

Improved Displacement Measurement in Bend Testing

Removable spacers extend displacement range and increase accuracy.

Lewis Research Center, Cleveland, Ohio

A new method increases the accuracy and range of displacement measurement in bend testing. This innovation resulted from a need to accurately measure the displacement between the ram and load applicator of a compression testing machine during bend testing. Some displacement ranges were beyond the limits of an existing conventional device (in this case, a piston-actuated clip gage as described in ASTM Test Method E-399-74). A larger clip gage would increase the range but would decrease sensitivity and maneuverability. In addition, an increased displacement range would require that the scale of a conventional X-Y recorder be reduced to fit the complete test record on the chart.

The use of spacers between the load applicator pin and the piston of the measuring device, as shown in Figure 1, proved to be a simple and effective method of extending the range of the conventional measuring device during bend testing. In the application shown, each of the four spacers is 0.10 inch (2.5 mm) thick for a total increase in displacement measurement capability of 0.40 inch (10.2 mm). A conventional X-Y recorder with a 1:1 scale relationship is used to record the gage output as the load on the specimen is increased.

During the progress of a bend test, as the displacement gage or recorder reaches a limit, the topmost spacer is removed by sliding it from the spacer stack with the hooking device shown. This is done without unloading or interrupting the test. The spring force of the clip gage causes the adapter piston to "reset" an amount equal to the spacer thickness. The reset on the chart is proportional to the spacer thickness (Figure 2).

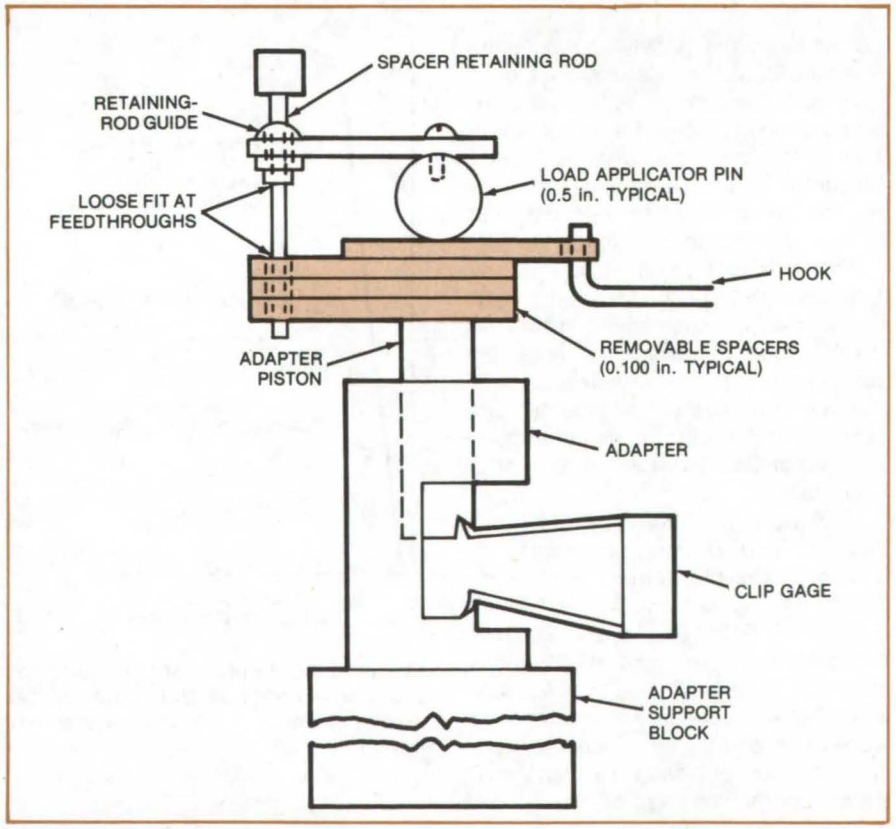

Figure 1. **Removable Spacers** can be used to extend the range of displacement gages. (A displacement gage consists of a clip gage in its adapter.)

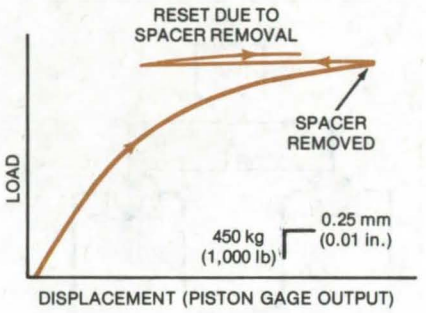

Figure 2. **Bend Test Record** is shown as obtained using spacer-removal technique. Removal of spacer allows piston gage to reset by an amount equal to spacer thickness, causing the pen to retrace as shown.

Several features of this innovation that were found to be especially attractive are:

- It increases operating capability for existing piston-type gages with very little modification.
- It permits short-range, highly-sensitive measurement devices to be utilized repeatedly over their optimum ranges to obtain long-range test results.
- It allows greater latitude in the selection of optimum recorder scales without risking loss of the latter portion of the test record.

This work was done by Robert J. Buzzard and Douglas M. Fisher of **Lewis Research Center.** *Further information may be found in NASA TM-X-73596 (N77-19486), "Load Displacement Measurement and Work Determination in Three-Point Bend Tests of Notched or Precracked Specimens," a copy of which may be obtained at cost from the New England Research Application Center (see page A7).*

LEW-13035

Displacement Gage Modified for Multiple Measurements

Extra contact points allow additional measurements during fracture toughness tests.

Lewis Research Center, Cleveland, Ohio

Standard clip-in gages of the type used in fracture toughness testing can be modified to permit the acquisition of additional displacement data. For example, with this innovation, displacement can be measured simultaneously at several locations along the concave face of a C-shaped test specimen. Figure 1 shows a standard 2-inch (5-cm) inner-radius C specimen with modified and standard gages attached. In a standard test setup the specimen (loaded in tension) has a clip-in gage measuring displacement at the center notch. Measurements at secondary locations are generally not possible with existing gage design and size. Modification of this gage permits acquisition of additional displacement data.

The span of standard gages is limited to 0.2 in. (0.5 cm), and they therefore cannot record complete data without modification. Gage versatility has been increased with longer spacer blocks and by incorporating contact points on the free ends of the gage arms. While modification of spacer blocks is an accepted ASTM technique, the addition of more contact point is unique and permits a wider use of gages with a standard specimen.

The contact points were added by installing outward-facing tines fabricated from 6-32 machine screws in the free ends of the gage beams as shown in the enlarged section of Figure 1. The nut attachments permit fine adjustments of gage length. Points on the machine screws allow the gage to seat in punched indentations on the concave surface of the test specimen. Spring tension in the beams maintains the screw points in the seats. The tines may also be fixed to point inward for measuring tensile displacement across the outer surfaces of flat compact specimens. This device could also measure diametral or chordal strains across the outside surfaces of tubes or cylinders. Additional modifications are possible to measure strain in restrictive environments such as vacuum or high temperature, as depicted in Figure 2.

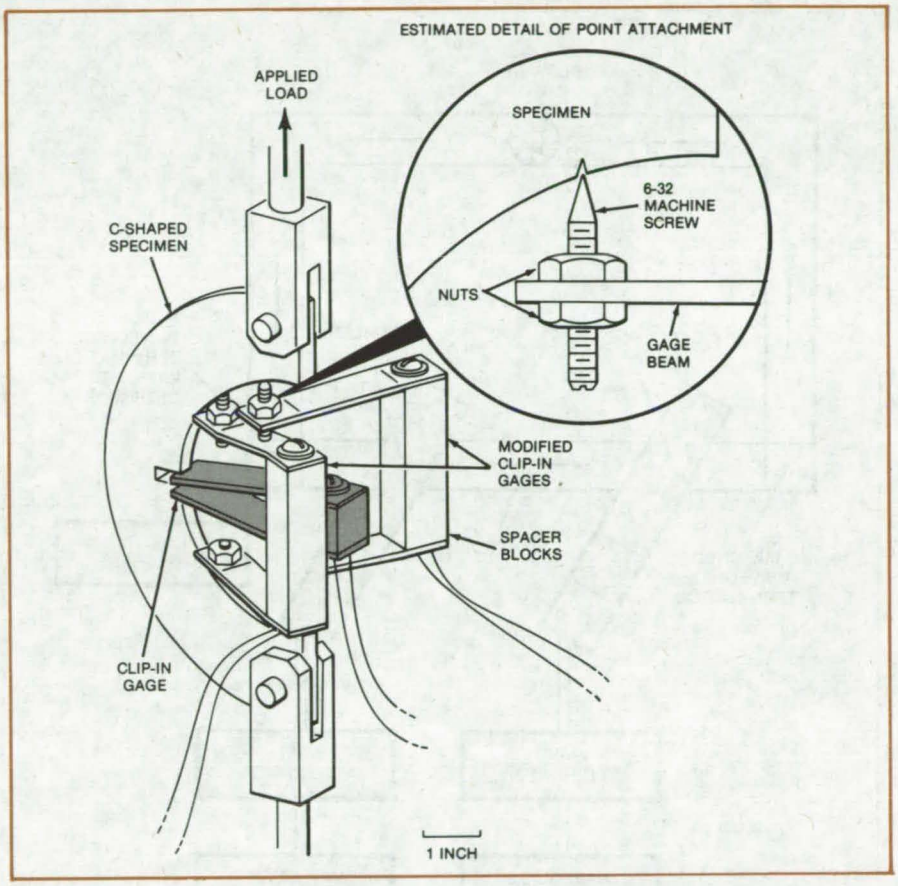

Figure 1. Schematic **C-Shaped Specimen** test setup is shown with three clip-in displacement-measurement gages in place.

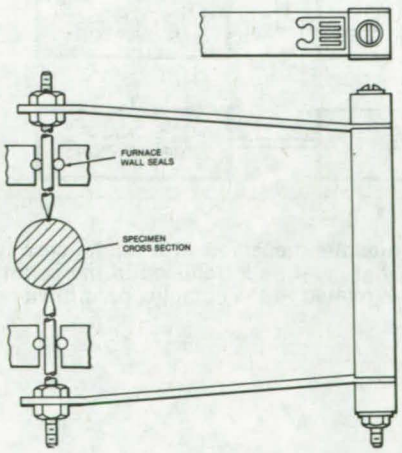

Figure 2. **Proposed Gage Application** measures diametral strain in restrictive environments.

Use of this innovation can also result in reduced specimen-fabrication costs and improved test techniques. Specimen testing is simplified since gages can be pivoted on the screw points to minimize gage interference where multiple gages are desired. Gage calibration has been determined to be well within the limits set forth in ASTM Test Method E 399-74.

This work was done by Robert J. Buzzard and Douglas M. Fisher of **Lewis Research Center.** *Further information may be found in NASA TM-73731 [N77-30500], "C-Shaped Specimen Plane Strain Fracture Toughness Tests," a copy of which may be obtained at cost from the New England Research Application Center* *[see page A7]*.

LEW-13036

Measuring the Permittivity of Gases and Aerosols

A two-coupler microwave technique measures complex permittivity.

John F. Kennedy Space Center, Florida

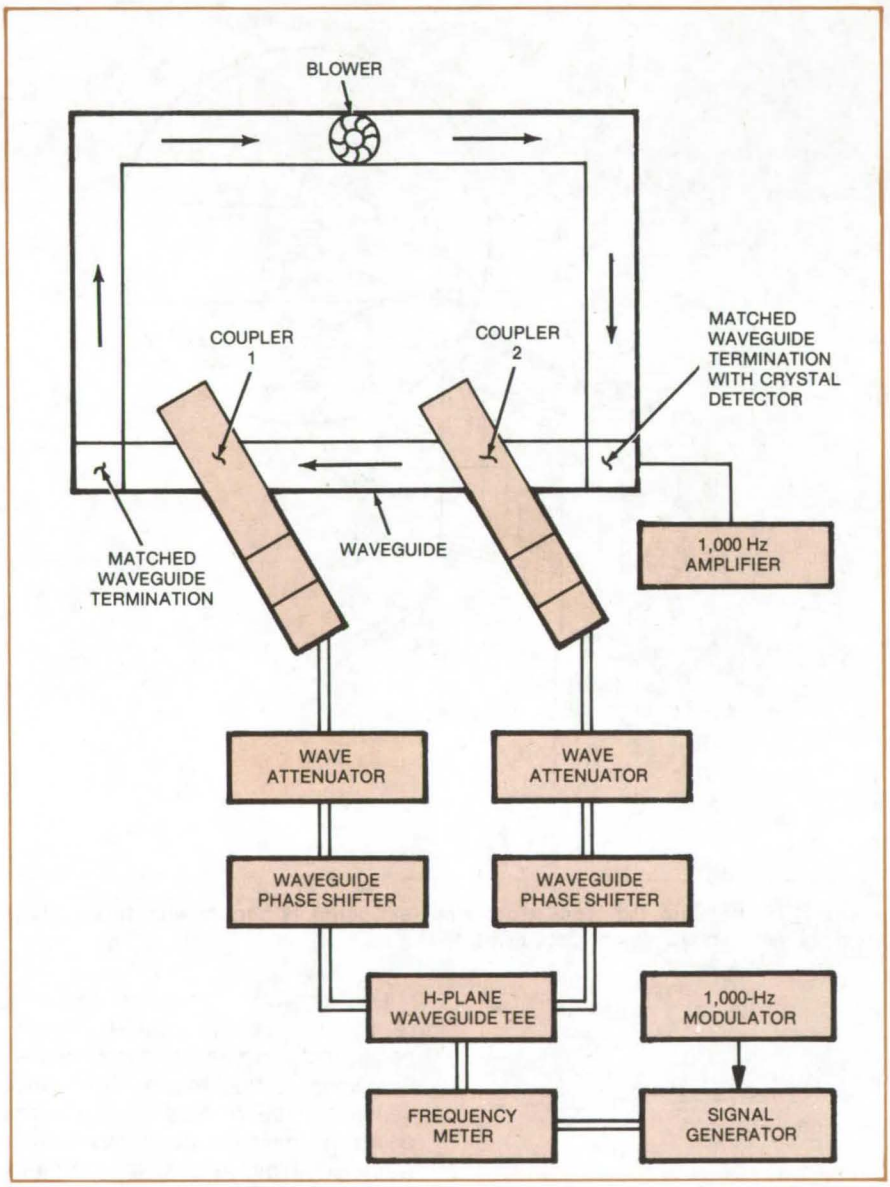

Figure 1. **Gas and Aerosol Dielectric Properties** are measured with this microwave apparatus. The attenuation and phase shift that must be introduced in the coupler arms to obtain a power null at the detector are related to the complex permittivity of the dielectric between couplers 1 and 2.

The complex permittivity of a gas or an aerosol at microwave frequencies is difficult to determine accurately because of problems in containing a homogeneous gaseous sample within a well-defined electromagnetic boundary. Reliable complex permittivity measurements can be made, however, by using the two-coupler power-nulling technique shown in Figure 1.

In this system, the waveguide that encloses the gas or aerosol is part of a closed-loop duct, and a blower continuously circulates the gas or aerosol to keep it homogeneous. Microwave energy is injected into the waveguide through the two directional couplers. The couplers are fed from the same microwave source, through a power divider, attenuators, and phase shifters. A load termination at each end of the waveguide absorbs the microwave energy, and a crystal detector measures the power of the superimposed signals from the couplers.

The real and imaginary parts (ε' and ε'', respectively) of the complex permittivity of the dielectric medium in the waveguide can be determined from the attenuation and phase shift that must be introduced to register a power null at the detector.

To measure ε', the detector is first nulled at a reference frequency. Then, the frequency is changed, and the phase shift (Δn) that must be introduced into arm 2 to compensate for the phase change in the dielectric is recorded. This procedure is also carried out at a third frequency, and the results of these measurements are used with equation 2 in Figure 2 to set up two coupled equations. These equations are solved for ε' and n, the number of wavelengths in the dielectric at the reference frequency.

$$a = n\lambda_g \quad (1)$$

$$= \frac{(n + \Delta n)\,\lambda_o}{\sqrt{\varepsilon' - (\lambda_o/\lambda_c)^2}} \quad (2)$$

$$\varepsilon''/\varepsilon' = \frac{a\lambda_g}{\sqrt{|\,1 - (\lambda_g/\lambda_c)^2}} \quad (3)$$

where
- a = distance between the coupling holes,
- n = number of wavelengths between the coupling holes at a reference frequency,
- Δn = change in n when the frequency is changed,
- λ_g = guide wavelength (in dielectric),
- λ_o = free space wavelength,
- λ_c = cutoff wavelength (twice the guide width),
- ε' = real part of the complex permittivity,
- ε'' = imaginary part of the complex permittivity, and
- α = guide attenuation constant.

Figure 2. **Equations for Determining the Complex Permittivity,** using the two-coupler method, are discussed in the text.

The parameter ε'' is found from equation 3 by measuring the attenuation inserted in arm 2 to compensate for the attenuation introduced by the gas or aerosol. Although this could be done by first obtaining a power null with air in the guide and then renulling while the gas is flowing, in practice it is easier to incorporate a waveguide switch between arms 1 and 2. After a power null is obtained with the switch in one position, the inputs to the couplers are interchanged and a new null is adjusted. Under these conditions, the amount of attenuation added is twice the attenuation of the dielectric in the waveguide section between the couplers.

For accurate results, several precautions should be followed. The loads and the probe should be matched to minimize reflections in the waveguide, and a very thin dielectric window should be placed in each of the coupling holes to prevent leakage of the gas into the couplers (otherwise, the accumulation of powder from the aerosol could alter the coupling factors of the holes). To prevent powder accumulation on the interior surface of the waveguide, the medium should flow through the guide at a high rate.

This work was done by Witold J. Trett of **Kennedy Space Center.** *For further information, Circle 57 on the TSP Request Card.*
KSC-11090

Improved Split-Film Vector Anemometer

Only one of three previously-used split films would be required in proposed design.

Langley Research Center, Hampton, Virginia

A proposed split-film vector anemometer could accurately measure the magnitude and direction of fluid flow velocity in three-dimensional space. Only one of the three split films in the previously-used three-prong split-film system would be required.

Other methods for measuring fluid flow velocity include the very-accurate laser velocimeter and the three-hot-wire system. However, the cost of the laser is at least 100 times higher than the proposed system, and the three-hot-wire system is very vulnerable to handling and particle damage and is usable only over a semisphere velocity range.

The three-prong split-film system encounters flow interference problems when the flow is parallel to one of the sensors, when two sensors are alined with the flow, or when sensor support arms interfere with the flow. These problems could be avoided by using a single sensor that is rotated about the probe axis and controlled by a position indicator. The pertinent sensor information, which is recorded continuously, is measured at any three probe-roll angles 120° apart. The effects of the probe-roll rotation can be balanced out with proper calibration. Thus one sensor develops all the data that previously required three sensors.

Only one sensor needs to be maintained and calibrated rather than three with the existing system. Furthermore, with only one sensor, flow interference between sensors (when one sensor is downstream of another) is eliminated. The flow interference effects associated with the sensor support arms or difficulties associated with flow parallel to the sensor axis could be eliminated by choosing the three 120°-separated data points appropriately. A further advantage of the proposed system is that three data sets can be taken and reduced. If one set disagrees with the other two, the reason could well be due to flow interference. Thus, the two data sets that agree can be accepted. Therefore, this new design provides sufficient data to check the measured results.

This work was done by James Scheiman of **Langley Research Center.** *No further documentation is available.*

Inquiries concerning rights for the commercial use of this invention should be addressed to the Patent Counsel, Langley Research Center [see page A8]. Refer to LAR-12391.

Testing Panels in Shear and Biaxial Compression

Hydraulic jacks simultaneously apply torsion, axial compression, and lateral compression to structural panels.

Lyndon B. Johnson Space Center, Houston, Texas

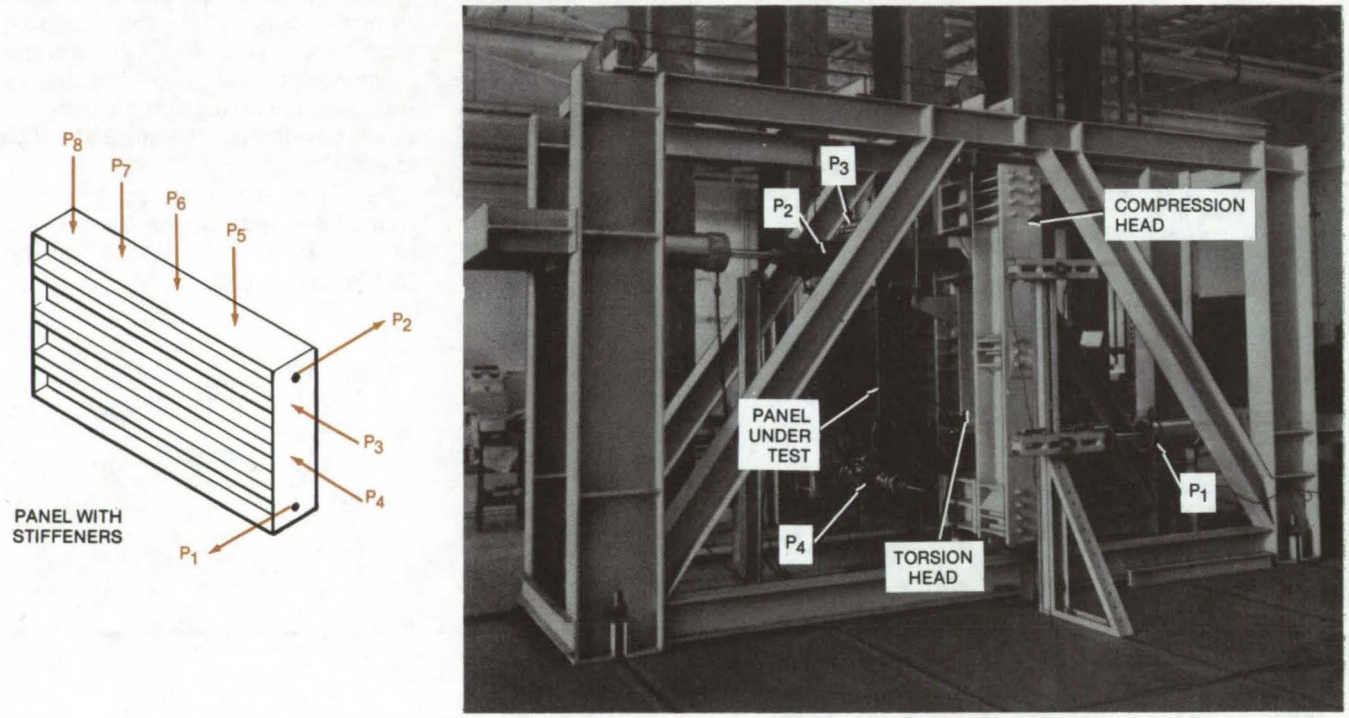

A **Ribbed Structural Panel** is tested for buckling and failure mode by torsion from jacks P_1 and P_2, axial compression from P_3 and P_4, and lateral compression from jacks P_5, P_6, P_7, and P_8. The lateral compression jacks cannot be seen in the photograph, but their loads are indicated in the diagram at the left.

A testing machine subjects structural panels to three simultaneous stresses: torsion, compression along the torsion axis, and compression along an orthogonal axis. The machine was developed for applying realistic test loads to Shuttle Orbiter fuselage panels and is suitable for testing other large panels, such as those for aircraft, lightweight trucks, buses, and railroad cars. The testing machine is used to determine the best relationship between the stiffener dimensions and the panel skin thickness.

The tester is an adaptation of an earlier test fixture [NASA Tech Brief B75-10319 (MSC-14883)] that could apply only shear and axial-compression loads simultaneously; it could not apply a lateral compression load. With the earlier machine, it was necessary to make calculations and estimates to determine the combined effects of shear and biaxial-compression loads on buckling and failure mode. However, with the augmented fixture, empirical data can be gathered under the conditions of simultaneous loading.

The tester is designed to accomodate 36- by 78-inch (92- by 198-centimeter) panels. A panel is installed as one side of a torque box that is bolted to a steel wallplate on one end and to a steel torsion head on the other. Torque is applied by two hydraulic jacks (P_1 and P_2 in the figure), which apply a force couple to the torsion head. Axial compression is applied by two tension jacks, P_3 and P_4, installed between the wallplate and a compression head.

Lateral compression is applied, via a compression head attached to the torque box, by four jacks acting in tension: P_6 and P_8 inside the torque box and P_5 and P_7 outside the box. To ensure that the lateral load is distributed uniformly along the test panel, the lateral compression head contacts the panel by spherical-ended setscrews threaded into holes along the length of the head. The setscrews are seated in hardened steel blocks, which in turn distribute the load to aluminum blocks on the torque box. Lubricant between the blocks minimizes the axial load transferred to the lateral compression head during biaxial compression loading.

The deadweight of the lateral compression head and jacks is compensated by a single overhead jack. The head is also supported by aluminum flexures that allow vertical movement but block movement caused by inadvertently unbalanced loading.

This work was done by James K. Neary of Rockwell International Corp. for **Johnson Space Center.** *For further information, Circle 58 on the TSP Request Card.*
MSC-16132

Predicting the Wet Strength of Laminates

Graphite/epoxy strengths at various moisture contents can be estimated by extrapolating from a relatively-small data base.

Lyndon B. Johnson Space Center, Houston, Texas

A simple extrapolation predicts the effects of absorbed moisture on the strength of graphite/epoxy laminates. Used extensively in spacecraft, such laminates are also attractive structural materials for terrestrial vehicles and household appliances, but their usefulness has been limited by the lack of quantitative data on moisture effects.

Graphite/epoxy laminates readily absorb moisture from the atmosphere, and their shear and compression strengths are thereby severely degraded, particularly at elevated temperatures. For example, at 350° F (177° C) and 0.77 percent moisture content, the longitudinal compressive strength of one type of composite considered for the Space Shuttle is reduced 70 percent below the dry value.

Previously, in the absence of detailed data on moisture effects, the only alternative was to design the graphite/epoxy Shuttle panels as though they were saturated with moisture at their operating temperature. However, this practice yields unrealistically low predicted strengths, and the structure becomes grossly overdesigned.

A more realistic approach is to predict the moisture content from the temperatures and humidities to which it will be exposed and to use the strength at that moisture content in the structural design. However, obtaining such strength data can be a formidable task. For example, the Space Shuttle aft propulsion subsystem contains at least six different laminate configurations for which five design-strength properties are required under dry and wet (0.6 and 0.8 percent moisture) conditions, at room temperature and 350° F. It is not practical to test for all these conditions to obtain sufficient data to make a reliable statistical analysis that can be applied with confidence.

With the new procedures, this massive testing is not necessary. The procedure takes advantage of a large data base already available for 0.2 percent moisture content in laminates. Only three to five test specimens per condition are measured for strength at 0.6 and 0.8 percent moisture. The data are compared with the strengths at 0.2 percent moisture, and "strength-reduction factors" are calculated. These factors are then applied to the 0.2 percent moisture data to determine the strengths of other specimens at 0.6 and 0.8 percent moisture.

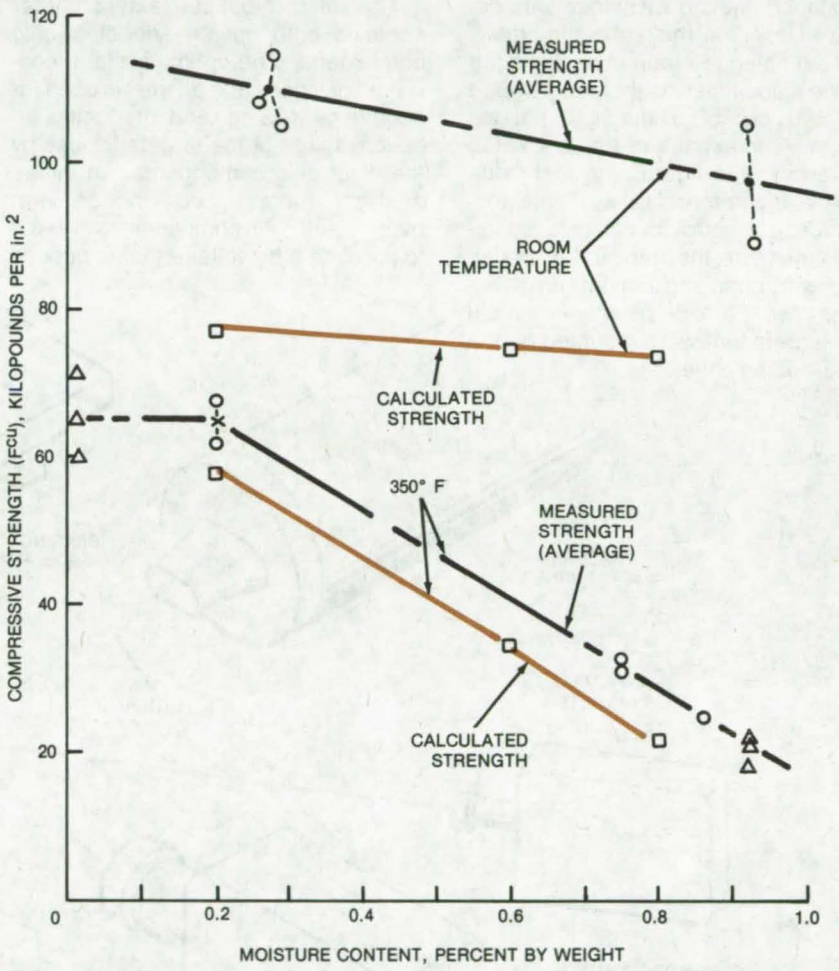

Allowable Design Strengths estimated by a new procedure are approximately 20 percent less than the average of test values. The estimated strength could therefore serve as reliable design values.

Allowable laminate strengths determined this way are typically 20 percent less than test measurements (see figure). Thus, the results indicate that the predicted strengths could serve as reliable design values.

This work was done by Raymond E. Bohlman of McDonnell Douglas Corp. for **Johnson Space Center.** *For further information, Circle 59 on the TSP Request Card.*
MSC-18022

Noncontact Strain Measurement

Electro-optical extensometer measures displacement.

Lewis Research Center, Cleveland, Ohio

A noncontacting technique was developed to determine experimentally the leading-edge strain in a simulated turbine blade that was thermally cycled into and out of a mach 1 hot-gas stream. A schematic of the test setup is shown in the figure. The technique employs a commercially-available noncontacting electro-optical extensometer to measure the transient displacement with changing temperatures between two parallel platinum/rhodium wire targets that were mounted on the blade leading edge.

The electro-optical extensometer contains both optical and electronic components. The optical system, consisting of lenses and prisms, is used for acquiring, viewing, and producing an optical image of the targets for use by the electronic components. An image analyzer tube, in conjunction with other electronic components, is used to produce a dc voltage that is directly proportional to the target displacement. System calibration, employing a micrometer mechanically to produce known displacements, is necessary to determine the proportionality constant between displacement and dc voltage output. The calibration error was no greater than 50 microinches (127 microcentimeters).

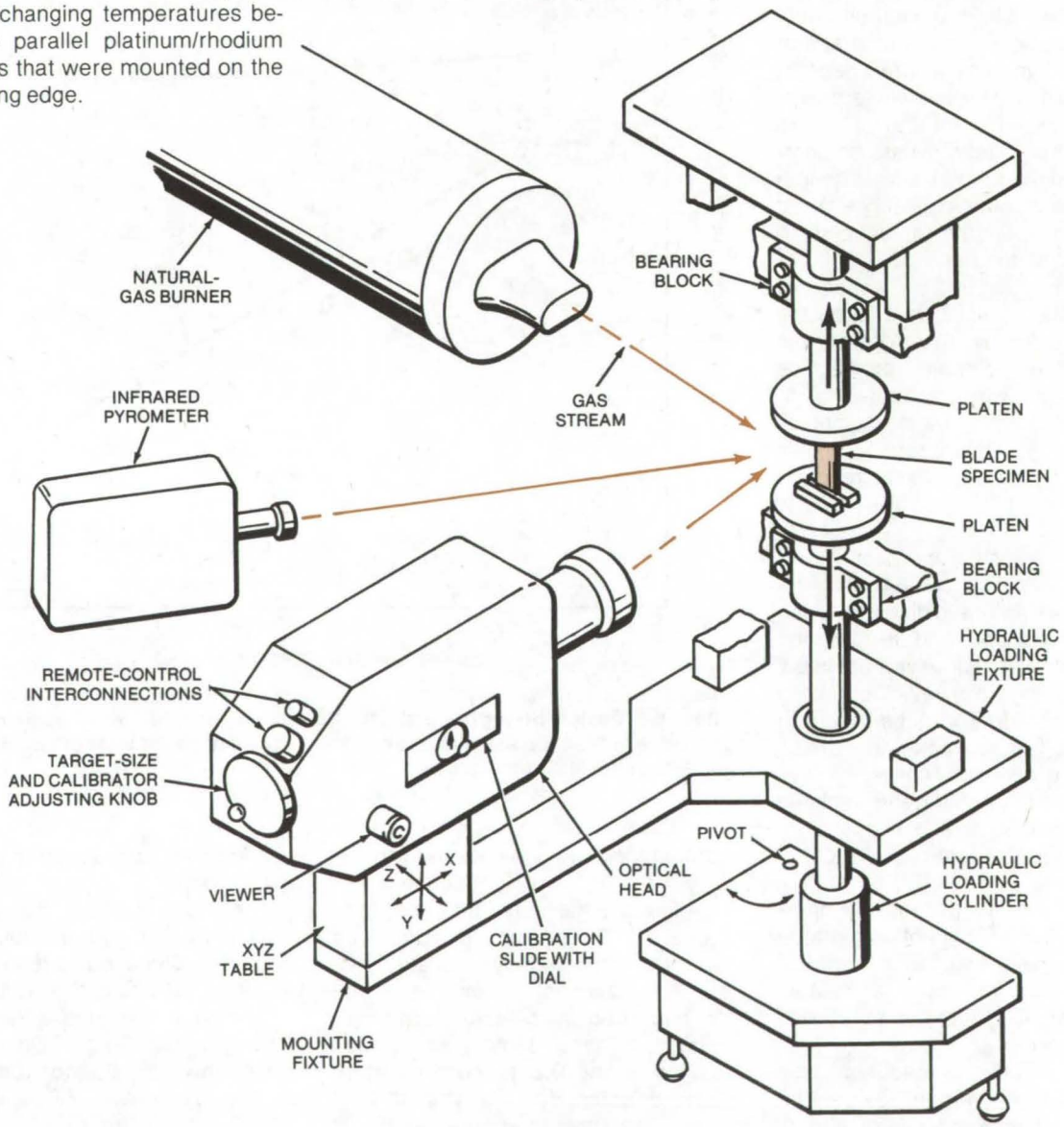

Test Setup for thermal fatigue testing of simulated turbine blades includes load frame, specimen, burner, and instrumentation.

The turbine blade was heated for 3 minutes and cooled for 1 minute so that metal temperatures ranging from 2,000° F (1,370 K) to 80° F (300 K) were obtained. Displacements during the complete heating and cooling cycle were measured to ±0.04 percent of the 0.561-in. (1.47-cm) gage length (distance between the targets at room temperature). Total leading-edge strain was determined from the ratio of the displacement at temperature to the gage length. A maximum total strain of 1.27 percent occurred at the end of heating. After 10 seconds of heating, the leading-edge strain was about 80 percent of the maximum strain. The minimum total strain at the end of cooling was 0.31 percent. For the simulated turbine blade the results were reproducible within 4 percent.

This strain measurement technique could significantly aid in obtaining accurate strain histories for components that are subjected to severe thermal environments where conventional strain measurement techniques are not feasible. Problems normally encountered with more conventional gage methods, such as calibration drift or other effects due to severe environmental change, are eliminated since the instrument is external to the test specimen environment.

This work was done by Peter T. Bizon and Frederick D. Calfo of **Lewis Research Center.** *Further information may be found in NASA TM-73886 (N78-19161), "Experimental Determination of Transient Strain in a Thermally-Cycled Simulated Turbine Blade Utilizing a Non-Contact Technique," a copy of which may be obtained at cost from the New England Research Application Center (see page A7).*
LEW-13091

Thermographic Inspection of Welded Contacts

Good and poor-quality welds are identified by their temperatures.

Marshall Space Flight Center, Alabama

Solar-cell welds can be inspected by digitized thermography, an approach developed to improve the reliability of solar arrays on space probes. The weld is heated by passing current through it, and the surface temperatures are mapped by a commercial thermal-imaging device. Unwelded contacts pass no current and show up as "cold" spots on the image. Good welds, on the other hand, do heat up but since they have relatively low resistance, they do not get as hot as a marginal weld. Thus far, only qualitative information has been extracted from the images. However, they can be complemented by the quantitative holographic method described in the following article. Moreover, thermography could be made quantitative by correlating the images with weld pull-test data. Since the digitized images are easily stored and processed by a computer, the method could be adapted for automated online inspection of solar arrays.

Solar-cell arrays have been studied in both black-and-white and color thermography while currents of up to 1 ampere were passed through the welded contacts. Unbonded contacts are readily identified (see figure), and structure in the temperature profile across a contact is visible in magnified images. The images are magnified either by adding a germanium lens to the collecting optics or by using the entire viewing screen to display a portion of the image.

The system can repeatedly sample a single scan line across the image and give a measure of the temperature profile by averaging the samples. Potentially useful for automated inspection, this mode also brings out other features, such as temperature gradients across the entire array. Image details can be enhanced by subtracting out the background temperature profile of the cell backing. "Isotherm" imaging, in which regions that fall within a selected temperature range are displayed either black or white against a contrasting background, can also give useful information.

This work was done by Gary L. Workman of North Alabama Scientific & Engineering Consultants, Inc., for **Marshall Space Flight Center.** *For further information, Circle 60 on the TSP Request Card.*
MFS-25093

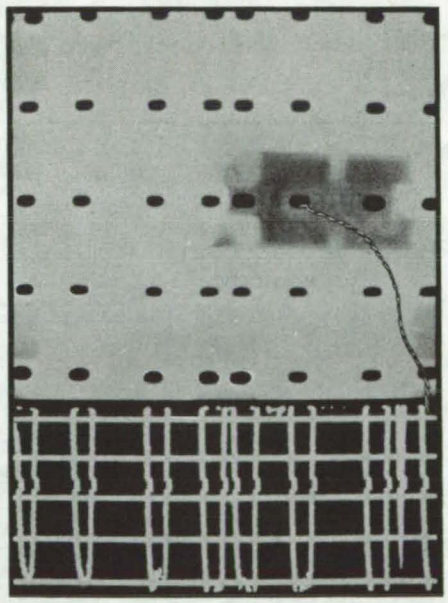

A **Thermographic Image** of a solar array, taken from the weld side, shows two unbonded welds. The temperatures along a single scan line near the midline of the array are plotted at the bottom of the photo.

Nondestructive Weld Test by Holography

A hologram, with magnification, locates poorly bonded pads on solar-cell arrays.

Marshall Space Flight Center, Alabama

Recent tests show that the fringe pattern in a magnified hologram of a welded contact contains information on the quality of the contact and on its area. Potentially useful as a test during the assembly of large solar-cell arrays, holography would be an accurate, nondestructive method for screening marginal and defective welds.

A hologram is formed (see Figure 1) by splitting an argon laser beam into reference and object beams, reflecting the object beam off the surface being inspected, and recombining the beams at the film plate. A magnifying lens is placed in the object-beam path between the reflecting surface and the film. The recorded fringe pattern is a measure of the contours of the surface from which the object beam is reflected.

Two images of the bond area are taken. In the first, the area is in its "normal" state; in the second, the bond is thermally stressed by heating it with a lamp. The fringe pattern of the stressed state, shown in Figure 2, clearly defines the bond area. The fringe displacements from the unstressed pattern (not shown) are largest in the unbonded areas, since these regions are able to move more freely than the bonded areas. Also, the fringes in the bond area exhibit a symmetry around the geometrical center of the bond. (Two bonds are seen in the weld pad shown in Figure 2.) The area of the bond is determined by measuring the size of the region in which the fringes are not substantially displaced from their unstressed locations.

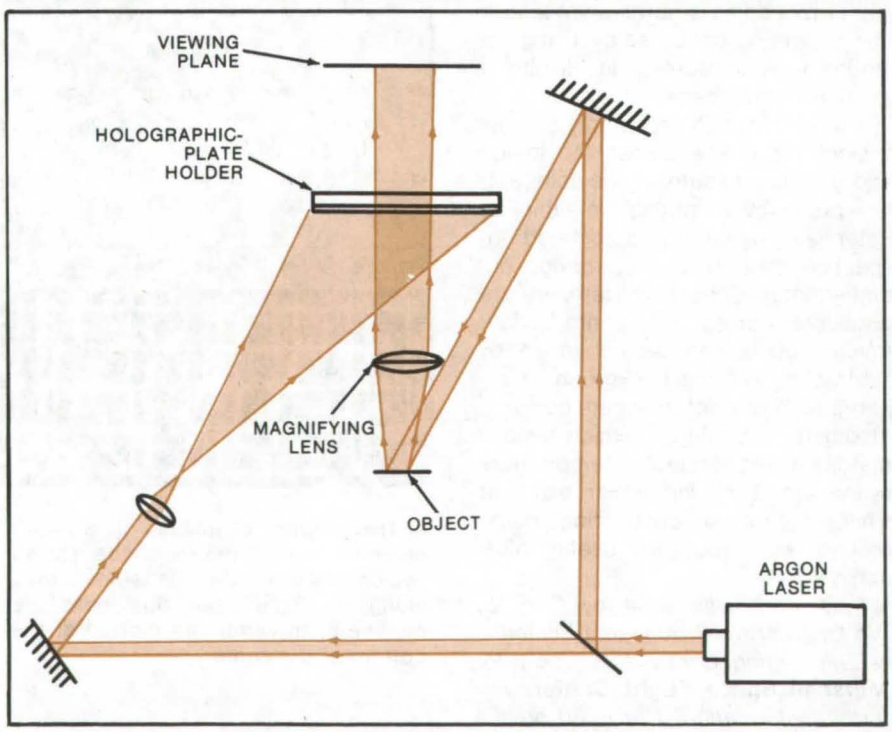

Figure 1. The **Holographic Test Setup** forms a magnified image of a welded pad on a solar-cell printed-circuit substrate. A continuous argon-laser source is used here; a higher-energy pulsed laser might be used in inspecting welded contacts on large solar-cell arrays.

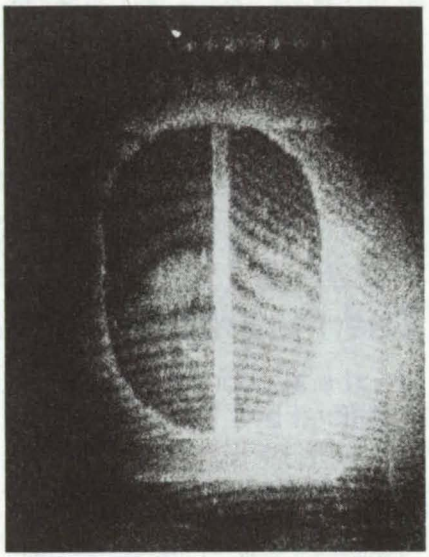

Figure 2. The **Holographic Image** of a thermally stressed contact on a solar-cell printed-circuit substrate shows two welded areas. By measuring the fringe shifts between the stressed and unstressed states, the weld at the right was found to have approximately twice the area of that on the left.

This work was done by Mike Perry and Gary L. Workman of North Alabama Scientific & Engineering Consultants, Inc., for **Marshall Space Flight Center.** *For further information, Circle 61 on the TSP Request Card.*

Inquiries concerning rights for the commercial use of this invention should be addressed to the Patent Counsel, Marshall Space Flight Center [see page A8]. Refer to MFS-23826.

Diazo Techniques for Remote-Sensor Data Analysis

Low-cost method helps interpret images.

Marshall Space Flight Center, Alabama

The cost and time to extract land-use maps, natural-resource surveys, and other data from aerial and satellite photographs (e.g., Landsat images) are reduced by diazo processing. The film and processing equipment are available commercially; no darkroom is needed; and once a few fundamentals have been mastered, the process can be controlled to enhance or deemphasize selected features, such as vegetation, land boundaries, and bodies of water.

The term "diazo" refers to a compound containing a pair of nitrogen atoms bonded to an organic molecule. A diazo film consists of a layer of diazo and a coupler compound on a plastic film base. When the film is exposed to ultraviolet light, the diazo loses its nitrogen and hence its ability to combine with the coupler. Exposed film is developed in ammonia gas, which allows the unexposed diazo to react with the coupler and form a dye. Diazo film is available in a wide range of dyes, including magenta, cyan, yellow, blue, orange, and violet.

As shown in the figure, an image is made by placing a black-and-white photographic transparency over a diazo emulsion, exposing them to ultraviolet light, and developing the emulsion in ammonia. Several images in different colors are prepared this way and superimposed in perfect register.

When the layup is viewed in white light, the diazo images act as filters that give a composite image, the colors of which depend on the rules of subtractive color theory. By properly selecting the diazo colors, specific features of the original photograph can be brought out and others can be suppressed. Other variables that can be controlled are the spectral filters used to make the original photographs and the possibility of exposing either negative or positive transparencies (or both) of the original image with different diazo color emulsions.

The diazo equipment can be as simple as a frame to hold the film and the original, a Sunlamp, and a large developing jar. More-sophisticated semiautomatic modules for printing and developing are available commercially.

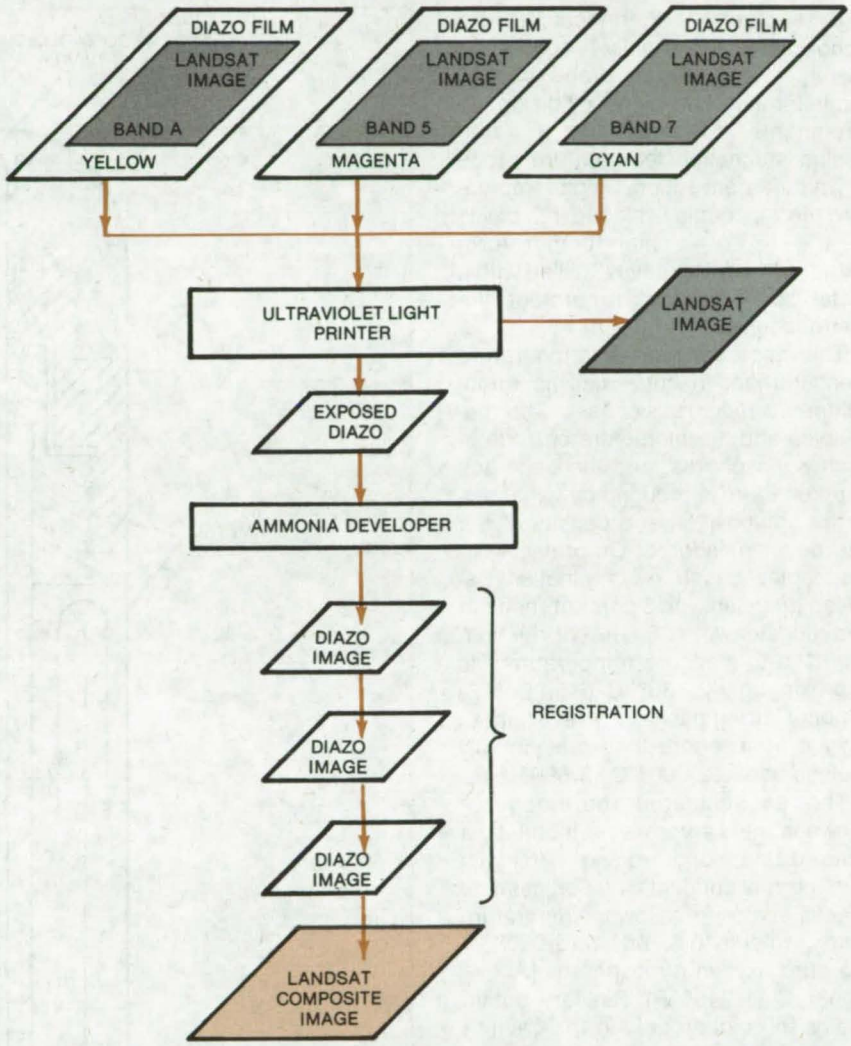

This Diazo Processing Procedure produces a composite image as its end product. Transparencies in shades of gray obtained by using different camera filters, such as those of the spectral bands of Landsat satellites, are placed over diazo emulsions of different colors and exposed to ultraviolet light. When the emulsions are developed in ammonia and superimposed in register, the layup acts as a spectral filter that enhances selected features of the ground scene in the original photographs.

This work was done by Shara Mount and Lee E. Whitebay of the University of Missouri — Rolla — for **Marshall Space Flight Center.** *Further information may by found in NASA CR-2953 [N78-17447], "Technique for Using Diazo Materials in Remote Sensor Data Analysis," a copy of which may be obtained at cost from the New England Research Application Center [see page A7].*

MFS-25110

A Thermocouple for Hot, Oxidizing Environments

Proposed temperature probe is enclosed in a nonoxidizing metal for use in harsh environments.

Langley Research Center, Hampton, Virginia

By enclosing a thermocouple in a nonoxidizing thermally conductive metal, a temperature probe can be made for very hot, highly oxidizing environments. It is made like a water-cooled stagnation temperature probe in which a conventional high-temperature thermocouple is placed in a cavity at the tip of a high-temperature-ceramic head. The cavity is filled with a metal such as gold to protect the thermocouple.

This approach makes temperature measurement in hot, oxidizing atmospheres a much easier task. Thermocouples and thermometers corrode in such atmospheres, and the accuracy of pyrometers is reduced by variations in the composition and density of the gas being monitored. Currently, thermocouples based on a junction between tungsten with 3 percent rhenium and tungsten with 26 percent rhenium are used to measure temperatures to approximately 2,730° C (≅5,000° F) in nonoxidizing gases. However, in an oxygen atmosphere they are virtually useless above 2,000° C (3,600° F).

The encapsulated thermocouple shown in the diagram is protected by a nonoxidizing, noncorroding metal with high thermal conductivity. For instance a gold enclosure allows temperature measurements to 2,760° C (5,000° F) in a pure oxygen atmosphere. [Above 1,063° C (1,945° F) capillary action retains the molten gold in the cavity.] By using shielding materials with the desired properties, similarly-constructed thermocouple probes could be made for other harsh environments as well.

This work was done by Renaldo V. Jenkins of **Langley Research Center.** *No further documentation is available.*

Inquiries concerning rights for the commercial use of this invention should be addressed to the Patent Counsel, Langley Research Center [see page A8]. Refer to LAR-12229.

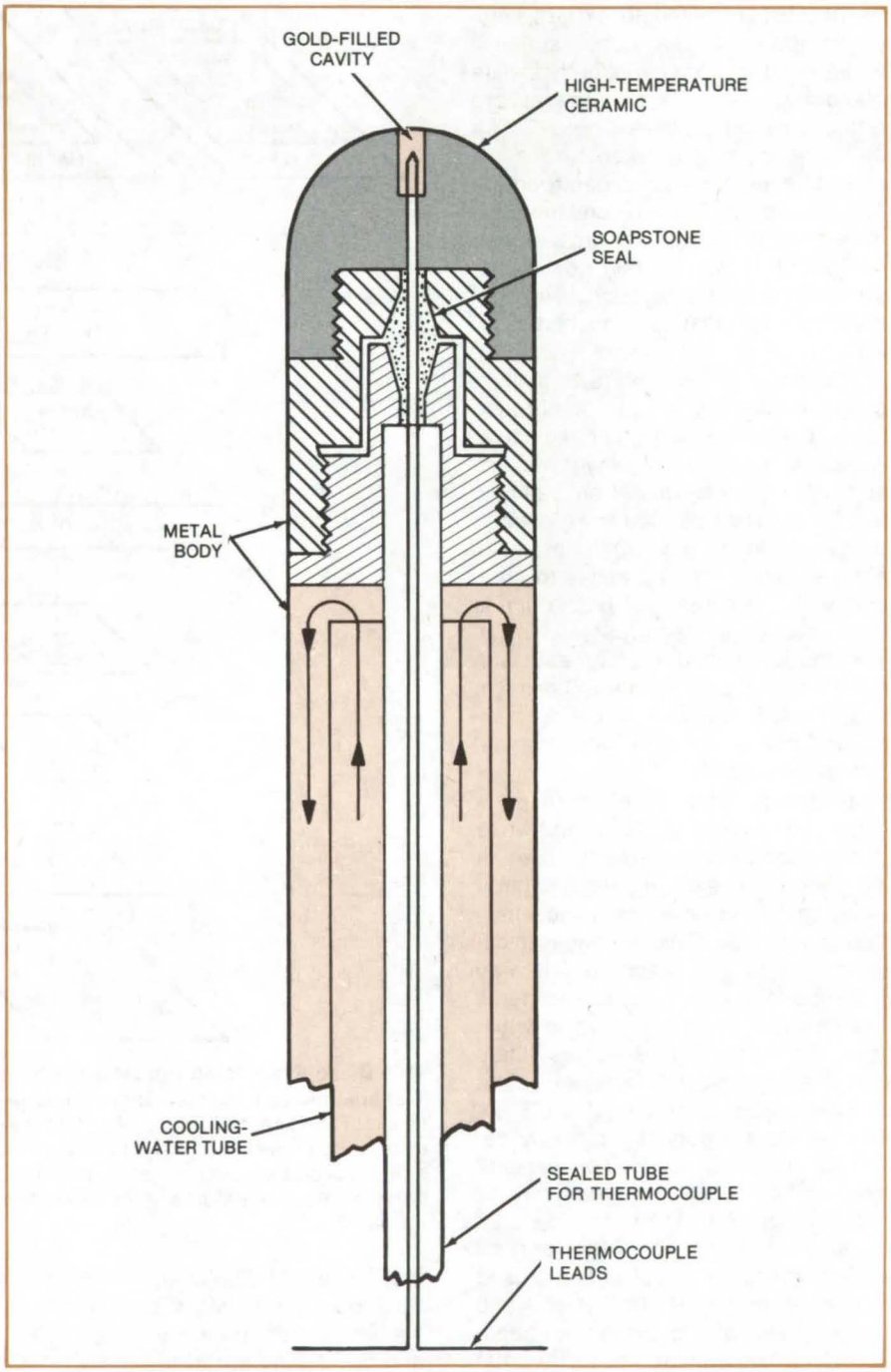

An **Encapsulated Thermocouple** makes this temperature probe useful in oxidizing environments at temperatures up to 2,760 ° C.

Airplane Stability Programs for Pocket Calculators

Three general-use programs and three stability programs are written for pocket calculator.

Langley Research Center, Hampton, Virginia

Six programs have been developed for use with card-programable pocket calculators utilizing "Reverse Polish Notation." Three of them are stand-alone equation-solving programs that will be useful for many applications. They were written to support three other programs to calculate longitudinal and lateral airplane stability.

The programs are summarized in the table. The first three are written for the International System of Units, stability axes, and the dimensional form of the stability derivatives. The equations programed include the effects of wind shear.

Program 4 applies Ferrari's methods for the roots of a quartic equation to the output of either Program 1 or Program 3 to determine the remaining eigenvalues of the characteristic equation of longitudinal or lateral motion. Normalized coefficients must be used for this program. Program 4 can be used as a stand-alone program to obtain the roots of a quartic equation, the highest order polynomial for which an explicit analytical solution for the root exists. In addition, this program may be used to solve for the roots of lower order equations, such as quadratics, cubics, and first-order equations.

Program 5 utilizes the eigenvalues computed by Program 4 to calculate such parameters as damping ratio, logarithmic decrement, and time to damp to one-half amplitude. These parameters are of use not only in aeronautics but in electrical engineering and in system studies.

Program 6 uses the polar-rectangular keys of the calculator to implement the Euler transformation used in rigid-body rotation. The transformation programed is the ψ, Θ, $\varnothing$ transformation that is frequently used in aeronautics. The use of the polar-rectangular keys permits a short program for this type of transformation. Both two-dimensional and three-dimensional transformations may be made. A comparison of the polar-rectangular method for three-dimensional transformation with a program that uses the traditional method of calculating the direction cosines shows that only 67 steps and 10 storage registers are required with Program 6, while a reasonably-efficient traditional program requires 124 steps and 20 storage registers.

Over the past several years, programable pocket calculators have developed into sophisticated devices having almost computer characteristics. Because of this sophistication, the newer models are capable of being programed to make very complicated calculations. It is to take advantage of the enhanced abilities of programable pocket calculators that these programs have been developed.

Program	Description
1	Calculates the elements of longitudinal stability determinant and normalized coefficients for characteristic equation.
2	Calculates the elements of lateral stability determinant and starts calculating coefficients of the characteristic equation.
3	Completes calculating coefficients of characteristic equations of lateral motion, calculates a real root of a fifth-order polynomial, and reduces the fifth-order polynomial to a fourth-order one; also calculates time to damp to one-half amplitude or to double amplitude for the real root determined.
4 (Stand-alone)	Uses Ferrari's method to calculate the roots of a fourth-order polynomial and can be used as a stand-alone program; will also determine the roots of cubic, quadratic, and first-order equations.
5 (Stand-alone)	Calculates stability parameters, such as time to damp to one-half amplitude and double amplitude, and the number of cycles to damp to one-half amplitude and double amplitude.
6 (Stand-alone)	Uses the polar-rectangular transformations of the calculator to implement the Euler transformation between space and body axes or body and space axes; saves about 57 program steps when compared with the more usual methods of programing.

Pocket Calculator Programs have been written for problems in airplane stability. Three of the programs may be used independently to solve problems in other disciplines.

This work was done by Windsor L. Sherman of **Langley Research Center.** *Further information may be found in NASA TM-78678 [N78-30138], "Airplane Stability Calculations With a Card Programmable Pocket Calculator," a copy of which may be obtained at cost from the North Carolina Science & Technology Research Center* [see page A7].

LAR-12479

Controlling a Wide Range of Flow Rates

A servo-operated valve and two flowmeters allow accurate control over a 1,900:1 flow-rate range.

NASA's Jet Propulsion Laboratory, Pasadena, California

A flow-control system regulates fluid flow over a 1,900:1 range of flow rates accurately to within 5 percent. The flow-control system was developed as part of a laboratory instrument for measuring the properties of confined fluids under conditions analogous to those encountered in deep drilling operations. Normal temperatures and pressures of these fluids are about 700° F (370° C) and 20,000 psi (140×10^6 N/m^2).

The system pressurizing pump must provide 20,000 psi pressure over an accurately-metered flow-rate range from 2 ml/min to 3.785 l/min. The larger flow rates dictate a large-diameter hydraulic cylinder for the pump. For the smaller flow rates, however, the velocity of the piston in a large cylinder would be only a few microinches per second. Such slow movement is extremely difficult to control. Moreover, reverse leakage around a large piston seal could be significant with respect to the low forward-flow rate.

To perform satisfactorily in all these conditions, the new flow-control system uses a servo-controlled hydraulic valve that admits driving fluid to an actuating cylinder, which drives another cylinder that provides operating fluid to the laboratory test system. The flow rate to the test system is sensed and compared with a desired-flow-rate setting, and the resulting error signal is used to adjust the servo-controlled valve.

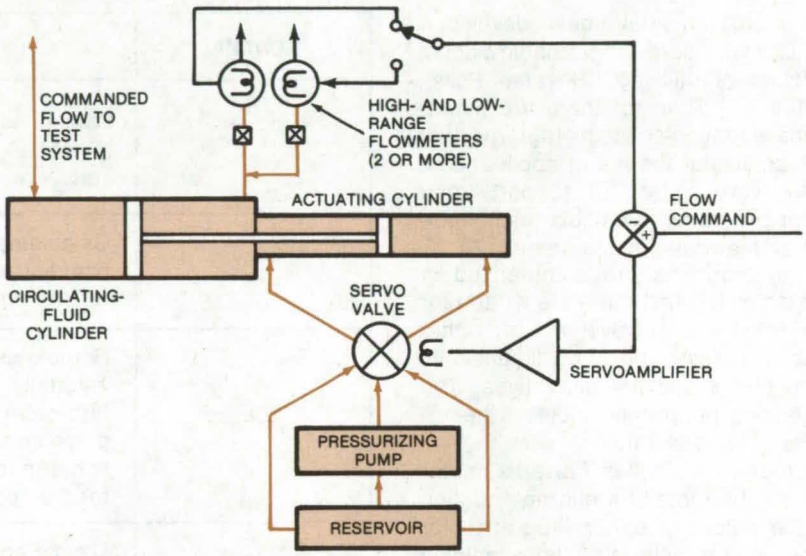

Flow-Rate Control (provided by the servo valve, actuating cylinder, and flowmeters) is kept separate from the pressurizing function (performed by the pump and reservoir) to ensure accuracy over a wide range of flow rates.

The servo-controlled valve admits only enough fluid to the actuating cylinder to provide the required flow in the instrument system. The unneeded fluid is returned to a reservoir. The pressurizing pump is therefore not a part of the control system; its sole function is to provide a 20,000-psi ambient. The actuating cylinder supplies and regulates the fluid that actually flows through the test instrument. Two or more flowmeters with slightly overlapping ranges accommodate the wide range of flow rates.

This work was done by Gerald S. Perkins of Caltech for **NASA's Jet Propulsion Laboratory.** *For further information, Circle 62 on the TSP Request Card.*
NPO-14312

Noninterfering Support for Aerodynamic Models

Metric half-span support increases the accuracy of subsonic and supersonic wind-tunnel measurements.

Langley Research Center, Hampton, Virginia

A new way of supporting wind-tunnel models does not distort the model or interfere with measurements of aerodynamic forces and moments. The support consists of a "sting," or cantilevered faired beam, attached to one wingtip of a symmetrical model (see figure); forces and moments are measured on the other half of the model.

The support — called the metric half-span support — is far enough away from the measurement half of the model that it has negligible effect on measurements at subsonic airspeeds. At supersonic airspeeds, the measured half of the model is forward of the shock wave emanating from the support and this is unaffected by the support.

The metric half-span support supplants two older types of support:

- The symmetric sting/balance support, in which balances (force and moment transducers) either internal or external to the model are mounted on a support sting: for performance measurements of a complete configuration, a rear sting supports the model for measurements on the fore-

body and wing, and for measurements on the afterbody and tail, the model is supported by a forward sting; and

- The half-span splitter-plate support, in which a plate parallel to the airstream supports the model at its plane of symmetry.

Both of these older types of support interfere with measurements, and the rear sting support distorts the model geometry.

In the metric half-span support, the support half of the model and the measurement half are joined at precisely the plane of symmetry of the model. This junction — the metric break — requires an airtight seal with low mechanical resistance. The force and moment transducer is constructed to cause minimum deflection at the metric break. With proper design of the support, there is no "scissors effect" across the break under aerodynamic loading, and distortion of the measurement half due to the support half is minimal.

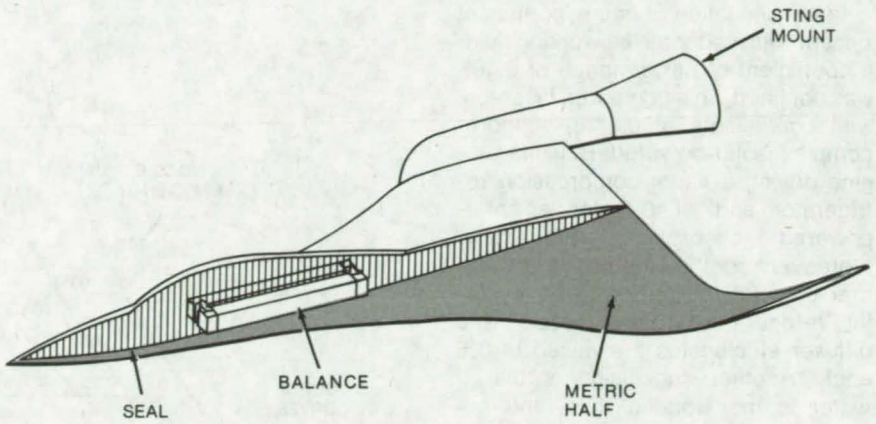

The **Metric Half-Span Support** holds a model at a remote corner. Forces and moments are measured on the shaded half of the model — far enough away from the support that it does not affect the accuracy of the measurements.

This work was done by Samuel M. Dollyhigh, Charlie M. Jackson, Jr., and David S. Shaw of **Langley Research Center.** *For further information, Circle 63 on the TSP Request Card.*

Inquiries concerning rights for the commercial use of this invention should be addressed to the Patent Counsel, Langley Research Center [see page A8]. Refer to LAR-12441.

Solar-Powered Jet Refrigerator

Design criteria are easily evaluated by a new analytic tool.

NASA's Jet Propulsion Laboratory, Pasadena, California

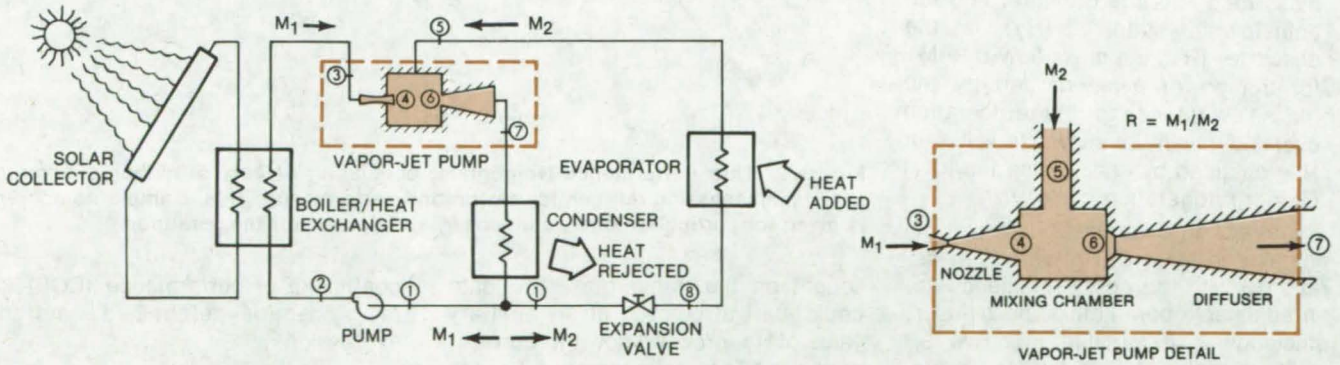

Figure 1. The **Vapor-Jet Refrigerator** is analogous to a single-fluid turbocompressor system with the turbocompressor replaced by a vapor-jet pump. The convergent/divergent nozzle converts the enthalpy drop between the boiler and evaporator to kinetic energy (analogous to the turbine function) and then converts the kinetic energy back into an enthalpy increase in the diffuser, raising its pressure to the condenser pressure (analogous to the compressor function). Performance is comparable to a solar-powered turbocompressor system, yet the hardware is much simpler.

The coupling of a solar collector to a vapor-jet refrigerator (see Figure 1) offers one interesting alternative to conventional solar-powered cooling systems. The design is simple, rugged, reliable, and vibration-free; and it can be operated and maintained at relatively low cost.

A new thermodynamic analysis of a solar-powered vapor-jet refrigerator combines important performance parameters in a nomogram that can assist in the design of a practical system. Projected coefficients of performance for different ejector configurations, working fluids, and other design variables are easily obtained from the nomogram.

(continued on next page)

In an evaluation of one hypothetical system, with water as the working fluid, a coefficient of performance of 0.465 was obtained. This compares favorably with coefficients of 0.5 for a more-complex solar-powered Rankine engine driving a vapor-compression refrigerator and of 0.6 for a solar-powered absorption refrigerator. Moreover, coefficients above 0.6 are predicted for a solar-powered vapor-jet refrigerator if the nozzle and diffuser efficiencies are raised to 0.9 each. Another conclusion is that if water is the working fluid, the coefficient of performance is double that of several organic fluids (such as butane).

As shown in Figure 1, solar energy vaporizes the power-cycle working fluid to saturated vapor in the boiler. Instead of the conventional turbine/compressor, a vapor-jet pump supports all of the enthalpy conversions. The balance of the system operates as a conventional single-fluid refrigerator.

The nomogram, illustrated in Figure 2, consists of four curves, one for each quadrant. By knowing the three independent temperatures of the system (boiler, condenser, and evaporator) and assuming saturated conditions, the thermodynamic properties of the coolant states 1, 3, and 5 labeled in Figure 1 are determined.

Curve 1 is constructed from the energy balance of vapor-jet pump. The mass ratio R is the ordinate, and the enthalpy in state 7 (H_7) is the abscissa. (R is the mass flow rate M_1 for the power cycle divided by the mass flow rate M_2 for the refrigeration cycle.) A minimum allowable value for R is obtained by considering the ideal Carnot refrigeration cycle.

Curve 2, in quadrant 2, is a plot of enthalpy in state 6 (H_6) versus mass ratio (R) with the nozzle efficiency as an adjustable parameter. The diffuser efficiency is a variable in curve 3, which is a plot of enthalpy H_7 versus H_6. Finally, the nomogram is completed by drawing a 45°-slope straight line through the origin in the fourth quadrant.

To determine the performance of a refrigerator with known operating temperatures and nozzle and diffuser efficiencies, a rectangular path is sought on the nomogram. The path could start at point A at an arbitrary value of H_7, proceed down to curve 4, continue horizontally to curve 3 at the selected diffuser efficiency, move up to curve 2 at the nozzle efficiency, travel horizontally to curve 1, and finally drop vertically back to A. If the selected value of A does not form a closed loop, the process is repeated until the loop converges and the value of R will then be determined. The coefficient of performance (COP) for the system is determined from the expression

$$COP = \frac{H_5 - H_1}{R(H_3 - H_1)}$$

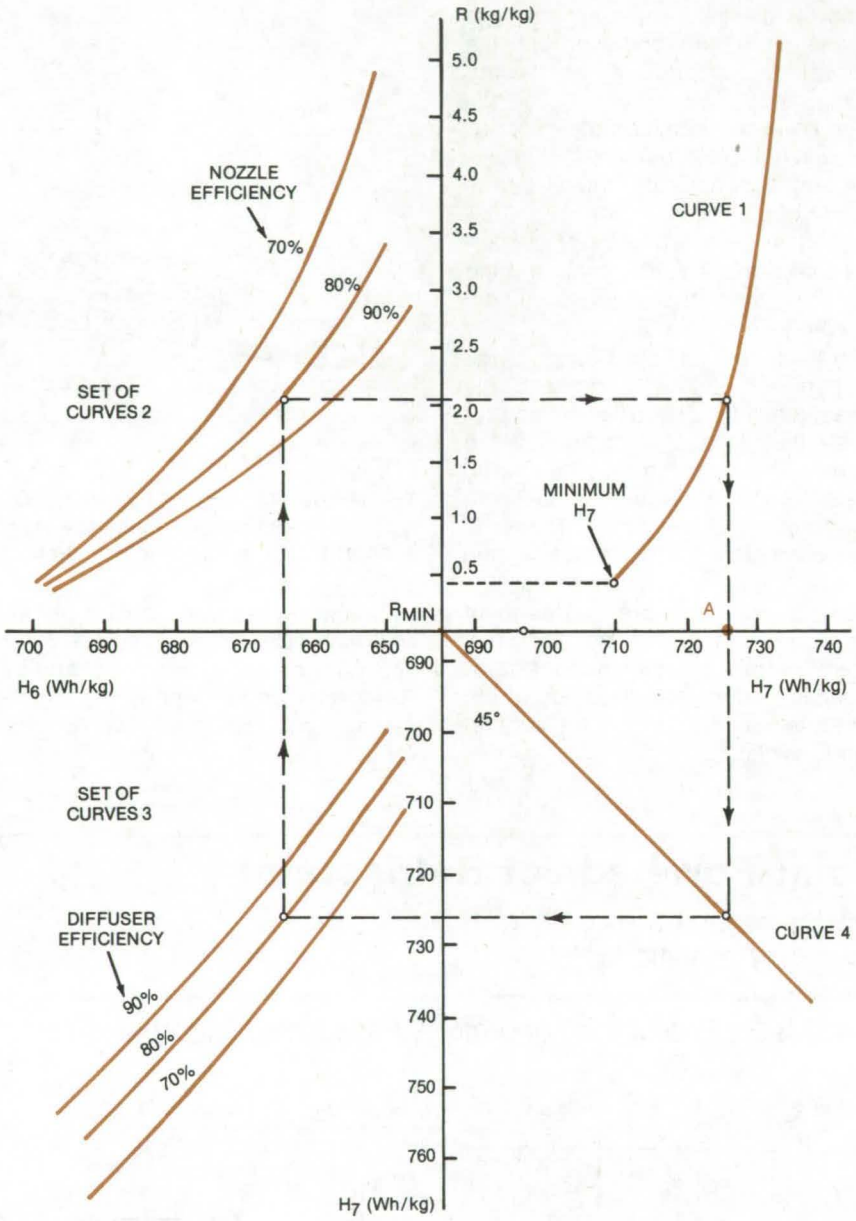

Figure 2. This **Performance Nomogram,** consisting of curves in four quadrants, assists in assessing refrigerator design and performance. This example nomogram is given for particular boiler, condenser, and evaporator temperatures.

This work was done by Victor W. Chai and Fikry L. Lansing of Caltech for **NASA's Jet Propulsion Laboratory.** *For further information, Circle 64 on the TSP Request Card.*
NPO-14550

Books and Reports

These reports, studies, and handbooks are available from NASA as Technical Support Packages (TSP's) when a Request Card number is cited; otherwise they are available from one of NASA's Industrial Application Centers or the National Technical Information Service.

Estimating Effects of Accidental Propellant Explosions

Workbook guides estimates of possible explosion damage during storage or handling.

A workbook has been written for assessment of the magnitudes and effects of blasts and fragments from ground system explosions. This workbook provides the designer and the safety engineer with rapid methods for predicting damage and hazards from explosions of liquid-propellant and compressed-gas vessels used in ground storage, transport, and handling.

Major topics covered in the workbook include:

- estimates of explosive yield,
- characteristics of pressure waves,
- effects of pressure waves,
- characteristics of fragments, and
- effects of fragments and related topics.

The information is presented in the form of graphs, equations, and tables for easy calculation using only desk or hand-held calculators. Complex methods used to develop some of the simple prediction aids are described in the appendixes. The workbook includes detailed solutions to sample problems and an extensive bibliography.

The methods described can also be applied to many types of industrial explosive-accident situations such as: gas pressure-vessel failures, road and rail tanker accidents with fuels such as liquefied petroleum gas, and chemical-plant piping failures.

A companion workbook for predicting damage and hazards from accidental explosions involving liquid propellants and compressed gases in flight vehicles and flight systems is included in this workbook in microfiche form and was previously published as "Workbook for Predicting Pressure Wave and Fragment Effects of Exploding Propellant Tanks and Gas Storage Vessels" (LEW-13042).

This work was done by Paul M. Ordin of **Lewis Research Center** *and W. E. Baker, J. J. Kulesz, P. K. Moseley, V. B. Parr, R. E. Ricker, L. M. Vargas, and P. S. Westine of Southwest Research Institute. A copy of this workbook, NASA CR-3023 [N79-10226], "Workbook for Estimating Effects of Accidental Explosions in Propellant Ground Handling and Transport Systems," and a copy of the previous publication, NASA CR-134906 [N76-19296], "Workbook for Predicting Pressure Wave and Fragment Effects of Exploding Propellant Tanks and Gas Storage Vessels," may be obtained at cost from the New England Research Application Center* *[see page A7].*

LEW-13247

Computer Programs

These programs may be obtained at very reasonable cost from COSMIC, a facility sponsored by NASA to make new programs available to the public. For information on program price, size, and availability, circle the reference letter on the COSMIC Request Card in this issue.

Flow Fields in Supersonic Inlets

Calculation based on method of characteristics

The flow fields in two- or three-dimensional axisymmetric supersonic inlets can be calculated with a computer program that uses the method of characteristics to compute an array of points in the flow field. At each point the total pressure, local mach number, local flow angle, and static pressure are calculated. The program can be used to design and analyze supersonic inlets by determining the surface compression rates and throat flow properties.

The method of characteristics for a perfect gas is used. The basic equation is the compatibility equation, which relates the change in stream angle to the change in entropy and to the change in flow velocity. To facilitate the computation, the flow field behind the bow shock wave is broken into regions bounded by shock waves. In each region, successive rays are computed from a surface to a shock wave until the shock wave intersects a surface or falls outside the cowl lip.

As soon as the intersection occurs, a new region is started, and the previous region is continued only in the area in which it is needed, thus eliminating unnecessary calculations. The maximum number of regions possible in the program is ten: This allows the simultaneous calculation of up to nine shock waves.

Inputs include surface contours, free-stream mach number, and various calculaton-control parameters. Outputs can be printed and/or plotted results. For plotted results, an SC 4020 or similar plotting device is required.

This program is written in FORTRAN IV to be executed in the batch mode and has been implemented on a CDC 7600 with a central memory requirement of approximately 27K octal of 60-bit words.

This program was written by Virginia L. Sorensen of **Ames Research Center.** *For further information, Circle E on the COSMIC Request Card.*

ARC-11098

Characteristics of Wing/Body/Tail Configurations

Static longitudinal aerodynamic for high angles of attack

Over the years, the high angle-of-attack aerodynamics of aircraft have become increasingly important in such areas as spin avoidance and the maneuverability of military aircraft at high altitudes. A principal distinguishing feature of high angle-of-attack aerodynamics is that the aerodynamic lift and pitching moments are no longer linear functions of the angle of attack. Another feature that requires special attention is the interference effect between the components of the complete configuration.

A package of computer programs is available that determines the longitudinal aerodynamic characteristics of wing/body/tail combinations including the effects of nonlinear aerodynamics of components and interference between components. Nonlinearities associated with symmetrical vortex shedding from the body nose are considered as well as the nonlinearities associated with the separation vortexes from the leading and side edges of the lifting surfaces. The wing and tail characteristics are calculated using lifting-surface theories, which include the effects of incidence, camber, twist, and induced velocities from external sources of disturbance such as bodies and vortexes. Comparisons between predicted and measured characteristics have been generally fair.

This package consists of the four programs: R1307, CRSFLW, SUBSON, and SUPSON. The R1307 program calculates aerodynamic characteristics based on a linear method and is limited to the small range of angles of attack for which the lift and moment characteristics of wings and bodies are linear with the angle of attack. The CRSFLW program uses a crossflow method to calculate the forces and moments on bodies alone or on wing/body combinations over a large angle-of-attack range. The SUBSON program calculates the longitudinal aerodynamic characteristics of wing/body/tail combinations at subsonic speeds. The SUPSON program calculates the longitudinal aerodyanic characteristics of wing/body/tail combinations at supersonic speeds.

Both SUBSON and SUPSON are intended for making calculations at angles of attack for which symmetrical pairs of vortexes are shed from the body nose and the leading and side edges of the lifting surfaces. The linear method used is by Pitts, Nielsen, and Kaattari and is one of the common methods for predicting lift and moment characteristics of wing/body/tail configurations at subsonic and supersonic speeds in the low angle-of-attack regime.

All of the computer programs retain as much of the linear method as possible. The linear method has been extended to include the effects of the vortexes. One basic modification made to the linear method is that lifting-surface theory is used to calculate the loading on the lifting surfaces since it can readily handle the induced camber associated with vortexes. The distributions of leading-edge and side-edge suction are converted to vortex lift using the Polhamus suction analogy.

These programs are written in FORTRAN IV for batch execution and have been implemented on an IBM 360 computer. The largest program, SUPSON, has a central memory requirement of approximately 259K of 8-bit bytes.

This program was written by Marnex F. E. Dillenius, Fredrick K. Goodwin, David M. Kline, and Michael R. Mendenhall of Nielsen Engineering & Research, Inc., for **Ames Research Center.** *For further information, Circle F on the COSMIC Request Card.*
ARC-11224

Advanced-Panel Pilot Code

Higher-order surface-paneling program for subsonic and supersonic flows

A numerical research program has been written to help establish "proof-of-concept" for a newly-developed higher-order panel method applicable to both subsonic and supersonic flows about nearly-arbitrary aircraft configurations. It is intended to solve a variety of boundary-value problems in steady-subsonic or supersonic inviscid flow. The software was developed as a vehicle for numerical experimentation, and it is based on linearly varying source and quadratically-varying doublet distributions for computing solutions to the linearized potential flow equations.

The configuration to be analyzed is divided into a number of networks, which collectively describe the outer or wetted surfaces of the configuration and its wakes. Every network surface is specified by giving the coordinates of an array of grid points, which the program connects with contiguous panels.

Generally, every panel of every network is covered with a distribution of sources and doublets. The quadratic doublet strength is made continuous across panel and network edges to eliminate spurious line vortex effects.

Having been developed primarily for proof-of-concept and numerical experimentation, this program is not completely user oriented; however, results to date indicate that the underlying methodology is sound. Inputs to the program include flow conditions, network-geometry specifications, and boundary conditions. Outputs consist of geometry or mesh point data, control point data, boundary-condition defining parameters, problem and network indices, equation-solution data, aerodynamic input data, singularity data, local aerodynamic data, and force and moment data.

This program is written in FORTRAN IV for batch execution and executes on CDC 7600 computers operating under SCOPE 2.1.3. and CDC 6600 and Cyber 175 computers under NOS 1,2. The program uses overlay structure and has a central memory requirement of approximately 132K (0ctal) of 60-bit words.

This program was written by Gary R. Bills, Michael A. Epton, and Forrester T. Johnson of the Boeing Commercial Airplane Co. for **Ames Research Center.** *For further information, Circle G on the COSMIC Request Card.*
ARC-11278

Arbitrary Aircraft-Geometry Generator

Fuselage and planar-surface geometries are determined.

GEMPAK helps designers to generate detailed configuration geometry with much flexibility in their choices of configurations and details of description. At the same time, input requirements, program turnaround time, and cost are kept low. The program consists of routines that generate fuselage and planar-surface (winglike) geometries and a routine that determines the true intersection of all components with the fuselage.

GEMPAK consists of three major parts: the fuselage generator, the generator for planar surfaces, and the module for integrating the planar-surface components with the fuselage. Each component is input and generated independently. The program then scales the resulting individual geometries for compatibility and merges the components into an integrated configuration. This technique permits the user to easily make isolated changes to the configuration.

There are three modes of modeling the fuselage. The first is complete lofting where the fuselage is defined analytically by from 3 to 11 lofting curves that may be continuous or discontinuous. The user needs to input only the minimum number of points that can be fitted with conic sections for a good reproduction of his configuration. The second mode of fuselage modeling is cross-section lofting. This mode is structured around lofting data input for discrete prescribed cross-section locations. The model is not analytic in the longitudinal direction.

The third mode is a point-by-point mode and requires that all surface points be input at discrete longitudinal locations. The model resulting from this mode is completely nonanalytic. No interpolation routines are provided in either longitudinal or cross-sectional directions. The amount of required input is least for mode 1 and greatest for mode 3.

The wing, canard, horizontal tail, fin, and elevon are all generated in an identical manner. There are two basic options for input to this planar-surface section of the program. The first is to generate a one- or two-panel surface with such basic input parameters as aspect ratio, taper ratio, and sweep angles. (A slab-sided airfoil or a circular arc airfoil can be input with a minimum of input, or the coordinates of an arbitrary airfoil can be listed.) The second is to input a point-by-point description of all airfoils. Once the planform and airfoil descripton have been entered by either method, there are program options to change dihedral, twist, coordinate translation, angle of attack, and roll angle of the previously defined wing. Control surfaces may also be defined and deflected. After all of the geometry for the separate parts has been generated, then control passes to the merge section of the program. Merge calculates the intersection of all the planar surfaces with the fuselage.

Inputs consist of program option flags and data to define the geometry of the fuselage and the winglike portions of the aircraft.

This program has been implemented in FORTRAN IV on a CDC 6000-series machine with a central memory requirement of approximately 65K (octal) of 60-bit words.

This program was written by Clyde L. W. Edwards, William J. Small, and Sharon H. Stack of **Langley Research Center.** *For further information, Circle H on the COSMIC Request Card.*
LAR-12515

Reliability of Nondestructive Evaluation Data

Probability of defect detection for small sample sizes

A new program calculates the probability of detection of defects at selected confidence levels from nondestructive evaluation data. It provides an alternate method of grouping sample data to obtain a reasonable value for the lower confidence limit with a small sample size.

In nondestructive evaluation (NDE) of structural components that might contain defects, two significant events can occur: (1) detection of a defect that is present or (2) nondetection of a defect that is present. An event that has two possible outcomes such as detection or nondetection is referred to as a binomial event and is best described by a binomial distribution. The lower confidence limit [p(1)] for a given defect size can be calculated using the binomial distribution. The spread between the point estimate [p(av) = number of detections (n) divided by the sample size (N)] and p(1) increases as the sample size decreases.

The technique used by this program to overcome problems of small sample size is called the optimized probability of detection (OPD) method. When a limited number of data points is available for calculating inspection reliability, it becomes essential to use alternative methods for grouping the data to overcome the problem of small sample size. The optimized probability method is one such alternative. It demands significantly greater computational effort than other methods but offers the potential for producing less spread between p(av) and p(1). The improvement is entirely the result of increasing the size of the sample that forms the basis for calculating p(1).

The data are arranged in order of decreasing flaw size. They are then divided into m intervals with the largest flaws grouped in the interval with the maximum flaw size. There can be as few as one data point in each interval, but the maximum number of intervals is generally controlled by computer limitations. The first value of probability for the reliability curve is obtained by calculating the value of p(1) for each of the following intervals: m; [m + (m − 1)]; [m + (m − 1) + (m − 2)]; . . . [m + (m − 1) + (m − 2) + (m − 3) + . . . 1]. The maximum value of p(1) as defined by this series of computations is plotted at the largest flaw size in interval m. Next, the data in interval m are deleted, and the calculations of p(1) are repeated for intervals (m − 1);

(continued on next page)

$[(m-1)+(m-2)]$; $[(m-1)+(m-2)+(m-3)]$; . . . $[(m-1)+(m-2)+(m-3)+\ldots 1]$.

The maximum value of p(1) in the second series is plotted at the largest flaw size in interval $(m-1)$. The computations are repeated until the data are exhausted. Each time, the interval containing the largest flaws that was included in the previous computation is dropped, and a maximum value of p(1) is computed and plotted. The computed value of p(1) for the interval containing the smallest flaws is the last entry on the reliability curve.

In all instances, the plotted value of p(1) is biased conservatively by the inspection results from smaller flaws. Using the OPD technique, probability-of-detection is a much smoother function of defect size or crack length than in either the equal-flaw-size-interval method or in the overlapping-interval, equal-sample-size method. The maximum crack size that can be stored and analyzed is 1 in. (2.54 cm). The maximum number of data points that can be combined into a set is 1,000.

This program has been implemented in FORTRAN IV on a UNIVAC 1100-series computer with a central memory requirement of 21K of 36-bit words and uses the CALCOMP plotting package to produce plotted output.

This program was written by J.C. Couchman and B.G.W. Yee of General Dynamics Corp. for **Lewis Research Center.** *For further information, Circle J on the COSMIC Request Card.*
LEW-12908

Machinery

Hardware, Techniques, and Processes

Books and Reports

Extra-Safe Tractor-Trailer Coupling

A built-in safety mechanism prevents trailer uncoupling in case of kingpin failure.

Dryden Flight Research Center, Edwards, California

A built-in safety mechanism for a tractor-trailer "fifth-wheel" coupling (see Figure 1) keeps the rig together in case of kingpin failure. The modified coupling utilizes all the standard components, such as two wear plates, a kingpin, and a kingpin latch. As in a conventional fifth wheel, with the coupling in position and latched, the tractor and trailer are free to pivot in the horizontal plane about the kingpin.

The coupling is modified by adding a semicircular lip to the top wear plate, a matching semicircular slot to the bottom wear plate, and two latching stop mechanisms. The stops are roughly 90° apart in the horizontal plane, adjacent to the semicircular slot on the lower wear plate. Each mechanism (one is shown in Figure 2) has a dog that holds the semicircular lip in the slot. The up and down positions of the dog are controlled by a horizontally-traveling lever arm. The arm extends through a slot to impart downward motion to the dog. A curved leaf spring continuously applies an upward force to the dog.

The tractor is backed in and positioned so that the kingpin moves through a throat on the bottom wear plate. As the pin comes to rest in its latch, the curved lip engages its slot, first depressing and then releasing the dog. The dog springs back, locking the lip in place.

The mechanism is disconnected by throwing the lever arm horizontally so that the arm locks into a relief. This depresses the dog, allowing the curved lip to clear the entire assembly.

This work was done by William P. Albrecht and Ralph H. Sparks of **Dryden Flight Research Center.** *For further information, Circle 65 on the TSP Request Card.*

This invention has been patented by NASA [U.S. Patent No. 3,995,877]. Inquiries concerning nonexclusive or exclusive license for its commercial development should be addressed to the Patent Counsel, Dryden Flight Research Center [see page A8]. Refer to FRC-10081.

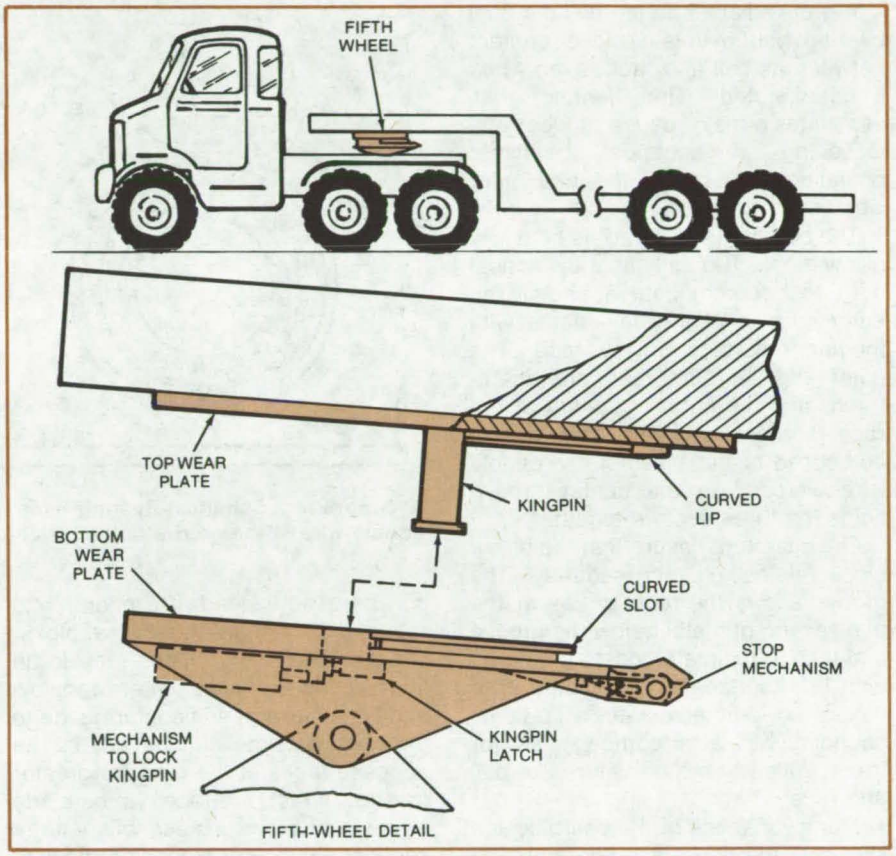

Figure 1. This **Modified "Fifth-Wheel" Coupling** has the usual top and bottom wear plates, kingpin, and kingpin latch. A curved lip, a curved slot, and two identical stop mechanisms are added (one is shown) to prevent the coupling from disengaging in the event of kingpin failure.

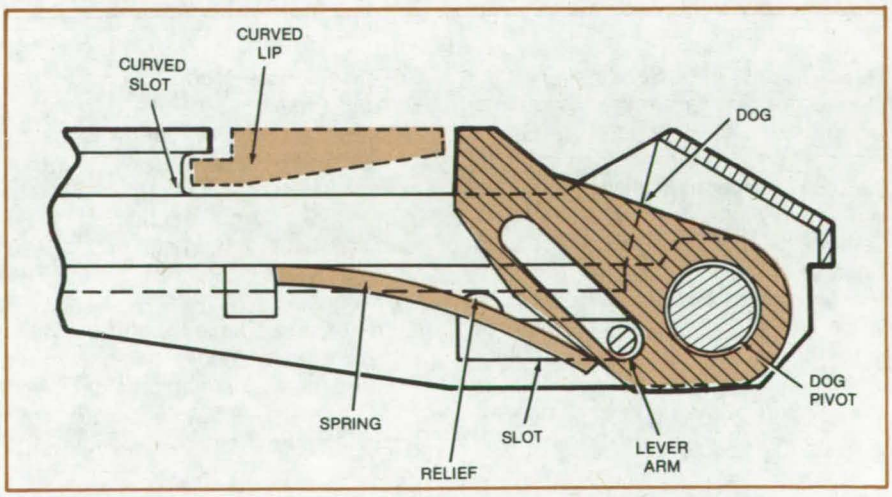

Figure 2. A **Detailed View of the Stop Mechanism** shows a horizontally-traveling lever arm. When the arm is moved to the left, it depresses the dog, allowing the trailer to disconnect.

Lash-Free Spherical Bearing

Conforming race eliminates pounding when the bearing vibrates.

Marshall Space Flight Center, Alabama

A grooved and chamfered spherical bearing can maintain close contact between its ball and race, even when it is vibrated. The bearing thus eliminates a major cause of wear and loosening in spherical bearings: pounding of the ball on the race under vibration.

The bearing (see figure) is held in a pillow block. The ball has a cylindrical bore to accommodate a shaft. The outer surface of the ball mates with the inner surface of the race. The outer edges of the race are chamfered, and the outer periphery of the race is deeply grooved. The race is composed of three sectors; a double wire wrapped in the center groove holds the three sectors together.

The chamfers ensure that the pillow block retains the race securely. The groove allows the race to flex at the thin section of metal below the groove and thus to maintain constant contact with the surface of the ball. The flexure not only eliminates vibrational pounding but also compensates for irregularities in the curvatures of ball and race.

Many variations of the basic design shown in the figure are possible. For example, additional shallower grooves can be provided for the wire that holds the race sectors together. A flange can be used instead of a chamfer to retain the race in the pillow block. Grooves can be cut in the race in an intersecting wafflelike pattern to allow additional flexture and conformance to the ball; or slots can be cut in the opposite faces of the race for greater flexure. In fact, the race can be made in a single piece instead of in three sections, if slots, extending beyond the centerline of the race, are cut in an interleaving pattern from opposite faces of the race.

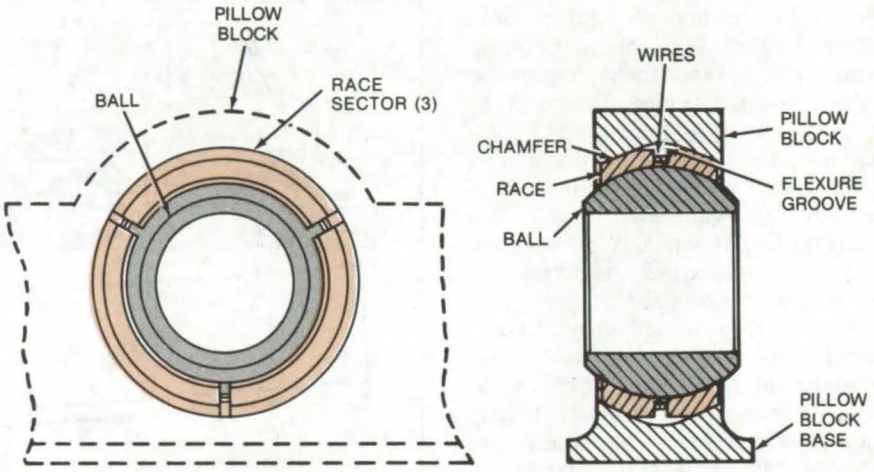

A **Groove in a Spherical-Bearing Race** allows the race to flex around the ball. The double wire in the groove holds the three sectors of the race together.

This work was done by Leopold A. Hein and W. Neill Myers of **Marshall Space Flight Center.** *For further information, Circle 66 on the TSP Request Card.*

This invention has been patented by NASA [U.S. Patent No. 4,105,261]. Inquiries concerning nonexclusive or exclusive license for its commercial development should be addressed to the Patent Counsel, Marshall Space Flight Center [see page A8]. Refer to MFS-23447.

Transducer With a Sense of Touch

A sensor that determines the shape and pressure distribution of an object in contact with its surface can improve the utility of mechanical manipulators and other remotely controlled devices. Comprised of an array of electrodes beneath a covering of pressure-conductive plastic, the sensor output can be displayed on a video monitor or used to control mechanical or electrical equipment. The sensor is already part of the hand of a robot.
(See page 173.)

Splicing Single-Mode Optical Fibers

A precision cleaver with a tungsten carbide knife edge and a welding tool that consists of a micromanipulator, microscopes, and vacuum chucks combine in a procedure for cutting and splicing hairlike optical fibers. The fiber ends, typically only 4 mils in diameter, are cleaved, butted together, and then welded with an electric arc. The three-axis manipulator makes it easy to aline the fiber ends precisely and to guide them into contact for welding.
(See page 296.)

Tool Cuts Self-Locking Joints in Plastics

Three lathe tools were developed to skive strips roughly 0.1 in. thick by 0.5 in. wide and several hundred feet long from disks of PTFE and 25 percent glass fibers. Used to form a self-locking spiral-wound seal, the strips are cut with either flat or interlocking surfaces. A triangular projection on one tool and a triangular notch on another cut the interlocking surfaces.
(See page 290.)

Cryogenic-Container Suspension Strap

A supporting strap has low thermal conductivity.

Ames Research Center, Moffett Field, California

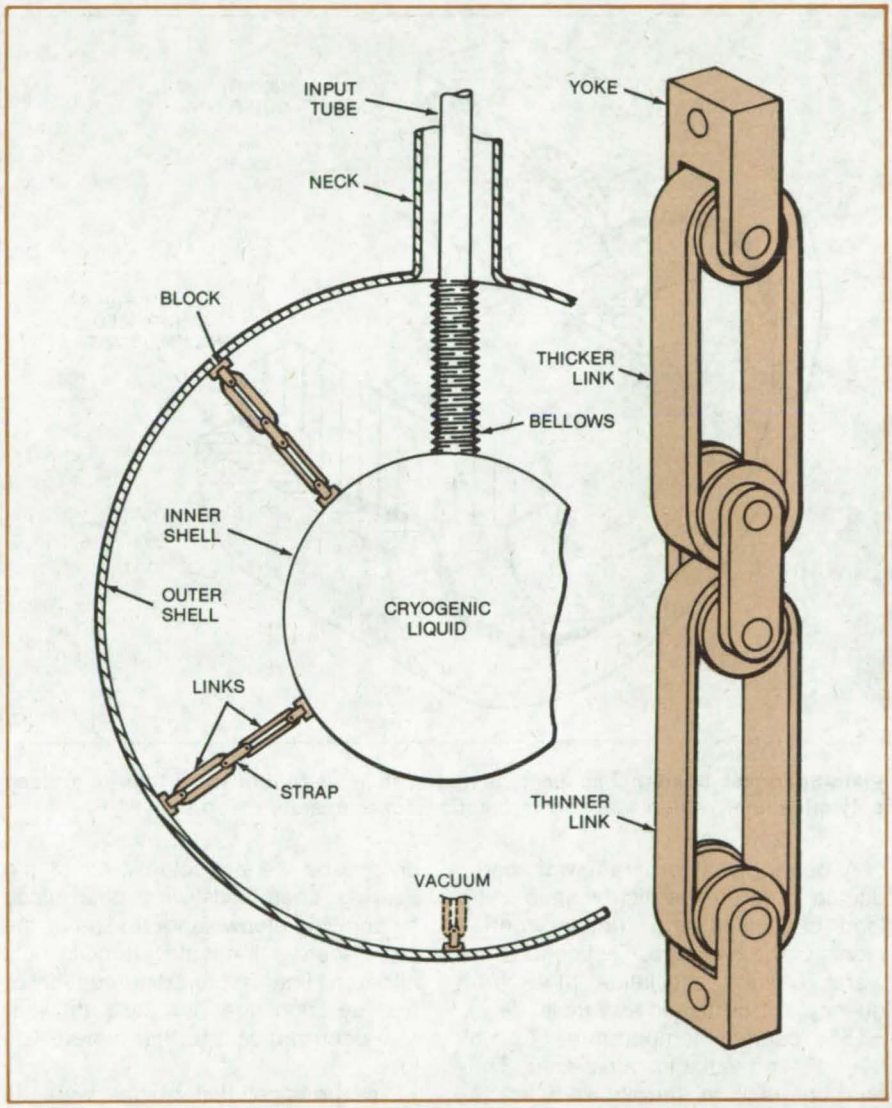

A **Cryogenic-Container Suspension Strap** is made from two fiberglass/epoxy links. The inner link adjacent to the colder environment is half as thick as the outer link. This reduces the heat leakage from the outside by one-half and retains uniform strap strength. The composite material strengthens with cold.

A fiberglass/epoxy supporting strap holds the inner shell of a cryogenic storage tank away from the outer shell. The strap, made of two or more links, reduces the heat leakage into the cryogenic fluid more efficiently than conventional suspension systems.

The strap is made from a unidirectional fiberglass/epoxy composite material, which has high strength-to-density and strength-to-thermal conductivity ratios at cryogenic temperatures. At a temperature of 4 K, the tensile strength and fatigue strength of the material are about double those at room temperature.

A typical strap (see figure) is made by joining two links by a bar secured on both ends by connecting pins inserted through spools. An additional pair of connecting pins secures yokes on the strap ends to the inner and outer shell walls; the space between the walls is evacuated.

The thickness of the link connected to the inner shell is about one-half that of the outer link. This reduces the transfer of heat from the outside by one-half what it would be with identically thick links. The strap strength remains uniform because the thinner link is next to the colder environment. A number of these straps supports the inner storage tank.

This work was done by John W. Vorreiter of **Ames Research Center.** *For further information, Circle 67 on the TSP Request Card.*

This invention is owned by NASA, and a patent application has been filed. Inquiries concerning nonexclusive or exclusive license for its commercial development should be addressed to the Patent Counsel, Ames Research Center *[see page A8].* *Refer to ARC-11157.*

Composite Bearing Liners Have Service Temperature of 600° F

Self-lubricating graphite-fiber-reinforced polyimide liners for plain bearings raise service temperature from 325° to 608° F.

Lewis Research Center, Cleveland, Ohio

Plain-spherical bearings with molded liners of self-lubricating graphite-fiber polyimide composite were developed, and their dynamic load capacities were determined. Liners were prepared by transfer-molding a prepolymer resin/fiber mix into the space between the ball and outer race, then completing polymerization under heat and pressure. The upper service temperature was increased from 325° F (163° C), which is the limit in current polymer-lined bearings, to 608° F (320° C) by developing bearing liners of graphite-fiber-reinforced polyimide. The liner composition is 50 weight percent, chopped, random, graphite fibers in a polyimide resin. Most of the work was concentrated on the plain-spherical bearing design shown in the figure.

Self-lubricating polymer composites are often used as liners for plain-cylindrical and plain-spherical sliding-contact bearings. Most of these polymer-base materials are limited to fairly-low-temperature service. For example, fiber-reinforced polytetrafluoroethylene (PTFE) liners have excellent lubricating characteristics but are limited for high load applications to a maximum recommended service temperature of 325° F. The problem was to develop a self-lubricating polymer-base bearing liner with higher temperature capabilities.

The molded liners for plain-spherical bearings were made by transfer-molding a mixture of partially polymerized (B-staged) polyimide and graphite fibers into the space between the ball and race, then completing the polymerization under heat and pressure. During this procedure the ball and race were concentrically mounted and functioned as the main elements of the mold. The ball was precoated with a mold release to minimize adhesion between the ball and the composite. The inside of the outer race was precoated with a polyimide resin to enhance the adhesive bond of the composite.

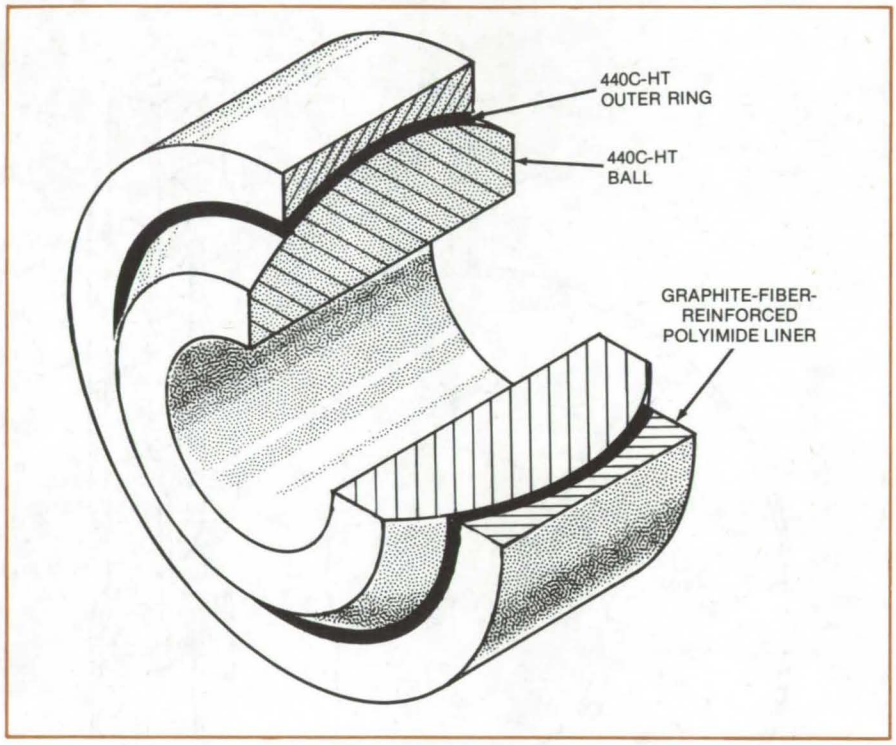

Plain-Spherical Bearing has been tested with a self-lubricating fiber-reinforced polyimide liner, which was shown practical for temperatures up to 608° F.

A bearing test program was conducted to determine the dynamic unit-load capacities and friction coefficients of the bearings. Test conditions were: bearing oscillation at a frequency of 1 hertz and an amplitude of ±15°, bearing temperatures up to 608° F, and variable radial load. The test bearings in the figure were a plain-spherical design with a 0.060-in.-thick (0.152-cm) self-lubricating (graphite-fiber-reinforced polyimide) liner, a 1-in.-diameter (2.5-cm) ball (440C-HT steel), and a 0.5-in.-wide (1.3-cm) outer ring (440C-HT steel) to give a projected load-bearing area of 0.5 $in.^2$ (3.2 cm^2). These liners were always used in contact with corrosion-resistant alloys because the graphite content can cause galvanic corrosion of active metals such as aluminum.

The dynamic unit-load capacity is the oscillating load limit of the bearing divided by the projected area of the bearing. Load limits were determined by applying stepwise increases in the radial load at 5-minute intervals until either the liner fractured perceptibly or a large, nonlinear increase in wear rate occurred with further increase in load.

The principal test results were as follows:

1. Dynamic load capacities were 23,000 psi (160×10^6 N/m^2) from room temperature to 392° F (200° C), 20,000 psi (140×16^6 N/m^2) at 500° F (260° C), and 100,000 psi (69×10^6 N/m^2) at 608° F. These values are about one-half of the load capacity specified for conventional airframe bearings with PTFE liners at room temperature but are much higher than the load capacities of the conventionally lined bearings above 325° F.

2. Friction coefficients tended to decrease with increases in temperature and load and were typically in the range of 0.15 to 0.20 at room temperature and 0.05 to 0.10 at 608° F.

This work was done by Harold E. Sliney of **Lewis Research Center.** *Further information may be found in NASA TM-78935 [N78-26445], "Some Load Limits and Self-Lubricating Properties of Plain Spherical Bearings with Molded Graphite Fiber Reinforced Polyimide Liners to 320° C," a copy of which may be obtained at cost from the New England Research Application Center [see page A7].*
LEW-13277

All-Metal Muffler for Ducts

Metal baffles attenuate sound in ducts without clogging or polluting the airstream.

Ames Research Center, Moffett Field, California

An all-metal muffler attenuates the sound of air flowing in ducts. Unlike silencers made of bulk materials, such as fiberglass, plastic foam, or mineral wool, the new all-metal muffler does not become clogged, packed down, or eroded; yet it has a broad bandwidth (in contrast to narrow-bandwidth honeycomb-core silcencers made without bulk material). Moreover, the metal muffler does not absorb oil and soot, which are potential fire hazards, and it does not release fibers, which can pollute the downstream air.

As shown in the figure, the muffler consists of streamlined parallel baffles with spaces between them for the airflow. Each baffle has a perforated metal skin and a series of triangular cavities formed by solid metal sheets. The airflow and sound waves pump air in and out of the holes in the skin, so that much of the sound energy is dissipated by viscous flow. Additional attenuation occurs in the cavities formed by the septa, through the process of resonant absorption. Because the septa are at an angle (diagonal) to the skin, the cavities respond to a wide range of sound frequencies. The varying depth also prevents flow-induced whistles.

The skin is galvanized steel or aluminum sheet with holes over 5 percent of its area. (The skin on the nose and tail sections is unperforated.) The holes are 1.5 to 3.2 millimeters in diameter. The baffle thickness and spacing depend on such factors as the allowable pressure drop in the airstream and the level of sound attenuation required.

Typically, the baffle thickness is one-quarter the wavelength of the highest frequency to be attenuated, and a baffle array blocks one-third to one-half of the duct area. These values are about the same as those typical of a fiberglass muffler. However, the metal muffler is 60 to 70 percent longer than a fiberglass one for the same attenuation. Although the metal muffler is longer than a fiberglass equivalent, the cost of the extra length is offset by the savings in the costs of fiberglass protective membranes, and screens.

The length of a cavity (dimension L in the figure) can be chosen to tune the muffler for a desired frequency range. The length should be half the wavelength of the primary frequency to be attenuated. The length can vary from one cavity to the next for broadband attenuation. More attenuation can be introduced by perforating the septa and covering them with a sound-absorbent material. The baffles can also be curved to obstruct the line-of-sight along the duct and thus block the propagation of sound in that direction.

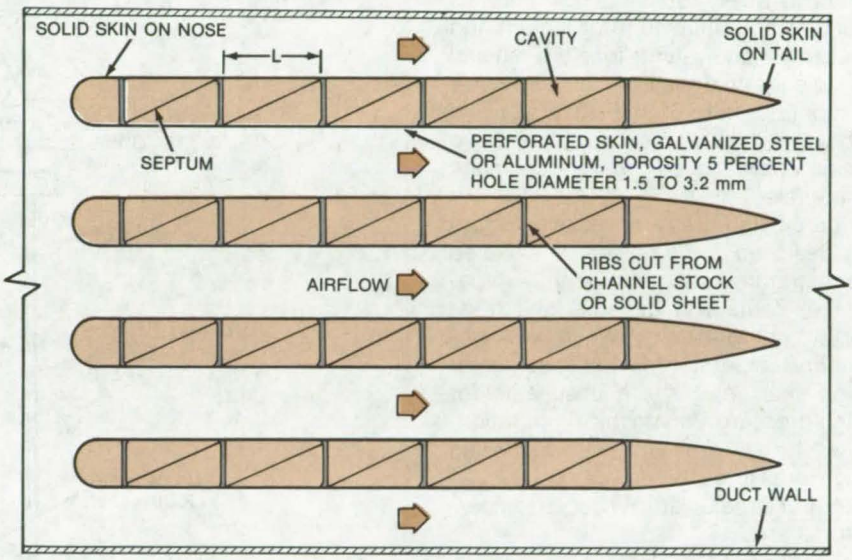

Steel- or Aluminum-Skinned Baffles absorb sound from air flowing over them. Because there is no bulk filler, the muffler does not collect contaminants. If dirt accumulates on the skin, it can be washed away without damaging the muffler.

This work was done by Paul T. Soderman of the U.S. Army and Terry D. Scharton of Bolt Beranek & Newman Inc. for **Ames Research Center.** *No further documentation is available.*
ARC-11159

Multipurpose Seals for Pressure Vessels

Cryogenic or multipurpose seals made by using new materials.

Lewis Research Center, Cleveland, Ohio

Several high-pressure, 40,000-psi (2,721-bar), cryogenic seal systems suitable for large pressure-vessel applications have been developed. The design uses indium seal rings, brass or 304 stainless-steel anvil rings, and two O-rings of silicone rubber or a commercially available material equivalent to Kel-F. Substituting materials such as soft aluminum for indium and Kalrez (or equivalent) for Kel-F should enable the seal systems to be used for temperatures to 600° F (316° C) and above at high pressure, although no seals have been made of such materials.

Large high-pressure vessels (Figure 1) designed for ambient or elevated temperatures are not presently capable of containing gaseous helium at equivalent pressures when at cryogenic temperatures, because common seal designs are unsuitable for high-pressure cryogenic operation. The primary problems with achieving high pressures of 40,000 psi (2,721 bars) or greater at cryogenic temperatures are:

1. Common seal designs are unsuitable due to extreme O-ring shrinkage as temperatures are reduced.
2. Elastomers become brittle and inflexible, lose compressibility to maintain a seal, and are susceptible to fracture and decompression blisters.

Pressure vessels must have the seal opening (Figure 2a) enlarged in order to allow installation of the high-pressure cryogenic seal system (Figure 2b). The seal system is an eight-part seal consisting of a 304 stainless-steel convex-wedge-shaped anvil backup ring, two brass double-convex anvil rings, three indium seal rings, and two Kel-F O-rings. This seal system has successfully contained pressures to 30,000 psi (2,040 bars) with liquid nitrogen (77.3 K) and 40,000 psi (2,721 bars) with liquid helium (4.2 K), which were the vessel-pressure design limits.

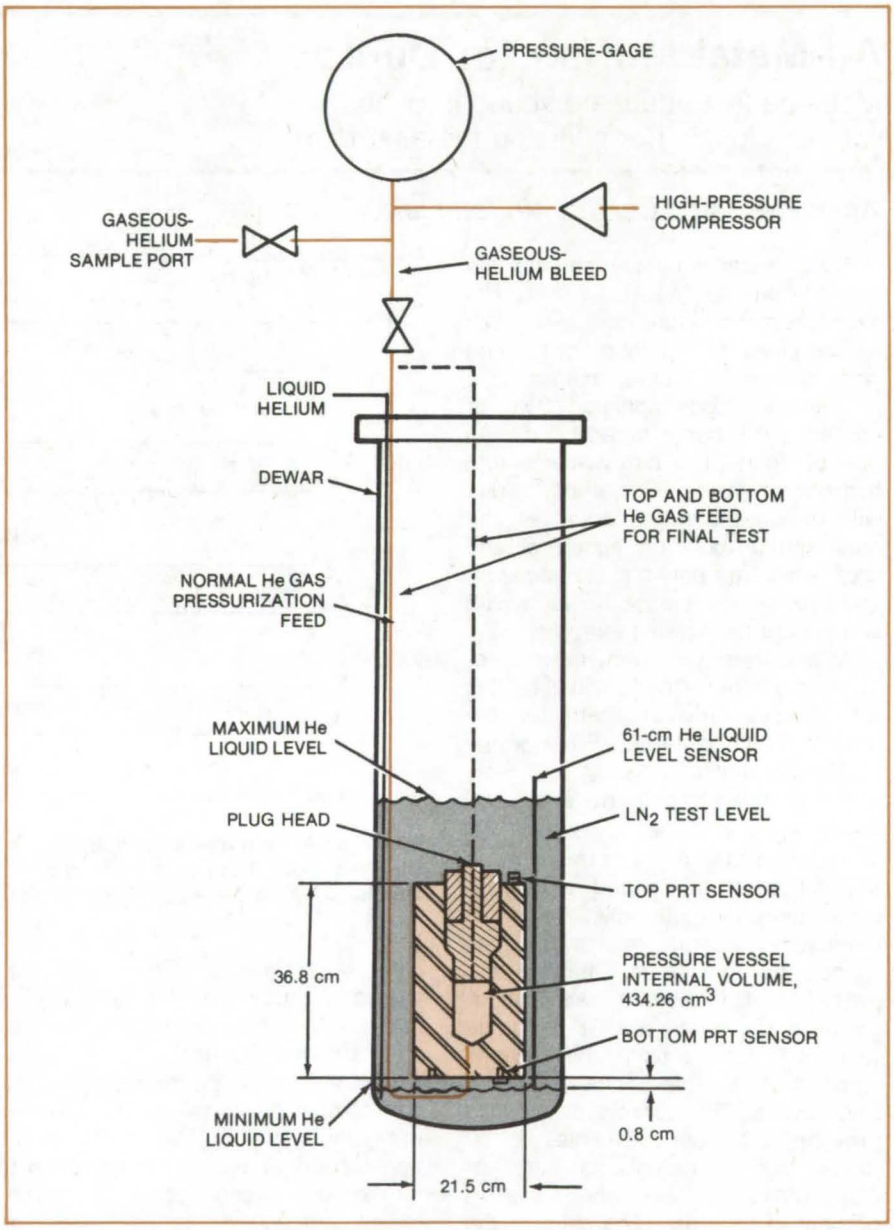

Figure 1. **Relatively-Large High-Pressure Vessel** originally designed for ambient or higher temperatures is shown as used at cryogenic temperatures. At these low temperatures, the conventional pressure seals shrink, and their properties degrade, making it impossible to maintain high pressures within the pressure chamber.

This newly developed seal possesses sufficient flexibility to contain high-pressure fluids regardless of dimensional changes from either pressure and/or temperature effects. The seal system operates in a dual mode. Increased pressure supplements the total sealing effort of the seal system, which self-compensates for vessel expansion and yet has the capability to flex and compensate for thermal contraction.

These capabilities are inherent in the seal system due to the double O-ring that functions as a pneumatic piston by providing a sustaining compressive force to enable a continuous extrusion of the indium seal rings. The extruded seal rings sandwiched between the anvil rings are compressed with increasing pressure resulting in plastic flow, thus causing the indium seal rings to extrude further past the convex wedge and thereby increase the total indium-seal surface area in contact with the pressure vessel.

This seal system is capable of undergoing repeated pressurization/depressurization cycles. Altogether, a combination of 51 seal materials and configurations were tested, as described in the report referenced below. A variation of this seal system using silicone rubber O-rings in place of Kel-F was successfully tested to 22,500 psi (1,530 bars) in liquid nitrogen and liquid helium, but prepressurization at ambient temperature was required.

This work was done by A. E. Buggele of **Lewis Research Center.** *Further information may be found in NASA TM-X-73680 [N77-28493], "High-Pressure Cryogenic Seals for Pressure Vessels," a copy of which may be obtained at cost from the New England Research Application Center* *[see page A7]*.

This is the invention of a NASA employee, and a patent application has been filed. Inquiries concerning license for its commercial development may be addressed to the inventor: Mr. Alvin E. Buggele, Mail Stop 77-2, NASA Lewis Research Center, 21000 Brookpark Road, Cleveland, Ohio 44135.
LEW-12944

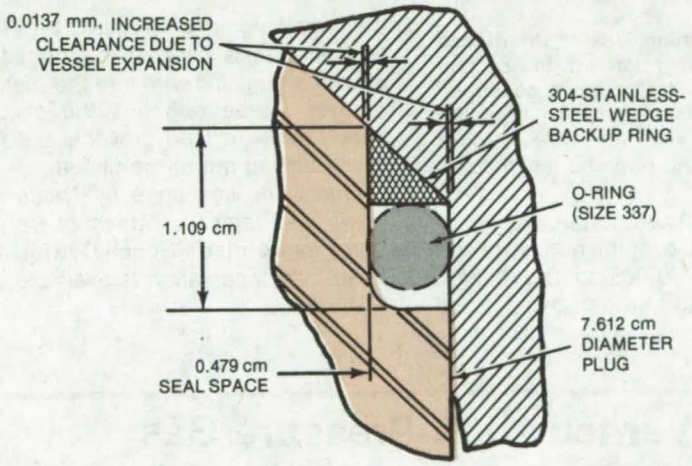

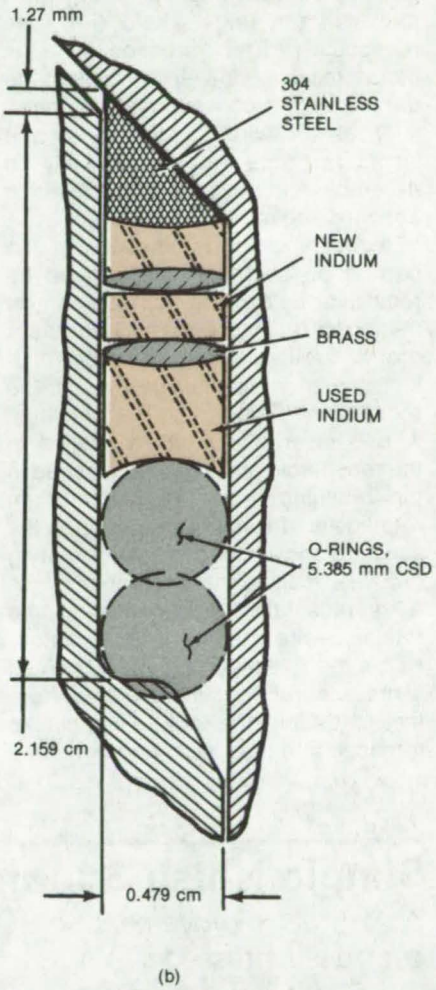

Figure 2. An **Improved Cryogenic Seal** requires that the conventional seal opening (left) be enlarged. The improved seal (right) has eight components that successfully contain pressures of 30,000 psi at 4.2 K.

Retainers for Threaded Parts

A retaining ring and fine wire secure nuts or screws reliably.

Lyndon B. Johnson Space Center, Houston, Texas

Threaded parts can be held in place securely by a fine wire that fits in grooves in a retaining ring and the part to which the ring is held (i.e., the receptacle). The retention wire is more reliable and less subject to breakage than conventional retainers, such as lockwires, cotter pins, and keys. The wire retainer is easy to assemble and to disassemble, even in confined areas.

A retaining ring is placed over the part to be secured, which must be recessed below the surface of its mating part. The retaining ring has a groove around its circumference that alines with a similar groove in the receptacle (Figure 1). The retaining wire is inserted through a scallop in the receptacle and into a hole drilled in the retaining ring. The ring is then rotated and draws the wire through the scallop and into the two mating grooves, locking them together.

A representative application of the retaining-wire method is in a piston, where the retaining ring and wire hold a nut securely but are isolated from the loads on the nut. The nut is threaded into the piston and tightened to a predetermined torque value. A shim is inserted over the nut to provide a clearance of 0.005 to 0.010 inch (0.1 to 0.2 mm) between the nut and the retaining ring (Figure 2). The retaining ring is inserted and rotated to draw the retaining wire into the mating grooves in the ring and the pistonhead. The wire then prevents the nut from backing out of the piston.

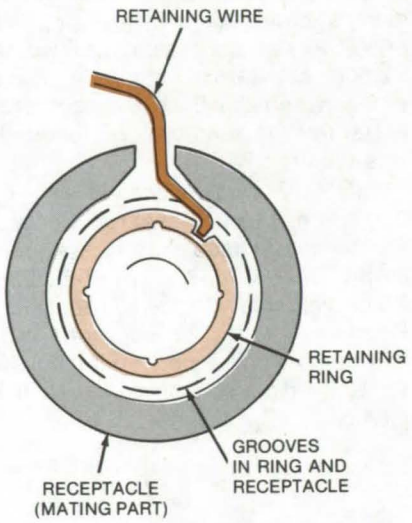

Figure 1. **Retaining Wire Is Positioned** by rotation of the retaining ring so that the wire is drawn through a scalloped opening in the receptacle (i.e., the mating part) and into the groove between retaining ring and receptacle.

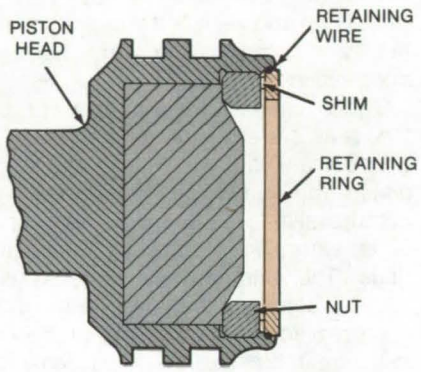

Figure 2. **A Nut in a Piston** is prevented from loosening by a wire in the groove between the pistonhead (receptacle) and the retaining ring.

This work was done by Neale M. Davis and James L. Mann of Bertea Corp. for **Johnson Space Center.** *No further documentation is available.*
MSC-16198

Simple Noise Suppressor for Vented High-Pressure Gas

A 21.5 dB improvement over unsuppressed vents

Lewis Research Center, Cleveland, Ohio

The venting of gases at pressures over 20 psia creates excessive jet noise that may be intolerable to personnel working in the area or residents of the surrounding community. The use of a technique developed for an experimental aircraft jet-noise suppressor can significantly reduce the noise level. This technique uses the principle of overexpansion of a supersonic jet to create a multiple, strong shock-wave system in a pipe, thereby decreasing the exit velocity of the jet and the associated jet-mixing noise.

The suppressor configuration is shown in the figure. As the flow exits from the vent pipe into the suppressor pipe, the space between the jet streamline and pipe enclosure is evacuated to a lower pressure. This low pressure causes the flow to overexpand; thus the gas reaches a high supersonic mach number prior to striking the pipe wall. This high mach number and the forced turning of the flow as it strikes the pipe wall create shock waves in the flow. These shock waves cause large total pressure losses to occur in the gas and result in a decreased mach number or jet velocity. Since the primary cause of jet noise is the jet velocity, the overall sound level from the vent pipe is reduced.

Acoustic tests performed on scale models of the suppressor showed the maximum noise suppression compared to an identical vent without a

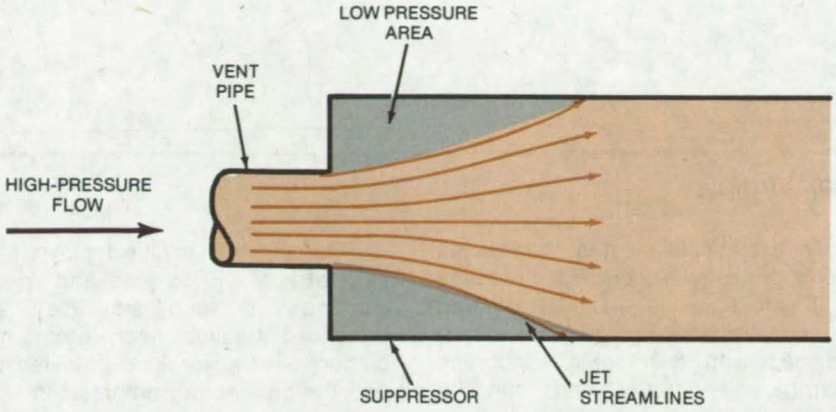

Noise Suppressor for high-pressure gases creates a low-pressure area around the vent that causes the gas to overexpand and strike the wall at a higher velocity. At the wall, interfering shock waves are produced that lower the velocity at the suppressor exit, and thus the noise is lowered.

suppressor was 21.5 dB(c) [135.5 - 114.0 dB(c)]. This occurred just before the normal shock wave was forced from the pipe exit.

A procedure for calculating approximate, but not exact, dimensions of a suppressor for a particular application has been formulated. Exact dimensions depend on the particular gases used and their conditions. Some empirical adjustments to the dimensions may improve any given installation.

This work was done by Ronald G. Huff of **Lewis Research Center.** *For further information, Circle 68 on the TSP Request Card.*
LEW-13231

Bifunctional Gas-Flow Regulator

A high-pressure shutoff feature is added to a conventional regulator.

NASA's Jet Propulsion Laboratory, Pasadena, California

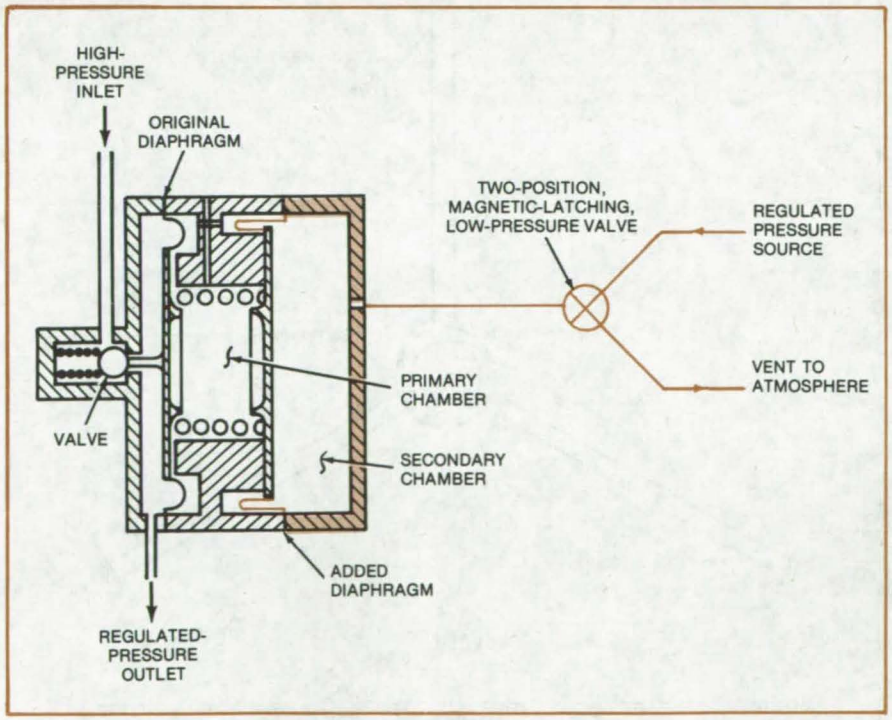

This **Modified High-Pressure Regulator** (modifications are in color) is also a shutoff valve when pressure is removed from the secondary chamber. This removes the reactive force applied by the spring, and the valve remains closed until the regulated-pressure source is diverted to the secondary chamber.

A simple modification converts a conventional high-pressure regulator to a combination pressure-regulator/shutoff valve. The modification entails adding a second diaphragm and pressure compartment. The modified valve is switched between its two functions by an external two-position low-pressure valve.

Typical inlet pressures in a regulator aboard the Mariner spacecraft are over 3,000 psi (20.6×10^6 N/m^2), and the downstream pressure to be regulated is 15±1 psi ($0.1\times10^6\pm0.006\times10^6$ N/m^2). Referring to the figure, the two-position, magnetic-latching valve selects either the 15-psi reference pressure or zero pressure to be diverted into the secondary chamber. When the secondary chamber pressure is zero, the spring expands to its unloaded height, and all reactive force is removed from the primary diaphragm. In this mode, the regulator valve will be closed regardless of the outlet pressure. Regulator function can be restored at any time by reapplying the 15-psi reference pressure to the secondary chamber.

This work was done by Edgar F. Koch of Caltech for **NASA's Jet Propulsion Laboratory.** *For further information, Circle 69 on the TSP Request Card.*
NPO-13135

Extendable Mast

A sturdy mast deployed from a compact package

Langley Research Center, Hampton, Virginia

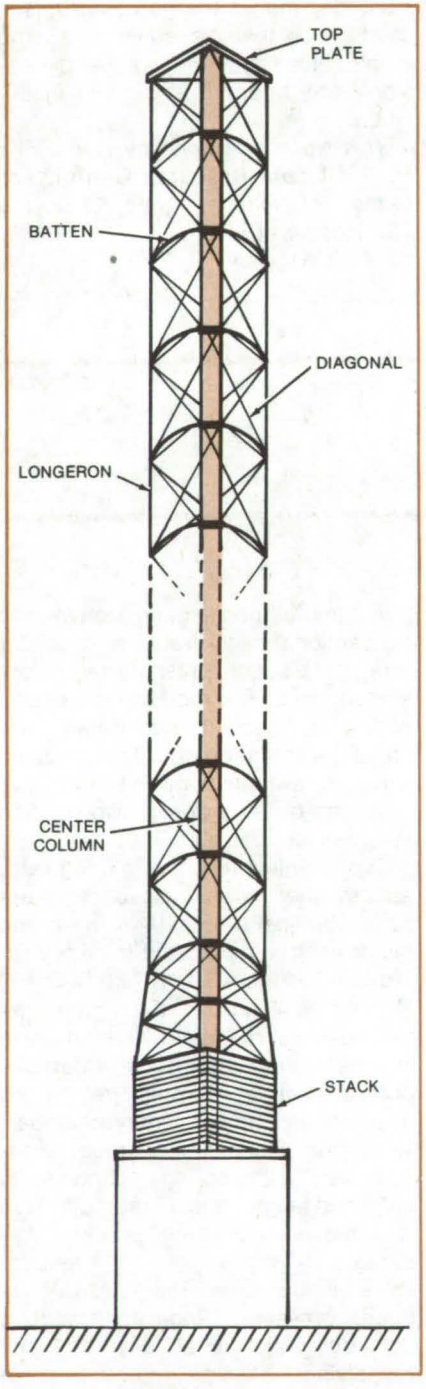

Figure 1. **Extendable Mast Configuration** incorporates a series of preloaded components, which together form a very sturdy structure. The mast is shown partially deployed from a compact package.

An extendable mast is constructed from mutually supporting members that unfold as the mast is deployed from a compact package. The extended mast with its mutually supporting members is sturdy and can be compared to conventional rigid structures.

Figure 1 shows the mast composed of a center compression column, tensioned longerons and diagonals, and compression-loaded battens. The center column is an extendable member capable of carrying compression loads. The column deploys the mast, preloads the longerons, and preloads the diagonals, which load the battens. The longerons and the diagonals are attached to the batten arms in the points shown in Figure 2.

When the mast is fully deployed, the geometry of the battens and of the diagonals is such that they are preloaded against each other, the diagonals being preloaded in tension and the battens in compression. The battens are buckled in a fully deployed configuration (see Figure 2).

The tensioned longerons and diagonals serve two purposes: First, they increase the effective bending stiffness of the center column; and second, they support and preload the battens. The battens, in turn, support the center compression members at intervals and thus increase the Euler buckling strength of the center column.

The battens effectively form equally-spaced intermediate elastic supports

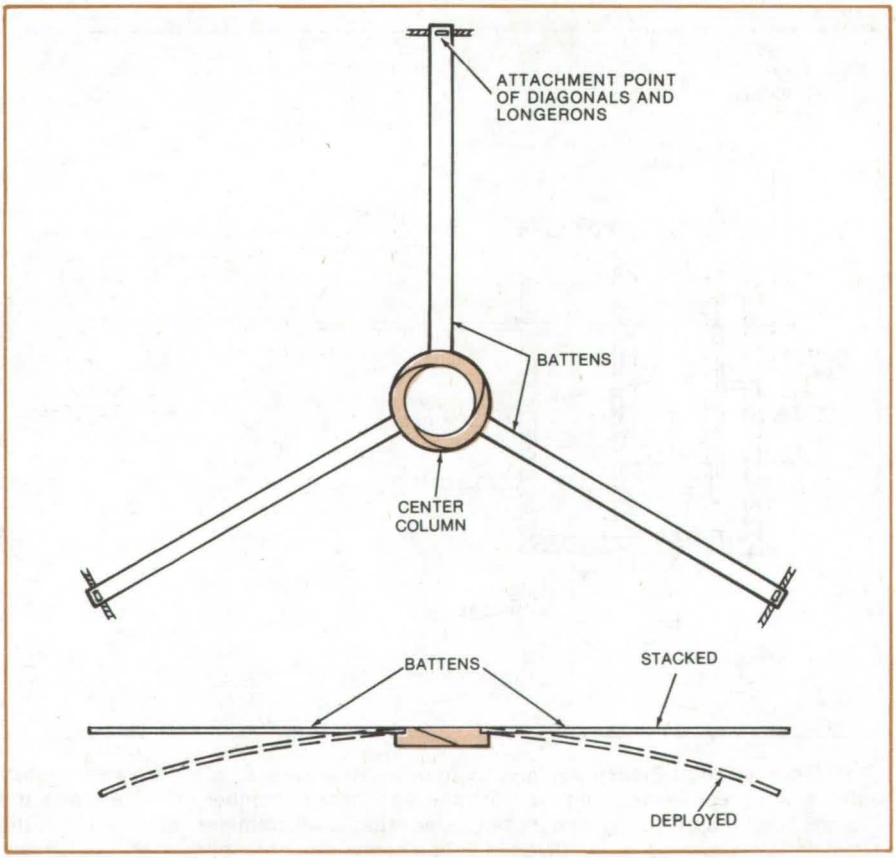

Figure 2. A **Typical Batten Arrangement** uses three battens at equal intervals along the column. The battens increase the buckling strength of the center column. Straight when the mast is stacked, the battens become curved under compressive forces when the mast is deployed.

of equal rigidity, so the buckling column has inflection points at these supports. A further increase in the rigidity of the supports above the required minimum has no effect on column buckling.

The required lateral stiffness of the supports is given by

$$a = \frac{mP}{\gamma L}$$

where

m = number of spans,

γ = numerical factor that depends on the number of spans (0.250 for $m \geq 12$),

L = total length of center column, and

P = critical buckling load for one span of the column, which = $m^2\pi^2 \frac{EI}{L^2}$ (where EI is the effective bending stiffness).

This work was done by John V. Coyner, Jr., and John M. Hedgepeth of Astro Research Corp. for **Langley Research Center.** *No further documentation is available.*
LAR-12078

Low-Cost Boring Mill

Portable unit and special fixture serve as boring mill

John F. Kennedy Space Center, Florida

A "homemade" mill for in-line boring of shoes for the "crawler/transporter" (a large track vehicle for transporting the Space Shuttle to its launchpad) has freed a commercial milling machine for other shopwork. Previously, the commercial mill had been fully occupied repairing the crawler shoes. The new mill, which is only a fraction of the cost of a standard mill, also resolved the problem of having to transport the 2,600-lb (1,180-kg) shoes across a busy shop area to deliver them to the original mill location.

In the new setup (see figure), a portable milling machine is the power source, and a special fixture handles the crawler shoes. The fixture table is constructed of sheet steel 1-1/2 to 2 in. (3.8 to 5 cm) in thickness. The legs are 6-in. (15-cm) box beams, and the sides and bottom are boxed in for strength. The table can also serve as a lockable tool storage. The top table plate can be adjusted in any direction to level the shoes.

Mounted on the top plate are two floating V-blocks and one parallel alining bar. The shoes are precisely alined with this arrangement, regardless of any difference in size.

The specially-designed boring bar can be used for either line boring or, by adding a specially-made two-piece cutter, for boring shoes that have been bushed. The boring bar is easily moved from one side to the other by swivel rollers. The mill is moved by adjustable rollers, and the center distance is maintained by the dowel pins.

The new machine, fabricated primarily from scrap material, was designed and set up in about 12 working days. It has reduced the setup and boring time by 66 percent as compared with existing boring mills, thereby making the latter available for other jobs. The new unit is portable and can be operated by one man.

This work was done by Robert A. Hibdon of Boeing Services International, Inc., for **Kennedy Space Center.** *No further documentation is available.*
KSC-11112

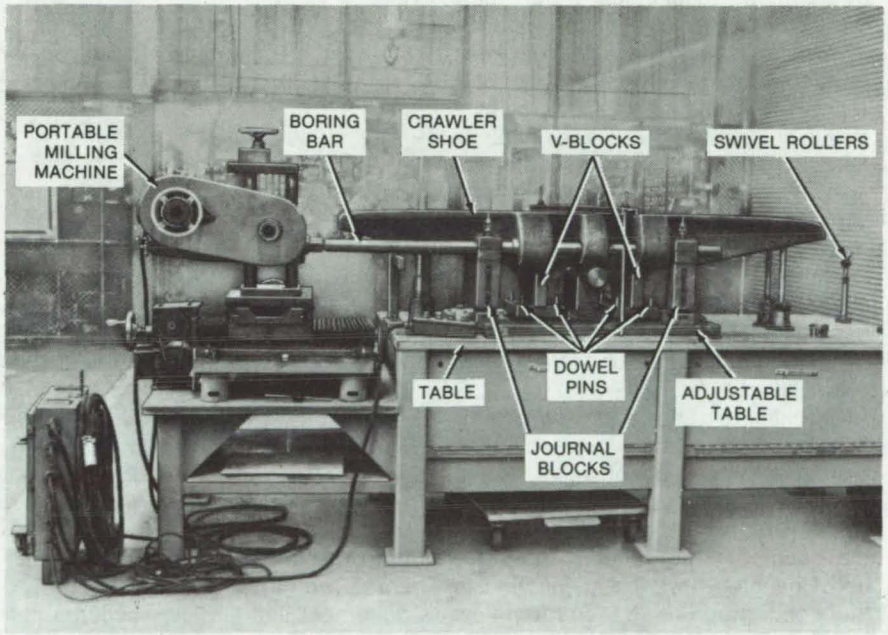

A **Portable In-Line Boring Mill** relieves a standard mill in fabricating heavy crawler/transporter shoes. The mill is portable and can be operated by one man.

Bond Graph for Modeling Valves and Switches

A digital graph element represents two-state devices.

Lewis Research Center, Cleveland, Ohio

A new bond-graph element, the D (for digital) element, has been devised for use in simulations of two-state devices such as valves and switches. The D-element can also be used in modeling mechanical stops, backlash, and other discontinuities that occur whenever subsystems are connected or disconnected.

Bond graphs are compact mathematical diagrams, resembling the conventional structural graphs of chemical formulas, that can be applied to the analyses and syntheses of electrical, mechanical, fluid, thermal, and other types of dynamic systems. In bond graphs of such physical systems, alphabetic symbols represent functional relations of system elements, and numeric symbols describe system structures. Straight lines between symbols are coded to show interrelationships of dependent and independent variables. The D-element was derived from the observation that two subsystems connected by a junction element become uncoupled when the junction outputs are nullified.

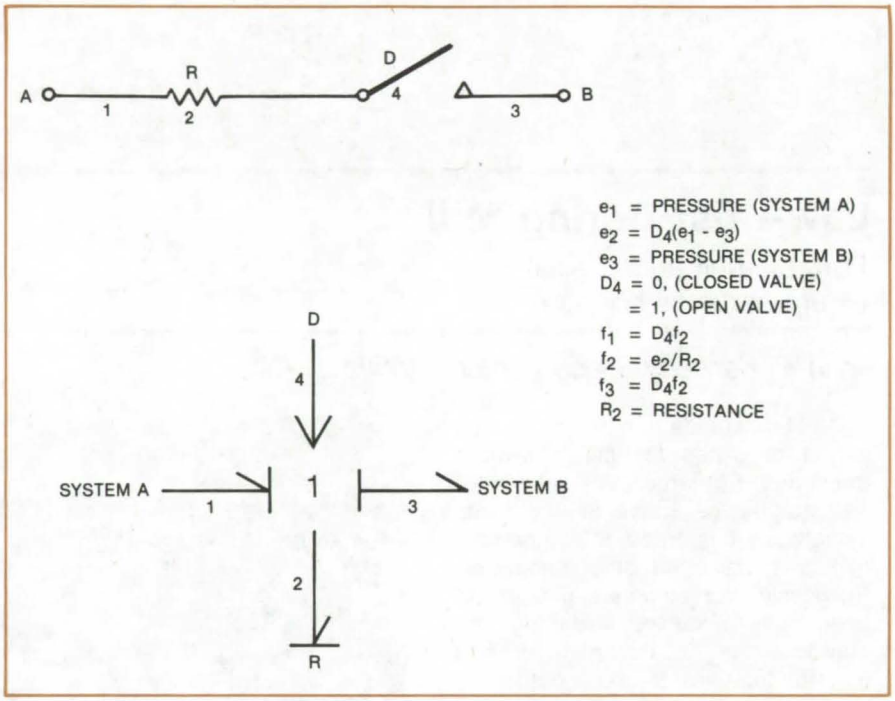

Bond Graph of an On/Off Valve includes a D (for digital element). Two systems (A and B) are connected by the valve. R is the flow resistance of the open valve; e variables are pressures, and f variables are flows. D takes on the values 0 (closed) and 1 (open).

The figure shows a schematic illustration and the corresponding bond graph for an on/off valve. A and B represent systems connected by the valve. R represents flow resistance of the open valve, e denotes pressure, and f denotes flow. The 1-junction in the bond graph is a common flow junction that represents components connected in cascade. D denotes the new element that provides a digital-type variable. In the figure, variable e_1 represents pressure in system A, variable e_2 represents pressure across R_2, and variable e_3 represents pressure in system B. The pressure drop across the valve is equal to e_1 minus e_3.

The equations shown describe both the open-valve and closed-valve pressure-flow characteristics. When the valve is open (D = 1), the pressure across the valve and the pressure across R_2 are identical. When the valve is closed (D = 0), the flow through the valve is zero, and hence the pressure across R_2 is physically zero. The model also satisfied the requirement that all flows become zero when the valve is closed. Since f_2 becomes zero when e_2 is zero, the equations could be simplified by using $f_1 = f_2$ and $f_3 = f_2$. However, the method shown with D_4 applied to all junction outputs is preferred for it preserves the conventional bond-graph methodology of having inputs to elements as independent variable of the outputs.

The D-element method has also been used to model stops and backlash. In these cases, the common variable of interest is pressure (effort), which becomes zero when bodies separate. This situation can be represented by a D-element applied to a common effort junction (O-junction). The only requirement is that all pressure variables associated with the junction become zero when D is zero.

The theory and use of bond graphs are described in several textbooks on system dynamics and in Transactions of the American Society of Mechanical Engineers. A comprehensive bibliography of the current bond-graph literature compiled by Vernon D. Gebben is being published by the Journal of the Franklin Institute, Pergamon Press Ltd., Headington Hill Hall, Oxford OX3 OBW, England.

This work was done by Vernon D. Gebben of **Lewis Research Center.** *No further documentation is available. LEW-13177*

Extra-Strong "Floating Nut"

Its increased bearing area withstands much higher torque than previous designs.

Lyndon B. Johnson Space Center, Houston, Texas

A new "floating-nut" retainer can withstand up to 700 pound-inches (79 newton-meters) of torque applied to a 3/8-inch (0.95-cm) bolt, nearly three times the maximum torque possible with a previous design. The floating nut makes it possible to fasten parts on heavy-duty equipment, such as tractors and cranes, even though they can be reached for tightening from one side only. The new design, which also makes it unnecessary to drill precisely alined holes in the mating parts, is suitable for use with bolts rated at up to 240 ksi (1.65×10^9 N/m^2) ultimate strength, whereas many conventional retainers are useful up to only about 160 ksi (1.11×10^9 N/m^2).

Some conventional floating-nut retainers consist of a nut plate secured in a holder by overlapping tangs. The tangs allow the plate to aline itself with the bolt. When the bolt is torqued, the plate bears against the tangs. However, the bearing surface is small, since only the corner points of the plate contact the tangs. Consequently, these retainers are limited to relatively low torques.

The nut plate and holder in the new design have elliptically-contoured mating surfaces that give a larger bearing area. A nut is press-fitted in a matching hole in the plate. Four tangs, bent inward over the plate, retain the nut and plate in the holder. The holder is riveted to a wall or mounting plate through holes at its four corners.

To use the retainer, a bolt is inserted through a center hole in the holder and into the nut. As the bolt is tightened, the float of the nut plate accommodates misalinement, and the plate butts against a diametrically opposed pair of tangs. When the bolt is removed, the other pair of tangs provides the reaction needed to accommodate the torque applied when loosening the bolt.

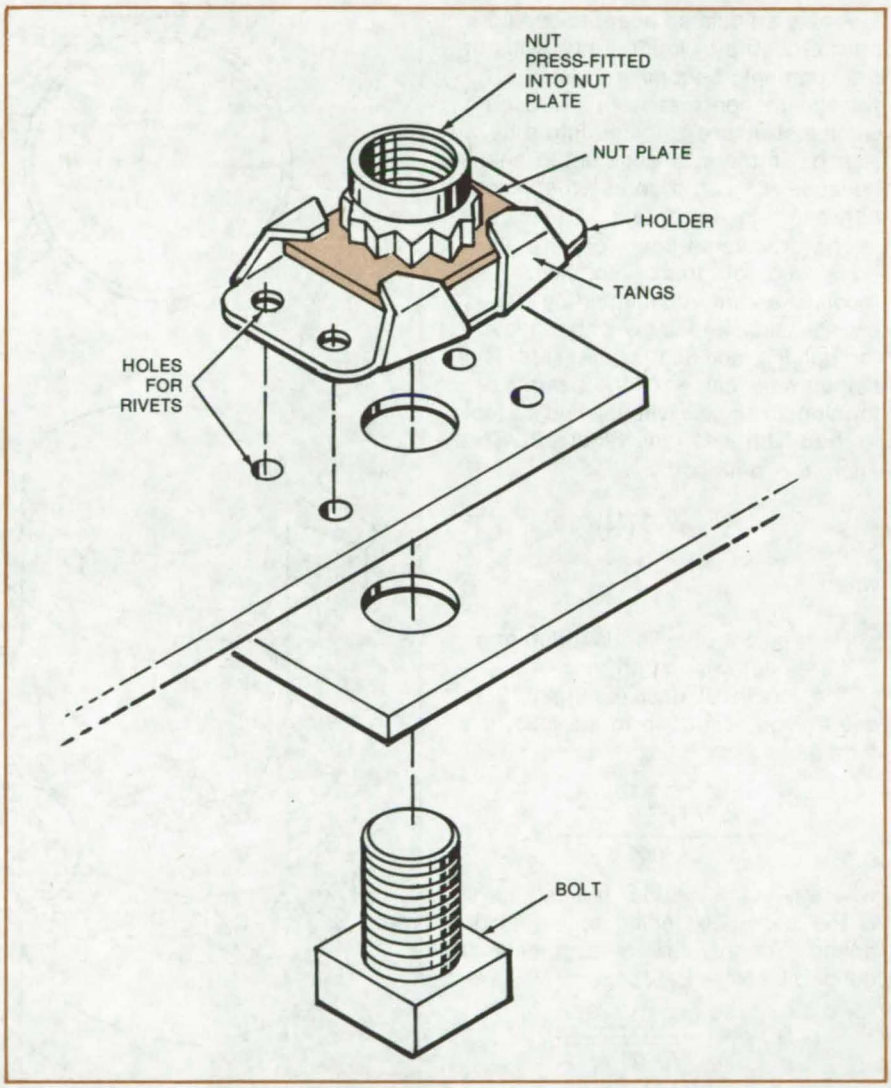

A **Heavy-Duty Floating-Nut Retainer** is riveted to its mounting plate. The elliptically curved sides of the nut plate and holder sides create a bearing area that is large enough to withstand large torques when a bolt is tightened or loosened in the nut.

This work was done by James F. Charles of Rockwell International Corp. and Harry Theakston of Standard Press Steel for **Johnson Space Center.** *For further information, Circle 70 on the TSP Request Card.*

This invention is owned by NASA, and a patent application has been filed. Inquiries concerning nonexclusive or exclusive license for its commercial development should be addressed to the Patent Counsel, Johnson Space Center [see page A8]. Refer to MSC-16938.

Foldable Beam

A beam structure folds into a compact helix.

Langley Research Center, Hampton, Virginia

A new articulated beam folds into a helix around a cylindrical hub without the segments becoming twisted. The twisting motion that normally occurs when a structure is folded into a helix is undesirable in a segmented beam because it complicates the joints between the segments.

The articulated beam (Figure 1) is composed of truss modules. The modules are interconnected by hinges on one side and by a cable reeved through the tube on the other side. The hinge axis is canted to the beam axis, forming an angle α with the line normal to the beam axis (see Figure 2). The angle α is defined by

$$\alpha = \sin^{-1}\left(\frac{H}{L}\right)$$

where

H = height of cylindrical hub and
L = beam rib length.

The length of each segment S is determined according to the following formula:

$$S = \frac{2\sqrt{r_H^2 - r_c^2}}{\cos\alpha}$$

where r_c is the cylinder radius and r_H is the radius extending to the hinge points. The number of segments N defined by N = L/S becomes

$$N = \frac{L\cos\alpha}{2\sqrt{r_H^2 - r_c^2}}$$

Although the illustrated structure is a truss beam, the same principle applies to any articulated set of rigid segments about a cylinder forming a helical folded configuration. In addition, although the illustrated deployed

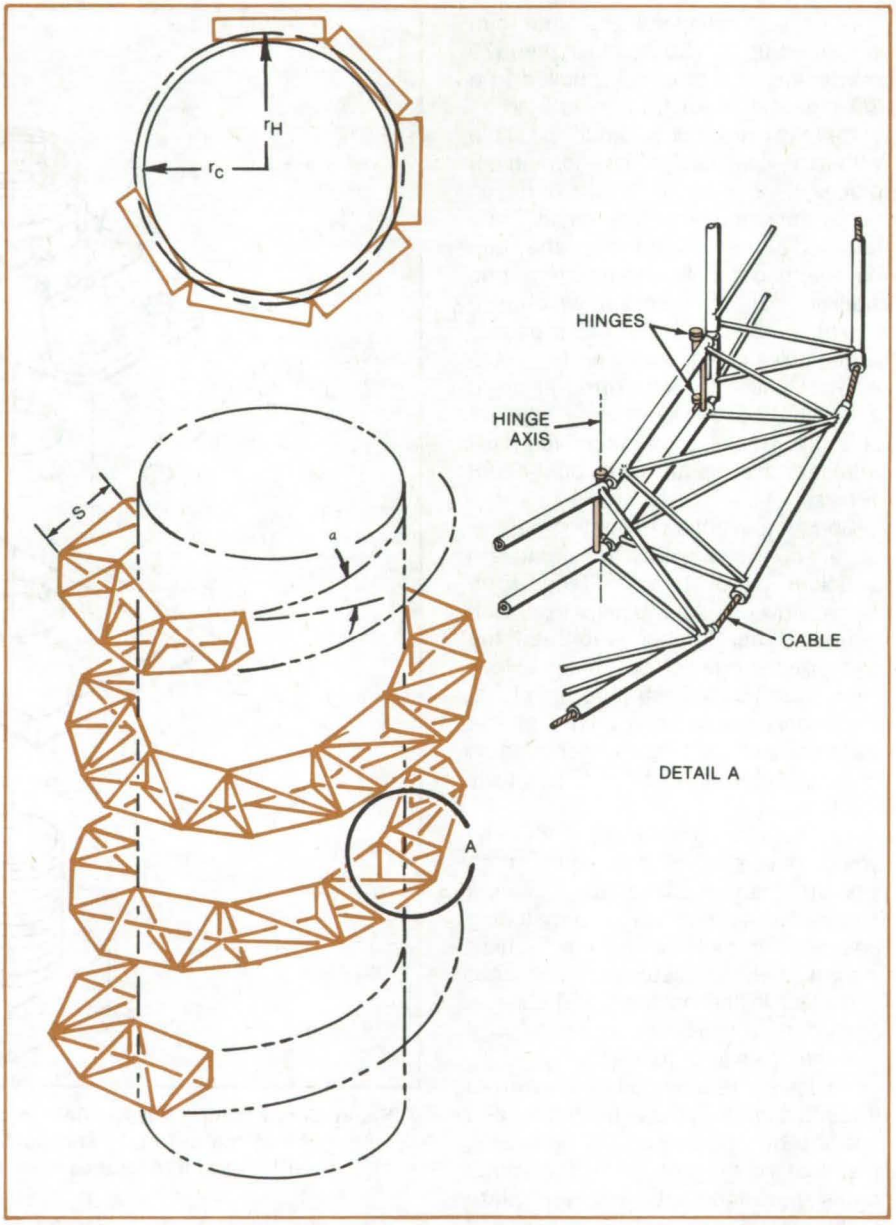

Figure 1. **Retractable Articulated Truss Beam** is shown in a fully retracted position. The beam is made from modules that are interconnected by hinges on one side and a cable reeved through the tube on the other side. The top view of the cylinder hub shows the radii used in computing the segment length.

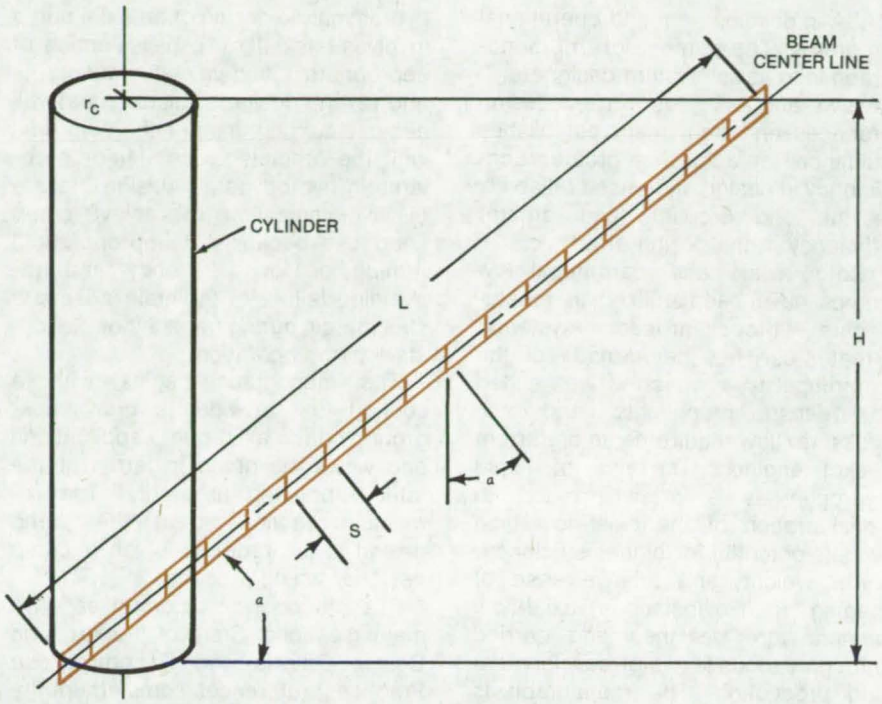

Figure 2. The **Geometry of the Helically Foldable Beam** shows the angle relationship of canted hinge axis to normal to the beam axis.

beam is straight, curved beams can also be used without twisting.

[See related article, "Foldable Beam" (LAR-12077), on page 525 of *NASA Tech Briefs*, Vol. 2, No. 4.]

This work was done by Robert F. Crawford of Astro Research Corp. for **Langley Research Center.** *No further documentation is available.*

This invention is owned by NASA, and a patent application has been filed. Inquiries concerning nonexclusive or exclusive license for its commercial development should be addressed to the Patent Counsel, Langley Research Center [see page A8]. Refer to LAR-12076.

Books and Reports

These reports, studies, and handbooks are available from NASA as Technical Support Packages (TSP's) when a Request Card number is cited; otherwise they are available from one of NASA's Industrial Application Centers or the National Technical Information Service.

Rotating-Shaft Seals

Design-criteria monograph for turbopump shaft seals

A monograph was written to organize and present significant experience and knowledge accumulated by NASA in development and operational programs. The purpose is to assist designers. It reviews and assesses current design practices and from them establishes guidance for achieving greater consistency in design, increased reliability in the end product, and greater efficiency in the design effort.

The design and application of rotating-shaft seals for turbopumps in rocket engine systems required consideration of many factors that normally are not critical in conventional turbopump applications. The extreme operating conditions combined with the high-reliability and fail-safe requirements dictate a thorough analysis of each detail design factor with consideration of all possible failure modes and operating variations. Because of severe operating conditions, most turbopump seal designs have required considerable development and have extended the state of the art, particularly in the areas of materials compatibility, low-temperature capability, and high-speed service.

Compatibility of seal materials with rocket engine propellants has been a major problem. The highly reactive propellants are not compatible with many of the conventional seal materials. Much effort was expended over the years to compile data on materials compatibility and to make effective use of the information in successful seal design.

The low temperatures of cryogenic propellants, -297° F (-182° C) to -423° F (-253° C), precluded the use of conventional elastomer seals and resulted in the development of the plastic-lip and metal-bellows designs. The low-temperature problem is compounded on some turbopump seals by the extreme temperature gradient that occurs when the cryogenic fluid must be sealed along a shaft that is adjacent to a high-temperature, 1,200° F (649° C), turbine.

The shaft seals currently in use on rocket engine turbopumps are primarily the face-contact and circumferential types. In general, the face-contact seals (face seals in rubbing contact with the mating surface) are used for sealing liquid propellants, and the circumferential seals are used for sealing turbine hot gases. Welded metal bellows are currently the most common seal configuration in use with cryogenic fluids. Because cryogenic fluids do not provide significant lubrication,

(continued on next page)

materials combinations that are self-lubricating have been developed.

The monograph deals primarily with the experience and knowledge accumulated in development and operational programs to date; therefore, most of the information concerns the face-contact, circumferential, and labyrinth seals. Because future requirements indicate the need for more advanced configurations, such as the hydrostatic and hydrodynamic seals, these designs are also treated.

The monograph comprises two major sections: State of the Art, and Design Criteria and Recommended Practices; references complement the text. Both major sections are divided into three subjects: Seal Systems (environment, speed, cooling and lubrication, leakage, fluid separation, and purge and fail-safe provisions); Seal Assembly (pressure and temperature capability, speed, wear life and leakage, misalinement, vibration, contamination, and seal-mounting requirements); and Seal Components (materials, rubbing elements, clearance elements, secondary elements, spring load, and pressure balance).

(The monograph is one of a series being published on space-vehicle chemical propulsion, environment, structures, and guidance and control. A list of all monographs issued prior to this one is presented on the final pages of the report.)

This work was done by the Space Propulsion & Power Division of **Lewis Research Center.** *Further information may be found in NASA SP-8121 [N78-30584], "Liquid Rocket Engine Turbopump Rotating Shaft Seals," a copy of which may be obtained at cost from the New England Research Application Center* [see page A7].
LEW-13227

Axial-Flow Turbopumps

Critical-design monograph on reliability and consistency guides

A monograph was written to organize and to present significant experience and knowledge accumulated by NASA in development and operational programs. The purpose of the monograph is to assist system designers; it reviews and assesses current design practices and from them establishes guidance for achieving greater consistency in design, increased reliability in the end product, and greater efficiency in the design effort.

Both axial- and centrifugal-flow pumps have been utilized in rocket-engine propellant-feed systems. Greater use has been made of the centrifugal type, which is well suited for dense propellants and the pressure/flow requirements of current rocket engines. The use of liquid hydrogen as a propellant led to consideration of the axial-flow type with its potential for higher efficiency, lower weight, and relative ease of staging. In five instances, axial-flow pumps were designed and carried through various levels of development and production. The monograph is based on the experience with the five pumps and as such reflects pump technology based on a relatively small number of configurations, all of which involved liquid hydrogen as the pumped fluid.

In the development of this technology, particularly in the area of hydrodynamic design and the mechanical design of the blading, extensive use was made of the substantial applicable experience acquired in the design axial-flow compressors. No attempt was made to incorporate any axial-flow compressor technology that evolved subsequent to the design of the pumps discussed even though some of that technology may be useful in the design of axial-flow pumps. Some of the areas treated in the monograph are applicable to both axial and centrifugal pumps. In most instances, areas generally applicable to both types of pumps (primarily volutes) are only briefly discussed, because the subject mater is covered fully in a companion design-criteria monograph on the centrifugal-flow pumps, NASA SP-8109, (N74-28961).

The axial-pump design process is directed toward achieving a hydrodynamic and mechanical design configuration that will meet the requirements of the engine system within the constraints imposed by other components in the turbopump assembly. The hydrodynamic design of an axial pump involves basically (1) the selection of appropriate fluid-velocity diagrams and (2) the design of blading that will achieve fluid turning per the diagrams with the predicted loss. Major problems in hydrodynamic design include (1) avoiding failure to achieve pump head rise because of improper fluid turning or low efficiency and (2) avoiding failure to maintain adequate stall margin during transient or steady-state pump operation.

The monograph begins with a section that provides a brief background on the axial-pump applications and views the pump in terms of the total turbopump assembly. The remaining sections treat the pump design in the order in which a pump designer would proceed.

The monograph comprises two major sections: State of the Art, and Design Criteria and Recommended Practices; references complement the text. Both major sections are divided into six subjects: Overall Turbopump Design (turbopump speed and rotor dynamics); Stage Design (realm of operation and stage hydrodynamic design); Pump Rotor Assembly (blades, blade attachment, rotor, and axial thrust balance system); Pump Stator Assembly (vanes, vane attachment, stator and volute housings, bearing housings, housing interfaces, and static sealing); Materials; and Safety Factors.

(This monograph is one of a series being published on space-vehicle chemical propulsion, environment, structures, and guidance and control. A list of all monographs issued prior to this one is presented on the final pages of the report.)

This work was done by the Space Propulsion & Power Division of **Lewis Research Center.** *Further information may be found in NASA SP-8125 [N78-31164], "Liquid Rocket Engine Axial-Flow Turbopumps," a copy of which may be obtained at cost from the New England Research Application Center* [see page A7].
LEW-13228

Fabrication Technology

Hardware, Techniques, and Processes

Books and Reports

Rotatable Fixture for Spray Coating

Fixture that rotates about two axes ensures a uniform coating and minimizes handling of the coated workpiece.

Ames Research Center, Moffett Field, California

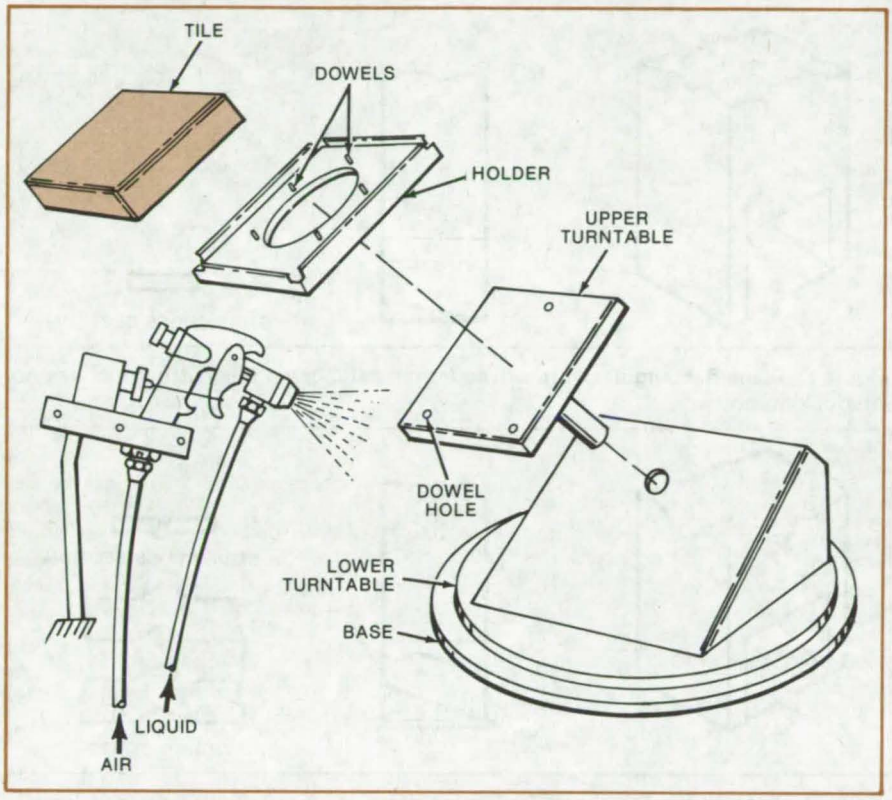

This **Rotating Fixture** supports a tile for spray coating. Dowel pins, which hold the tile on the holder and the holder on its turntable, could be replaced by a rotatable vacuum joint.

The rotatable fixture shown in the figure, developed for production spraying of Space Shuttle surface-insulation tiles, makes the coating process more efficient in several ways: (1) It rotates about two axes, presenting all sides of the tile to the spray; (2) it masks parts of the tile that are not to be coated; and (3) it allows the tile to be removed without handling the coated surfaces. Sprayed coatings are applied faster than with nonrotating or single-axis rotating fixtures, and the coatings are more uniform and less subject to handling damage. With some modifications, the fixture could be adapted for spraying parts other than tiles.

The tile holder is supported by a turntable canted 45° to the horizontal. Upwardly projecting lips along the edges of the holder shield part of the sides of the tile from the spray. A tile is installed by placing it on dowel pins extending up from the holder. Other dowels, extending down from the holder (not seen in the figure), engage holes in the top face of the turntable. A second turntable, which rotates in the horizontal plane at the base of the fixture, supports the 45° surface on which the tile turntable rests.

The 6- by 6- by 2-in. (15- by 15- by 5-cm) Shuttle tiles are held in the holder by pins 1/4 in. (0.62 cm) in length. With the tile holder in place, a glass slurry is sprayed from a gun roughly 6 to 8 in. (15 to 20 cm) from the surface to be coated. Each side of the tile is coated in sequence by moving the turntables until the surface is perpendicular to the spray. The front face is moved to face the sprayer by rotating the lower turntable. Approximately 0.0012 to 0.0015 in. (0.003 to 0.004 cm) of coating is applied on each pass, and the process is repeated until the desired thickness has built up.

To remove the tile, it and the holder are removed from the fixture and placed on a round pedestal that projects through the central aperture of the holder. The holder is lowered, leaving the tile on the pedestal.

This work was done by Victor Katvala, Ernest Porter, and Marnell Smith of **Ames Research Center.** *For further information, Circle 71 on the TSP Request Card.*

This invention is owned by NASA, and a patent application has been filed. Inquiries concerning nonexclusive or exclusive license for its commercial development should be addressed to the Patent Counsel, Ames Research Center [see page A8]. *Refer to ARC-11110.*

Tool Cuts Self-Locking Joints in Plastics

Three lathe tools form different joints in gasket material.

Langley Research Center, Hampton, Virginia

During development of a continuous-strip self-locking spiral-wound seal, several lathe tools with special cutting edges were fabricated to skive long thin strips 0.104 in. (0.264 cm) thick, 0.500 in. (1.27 cm) wide, and several hundred feet long from disks of material made of PTFE and 25 percent glass fibers. These strips were then spiral wrapped, like a roll of tape, to form a strip gasket. Some strips were cut so that the contact surfaces of adjacent strips were smooth and flat; others were cut so that adjacent surfaces were interlocking to prevent separation of the wrappings in the axial direction.

Figure 1 illustrates the tool used to skive a plane strip of rectangular cross section, and the resulting cross section. The cutting edge is formed at an angle of 10° and is supported on each side by a 0.125-in. (0.318-cm) wall. There is no locking provision in this configuration.

Figure 2 illustrates one of the tools used to form a surface that interlocks with an adjacent strip. The upper surface of the cutting edge makes an angle of 20° with the bottom. A triangular projection, 0.125 in. wide and 0.030 in. high (0.318 by 0.762 cm), is machined on the bottom cutting surface and intersects with the upper surface, forming a triangular point. The tool cuts with a gouging action ahead of the knife edge. The resulting shape is a continuous strip with a male vee on one side and a female vee on the other side. The male and female vees are not an exact match due to rounding of the male vee as it rubs along the flat surface forming the cutting edge.

Figure 3 illustrates another tool that forms a surface configuration that will interlock with an adjacent strip. It is the same as the tool in Figure 2 except that a female vee is cut in the upper surface of the cutting edge and parallel to it. The intersection of this female vee with the profile of the male vee forms a knife edge. Consequently, both cutting edges of the tool are knife edges, and the resulting shapes of the cut are interlocking vees that are an exact match.

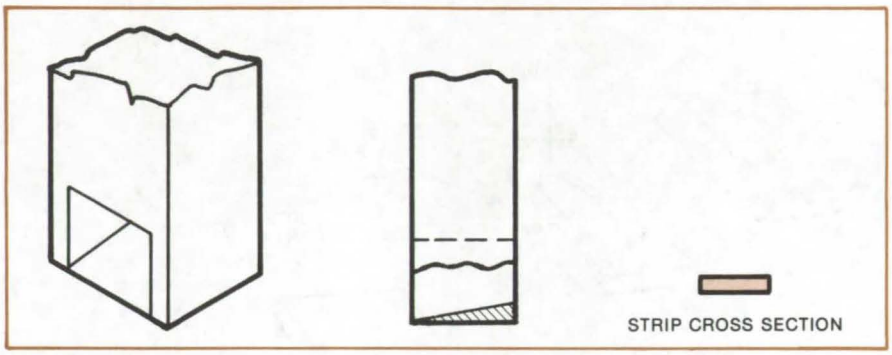

Figure 1. **Plane Rectangular Strip** skived from plastic using this cutting tool has no interlocking notch.

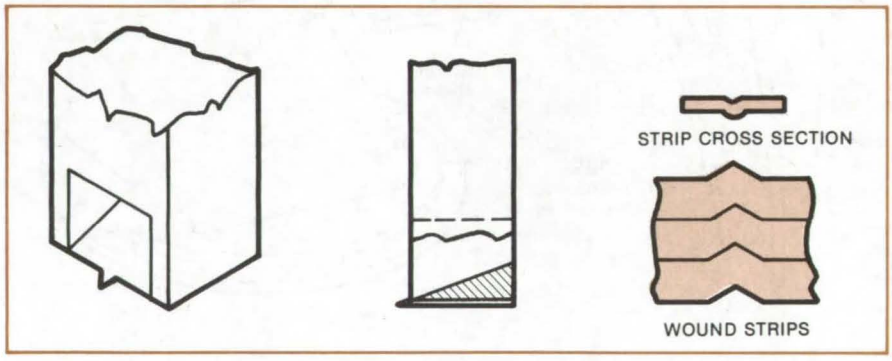

Figure 2. **Tool With a Triangular Projection** produces a strip with male and female vee notches. Because the male notch is somewhat rounded, the two notches do not match exactly.

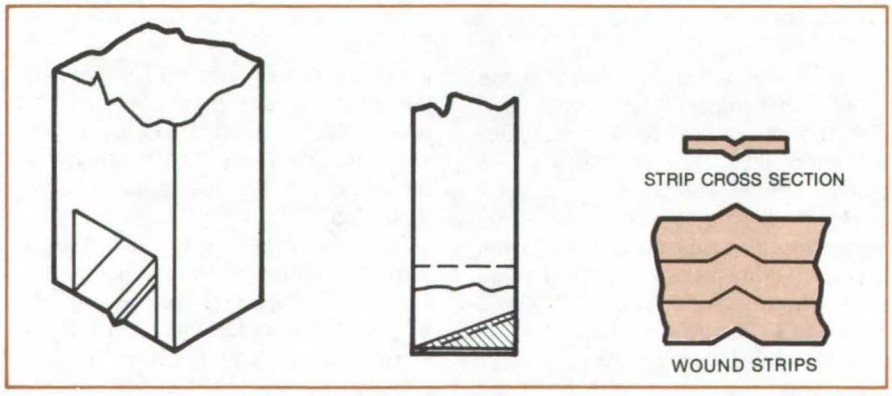

Figure 3. **Tool With Triangular Notch** produces male and female notches that match exactly.

The tool in Figure 2 is a cost effective modification of the tool in Figure 3. For such applications as bearings and low pressure seals, and where the temperature and gasket loading are sufficient, the small imperfection produced by the tool of Figure 2 does not affect the use of the product or is eliminated by cold flow of the material. The dimensional toler-

ance of the finished part is excellent. The variance in thickness of a single strip is less than a mil but is ultimately dependent upon the length of cut and the sharpness of the tool. The original tool material was selected for toughness; wear with that material has been satisfactory. However, with the final designs shown, and by cutting the material blank into a cam shape prior to machining, the tip loading is greatly reduced; this allows emphasis to be placed on abrasive resistance of the tool material.

This work was done by David F. Gourley, Stephen C. Irick, and Hale H. Marshall of **Langley Research Center.** *No further documentaion is available.*
LAR-12427

Fastener for Easy Installation and Removal of Tiles

Mating strips, one with metal hooks and one with metal loops, allow convenient mounting and removal of many kinds of modules.

Lyndon B. Johnson Space Center, Houston, Texas

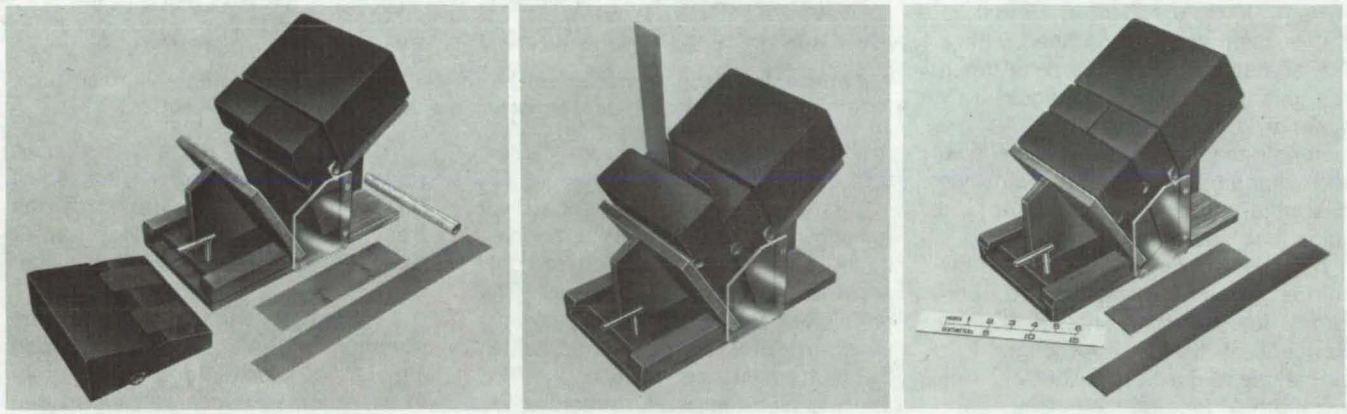

[a] [b] [c]

Metal Hook-and-Loop Strips hold thermal-protection tiles in place. The mating strips can be seen in (a); in (b), thin pieces of aluminum separate the strips to allow installation (or removal) of the tile; and a complete assembly is seen in (c).

The thermal insulation tiles used on the nose cone of the Space Shuttle Orbiter are held in place by hook-and-loop fasteners. The fastening system is similar to synthetic-textile fasteners (e.g., Velcro or equivalent) ued in packaging and clothing; however, the fasteners for the Orbiter tiles are stainless steel hooks and Iconel loops. Their easy removal and installation makes them ideal for the Space Shuttle Orbiter.

Hook-and-loop attachment allows the tiles to move slightly sideways and in compression and allows them to be installed and removed — without breakage — quickly and easily in a space with limited access. These features, necessary in the Orbiter nose cap to permit access from the crew module, are not possible if the tiles are attached by adhesive. Although metal carriage plates could be used to hold the tiles, the plates are thermally conductive and would allow the intense heat outside the nose to penetrate into the spacecraft. The stainless-steel hooks and Inconel loops can withstand the hostile environment and transfer little heat.

The principle is adaptable to applications where shear-resistant, compliant, removable fastening is needed in hard-to-reach places, especially when the attached part is lightly loaded or fragile. This metal fastener can also be used instead of conventional fasteners to attach modular components in hard-to-reach places — a car radio in a dashboard, for example.

In the Orbiter application, the hook-and-loop mating strips are cemented on tiles that will be placed adjacent to each other. The accompanying figure shows how a tile is installed: One places a spatula (a strip of scrap aluminum will do) over the fastener strip on an in-place tile and slides in another tile, oriented so that a loop strip on one of the tiles faces a hook strip on the other. The spatula is then slowly withdrawn, and the hooks and loops engage each other. To remove a tile, one gently inserts the spatula and wobbles it back and forth to loosen the hooks and loops.

This work was done by Len H. Maletz of Rockwell International Corp. for **Johnson Space Center.** *No further documentation is available.*
MSC-16892

Distortion-Free Foamed-Plastic Parts

A perforated die vents gases as liquid expands into foam.

Ames Research Center, Moffett Field, California

In a new process for molding foamed-plastic products, gases that are formed as byproducts of the foaming reaction escape through a perforated die. Thus, the volatiles are not trapped in pockets that can deform and weaken the molded part.

The die is perforated with small holes [0.060 to 0.100 in. (0.15 to 0.25 cm) in diameter] and is lined with a TFE-coated permeable fabric. After it has been charged with liquid raw material, the die is closed. As the materials react, bubbles of gas evolve and expand the liquid into a foam; gas is vented through the die liner and holes (see figure).

As the process continues, the charge cures, forming a hard, uniformly foamed part shaped by the contours of the die. Although it is permeable to gases, the liner ensures a smooth surface on the finished part. It also prevents the part from sticking to the die.

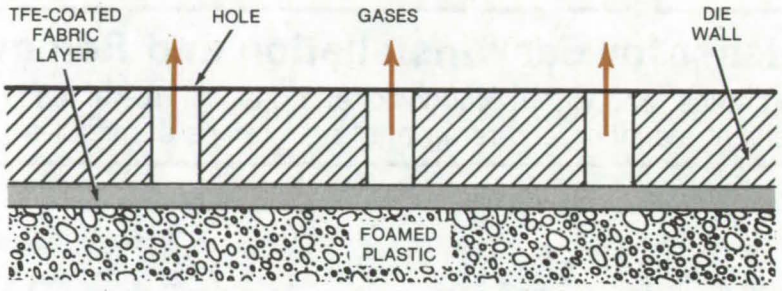

A **TFE-Coated Fabric Liner** and a perforated die ensure a smooth surface on a foamed part by releasing gases that evolve during the foaming reaction.

This process was developed for making heat insulators from a polyimide foam that cures at room temperature and atmospheric pressure. The principle can be adapted easily to vacuum or pressure curing and (within the heat-resistance limits of the TFE liner) to high-temperature molding.

This work was done by Peter A Hogenson and Richard G. Jackson of Rockwell International Corp. for **Ames Research Center.** *For further information, Circle 72 on the TSP Request Card.*

Inquiries concerning rights for the commercial use of this invention should be addressed to the Patent Counsel, Ames Research Center [see page A8]. Refer to ARC-11233.

Vacuum Casting of Thick Polymeric Films

New process produces uniform, bubble-free film from polymer solution.

NASA's Jet Propulsion Laboratory, Pasadena, California

Uniform, bubble-free polymeric films, typically 0.2 cm in thickness, are formed from polymer solutions by a new vacuum-casting process. Segmented polyurethane elastomer films, which took 45 days to produce by conventional evaporative casting, are formed in only 9 days by the new process; and problems such as thickness variations, opacity, and poor surface texture are eliminated. Bubble formation and layering, which often plague vacuum-evaporated films, are prevented by properly regulating the process parameters. Moreover, vacuum casting may be applicable to forming thick films of other polymer/solvent solutions.

The new technique was developed after a systematic study of the dynamics of vacuum casting for segmented polyurethane. Bubble formation and layering were found to occur at different phases of the casting operation: Bubbles form during the initial outgassing stage, and layering occurs at final gelation. Both are avoided by regulating the rate of solvent removal under vacuum to below a certain "natural" maximum. The natural solvent-removal rate can be determined by rapidly removing solvent under full vacuum.

The removal-rate/concentration plot for segmented polyurethane (SPU) dissolved in dimethyl formamide (DMF) is shown in the accompanying figure. Solvent removal at the rapid rate of 7.6 cm^3 per hour from a circular casting pan 18.4 cm in diameter proceeds until gelation begins, at a concentration of about

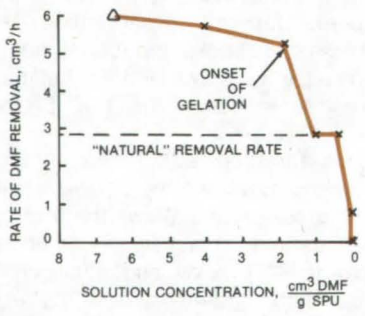

When the **Solvent-Removable Rate Is Plotted Against Solution Concentration** during vacuum casting of segmented polyurethene (SPU) dissolved in dimethyl formamide (DMF), the onset of gelation is evidenced by an abrupt drop and then a leveling off of the removal rate. For uniform bubble-free films, the removal rate should be kept below the step value (2.8 cm^3/h for this example).

1.8 cm^3 (DMF)/g (SPU). At this point, the removal rate falls rapidly to about 2.8 cm^3/h and then levels off until nearly the end of the process.

It is found that if the removal rate is allowed to rise above 3.0 cm^3/h at the beginning of the process (for roughly the first 24 h), bubbles are retained in the final product; if the rate is kept below this value at the initial phase but rises above 2.8 cm^3/h during gelation, layering occurs, but the films are bubble free. Both effects, however, are prevented by keeping the removal rate below 2.8 cm^3/h during the entire process.

The near equality of the removal rates for bubble formation, for layering, and for the step in the gelation curve is thought to reflect the existence of a "natural" solvent-removal rate for SPU dissolved in DMF. Keeping the removal rate below this rate gives a uniform high-quality film. If this behavior is universal, maximum removal rates could be found for other polymer/solvent systems.

This work was done by Edward F. Cuddihy and Jovan Moacanin of Caltech for **NASA's Jet Propulsion Laboratory.** *For further information, Circle 73 on the TSP Request Card.*
NPO-14534

Cleaning Contaminated Superalloy Powders

Combined vacuum-and-hydrogen cleaning effectively reduces O, N, C, and H contamination.

Lewis Research Center, Cleveland, Ohio

Nickel-base superalloys are used for high-temperature components such as blades, vanes, and disks in aircraft and ground turbine engines. Major strengthening improvements have recently been achieved in some of these alloys by combining oxide dispersion strengthening with the usual gamma prime strengthening. The development of these improved alloys has been achieved through powder metallurgy techniques. Elemental powders of the alloy composition and yttrium oxide (Y_2O_3) additions are ground in a ball or attrition mill to a fine particle size to insure the interparticle spacing (less than 1 millimicron) necessary for improved high-temperature strength.

Ball milling is a generally available method of grinding; and heptane, alcohol, and/or oleic acid additions are normally used to decrease grinding time and insure homogeneous mixing of the ground powder. However, such wet grinding normally contaminates the powder with high levels of oxygen, carbon, nitrogen, and hydrogen, all of which reduce satisfactory performance of the end product.

A cleaning process has been developed to reduce the level of these contaminants in the superalloy end product. For example, elemental powders of a modified WAZ-20 alloy (a composition by weight percent of 18 tungsten, 7 aluminum, 1.5 yttrium oxide, and the balance nickel, without the normal 1.5 zirconium and 0.15 carbon) were ground in a ball mill with 1 weight percent oleic acid for 100 hours. Then a combined hydrogen-and-vacuum cleaning cycle was used to clean the contaminated powder. The powder was slowly heated in a retort with flowing hydrogen at 750° and then at 1,790° F (673 and 1,250 K) for 24 hours at each temperature. After cooling, 50 percent dense billets were produced by isostatically cold-pressing the powder. The billets were then loaded into a vacuum furnace and slowly heated to 2,192° F (1,473 K) and held for 2 hours at 10^{-6} torr. After this, the billets were loaded into extrusion cans, evacuated, electronbeam welded, and hot-extruded at 2,200° F (1,473 K) at a 20/1 reduction ratio. Samples for chemical analysis were taken from the powder after grinding and were also cut from the extrusions.

Typical analyses of oxygen, carbon, nitrogen, and hydrogen in the WAZ-20 samples after ball milling and after the cleaning steps are shown in the figure. Contamination levels, all expressed on a weight percent basis, were reduced by this cleaning process as follows:

a. Oxygen from 1.7 to 0.5 weight percent (of which 0.32 weight percent had been added as Y_2O_3).
b. Carbon from 1.0 to 0.015 weight percent.
c. Nitrogen from 75 parts per million (ppm) to less than 20 ppm.
d. Hydrogen from 300 ppm to less than 2 ppm.

All of these results represent the average of at least two separate analyses, with reproducibility to within 5 percent. This combined hydrogen-plus-vacuum cleaning process resulted in far lower contamination levels than several other cleaning processes (hydrogen alone or vacuum alone) studied in this as well as other investigations of superalloy powders.

This cleaning procedure should have application to a variety of powder metallurgy contamination problems. For example, other contaminants such as hydrocarbons, sulfur, and chlorine appear capable of being reduced by this cleaning process. Superalloy powders initially contaminated during atomization, electrolytic processes, handling, or storage might be cleaned by this hydrogen-and-vacuum cleaning process. It is also possible that atomization of prealloyed superalloys, currently done in argon at significant expense, could be done more economically in less expensive gases followed by cleaning to reduce the resultant contaminants.

This work was done by Albert E. Anglin of **Lewis Research Center.** *For further information — "Cleaning Process for Contaminated Superalloy Powders," Powder Technology, Vol. 20, pp. 137-138, 1978 — Circle 74 on the TSP Request Card.*
LEW-13041

Confined Explosive Joining of Tubes

Clean explosive process produces joints with matching parent-metal strengths.

Langley Research Center, Hampton, Virginia

A technique recently developed and demonstrated at Langley Research Center uses an explosive ribbon to join and seal tubes hermetically while totally confining the explosion products, such as smoke, light, and sound. Only a click of metal impact is audible. The process has been used to join 6061-T6 aluminum tubes 2 and 4 in. (5 and 10 cm) in diameter and 0.063 in. (1.60 mm) in wall thickness, yielding joints of the same strengths as the parent metal.

Before the joining operation, the edge of the male tube is machined to a V-shape (see Figure 1), and the female tube is flared if it is not already of a larger diameter (as shown). The joining procedure is as follows:

a. A ring-shaped ribbon explosive is attached inside the male tube with a double-backed tape; the explosive centerline is directly over the peak of the machined area.
b. A blasting cap is taped to the center along the entire length of the ribbon explosive.
c. The male tube is inserted to any depth desired (limited only by the flared portion).
d. An anvil ring that prevents tube swelling is positioned outside over the explosive area.
e. The explosion is detonated remotely.

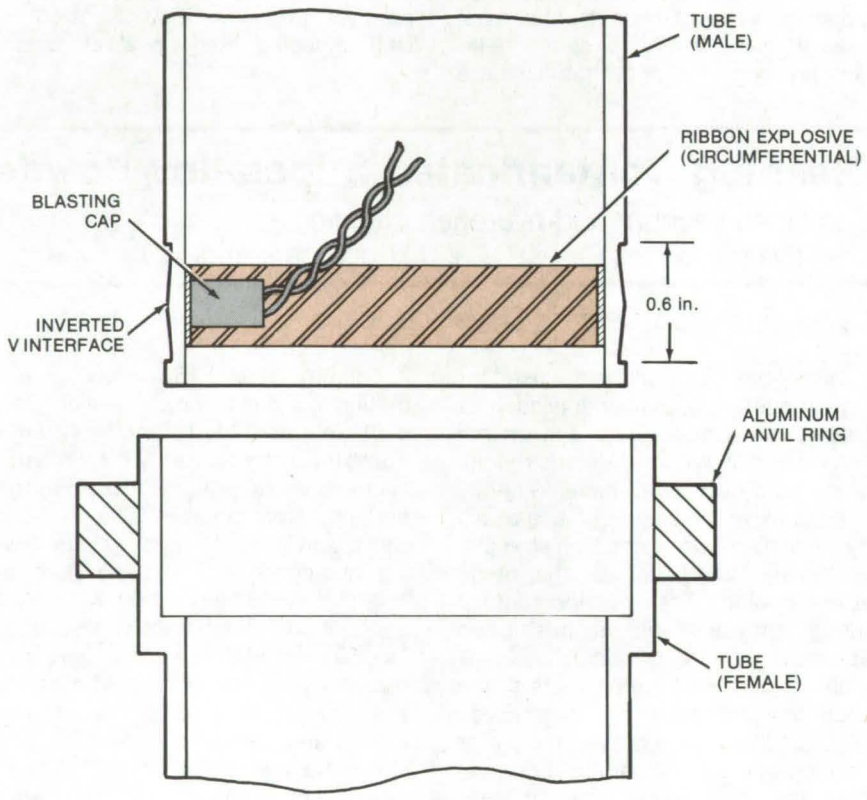

Figure 1. The **Tubes Are Joined Via Explosive Ribbon** activated remotely. During the explosion the wall of the male tube is driven against the wall of the larger-diameter (or flared) female tube. A strong interatomic bonding results at the interface.

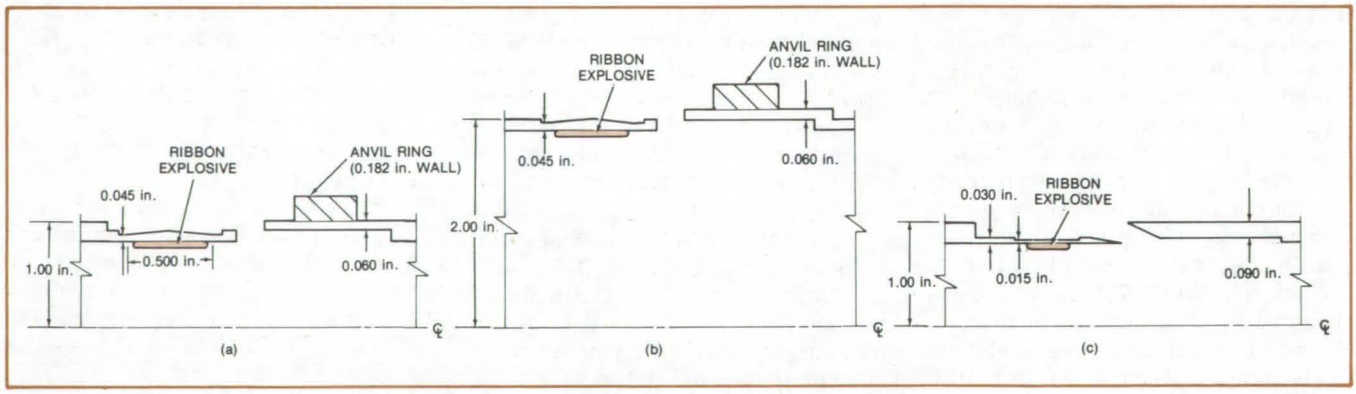

Figure 2. **Three Joint Configurations** have been studied: (a) a tube joint 2 in. (5 cm) in diameter having a 0.045-in. (1.14-mm) wall thickness, (b) a joint 4 in. (10 cm) in diameter, and (c) a tube 2 in. (5 cm) in diameter having a 0.015-in. (0.38-mm) wall thickness and using a weaker explosive without the anvil ring.

The process effaces the mating surfaces and presses the tubes together to effectively join them, producing interatomic bonding at the interface. Although currently tested in joining aluminum tubes with wall thicknesses to 0.125 in. (3.18 mm), the technique could be used to join thicker tubes.

Figure 2 shows three joint configurations that have been studied. In case (a), the joint was formed using a ribbon explosive rated at 15 gr/ft (32.9 mg/cm). The explosive was activated electrically. In two tests, the average joint strength of the 2-in. (5-cm) tube joint was 12,800 lb (56,960 N) [50,440 psi (3.48×10^8 N/m^2)], and the outside diameter of the tube expanded only 0.035 in. (0.89 mm).

In case (b), the tubes had a 4-in. (10-cm) diameter and a 0.060-in. (1.52-mm) wall thickness. An identical procedure was followed as in case (a). An average strength of the three joints tested was 23,240 lb (104,115 N) [41,382 psi (2.86×10^8 N/m^2)]. The explosion displaced the outside diameter to 0.045 in. (1.14 mm).

In case (c), the external aluminum ring was removed, and the explosive was reduced to 7 gr/ft (15.3 mg/cm). A lower strength interface was prepared as shown. Results, however, showed that two joints failed at an average of 3,195 lb (14,314 N) tension [38,414 psi (2.65×10^8 N/m^2)] and that three failed at an average of 2,310 lb (10,349 N) of compression, still parent metal strength.

The new technique can be used to join a wide range of tube diameters. Also, it can be used to join telescoping tubes at any final placement desired. The explosive ribbon can also be placed externally to join the tubes.

This work was done by Laurence J. Bement of **Langley Research Center** *and James W. Bailey of Vought Corp. For further information, Circle 75 on the TSP Request Card.*

Inquiries concerning rights for the commercial use of this invention should be addressed to the Patent Counsel, Langley Research Center [see page A8]. Refer to LAR-12248.

Low-Cost, High-Performance Separator for Alkaline Batteries

Ion-transporting polymeric films are fabricated by cross-linking polyvinyl alcohols in situ.

Lewis Research Center, Cleveland, Ohio

A new method for fabricating ion-transporting polymeric films and impregnates for use in alkaline electrolytes (e.g., concentrated aqueous potassium hydroxide) is based on the in situ self-cross-linking of polyvinyl alcohol with periodic acid. Treatment of polyvinyl alcohol with an aqueous solution containing periodic acid converts the water-soluble linear polyalcohol to a cross-linked insoluble material. Although the cross-linked polymer has a somewhat lower ionic conductivity in concentrated aqueous potassium hydroxide than the linear polymer, cross-linked polyvinyl alcohol films have significantly greater mechanical strength and increased resistance to chemical attack. Cross-linked polyvinyl alcohol films and impregnates have application for such devices as electrode bags, battery separators, and electrolytic cell diaphragms.

The first step in the process is the casting of the film, or the impregnation of a suitable matrix such as an asbestos sheet, with the polymer from an aqueous solution of polyvinyl alcohol. The dry film or impregnated asbestos sheet is then fabricated into an electrode bag, battery separator, or cell diaphragm. This fabricated article is subsequently treated with hot aqueous periodic acid, which effects cross-linking. Following the periodic acid treatment, the article is washed with water, then with dilute aqueous sodium bicarbonate to neutralize acid residues, and finally with water. The article is air-dried at room temperature.

A typical cross-linking treatment for a 6-mil-thick (0.15-mm) polyvinyl alcohol heat-sealed electrode bag is to immerse the bag in the following periodate solution at 90° C for about 30 minutes:

Periodate Solution	
Water	1 to 1.5 liters
KIO_4 or $NaIO_4$	50 g
Concentrated H_2SO_4	50 ml
Na_2SO_4	200 g

The Na_2SO_4 salts out the water-soluble bag film during treatment. Commercial-grade polyvinyl alcohol, although essentially a 1,3 diol, contains about 1 to 6 percent of 1,2 diol units in its polymer chain. These 1,2 diol units are readily cleaved by oxidation and, if nonspecific, can lead to the breakdown of the polymer backbone, thereby weakening the mechanical strength of polymer films. In this new technique, periodic acid oxidizes and cleaves the 1,2 diol with the specific formation of aldehyde end groups. The aldehyde end groups in acid media then react with the 1,3 diol units of polyvinyl alcohol to form acetals. The polymer chains are thus extended and cross-linked.

Other oxidizers involving a valence change of two such as ceric salts and tetravalent lead may also be used; however, the carefully controlled conditions required with ceric salts to prevent further oxidation of the aldehyde end groups and the necessity of using organic solvents for tetravalent lead salts (such as lead tetraacetate) have numerous disadvantages over the use of periodate solutions.

A major advantage of these strong, more chemically resistant films separators lies in their ease of fabrication. These ion-transporting polymeric films are fabricated and cross-linked in an aqueous system, thus avoiding the use of hazardous organic solvent.

This work was done by Li-Chen Hsu, Warren H. Phillipp, and Dean W. Sheibley of **Lewis Research Center.** *Further informaton may be found in NASA TP-1407 [N79-21128], "Three in situ Crosslinking Methods for Polyvinyl Alcohol Films for Application*

(continued on next page)

as Ion Conductors in KOH Electrolyte," a copy of which may be obtained at cost from the New England Research Application Center [see page A7].

This invention is owned by NASA, and a patent application has been filed. Inquiries concerning nonexclusive or exclusive license for its commercial development should be addressed to the Patent Counsel, Lewis Research Center [see page A8]. Refer to LEW-12972.

Splicing Single-Mode Optical Fibers

Small-diameter waveguides are welded in a special fixture.

NASA's Jet Propulsion Laboratory, Pasadena, California

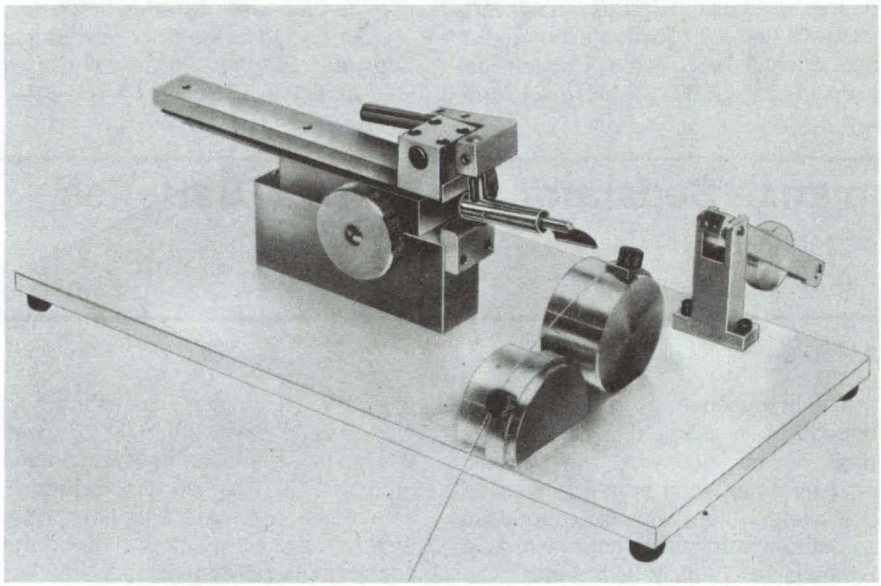

Figure 1. This **Precision Cleaver** with a tungsten carbide knife edge cuts single-mode optical fibers for welding.

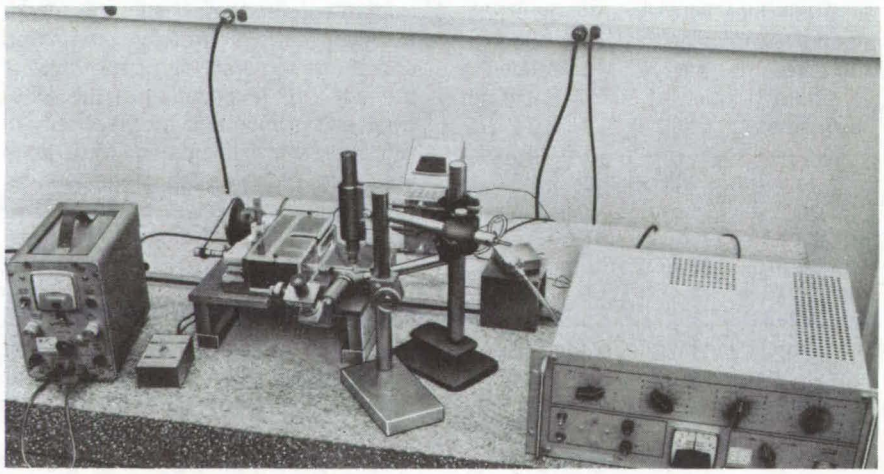

Figure 2. The **Welding Apparatus** includes a micromanipulator, microscopes, and vacuum chucks.

It is difficult to aline and weld single-mode optical fibers without changing the refractive index or causing reflections at the welded junction. A typical single-mode fiber has a light-carrying core that is only about 4.5 microns in diameter, which is considerably smaller than the 85-micron core of multimode fibers. Although, for strength, the outside diameters of both types are typically 100 microns, alinement is much more critical with the smaller-core single-mode fibers. Now, however, an approach that has been used to weld multimode fibers has been adapted for the more exacting splicing of single-mode fibers.

The fiber ends are first cleaved with a precision cleaver (Figure 1) to give a smooth, square surface suitable for a butt joint. The fibers are then locked in a vacuum chuck on a three-axis micromanipulator, are guided into contact with the aid of two microscopes, and are butted together with a slight pressure (see Figure 2). An electric arc is passed over the fibers to weld them. Finally, the weld is checked optically by shining a laser through one of the fibers and observing the end of the other for maximum transmittance.

This work was done by Raymond Goldstein and Willis C. Goss of Caltech for **NASA's Jet Propulsion Laboratory.** *For further information, Circle 76 on the TSP Request Card. NPO-14626*

High-Energy-Density Cylindrical Capacitors

Manufacturing technique for wound metalized-film capacitor

Lewis Research Center, Cleveland, Ohio

A manufacturing technique has been developed for producing high-quality metalized-film cylindrical capacitors of energy density greater than 0.1 J/g uncased, using either 24-gage (6-μm) polyvinylidene fluoride (PVF2) film or 14-gage (3.5-μm) polycarbonate (PC) film. The film components are wound wrinkle-free on hollow PTFE cores, using a winding machine that applies constant dynamically controlled tension to the film during the winding operation.

These capacitors can be used in electronic applications where minimum weight and size are required, since they are between 20 and 50 times lighter than conventional components. The winder is shown in Figure 1. The film bobbins are mounted on torque-motor shafts, and tensions for the widths and gages of the films used are controlled by setting the level of the 60-Hz input to the motors. The spindle is located midway between the film bobbins, with smoothing rollers located on either side of the spindle.

To wind a capacitor, a tubular PTFE core is mounted on the winding mandrel with the smoothing-roller fixture in place. The first film of the capacitor is alined over the core and then bonded to the core with adhesive.

Before bonding the second film to the core, metalization is removed around the bonding area on the second film to provide a margin at the beginning of the second film. The film is alined and bonded to the core, and the excess film is cut away. After winding the desired length of film, metalization is again removed from the end of the second film, and the second film is wound into the capacitor pad. The first film is cut, and the component is tied off with a piece of tape. After removal from the winder, the core ends are trimmed, and the component is ready for electrical termination with flame-sprayed tin alloy.

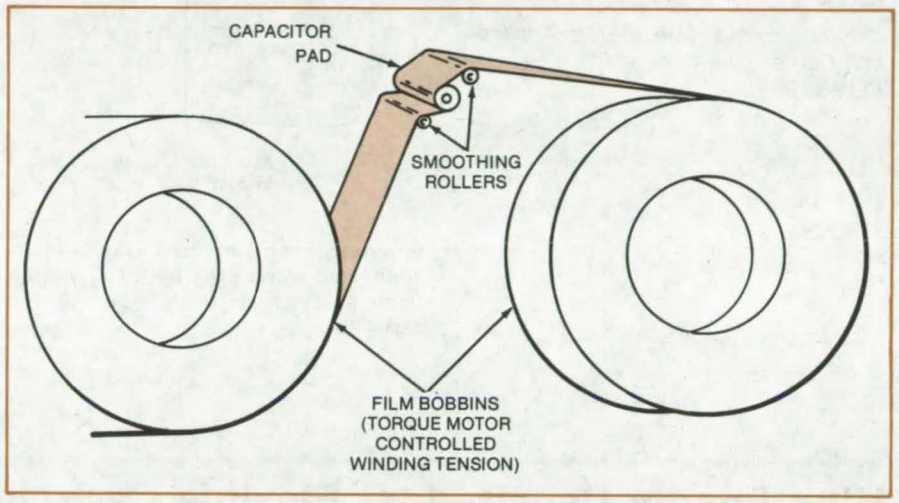

Figure 1. The **Capacitor-Winding Configuration** as shown in the simplified drawing above is used to apply a constant dynamically controlled tension to the metalized film.

The electrical connection to the metalization is accomplished by a variant of extended-foil construction common to larger components. Flame-sprayed tin alloy is used to connect the alternate layers, shown in Figure 2. A wire with two gold leads welded on is inserted into one end of the core, and the two gold leads are ultrasonically soldered to the tin, shown in Figure 3. The larger wires protrude through the case for the final termination. This termination is not particularly porous to capacitor impregnants, so stripes are masked off on each end and remain unsprayed to enhance impregnation.

Numerous fluids are used for capacitor impregnation, so the impregnation process is necessarily tailored to the peculiarities of the particular fluid. The process described here is for mineral oil. Very slight modifications are used for silicone fluids.

The capacitor sections are placed in a vacuum oven and baked at a temperature above 100° C (212° F) for at least 24 hours. While the sections are being baked, the fluid is treated to remove particles, moisture, and ionic contaminants. Particles are removed by filtering; moisture, by vacuum baking; and ionic contaminants, by clay filters. During this process, the impregnation fluid is also degassed by a vacuum-bake cycle. The cycle lasts 24 hours at 100° C and at 10 microns pressure or less.

The baked components are removed from the vacuum oven and placed in an oil impregnation unit. This apparatus consists of a heated vacuum chamber, an evacuated fluid storage reservoir, connecting tubes, and miscellaneous fixtures. The components remain in the heated evacuated chamber for 3 hours and are then filled with heated fluid from the fluid storage reservoir. Following this, the components are allowed to cool under vacuum to room temperature. Then the vacuum is broken, and the component cases are sealed.

The finished capacitor is corona-tested at 600 Vdc for 3 minutes. If no corona pulses are observed, the capacitors are considered to be of satisfactory quality. [For a related Tech Brief, see the following article (LEW-13000).]

(continued on next page)

This work was done by Robert D. Parker and Joseph A. Zelik of Hughes Aircraft Co. for **Lewis Research Center.** *Further information may be found in NASA CR-135286 [N78-24458], "Technological Development of Cylindrical and Flat Shaped High Energy Density Capacitors," a copy of which may be obtained at cost from the New England Research Application Center [see page A7].*
LEW-12999

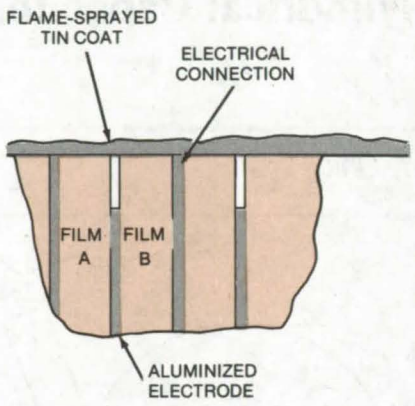

Figure 2. **Each Metalized Film Is Interconnected** electrically by a tin coating flame-sprayed on the "edge" of the capacitor.

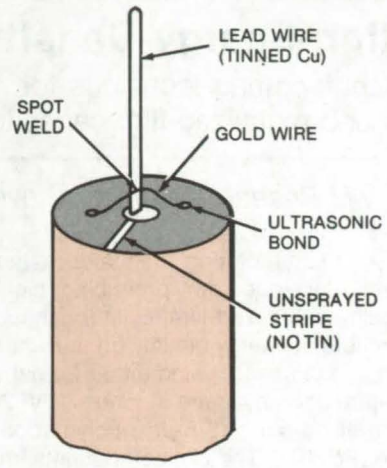

Figure 3. The **Capacitor End Connection** is a large lead wire inserted into the core and two smaller gold wires ultrasonically soldered to the tin coat. Only one termination is shown here; a similar one terminates the other film on the opposite side.

High-Energy-Density Flat Flexible Capacitors

Manufacturing technique produces uniform unwrinkled laminates.

Lewis Research Center, Cleveland, Ohio

A manufacturing technique has been developed for producing flat flexible capacitors of energy density greater than 0.1 J/g. These capacitors are of nominal 2-μF capacitance and consist of 11 layers of metalized 24-gage (6-μm) polyvinylidene fluoride (PVF2) capacitor film. They measure 6.3 inches (16 cm) long, 4.18 inches (11.2 cm) wide, and 0.003 inch (76.2 μm) thick. The overall width of the finished capacitor is wider than the 4.5-inch (11.4-cm) width of the film since the metalized edge of each successive layer is laid up 0.025 inch (0.063 cm) beyond the edge of the previously-laid-up layers. The resultant exposure of some of the metalized surface of each layer provides sufficient film surface to ensure good electrical connection to each layer of the capacitor.

The capacitors are relatively flexible and can be cemented to irregularly shaped surfaces. The capacitors are completely self-contained and need no case or impregnant because of their monolithic construction. Because of their unusual form, heat is dissipated more readily than with conventional designs. Energy densities 20 times greater than conventional designs are obtained.

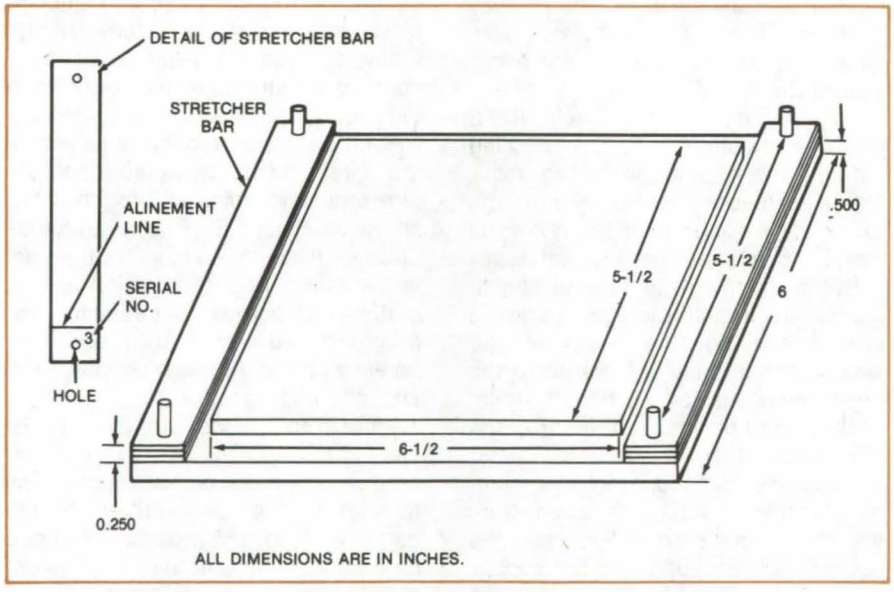

Figure 1. **Layup Fixture** for producing flat flexible capacitors holds each layer taut and without wrinkles at a precise position within the laminate.

To produce a high-quality flat capacitor, the component is laid up by using a fixture (Figure 1) that holds each layer taut and wrinkle-free and in a precise position within the laminate.

The first step in the fabrication of a flat capacitor is the attachment of stretcher bars to the film. A length of film adequate for five or six capacitor

layers is unrolled and held taut between two metal blocks with the metalized surface facing upward. Transfer adhesive is applied to the top surface of the stretcher bars. A pair of stretcher bars is placed on the laminating fixture with a spacer under each bar to hold it level with the midportion of the fixture. The fixture is placed under the film, and the film is carefully alined with the stretcher bars. The film is attached to the bars by pressing on the film near the centers of the stretcher bars and then smoothing the film along the bars with a tongue depressor. The bars are carefully lifted from the fixture, the fixture is repositioned, and another pair of bars is attached. The process is repeated until all the pairs of stretcher bars are attached to the film. The film is then cut into the individual layer segments, and the segments are hung using the stretcher bars to prevent wrinkling of the film.

An additional margin is etched on each film segment perpendicular to the existing film margin. This is done by placing the segments on the fixture and etching away the metalization along a zone 1/4 inch (0.635 cm) wide centered on the line that will be the edge of the finished component.

When laying up the capacitor, successive layers are rotated 180° with respect to the previous layer, so that the component has margins at all edges.

The layup procedure begins by covering the fixture with a sheet of nylon. Laminating adhesive is puddled on the nylon and distributed, using a squeegee. The adhesive acts as a lubricant to prevent damage to the first layer of the component during the squeegeeing operations. When cured, the adhesive weakly adheres to the nylon sheet. The first layer of the capacitor is laid onto the fixture with the metalized surface facing the fixture and is alined by the stretcher bars. Laminating adhesive is puddled onto the film and spread with the squeegee. Each additional layer is added, and the adhesive is applied and squeegeed as for the first layer. The layers are laid up with the metalized surface facing the fixture and in sequence such that each successive layer increases the overall width of the component by extending its metalized edge 0.025 inch beyond the edge of the existing layup. The lamination process is completed by adding a nylon vacuum bag and sealing it with a vacuum bag sealant. The bag is evacuated, and additional squeegeeing is done to remove all excessive adhesive from the laminate. Figure 2 shows the basic layup scheme for the finished component.

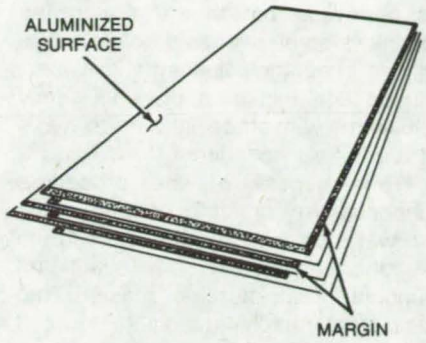

Figure 2. The **Finished Layup Scheme** for a flexible flat capacitor is a pyramid-like construction.

The squeegeeing operation must be done very carefully to be sure that the adhesive is completely distributed between each layer, so that no voids remain and the films are not damaged by wrinkling or by the metalization being scratched or cracked.

The laminate is cured for 17 hours at room temperature and then for 3 hours at 120° F (49° C). The component is removed from the fixture by cutting through the vacuum bag along the stretcher bars. The nylon surface layers are carefully peeled away, and the component is trimmed through the centerline of the etched margin areas with scissors.

Epoxy stripper is used to remove the laminating adhesive from the electrical contact areas of the capacitor. Conducting epoxy is applied over the contact areas, and one or more No. 32 AWG bare copper wires are embedded along the entire length of the contact area. The wires are extended one or more inches beyond the edge of the component to provide leads for the capacitor. The conducting epoxy is cured either at room temperature for 8 hours or at 160° F (71° C) for 3 hours.

The finished capacitor is corona-tested at 600 Vdc for 3 minutes. If no corona pulses are observed, the capacitors are considered to be of satisfactory quality. For a related Tech Brief, see the preceding article (LEW-12999).]

This work was done by Robert D. Parker and Joseph A. Zelik of Hughes Aircraft Co. for **Lewis Research Center.** *Further information may be found in NASA CR-135286 [N78-24458], "Technological Development of Cylindrical and Flat Shaped High Energy Density Capacitors," a copy of which may be obtained at cost from the New England Research Application Center* *[see page A7]*.
LEW-13000

Removing Overcoatings From Microcircuits

Concentrated sulfuric acid speeds up removal of silicone or elastomer.

Marshall Space Flight Center, Alabama

Silicone resin or elastomer overcoatings are removed more quickly from microcircuit chips with hot concentrated sulfuric acid. The process takes a few minutes as compared to a day or two, using commercial solvents based on toluene, xylene, and the like. The overcoatings are removed to expose the circuit for failure analysis.

The basic apparatus needed are a hotplate and a stirrer, a heat-resistant glass beaker, stainless-steel tweezers, and a hood or other area for work-

(continued on next page)

ing with dangerous fumes. The beaker is filled with 97 percent pure (or purer) sulfuric acid and is heated to 65° to 75° C. Since sulfuric acid is very hazardous, approved safety procedures and equipment must be used.

A decapped chip is immersed in the hot acid for 5 to 10 min, depending on the overcoating thickness. The liquid is mildly agitated with the stirrer operating at a very low speed. Slow agitation reduces the possibility of damage to the lead wires or the chip themselves. The processed device is removed from the acid with the stainless-steel tweezers. Next, it is rinsed in ethanol, flushed with water, rinsed again in ethanol, and gently blown dry with air or nitrogen to make it ready for inspection.

The success of the procedure depends very critically on there being no water on the microcircuit or in the sulfuric acid. When any significant amount of moisture is present, the acid very rapidly attacks the circuit leads and metalization. As a precaution, the acid can be preheated for approximately an hour to drive off water. (This must be done with approved safety measures.) When these precautions were taken, no corrosion of either gold or aluminum metalization or of leads was found in circuits that were immersed in the acid.

This work was done by J. G. Belcher, Jr., David P. Nicolas, and Felminio Villella of **Marshall Space Flight Center.** *No further documentation is available.*
MFS-23851

Economical Solder Connections to Thin Films

Leads can be attached to transparent conductive oxide films with indium/silver or indium/tin solders.

Goddard Space Flight Center, Greenbelt, Maryland

Vapor-deposited conducting films are used in liquid crystal displays, radio-frequency shields, window defrosters, solar cells, and some solar-cell coverglasses. Among approaches developed to attach wires to the film are multilayer depositions of metallic contacts followed by soldering or welding, a procedure that can be prohibitively expensive, and the application of a conductive paste or epoxy, a method that tends to give electrically unstable contacts.

However, a new soldering procedure, successfully tested for attaching leads to silicon solar cells, coverglasses, is simple, inexpensive, and very effective in forming a stable connection. The procedure uses solder of indium alloyed with either silver or tin. The 90-percent indium/10-percent silver and 50-percent indium/50-percent tin compositions have been found to be effective. For these alloys, indium oxide forms on the solder bead, which ensures good electrical contact with the conductive film layer.

Indium/silver solder has been used to attach leads to films of indium oxide (20 to 500 angstroms in thickness) on silicon solar cells. First, the indium oxide surface is washed with an alkaline detergent to remove contaminants, and the surface is rinsed with distilled water to remove the detergent.

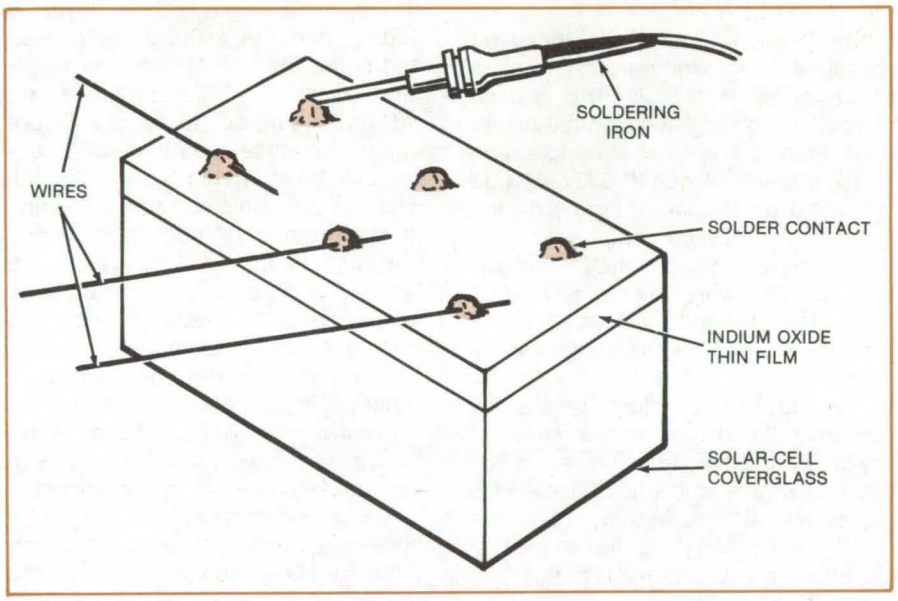

Molten Indium/Silver Solder is applied to an indium oxide film to form a contact. Wires are "tinned" with the solder and attached to the contact with a soldering iron.

An acetone wash is used to dry the indium oxide surface, and the indium/silver is heated to 290° C (40° C above its melting point) by an adjustable-temperature soldering iron. The molten alloy is rubbed on the indium oxide surface with the soldering iron until the alloy wets the surface and forms a blob (see figure). No flux is used in applying solder to the thin film since flux prevents the solder from forming the indium oxide outer layer essential for electrical and mechanical contact.

Finally, a tin-plated copper wire is attached to the blob of indium/silver solder. The wire is first cleaned with a rosin flux at 200° C, and the flux is rinsed away in ethyl alcohol. Indium/silver is applied to the tip of the wire with the soldering iron. The tip of the wire is placed on the indium/silver contact on the thin-film surface and is again heated with the soldering iron.

The contact and the solder on the wire flow together to form a strong, electrically conductive bond upon cooling.

This work was done by James A. Bass and Edward M. Gaddy of **Goddard Space Flight Center.** *For further information, Circle 77 on the TSP Request Card.*

This invention is owned by NASA, and a patent application has been filed. Inquiries concerning nonexclusive or exclusive license for its commercial development should be addressed to the Patent Counsel, Goddard Space Flight Center [see page A8]. Refer to GSC-12404.

Lift-Off Procedure Improves Pattern Definition

Layer of TiO_2, economically deposited during integrated circuit fabrication, allows "nonpattern" metal to be removed cleanly.

Langley Research Center, Hampton, Virginia

A new economical procedure more reliably forms the "negative angle" needed for "lift-off" in the fabrication of silicon integrated circuits. In making these circuits, a photoresist pattern is usually applied and followed by a blanket metal deposition. The underlying photoresist is then removed, and the metal is lifted off over all but the desired regions. This lift-off of the unwanted metal requires a negative angle around the edges of the desired pattern to insure clean removal of the metal on top of the photoresist layer without damaging the metal within the pattern.

In one earlier technique, the exposed photoresist layer was immersed in chlorobenzene before developing. This made the upper photoresist regions etch more slowly than the regions near the substrate, so that a negative angle was produced upon development. Another procedure was to deposit a specially sensitized photoresist, deposit a membrane of a much-slower-etching resist, and expose and develop conventionally. A negative angle was produced by the two different etch rates. Both these techniques were somewhat unreliable: They worked well under some conditions but not under others.

In a third, more reliable method, an aluminum layer was deposited between the two photoresist layers to prevent the second layer from dissolving the first layer. However, this aluminum-layer-evaporation method was costly and time consuming.

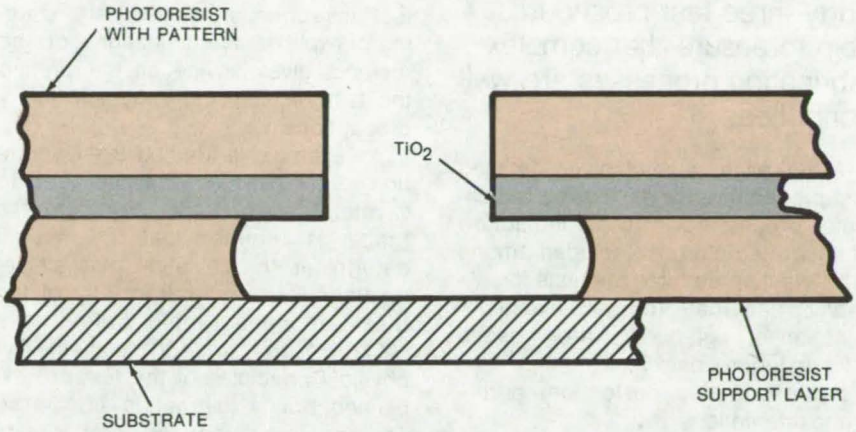

A **Negative Angle** is formed between two photoresist layers on a substrate for a silicon integrated circuit. The bottom photoresist layer was exposed throughout; the top layer was exposed according to the pattern. The pattern on the top layer was developed without affecting the bottom layer because of the protective TiO_2 layer. The TiO_2 under the pattern was etched away with HF. The bottom layer was then developed sufficiently to produce the undercutting shown above.

A more economical variation of the third method has been developed. Titanium dioxide (TiO_2) is deposited instead of aluminum. In this new process a first photoresist layer is deposited, the layer is blanket-exposed, and a TiO_2 layer is deposited by the low-temperature $Ti[OCH(CH_3)2]4$ (tetraisopropyl titanate) spray process, followed by a second photoresist layer.

The pattern is exposed onto the second photoresist layer and is developed down to the TiO_2 layer, which is easily etched in buffered HF. Finally, the sample is developed again. The thickness of the first photoresist layer and the second development period can be adjusted to obtain the desired degree of undercutting (see figure).

The main advantage of this process is that the TiO_2 can be deposited in air in a few minutes by a spray process that adds negligible cost. The TiO_2 can be deposited at a temperature as low as 45° C and will not affect the first photoresist layer. Thus, the process is not only reliable but also economical.

This work was done by H.J. Hovel and H.A. Huggins of IBM Corp. for **Langley Research Center.** *No further documentation is available.*

Inquiries concerning rights for the commercial use of this invention should be addressed to the Patent Counsel, Langley Research Center [see page A8]. Refer to LAR-12392.

Books and Reports

These reports, studies, and handbooks are available from NASA as Technical Support Packages (TSP's) when a Request Card number is cited; otherwise they are available from one of NASA's Industrial Application Centers or the National Technical Information Service.

Quality Control During IC Processing

Forty-three test procedures help to ensure that complex fabrication processes are well controlled.

A 260-page manual gives detailed test procedures for controlling silicon-wafer processing in the manufacture of integrated circuits. Included among the 43 test procedures are tests for:

- ionic, bacterial, and solids contamination of high-purity water needed for wafer processing;
- crystallographic perfection, purity, and orientation;
- substrate dimensions and finish;
- thickness of deposited epitaxial films;
- oxide quality;
- photoresist characteristics;
- pinholes in insulating layers;
- metalization adhesion; and
- quality of ohmic contacts.

Many other procedures for measuring physical and chemical properties of the substrate and IC structures are discussed.

For each method, the reader is told the purpose, the apparatus and materials needed, and the step-by-step procedure. When appropriate, a diagram of the test setup is included, as is information on calibration and accuracy of test instruments. A summary statement explains the limitations of the method, gives advice on interpreting the test results, and suggests safety precautions.

An example is Method 8, "Orientation of Substrate with Respect to Crystal Plane." Under Purpose, the reader is informed that the method determines the deviation of a single-crystal silicon wafer from one of the three crystallographic orientations (⟨111⟩, ⟨110⟩, or ⟨100⟩ planes). The physical principles of the test are explained briefly (diffraction of X-rays). The equipment required for the tests comprises an X-ray generator with a copper target, a goniometer calibrated in degrees and minutes, and a detector such as a Geiger counter.

The procedural steps are listed, including orientation and reorientation of the sample in the goniometer, exposure to X-radiation, and calculating the orientation from the measured data.

Under Summary, the reader is warned of X-ray hazards and is given practical hints on calibration, particularly the physical relationships among the X-ray beam, the sample holder, the reference surface, and the detector assembly. A diagram shows the relative positions of X-ray source, wafer, holding fixture, rotating table, and detector.

For many of the test procedures, the American Society for Testing and Materials has published acceptable alternative methods. The manual identifies these ASTM methods. For instance, ASTM F26, "Determining the Orientation of a Semiconductive Single Crystal," is mentioned as an alternative to Method 8.

This work was done by Integrated Circuit Engineering Corp. for **Marshall Space Flight Center.** *For further information, Circle 78 on the TSP Request Card.*
MFS-25112

Mathematics and Information Sciences

Hardware, Techniques, and Processes

Books and Reports

Programing Techniques for CDC Equipment

Core requirements are decreased, and throughput and versatility are increased.

Langley Research Center, Hampton, Virginia

Five new techniques reduce core requirements for fast batch turnaround time and interactive-terminal capability. These same techniques increase program versatility, decrease problem-configuration dependence, and facilitate interprogram communication. They are:

1. *Dynamic Storage Allocation* — Precise allocation (by input) of core requirements for individual jobs: No recoding is required when problem dimensions change.
2. *Automatic Core Sizing* — Computation of core requirements performed by the program during job execution based on input dimensions: This can be done several times during execution (for example, when a new overlay is called), thereby controlling the core allocation more precisely to that actually required. Costs are reduced, and computer resources are used more efficiently.
3. *Matrix Partitioning* — A means of handling operations involving matrices in sections when the matrices are too large to load into core: This enables one to analyze large problems and make efficient tradeoffs between input/output and core-storage requirements.
4. *Free-Field Alphanumeric and Integer Reading Combinations* — Enables the user to read in alphanumeric and integer variables using a free-field format; i.e., unformatted: This is especially helpful for interactive terminal use where alphanumeric names are a convenient form of input for the user.
5. *Incorporation of a Data Complex and Data-Complex Manager* — Relieves the user from much of the drudgery of data management and storage: This makes it easier to tie together programs with related inputs and outputs.

The programs to which the techniques were applied analyzed different aircraft configurations. Earlier, each change in the configuration necessitated recoding many of the array dimensions involved in the program. Also, large-core programs do not lend themselves to interactive use, since response time is somewhat proportional to core length. These problems led to the use of dynamic storage allocation and automatic core sizing. For many configurations the associated arrays were too large to retain in core at one time; this led to the necessity for partitioning arrays.

The last problem attacked was interprogram communication. To analyze different configurations, several programs had been developed to generate data for the analysis program; and much effort was spent in storing and saving data between programs, requiring a great deal of file management and editing. The data complex and its associated management routines were developed to facilitate this process.

In the report cited at the end of this article, several sample programs are presented that illustrate the five programing techniques. They were implemented on Control Data Corporation equipment.

This work was done by Jerry R. Newsom and Sherwood H. Tiffany of Vought Corp. for **Langley Research Center.** *Further information, including sample programs, may be found in NASA CR-3033 [N78-28832], "Some Programming Techniques for Increasing Program Versatility and Efficiency on CDC Equipment," copies of which may be obtained at cost from the North Carolina Science & Technology Research Center* [see page A7].
LAR-12486

Comparing Data Transmission Systems

The transmission rates of schemes for transmitting image and scientific data are graphed for easy comparison.

NASA's Jet Propulsion Laboratory, Pasadena, California

Schemes for coding and compressing data signals for transmission are compared by a new analytical technique. The transmission rate of several schemes are plotted for direct comparison and evaluation.

The comparison technique was developed for spacecraft communication systems that carry both image data and general-science and engineering (GSE) data signals. Usually, GSE data demand much lower error rates than image data. By using the new comparison method, it is possible to select an efficient transmission scheme, while ensuring that the error-rate requirements of all data are satisfied.

In the analysis, it is assumed that the GSE transmission rate is fixed and that this rate is the same for all systems being compared. One system is selected as a reference or "baseline" by fixing an allowed probability of error. Its maximum information-transmission rate is determined by fixing an allowed probability of error and considering such factors as its power and antenna capabilities.

(continued on next page)

The image-data-transmission rate for the baseline (the difference between the total information rate and the GSE rate) is then compared with calculated image-data rates for the other systems. The others can have higher or lower rates depending on how much better or poorer they protect against transmission errors. Equations for evaluating the transmission rates of the coding schemes are solved, using basic algebra, and plotted as a function of the fractional GSE rate for the baseline.

An uncoded channel is the baseline in the figure; it is compared with:

- Golay compression/uncoded transmission;
- convolutional coding/viterbi decoding;
- convolutional/Viterbi/Golay transmission, and
- advanced imaging communication system (AICS), which uses a combination of several compression, coding, and decoding algorithms.

Alternatively, any one of these systems could be the baseline, and the others can be compared with it.

This work was done by Robert F. Rice of Caltech for **NASA's Jet Propulsion Laboratory.** *For further information, Circle 79 on the TSP Request Card.*
NPO-14642

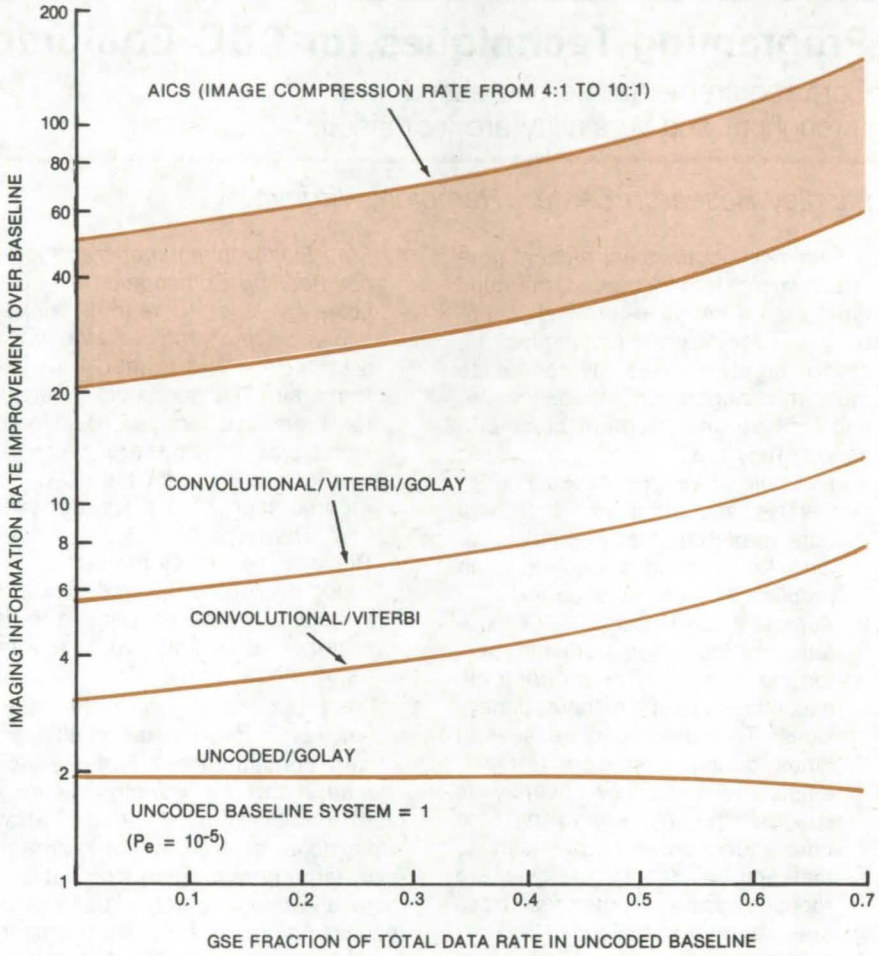

Data-Transmission Coding Systems are compared. With an uncoded system as the baseline, operated with an error probabiliby of 10^{-5}, the coded systems have higher image-transmission rates. If, for example, the power and antenna of the baseline can transmit at 1,000 bits per second and a GSE rate of 500 bits per second is required (f = 0.5), 500 bits per second would be available for image data. Using the AICS, the image-transmission rate is imporved by a factor of from 37 to 93, giving an image-data rate of up to 46,500 bits per second.

Computer Programs

These programs may be obtained at very reasonable cost from COSMIC, a facility sponsored by NASA to make new programs available to the public. For information on program price, size, and availability, circle the reference letter on the COSMIC Request Card in this issue.

Annuity-Estimating Program

Values of many options and possible situations are computed.

A newly available program computes benefits and other relevant factors for Federal Civil Service employees. Computed information includes:

- Retirement annuity (with and without survivor benefits) — optional, deferred, discontinued service, disability, or mandatory;
- Survivor annuity for each retirement annuity;
- Highest average annual consecutive 3-year salary;
- Length of service including credit for unused sick leave;
- Amount of deposit and redeposit plus interest;
- Effective date of disability retirement at expiration of sick leave;
- All of the above for the future for assumed future cost-of-living increases;
- Calculation of annuity at the last cost-of-living date and at the retirement date;
- Calculation of annuity at some assumed next cost-of-living date;
- Reduction in annuity for age under 55 years;
- Reduction in annuity for not repaying deposits; and
- Maximum annuity — 80 percent of the 3-year salary plus benefit from accumulated sick leave.

The program is written in FORTRAN IV for execution in the batch mode and has been implemented on an IBM 360 with a central memory requirement of approximately 54K (decimal) of 8-bit bytes.

This work was done by Don W. Jillie of **Ames Research Center.** *For further information, Circle K on the COSMIC Request Card.*
ARC-11139

Multipurpose Interactive NASA Information System

General-purpose modular system for manipulating data bases on small computers

The Multipurpose Interactive NASA Information System (MINIS) is a data-management system capable of retrieving descriptive data from Landsat photos. General enough to be used with other user-defined data bases, this interactive data-management and information retrieval system was especially developed for small and medium-size computers. It uses a free-form data base that allows one to create entirely new and different data bases and to control the format of output products.

Each major function of this interactive modular system is invoked by user requests in Data Base Access Language (DABAL). This language can be used to form sets, to perform mathematical calculations, to define new variables from the combinations of data-base fields and other variables, to sum a field or variable within a set, and to invoke any of the other modules in MINIS.

Because of its modular structure, additional features may be readily attached to MINIS. For instance MINIS has been used with Landsat photodescriptive data bases, land-use data bases, and census/socioeconomic data bases.

The program accommodates fixed-length-record data bases with up to 200 fields and as many records as available mass storage will permit. For each data base established, there are several files that must be defined and several optional files that can help data-base searches. The file-definition file is an information list of the other files and is automatically updated as files are changed. The main data file contains the actual data that make up the data base. The field-definition file represents a map for a data-base record. The user-message file contains all field titles, saved text, headers, formats, and namelists. Index files speed up the process of set formation by cross-referencing the value of a certain field and the corresponding record numbers.

The first step in working with a data base is to invoke the data-base-select module, which loads the data definitions, indexed variable information, and any special vocabulary. Control then passes to the main-system module, which accepts user commands and calls up the compiler routines to generate an internal interpretive code. This code invokes the appropriate execution submodule.

An argument list is automatically composed for subroutines with a variable list. The module is then loaded, and control is transferred to it with a pointer to the argument list. As each module completes its operation, program control is returned to the main-system module.

MINIS is coded in FORTRAN and Assembler for interactive execution and has been implemented on NOVA 1200 minicomputer under the ROS operating system.

This program was written by J. M. Hill, R. L. Keefer, D. R. Sanders, and R. N. Seitz of Computer Sciences Corp. for **Marshall Space Flight Center.** *For further information, Circle L on the COSMIC Request Card.*
MFS-23753

Model for Refining Operations

Production volumes are predicted, with emphasis on jet fuels.

A new program predicts the production volumes of petroleum refinery products, with particular emphasis on aircraft-turbine fuel blends and their key properties. It calculates capital and operating costs for the refinery and its margin of profitability. The program also includes provisions for the processing of synthetic crude oils from oil shale and coal liquefaction processes and contains highly-detailed blending computations for alternative jet-fuel blends of varying endpoint specifications. Volumetric and weight balances are computed along with sulfur, nitrogen, and hydrogen balances. Energy usage is reported in terms of net fuel power and steam consumption along with hydrogen usage.

The program requires basic information about the type and volume of crude oils used as feed and the specific refinery-processing units and their capacities. The complete slate of refinery products is then calculated with particular emphasis on accurately predicting the volumes and properties of jet fuel, distillage, and residual fuel-oil blends produced.

Economic calculations require the input of crude oil prices, refinery product realizations, electricity cost, and investment carrying charge. The model simulates refinery operation but does not optimize with respect to maximum dollar profit in the way that a linear-programing model does. The nonlinear relationships that have been programed, such as turbine-fuel smoke and freezing-point prediction, allow for greater accuracy than can be obtained in calculating the product blends normally obtainable with a conventional linear-programing approach.

An additional advantage is that less training is required, and less data input and program usage are needed in using a FORTRAN program as opposed to a complex linear-programing system. Optimization and parametric studies in general may be made by using the case-study feature incorporated into the model. This feature is used by establishing a base case and then specifying only the changes to the base case that are applicable to the case-study sequence. This reduces input requirements and permits large case-study sequences to be run without undue user or computer time.

The program contains two major data-base subroutines: (1) a Crude Assay subroutine and (2) a Refinery Process Yield subroutine. The Crude Assay subroutine comprises the yields and properties of the distillation products from a wide range of crude oils. The Refinery Process Yield subroutine contains typical process-unit yields, energy requirements, and stream quality factors for a variety of refinery-processing units. In addition, an economic-data base is included, which provides the fixed and variable components of operating costs and investment costs for individual refinery-process units.

This program is written in FORTRAN IV for the FORTRAN H compiler on an IBM 360, requiring approximately 400K bytes of central memory.

This program was written by Daniel N. Dunbar and Barry G. Tunnah of Gordian Associates, Inc., for **Lewis Research Center.** *For further information, Circle M on the COSMIC Request Card.*

LEW-13047

SUBJECT INDEX

*U.S. GOVERNMENT PRINTING OFFICE: 1979-281-448/3

National Aeronautics and
Space Administration

Washington, D.C.
20546

THIRD-CLASS BULK

NASA

The technology for this collapsible tower was originally developed for orbiting a large radio-telescope antenna. Today, with some modifications, the tower is commercially available as a support for stagelights and speakers, for antennas used in communications between firefighting crews, and as part of a transportable radar-site survey system. Variations of the design could be used for portable emergency bridges and scaffolding. [*See page A1.*]